

Development and Applications of Terahertz Near-Field Microscopes for Surface Plasmon Imaging

Raimund Mueckstein

A thesis submitted to the
University College London
for the degree of
Doctor of Philosophy

Department of Electronic and Electrical Engineering
University College London
May 2013

I, Raimund Mueckstein, confirm that the work presented in this thesis is my own. Where information has been derived from other sources, I confirm that this has been indicated.

Abstract

The confined nature of surface plasmons (SPs) often imposes challenges on their experimental detection and makes specific near-field probes necessary. While various SP detection methods have been developed in the optical domain, only a few examples of SP imaging have been reported in the terahertz range. In this thesis, specific problems of current terahertz near-field detection systems have been addressed which has led to the development of two new SP imaging methods.

In the first method, SP imaging is demonstrated using the integrated sub-wavelength aperture near-field probe. The photoconductive antenna inside the probe is sensitive to the SP electric-field despite the orthogonal spatial orientation between the antenna and the SP polarisation. This enables SP imaging directly on a metallic surface employing a photoconductive antenna. This unexpected sensitivity has been applied to SP imaging in two examples: first, the SP propagation has been imaged on a resonant THz bow-tie antenna and second, the SP excitation by a strongly focused terahertz beam directly on the metallic surface of the probe has been investigated.

The second method presents an electro-optic micro-resonator for SP imaging. A micro-resonator structure has the potential to provide a better sensitivity and spatial resolution, as well as a lower level of invasiveness compared to bulk crystals, which are commonly used in terahertz near-field systems. The micro-resonator design is explained in detail and the impact of the micro-resonator geometry on the probe operation is discussed. This micro-resonator has then been fabricated and embedded into an electro-optic detection system. This detection system has been fully characterised with the focus on two functional units which are essential for its performance: a tapered parallel plate waveguide for broadband terahertz transmission and the balanced detector for noise reduction. The overall performance of the detection system has been evaluated for its use as a terahertz near-field microscope.

Acknowledgements

First and foremost, I am grateful to my supervisor Dr. Oleg Mitrofanov for giving me the opportunity to work on such an interesting subject in order to pursue my doctoral thesis. His guidance, insight, and patience throughout the past three and a half years of my studies have been invaluable. Without his exemplary assistance, this work would have been impossible to accomplish.

I am also grateful to Dr. Miguel Navarro-Cía for the collaborative work during his post-doctoral research period at UCL, for the numerous discussions, and for his helpful attitude. I want to thank Prof. Huiyun Liu for putting so much effort into the fabrication of the electro-optic micro-resonator probe. I extend the same gratitude to all my colleagues and co-authors who I have interacted with over these years and whose names are, unfortunately, too many to mention here.

I also feel lucky and grateful for meeting many great people throughout these years who have made this period an extraordinary experience: my colleagues and friends from the UCL EE Department, from London, and from back home. In this context, I especially want to thank Matthew Ritchie, Carsten Behrens, and David Millar for being such wonderful friends. A very special thank you goes to my girlfriend Carolin for being such a supportive and encouraging character, especially during the last months of my project.

Finally, I want to thank my family and especially my parents for their support and all the sacrifices they had to make.

List of Publications

Contributions to Journals

- **Raimund Mueckstein** and Oleg Mitrofanov, "Imaging of terahertz surface plasmon waves excited on a gold surface by a focused beam," *Opt. Express*, Vol. **19**, pp. 3212-3217, February 2011.
- **Raimund Mueckstein**, Chris Graham, Cyril C. Renaud, Alwyn J. Seeds, James A. Harrington, and Oleg Mitrofanov, "Imaging and Analysis of Terahertz Surface Plasmon Polariton Waves with the Integrated Sub-wavelength Aperture Probe," *J. Infrared Milli Terahz Waves*, Vol. **32**, pp. 1031-1042, July 2011.
- Michele Natrella, Oleg Mitrofanov, **Raimund Mueckstein**, Chris Graham, Cyril C. Renaud, and Alwyn J. Seeds, "Modelling of surface waves on a terahertz antenna detected by a near-field probe, " *Opt. Express*, Vol. **20**, pp. 16023-16031, June 2012.
- **Raimund Mueckstein**, Miguel Navarro-Cía, and Oleg Mitrofanov, "Mode interference and radiation leakage in a tapered terahertz parallel plate waveguide, " *Appl. Phys. Lett.*, Vol. **102**, pp. 141103, April 2013.
- Miguel Navarro-Cía, **Raimund Mueckstein**, and Oleg Mitrofanov, "Comment on "The transition from a TEM-like mode to a plasmonic mode in parallel plate waveguides, " in *Appl. Phys. Lett.*, Vol. **98**, pp. 231113, June 2013.

Contributions to Conferences

- **Raimund Mueckstein**, Huiyun Liu, and Oleg Mitrofanov, "Development of an electro-optic resonator probe for Terahertz imaging," in *London Communications Symposium (LCS)*, London, Great Britain, September 2010.
- **Raimund Mueckstein** and Oleg Mitrofanov, "Imaging of Terahertz surface plasmon waves with a sub-wavelength aperture probe," in *Conference on Lasers and Electro-Optics (CLEO)*, Baltimore, USA, May 2011.

-
- **Raimund Mueckstein** and Oleg Mitrofanov, "Interpretation of THz surface plasmon patterns detected with sub-wavelength aperture near-field probe microscopy," in *4th Annual Meeting on THz sensing: techniques and applications organised on behalf of the Institute of Physics*, London, Great Britain, June 2011.
 - **Raimund Mueckstein** and Oleg Mitrofanov, "An integrated sub-wavelength aperture probe for surface plasmon imaging," in *International OSA Network of Students (IONS-10)*, Southampton, Great Britain, August 2011.
 - Oleg Mitrofanov and **Raimund Mueckstein**, "Near-field imaging of terahertz plasmon waves with a subwavelength aperture probe," in *SPIE 2011*, San Diego, USA, August 2011, paper 8096-4.
 - **Raimund Mueckstein**, Michele Natrella, Chris Graham, Cyril Renaud, Alwyn Seeds, and Oleg Mitrofanov, "Imaging and interpretation of surface waves on a terahertz bow-tie antenna," Presentation at *Metipho THz Summer School*, London, Great Britain, August 2012.
 - **Raimund Mueckstein**, Miguel Navarro-Cía, and Oleg Mitrofanov, "Origins of dispersive terahertz pulse propagation in tapered parallel plate waveguides," in *Conference on Lasers and Electro-Optics (CLEO)*, San Jose, USA, June 2013, paper CTh1K.5.
 - Michele Natrella, Oleg Mitrofanov, **Raimund Mueckstein**, Chris Graham, Cyril Renaud, and Alwyn Seeds, "Near-Field Probe Mapping of the THz Electric Field Distribution on Metallic Surfaces," in *Conference on Lasers and Electro-Optics (CLEO)*, San Jose, USA, June 2013, paper CM2J.3.
 - **Raimund Mueckstein**, Miguel Navarro-Cía, and Oleg Mitrofanov, "Understanding the Dispersion of THz pulses in Tapered Parallel Plate Waveguides: Role of the Multimode Propagation and Radiation Leakage," in *International Conference on Infrared, Millimeter, and Terahertz Waves (IRMMW-THz)*, Mainz, Germany, September 2013.

Contents

Abstract	3
Acknowledgements	4
List of Publications	5
1 Surface Plasmon Imaging in the Terahertz Range	10
1.1 The Promising World of Surface Plasmons	10
1.2 Theory of Surface Plasmons	12
1.3 Near-field Imaging of Surface Plasmon Polaritons	14
1.3.1 The Principle of Near-Field Imaging	15
1.3.2 Imaging in the Optical Domain	17
1.3.3 Imaging in the Terahertz Domain	18
1.4 The Research Project	24
1.4.1 Outline of this Thesis	26
2 Surface Plasmon Polariton Imaging with an Integrated Aperture Probe	28
2.1 The Coupling Mechanism	29
2.2 Surface Plasmon Polariton Imaging on a Bow-Tie Antenna	32
2.2.1 The Experimental System	32
2.2.2 Development of Surface Plasmon Polariton Patterns on a Bow-Tie Antenna	34
2.3 Surface Plasmon Waves Excited by a Focused Terahertz Beam	39
2.3.1 Imaging of Surface Waves Near a Focused Terahertz Beam	41
2.3.2 Surface Plasmon Character of the Detected Field Patterns	44
2.4 Suitability of the Integrated Near-Field Probe for Surface Plasmon Imaging	47
2.5 Conclusions	51
3 A Micro-Resonator for Electro-Optic Imaging	52
3.1 Optical Properties of Crystals	52
3.1.1 Isotropy and Anisotropy in Crystals	53
3.2 The Electro-Optic Effect	55
3.2.1 Mathematical Treatment of the Electro-Optic Effect	56
3.2.2 Physical Explanation of Electro-Optic Effect	57
3.2.3 The Electro-Optic Effect for Electric-Field Detection	58

3.3	Electric-Field Detection in the Literature	59
3.3.1	Electro-optic Detectors for Terahertz Surface Plasmon Imaging	61
3.4	The Fabry-Pérot Etalon	62
3.4.1	Fabry-Pérot Resonators in Electro-Optic Sampling	63
3.5	The Structure of the Micro-Resonator	64
4	Design and Fabrication of the Electro-Optic Micro-Resonator	69
4.1	Design Considerations	69
4.2	Simulation of the Micro-Resonator Response	74
4.2.1	Optical Admittance Approach	74
4.2.2	Model of the Refractive Index	75
4.2.3	Calculation of the Optical Response	78
4.3	Determination of the Micro-Resonator Structure	80
4.3.1	Choice of the Centre Wavelength	82
4.3.2	Minimum Requirements for the Resonator Performance	84
4.3.3	The Final Design	88
4.3.4	The Influence of the Pulse Width	89
4.3.5	Further Considerations	90
4.4	Reflectivity of the Fabricated Micro-Resonator	91
4.5	Conclusions	93
5	A Parallel Plate Waveguide for Terahertz Transmission	94
5.1	Parallel Plate Waveguides in Terahertz Technology	95
5.1.1	Terahertz Parallel Plate Waveguides in Literature	96
5.2	Design of the Parallel Plate Waveguide	97
5.2.1	Experimental System	99
5.3	Characterisation of the Parallel Plate Waveguide	100
5.3.1	Evaluation of the Invasiveness of the Near-Field Probe	101
5.3.2	Alignment of the Pump Beam	102
5.3.3	The Optimum Gap Size for Maximum Energy Transmission	104
5.4	Mode Structure in a Parallel Plate Waveguide	109
5.4.1	The Origin of the Transversal Electric Mode	111
5.4.2	Practical Implications of Multi-Mode Propagation in Parallel Plate Waveguides	113
5.5	Conclusions	114

6	Electro-optic Detection with a Micro-Resonator	116
6.1	The Electro-optic Detection System	116
6.1.1	The Detection of the Electro-Optic Phase-Shift	118
6.2	The Balanced Detector	122
6.2.1	Level of Balancing	124
6.3	The Terahertz Source	127
6.3.1	Optical Rectification in the Non-Linear Crystal ZnTe	128
6.3.2	Terahertz Electric-Field Estimation	130
6.4	Conclusions	131
7	Conclusions and Future Work	132
	References	137
	Symbols and Abbreviations	160
	Table of Figures	167
	List of Tables	174
	Appendix	176
	A - Surface Plasmon Polariton Dispersion Relation	177
	B - Diffraction Limit in Optical Imaging Systems	179
	C - Propagation of Electro-Magnetic Waves in Crystals	181
	D - Derivation of the Electro-Optic Phase-Shift	183
	E - Selection of Micro-Resonator Configurations	184
	F - Jones Matrix Formalism for the Detection System	186

1 Surface Plasmon Imaging in the Terahertz Range

This chapter gives an introduction to the research topic which has been investigated within the scope of this PhD project: terahertz surface plasmon near-field imaging. It explains the physical phenomenon of surface plasmons and the reasons for its current importance in research and engineering. A theoretical derivation explains the evanescent character of surface plasmons and the emanating need for near-field detection methods for its experimental investigation. A literature review presents and discusses current surface plasmon imaging methods in the optical and the terahertz domains and puts this work into the context of present research.

1.1 The Promising World of Surface Plasmons

The discovery and exploitation of electro-magnetic phenomena was one of the major driving forces behind the technological progress that shaped our world into the place we currently know. What used to be fundamental research only about two centuries ago conducted by ingenious minds such as Maxwell, Faraday, Oersted, Ampère, and Coulomb [1–5], led very quickly to the first commercialised products like the electro-dynamic engine by Werner von Siemens or single-wire telegraph systems by Samuel F.B. Morse in the middle of the 19th century. Beginning from that time, numerous scientists and engineers have been researching the technological exploitation of electro-magnetic energy with remarkable success: today, we have access to coherent light sources which, for example, can be used for material processing, high-precision surgery, or high-capacity communication systems. We are also able to use radio-frequency (RF)-technology for in-vivo medical scanning of internal organs, for global positioning systems, and even for communicating with a robot on the planet Mars. This range of examples is far away from being exhausted and can easily be extended by either adding more applications such as, e.g., solar energy and building illumination, or by moving to different frequency regions of the electro-magnetic spectrum.

Despite the impressive progress in this field throughout the last 150 years and the resulting plethora of applications, it took researchers until very recently to tackle one fundamental problem: to control electro-magnetic energy at spatial dimensions much smaller than the employed wavelength. One way to achieve this strong spatial energy confinement is the use of surface plasmons.

The actual phenomenon of an "electro-magnetic surface wave" has been known since the early 1900s. The main focus, thereby, was on its implications on telegraphy [6, 7] and on anomalies observed in diffraction gratings [8]. In the 1950s, the terminology of "surface plasmons" appeared for the first time and was also described theoretically [9–11]. The scientific breakthrough came only in the late 1990s when surface plasmons were suggested for applications which require electro-magnetic energy confinement to spatial dimension much smaller than the fundamental diffraction limit allows [12, 13]. This gave rise to the technologically interesting possibility of confining, guiding, and processing light on a sub-wavelength scale which pushed surface plasmons in the focus of current research. When reading books [14–16] or review articles [17–19] on this topic, one repetitively encounters terms such as highly integrated photonic circuits [20, 21], nano-resolution optical imaging systems [22, 23], high-sensitivity sensors [24–27], single-molecule spectroscopy [28, 29], high-efficiency solar cells [30], and optical antennas for light generation and detection [31–33]. This selection of current "hot topics" reveals the wide range of potential surface plasmon related applications and justifies the interest of the optical society in this research field.

In order to put these potential applications into practice, a wide range of problems still needs to be tackled: the recently emerged research field "Plasmonics" [34, 35], for example, aims at merging the compactness of electronic circuits with the vast bandwidth of optical systems. As a final goal, light circuits may replace electronic circuits as they are currently used for data transmission and processing. This requires passive elements such as plasmonic filters [36], waveguides [37–39], beamsplitters [40], and couplers [41] as well as elements for logical operations [42], signal modulation [43], or data storage [44]. For high-resolution optical imaging systems and high-sensitivity sensors, it is important to understand the interaction of surface plasmons with samples exhibiting different geometries, materials, surface properties, and imperfections [45–47]. The same knowledge about these mutual dependencies is required for applications where sub-wavelength features are used for local electric-field enhancements [48–50] or non-linear phenomena [51, 52]. In the field of bio-technology, it is important to know how energy can be guided to a single molecule and how complex organic samples interact with highly confined electro-magnetic energy [53, 54]. And, what is an essential question for all applications: how to optimise the coupling between surface plasmons and a free propagating wave for each individual case.

The visualisation of surface plasmon related process is a key requirement for the investigation of this physical phenomenon and for finding solutions to the sci-

entific problems stated above. The experimental investigation of surface plasmons gives the opportunity to understand their behaviour in a real, imperfect environment and to evaluate the correctness of numerical simulations. But before putting the focus on current surface plasmon imaging techniques, it is necessary to understand the distinct physical properties of surface plasmons.

1.2 Theory of Surface Plasmons

Surface plasmons describe a specific type of interaction between electro-magnetic energy and a dielectric/conductor interface. The conductor, in general, is metal. The optical response of the metal to the incident electro-magnetic field is determined by its ability to support collective excitations of the free conduction electrons. The energy is distributed both in the dielectric and the metal and propagates along the common interface. This form of surface wave is called "surface plasmon polariton" (SPP). A SPP is depicted in Fig. 1.1 (a) together with its most important parameters.

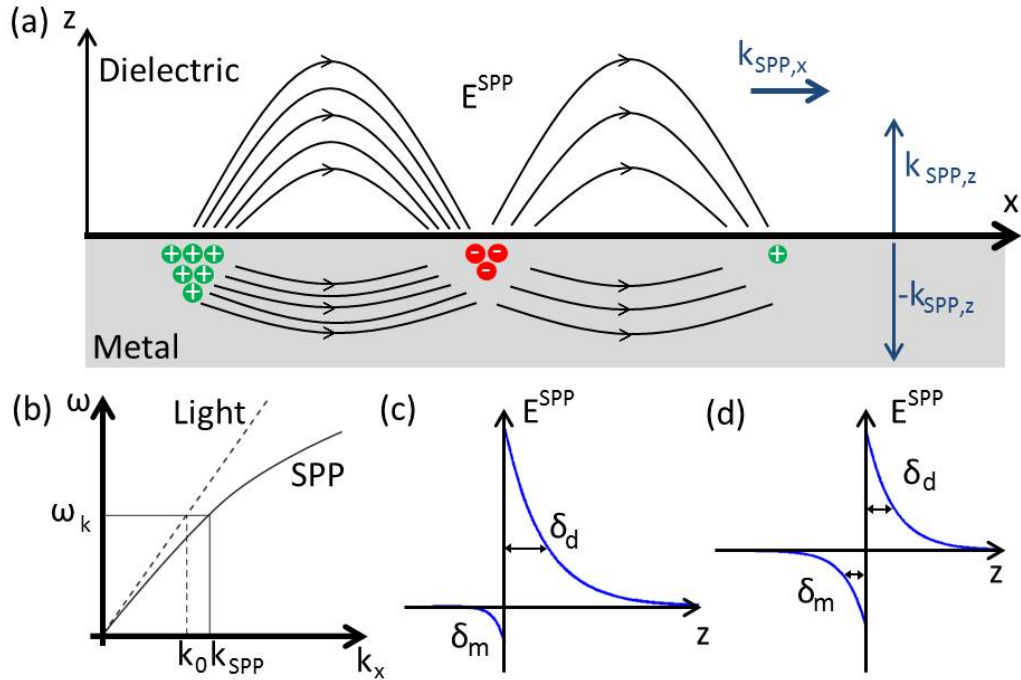


Fig. 1.1: (a) Propagation of a surface plasmon polariton on a metallic surface; (b) Surface plasmon dispersion relation; Electric-field E_z into the dielectric and the metal at THz frequencies (c) and at optical frequencies (d).

The SPP wavevectors pointing into the dielectric $k_{SPP,z}^{diel.}$ and the metal $k_{SPP,z}^{met.}$, as well as the one propagating along the interface $k_{SPP,x}$ are described in Eq. (1.1) to (1.3) as a function of the free-space wavevector k_0 . A derivation of these relations

from the wave equation as a starting point can be found in Appendix A.

$$k_{SPP,z}^{diel.}{}^2 = \frac{\epsilon_d^2}{\epsilon_d + \epsilon_m} k_0^2, \quad (1.1)$$

$$k_{SPP,z}^{met.}{}^2 = \frac{\epsilon_m^2}{\epsilon_d + \epsilon_m} k_0^2, \quad (1.2)$$

$$k_{SPP,x}^2 = \pm \frac{\epsilon_d \epsilon_m}{\epsilon_d + \epsilon_m} k_0^2 \quad (1.3)$$

The parameters ϵ_d and ϵ_m describe the permittivities of the dielectric and the metal, respectively. For the existence of surface plasmons, the negative real part of the metal permittivity ($Re\{\epsilon_m\} < 0$) plays the decisive role. Considering that its absolute value is greater than the positive one of the dielectric ($|Re\{\epsilon_m\}| > |Re\{\epsilon_d\}|$) and applying this to Eq. (1.1) to (1.3), one obtains negative values for the fractions in Eq. (1.1) and (1.2). This leads to the following three equations:

$$k_{SPP,z}^{diel.} = i \sqrt{\frac{\epsilon_d^2}{\epsilon_d + \epsilon_m}} k_0, \quad (1.4)$$

$$k_{SPP,z}^{met.} = i \sqrt{\frac{\epsilon_m^2}{\epsilon_d + \epsilon_m}} k_0, \quad (1.5)$$

$$k_{SPP,x} = \pm \sqrt{\frac{\epsilon_d \epsilon_m}{\epsilon_d + \epsilon_m}} k_0 \quad (1.6)$$

It becomes clear that the wavevectors in the z -direction (Eq. (1.4) and (1.5)) are imaginary and, hence, exhibit an evanescent behaviour. The only real wavevector is given in Eq. (1.6), which defines a propagating wave in a direction parallel to the metal/dielectric interface. The frequency dependence of the metal permittivity (ϵ_m) mainly governs the dispersion characteristic, as it is shown in Fig. 1.1 (b). In the low frequency regime, metals almost act as a perfect conductor and only a negligible fraction of the electro-magnetic wave penetrates into the metal (Fig. 1.1 (c)). The 1/e-decay length of the SPP electric-field E^{SPP} into the dielectric δ_d , on the contrary, can theoretically reach a couple of centimetres [55]. As a consequence, the SPP characteristic is mainly determined by the properties of the dielectric ϵ_d . In this case, the wavevector $k_{SPP,x}$ is barely distinguishable from the free-space wavevector k_0 ($k_{SPP,x} \cong k_0$). A SPP in the low-frequency range, therefore, resembles a homogeneous electro-magnetic field in a dielectric which is incident under a grazing angle to the respective interface. The SPP wave in this frequency region is also known as "Sommerfeld-Zeneck wave" in the literature [6].

For higher frequencies, metals behave comparably to lossy dielectrics. In

this case, the electro-magnetic field penetrates deeper into the metal and interacts more strongly with the free electrons (Fig. 1.1 (d)). The E^{SPP} pointing into the dielectric is closely bound to the interface and the respective decay length δ_d can be only as long as a couple of micrometers [17]. The stronger interaction of the electro-magnetic energy with the free electrons in the metal leads to a higher energy dissipation during propagation. Also, the SPP wavevector changes to higher values ($k_{SPP,x} > k_0$). The resulting difference in the wavevectors $k_{SPP,x}$ and k_0 requires special phase-matching techniques when coupling free-propagating light to the bound modes of SPPs. Common techniques to bridge the wavevector difference employ a dielectric to increase the momentum of k_0 ("Otto" [56]- and "Kretschmann" [57]- configuration), a grating [58, 59], or a sub-wavelength scatterer [60, 61].

Apart from propagating along a metal/dielectric interface, surface plasmons can also be confined to sub-wavelength sized geometries such as shells/dots [62, 63], apertures [64], or arrays of the latter [65, 66]. This type of interaction is often referred to as "localised surface plasmon" (LSP) [67]. The electro-magnetic energy, in this case, is spatially localised to the ultimate proximity of the respective sub-wavelength feature. The collective response of the free electrons to the external driving field can open the door to intriguing resonance effects. The resulting localised field enhancements, for example, can be used for enhanced transmission through sub-wavelength hole arrays [68, 69], sub-wavelength imaging [70, 71], or non-linear effects [51]. The broad wavevector distribution in the proximity of the sub-wavelength features allows for the excitation of LSPs by an incident electro-magnetic wave with a plane wavefront.

The evanescent character of surface plasmons imposes specific problems on the experimental realisation of surface plasmon imaging. A way has to be found to sample these strongly confined and non-radiating electric-fields and to convey this information to the far-field. This task can be fulfilled by an imaging technique named "near-field imaging". The principles of near-field imaging are explained in the next session and examples of different SPP imaging methods are presented for the optical and the THz domain.

1.3 Near-field Imaging of Surface Plasmon Polaritons

Near-field imaging was initially introduced to overcome the inherent diffraction limit of far-field optical imaging systems. When a detector is placed at a distance

of a wavelength or more away from the device under test (DUT), diffraction sets a limit to the resolving capability of an optical imaging microscope. Any optical far-field imaging system can resolve two points only when they are separated by a distance $d_{far-field}$ greater than about half a wavelength λ_0 :

$$d_{far-field} \geq 0.61\lambda_0 \quad (1.7)$$

A derivation of the so-called "Abbe's diffraction limit" [72] and its implications on the resolution of an optical imaging system can be found in Appendix B. Contrary to imaging in the far-field, a near-field imaging system is not affected by the diffraction limit. Edward H. Synge was the first to suggest a near-field imaging system by using a sub-wavelength aperture to increase the resolution in 1928 [73]. However, the requirements for fabricating such a small aperture for optical wavelengths could not be fulfilled at that time. The credits for realising the first near-field microscope are therefore granted to another person: Sir Eric Ash, a researcher from University College London. He imaged a sub-wavelength sized UCL logo in 1972, using radio frequencies and achieving a resolution of $\lambda/60$ [74]. Today, sub-wavelength imaging techniques are well developed also for optical frequencies which gave the research community eyes to study processes with a deep sub-wavelength resolution on a nanometer scale.

1.3.1 The Principle of Near-Field Imaging

Near-field imaging relies on the detection of high spatial frequency components $k_{Near-Field}$ which cannot be detected in the far-field. Far-field imaging can be understood as a transmission channel with ideal low-pass behaviour which allows only wavevectors $k_{Far-Field}$ smaller than the wavevector k_0 to propagate ($k_{Far-Field} \leq k_0$). The wavevector k_0 is determined by the employed wavelength λ_0 of the optical imaging system. The high spatial frequency components ($k_{Near-Field} \geq k_0$) are only present as evanescent fields and, hence, are strongly localised within a short distance from the sample surface [15].

Figure 1.2 depicts the differences in the image formation in the near- and far-field. In Fig. 1.2 (a), one can see a rectangular protrusion with the height $h_{prot.}$ and the width $w_{prot.}$. Both dimensions are greater than the wavelength of the incident light λ_0 . A sudden jump in height from $h=0$ to $h=h_{prot.}$ and vice versa can be considered as a step function and can be broken down in an infinite number of Fourier components according with Fourier Optics [75]. Reflected light from this protrusion propagates to the far-field detector at $h_{Detector}$ and contains only spatial

frequency components equal to or smaller than the incident light. The obtained image is the inverse Fourier transform of the received frequency components with wavevectors not greater than k_0 . This "smoothens" the image of the step function in the far-field to a degree which is determined by the employed wavelength. This is shown in Fig. 1.2 (b), where a step function (blue line) is converted into its frequency components and ideal low-pass filters with cut-off frequencies of 1 THz, 3 THz, and 5 THz are applied. The inverse fast Fourier transforms (FFTs) for all three cases are plotted in the same graph for comparison. One can see how the actually immediate transition from $h = 0$ to $h_{prot.}$ is resolved over a distance which is determined by the respective cut-off frequency. The real shape of the step function is approached more accurately for a higher frequency cut-off. Hence, the spatial resolution of an optical imaging system improves for smaller wavelengths λ_0 .

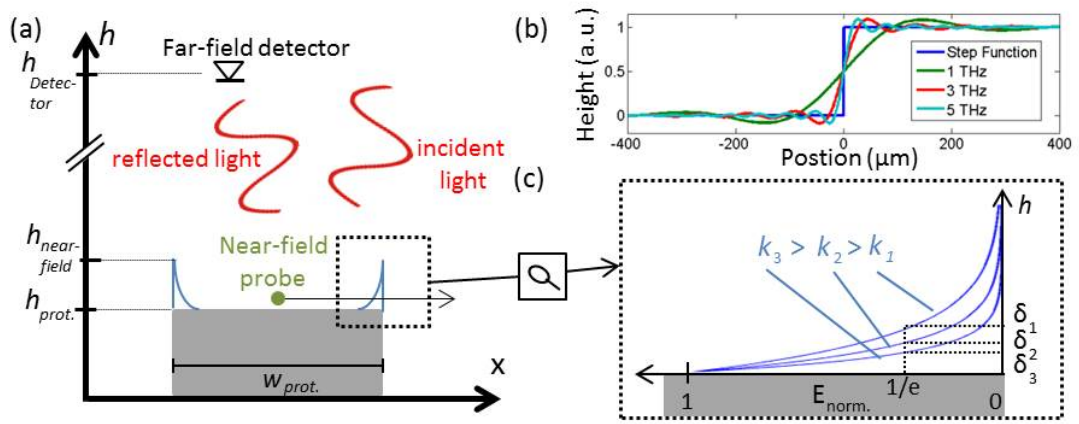


Fig. 1.2: (a) Far-field detection of light reflected by protrusions with spatial dimensions bigger (left) and smaller (right) than the employed wavelength λ_0 ; (b) A step function and its low-pass response for three cut-off frequencies; (c) Evanescent electric field decay for k -vectors bigger than k_0 .

For a fixed incident wavelength, however, the resolving capability of the microscope is limited by Abbe's diffraction limit (Eq. (1.7)). To overcome this inherent limit of far-field imaging techniques, a way has to be found to detect spatial frequency components beyond the cut-off frequency of the virtual low-pass filter. These inherently evanescent components are highlighted by the dashed box in the corner region of the protrusion and magnified in Fig. 1.2 (c). It shows the exponential decay of the respective electric-field components in the h -direction. Higher frequency spatial components obviously have shorter decay lengths than lower frequency components ($\delta_1 > \delta_2 > \delta_3$ for $k_1 < k_2 < k_3$). As a consequence, the resolution of an imaging system depends on its capability to probe these high spatial frequency components in the ultimate proximity of the sample. This can be achieved by the application of near-field imaging techniques.

There are two different techniques used in near-field imaging: In the first approach ("Aperture Mode"), a sub-wavelength source ("Illumination mode") [76, 77] or a sub-wavelength detector ("Collection mode") [64, 78] is used to locally confine or probe the electro-magnetic field in the near-field of the sample. In the second approach ("Apertureless Mode"), a sub-wavelength scatterer is positioned at a distance smaller than the wavelength away from the sample. This scatterer uses localised surface plasmon resonances, for example at the very tip of a metallic needle [79, 80], to transmit highly localised spatial information to the far-field. As a consequence, either an aperture- or a scatterer- type near-field probe needs to scan the sample surface to resolve spatial variations on a sub-wavelength scale (Fig. 1.2 (a)). In both cases, the resolution of the near-field imaging system is limited only by two factors: first, the geometric properties of the probe and second, the capability of the imaging system of introducing the probe as close to the sample as possible. As a result, the resolution of a near-field imaging system is independent of the employed wavelength λ_0 . This enables the observation of local optical interactions, high resolution mapping of electric field distributions, and looking into details of physical processes on the sub-wavelength scale.

The same principles which are valid for ordinary near-field imaging can be directly applied to SPP imaging. As stated in Eq. (1.4) and (1.5), the electric-field components of SPPs are evanescent in the z -direction and, therefore, near-field techniques are necessary for their detection.

1.3.2 Imaging in the Optical Domain

It was mainly the discovery of surface plasmon phenomena for applications in the optical domain that sparked the interest of the research community in the technological exploitation of this phenomenon. Due to the dispersion relation for optical frequencies (Fig. 1.1 (b)), it is possible to achieve SPP wavelengths λ_{SPP} of less than 100 nm together with a strong electric-field confinement to the dielectric/metal interface. For example, a wavelength of $\lambda_{SPP} = 70\text{ nm}$ is possible when coupling 633 nm light to a SPP wave on a Si/Ag interface [81]. This allows for designing highly integrated components for photonic circuits as well as for nano-scale sensors. In addition, the optics research community could draw on the existence of technically mature techniques of light generation and detection. This made the optical regime the driving force behind research on surface plasmons.

As a result of the intense research on this field, a wide range of surface plasmon imaging techniques has been evolving in the optical domain. Some of them are modifications of techniques that are already known from ordinary near-field imag-

ing: the oldest and most common one is scanning near-field optical microscopy (SNOM) [82]. Hereby, a fibre probe is placed into the near-field of the sample with a dielectric constant ϵ_{needle} greater than the surrounding dielectric ϵ_d [83, 84]. In this configuration, the dielectric tip frustrates the total reflection. The evanescent field components are converted into propagating ones and can be detected in the far-field. This configuration is also called Photon Scanning Tunneling Microscope (PSTM) and was firstly introduced by Reddick et al [85]. A small deviation from this configuration is a dielectric tip covered with a metallic coating. Only a small aperture at the very end of the tip is left blank through which the E^{SPP} can couple into the dielectric [86]. The advantage of this configuration is a higher resolution compared to the uncoated needle due to the spatially confined aperture. However, the metallic coating increases the degree of invasiveness of this detection method.

Another possibility of detecting the evanescent field is the use of a sharp metallic needle which acts as a sub-wavelength scatterer [70, 87]. This configuration can also be modified by attaching resonant structures to the tip of the needle to increase its sensitivity. This, for example, has been demonstrated using nanoparticles [88] or bow-tie antennas [89].

There are also some SPP imaging methods in the optical domain which cannot be considered as typical near-field techniques. These techniques rely on decoupling the SPP from the metal surface and detecting its intensity in the far-field. Decoupling, for example, can be achieved by placing a diffraction grating on the surface. For specific grating constants and geometries, the k_{SPP} is converted into the free-space wavevector k_0 and can be detected by an ordinary optical detector [59]. A further method is positioning fluorescent molecules on the metal-dielectric interface. These molecules absorb the SPP energy and re-radiate the fluorescent light into the far-field [40, 90]. Another type of microscope uses the so-called "leakage radiation" [91, 92] or "forbidden light" [93, 94]: this configuration inverts the principle of a Kretschmann configuration, in which a dielectric is used to match k_0 and k_{SPP} . Therefore, a propagating SPP radiates into a dielectric under the specific angle fulfilling the phase matching condition. These actual far-field techniques can be successfully used for SPP detection, although their spatial resolving capabilities are still limited by the diffraction limit.

1.3.3 Imaging in the Terahertz Domain

The optical domain is obviously rich in possible SPP applications and SPP imaging methods can draw on a vast experience that constantly enhanced from its first attempts in the 1980s. However, there is one frequency region which has its distinct

advantages over the optical domain and SPPs can have their own specific applications: the terahertz (THz) region, which is commonly defined for frequencies ranging from 0.1 THz and 10 THz [95, 96]. Scientific progress in this region bridges the technological gap between (high-frequency) radio waves and (low-energy) infrared radiation. Although this frequency region had not been exploited due to the lack of THz sources and detectors until about 20 years ago, it is currently an important field of research: familiar techniques from the microwave and from the optical domain were tailored to the demands and necessities of the sub-millimetre wavelength region. This made various THz generation and detection methods available [97, 98].

The most commonly used THz detectors are electro-optic crystals [99–102] and photoconductive antennas (PC-antennas) [103–106]. Both of these detectors are phase-sensitive to the THz electric-field. The incorporation of these detectors in THz time domain spectroscopy (THz-TDS) systems led to an advantageous feature of THz detection methods: the possibility of coherent and time-resolved electric-field sampling of frequencies within a wide spectral window between 0.1 and 40 THz [107]. This method was first developed by Auston and Cheung at Bell Laboratories in 1985 [108] and applied to THz imaging ten years later [109]. It is based on a pump-probe system in which a sub-ps optical sampling pulse is spatially split in two separate beams: one part ("pump beam") generates the THz electric-field E^{THz} and the second one ("probe beam") samples the respective field. Time-resolved detection is achieved by shifting the arrival time of one beam with respect to the other with a mechanical translation stage to sample the E^{THz} at different moments in time. It is also possible to use interferometric techniques in the optical domain, however, the smaller wavelength sets higher requirements to the detection system and obtaining the phase information is experimentally challenging.

The developments of the last two decades pushed the THz region into the spotlight of research and engineering, enabling for the first time in history the possibility of THz applications [110–113]. In some of them, SPP phenomena play an important role and allow the realisation of applications which are difficult - or even impossible - to realise in the optical domain. The next section introduces some of these applications and states why research on SPPs is particularly interesting in the THz domain.

1.3.3.1 The Need for Surface Plasmon Polaritons in THz Technology

The growing need for bandwidth in telecommunications has already created a demand for pushing relevant devices to THz frequencies. Since the bandwidth of

electronic systems is limited to some hundred GHz, there is a deep interest in expanding communication systems to the THz range. This requires the existence of efficient sources and detectors. Although there has been a lot of progress in this field recently (Chapter 1 and 4 in Ref. [55]), it is still important to know how incoming radiation interacts with metallic elements [114] and how the geometry [115] or the surface [116] of a device can be engineered to improve its performance. For this purpose, it can be beneficial to incorporate SPP phenomena in the design process of THz communication devices.

In communication systems, it is also important to know how to efficiently transmit energy from one point to another. In highly integrated THz photonic circuits, for example, this needs to be done by SPP waveguides. Work on integrated planar plasmonic THz waveguides, however, can barely be found in the literature [117, 118]. A reason for this might be the relatively long SPP decay length δ_d which is contradictory to a high level of integration. One can mitigate this problem by using corrugated surfaces, similar to the ones already used in RF-engineering. These engineered surfaces support the propagation of so-called "Spoof SPPs" [119, 120] with a stronger SPP confinement to the metal. Apart from integrated communication systems, THz SPP waveguides are also important for sensing or high-resolution imaging applications, which require to guide electro-magnetic energy to spatially confined spots.

Terahertz radiation has unique advantages for sensing applications. Due to its photon energy in the meV-range, THz radiation addresses a rich variety of light-matter interactions: rotational and vibrational transitions of single molecules can be identified due to their "THz fingerprint". This enables intriguing applications in drug and explosive detection [121, 122], security screening [123], and biomedical research [124]. In order to address single molecule characterisation, two problems need to be tackled: firstly, systems have to be built that are able to confine energy down to molecular or cellular dimensions [125] and secondly, the interaction of molecules with highly confined energy must be understood.

As a last point, devices based on SPP phenomena can be manufactured and investigated at sub-millimetre dimensions. This sets less stringent requirements to the fabrication process of SPP devices in the optical domain, which often requires an accuracy in the nanometre range. This holds also true for the experimental implication of THz SPP imaging systems.

1.3.3.2 Discussion on current Near-Field Imaging and Surface Plasmon Polariton Detection Methods in the THz Domain

The THz range obviously offers a wide range of potential applications. At the same time, there are still many open research questions which need to be addressed. The existence of SPP near-field imaging methods in this frequency range, therefore, is one of the key requirements for the experimental investigation of THz SPP phenomena.

The THz research community has already developed numerous near-field imaging methods and an exemplary selection is shown in Fig. 1.3. Terahertz near-field methods, for example, involve aperture techniques such as electro-optic sampling (a), integrated PC-antennas (b), or "dynamic apertures" in semiconductors (c). Also, aperture-less approaches were demonstrated, in which sub-wavelength diameter metallic tips act as scatterer (d, e).

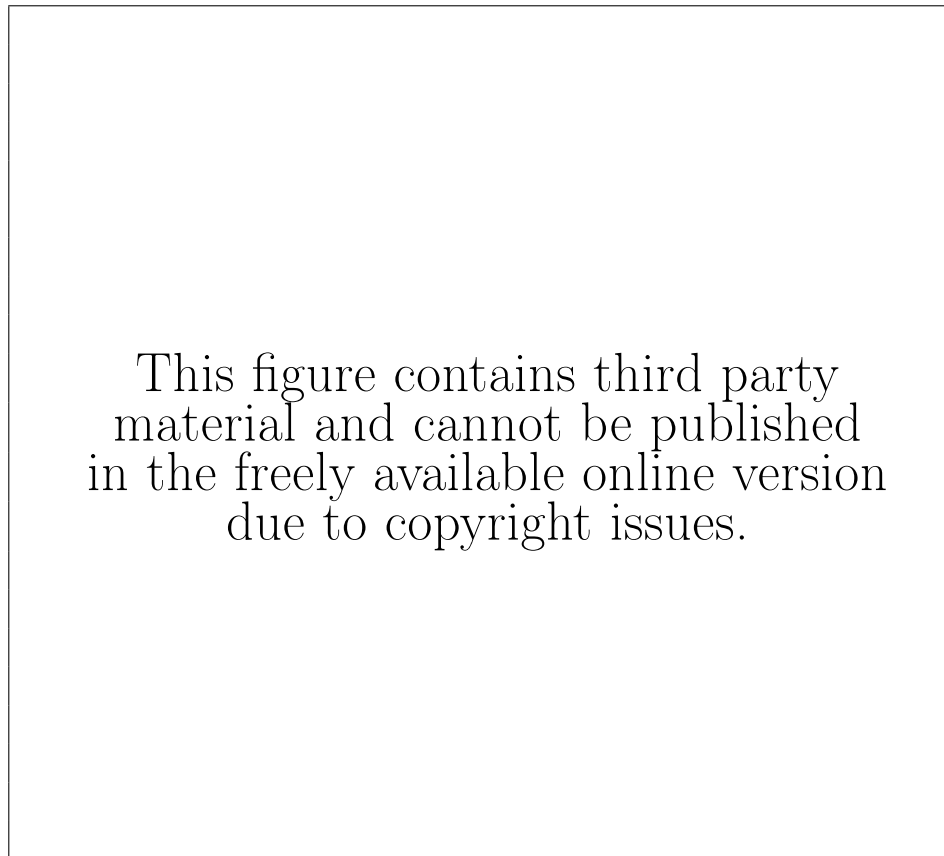


Fig. 1.3: (a) Electro-optic sampling with a $30\ \mu\text{m}$ -thick ZnTe crystal (from Ref. [101]); (b) Near-field microscopy with an integrated near-field probe (from Ref. [78]); (c) Dynamic aperture approach (from Ref. [126]); (d) A metallic tip acting as a scattering probe; the far-field THz detector includes a PC-antenna (from Ref. [127]); (e) A metallic tip scans a sample; the far-field THz detector also includes a PC-antenna (from Ref. [128]).

There are also a very small number of recent THz near-field approaches

employing THz detectors which are not phase-sensitive, such as bolometers [70]. Bolometers, however, show no distinctive advantage over the techniques presented above and will therefore be neglected in this summary. The significant majority of THz near-field methods utilises either electro-optic detection crystals or PC-antennas. From this, it is evident that THz SPP imaging techniques rely on the same two detection principles. The experimental approaches to probing the SPP field, however, are sometimes distinctively different from the examples in Fig. 1.3. The most common THz SPP detection/imaging techniques are presented in Fig. 1.4 and discussed in the following.

One approach is to convert the evanescent E^{THz} into a free-space propagating wave and to detect it in the far-field. Decoupling the E^{THz} from a metal surface, for example, is experimentally realised by sharp coupling plates which are introduced in the proximity of the surface. The decoupled electric-field can then be measured by a PC-antenna [129] (Fig. 1.4 (a)) or an electro-optic crystal [130] positioned in the far-field. In these examples, the SPP transmission properties of different dielectric coatings on the metal were investigated and, hence, high-spatial resolution imaging was not required. High-spatial resolution imaging of the SPP waves, however, can be realised when introducing a metallic needle into the evanescent electric-field. The tip with its sub-wavelength diameter scatters the evanescent field and allows its detection in the far-field. This technique, for example, was demonstrated for "edge-plasmon" imaging in the gap of a parallel plate waveguide [131] (Fig. 1.4 (c)), at the sub-wavelength sized output aperture of a parallel plate waveguide [127], or on gold gratings attached to semiconductor surfaces [132].

Terahertz SPP waves on metallic sheets or metal wires were investigated by placing a detector at the end of the wire [135–137] or at the edge of the metallic sheet [138], respectively. The detector can either be a PC-antenna or an electro-optic crystal, which are both aligned to be sensitive to the propagating E^{SPP} . While the E^{SPP} -amplitudes were probed at only one position to investigate the impact of different coatings in Ref. [136–138], Ref. [135], on the contrary, scanned the E^{SPP} field in the entire plane orthogonal to the wire orientation. This created an E^{SPP} -map at the tip of the metal wire waveguide. The E^{SPP} at different positions along a metallic wire was detected with a photoconductive-type probe in Ref. [133]. This probe is sensitive to the transient of the propagating E^{SPP} and is brought into the proximity of the wire by a thin metallic tip to minimise invasive effects.

A group at Freiburg University fabricated a "Silicon on Sapphire" detector-chip which comprises an H-shaped PC-antenna deposited on a Silicon wafer. This



Fig. 1.4: (a) Converting the E^{SPP} into a free-space beam (from Ref. [129]); (b) Detection of the E^{SPP} along a metallic wire with a photoconductive-type probe (from Ref. [133]); (c) Probing the "edge plasmons" inside a parallel plate waveguide with a needle-probe (from Ref. [131]); (d) SPP detection with a Silicon on Sapphire chip in the shading region of sub-wavelength holes; The SPP wave is shown in the bottom image for a specific moment in time (from Ref. [134]); (e) SPP detection with an electro-optic crystal in the shadow region of a sub-wavelength aperture (from Ref. [64]); the inset shows the measured E^{SPP} - distribution in the proximity of the aperture.

chip was invented for THz microscopy and imaging [139, 140]. When investigating the transmission of THz radiation through $300\ \mu\text{m}$ -diameter holes in metals, they also detected SPP waves spreading out from these holes (Fig. 1.4(d)) [134]. The obtained pattern was explained as an imaging artefact, since the detector should not be sensitive to this electric-field polarisation. This unexpected sensitivity was contributed to the formation of additional electric-field components between the metallic electrodes of the PC-antenna and the metallic sample which couple into the antenna. A similar phenomenon will be demonstrated in Chapter 2, in which an integrated sub-wavelength aperture probe is used for SPP imaging.

Surface Plasmon imaging on a gold surface using a bulk electro-optic crystal is demonstrated by a research group in Delft. They utilise a $300\ \mu\text{m}$ -thick GaP

crystal to observe the electric-field distribution of an incident THz pulse in the shadow region of sub-wavelength holes in gold layers. These holes can either be slits [141], single rectangular apertures [142], round apertures [64, 143], or arrays of the latter [66]. In all their experiments, the orientation of the GaP crystal was chosen to be sensitive to the electric-field components orthogonal to the gold surface and, hence, the detected electric-field can be directly related to the SPP wave (inset of Fig. 1.4(e)).

This section presented a selected range of state-of-the-art THz SPP imaging methods. Despite its variety, each individual imaging approach has its specific disadvantages. The approach shown in Fig. 1.4(a), for example, does not provide any information on the spatial E^{SPP} -distribution on the metallic surface. The photoconductive-type probe in Fig. 1.4(b), on the contrary, is a detector designed for this specific purpose. However, it only detects a transient of the propagating E^{SPP} and not the actual electric-field. The needle probe in Fig. 1.4(c) can only probe the field inside the waveguide as long as its diameter is smaller than the respective waveguide gap. The introduction of the metallic needle into the waveguide gap might also cause severe field distortions. Regarding the detector-chip in Fig. 1.4(d), the coupling mechanism between the E^{SPP} on the metal and the H-shaped electrodes of the PC-antenna seems to be more complex and is rather regarded as an imaging artefact. And the introduction of a 300 μm -thick electro-optic crystal into the entire shadow region of a sub-wavelength aperture, as it is done in Fig. 1.4(e), also causes distortions of the original electric-field pattern.

1.4 The Research Project

As one can see from the previous examples, current THz SPP imaging methods have still a great potential for improvements and a wide range of problems which need to be solved. It is the aim of this research project to extend the range of current THz SPP near-field imaging approaches and to provide improved methods for specific SPP imaging applications. The developed approaches in this project address two specific applications which can be summarised as follows.

In the first approach, an integrated sub-wavelength aperture probe is used for SPP imaging. This type of probe was developed by Dr. Oleg Mitrofanov as a probe for THz near-field microscopy [78]. It consists of a PC-antenna which is integrated in the proximity of a sub-wavelength aperture (see Fig. 1.3(b)). Although PC-antennas are one of the two most commonly used THz detector types, they have never been used for sampling the E^{SPP} -field distribution directly on

metallic surfaces. The reason for their limited SPP detection capability is that it is experimentally very difficult to introduce a PC-antenna, which involves metallic electrodes, connectors, and a holder, into the near-field of sample. It has to be kept in mind that the dipole orientation of the PC-antenna has to be orthogonal to the metal surface in order to be sensitive to the propagating E^{SPP} . The alignment of the gating beam and the respective focusing elements parallel to the sample surface is thereby especially challenging.

It is shown in this project that a combination of a sub-wavelength aperture and a PC-antenna can be used for SPP wave imaging directly on a metal. The sensitivity of this probe to SPPs is demonstrated in two examples: first, the probe was applied to SPP imaging on a bow-tie antenna and second, to imaging of a SPP wave which is excited by a strongly focused THz beam directly on the metallic surface of the probe. The coupling mechanism of the SPP wave into the probe is also discussed since it is important for the correct interpretation of the obtained images.

The second approach is devoted to improving THz SPP imaging using electro-optic detection methods. When using electro-optic crystals, one faces a particular problem: the electro-optic effect, which is the physical phenomenon electro-optic crystals rely on, is very small for commonly used detection materials. As a consequence, the probe beam experiences only a very tiny modulation due to the present THz electric-field E^{THz} when propagating through such a crystal. Therefore, it is necessary to use relatively thick electro-optic crystals (hundreds of μm) to enhance the modulation and to increase the sensitivity of the probe (see Fig. 1.4 (e)). The experimental detection of the E^{SPP} requires to introduce the crystals into the ultimate proximity of the sample. This, however, can cause severe electric-field distortions depending on the size and the material composition of the probe [144–147]. For this reason, non-invasive detection is a particularly difficult problem and requires special probes.

A possibility to mitigate the issue of high invasiveness is the use of an electro-optic micro-resonator. In this configuration, an ordinary bulk electro-optic crystal is replaced by a resonant structure. This extends the effective probe beam propagation length through the crystal and increases the probe sensitivity. Using this type of probe reduces the degree of invasiveness due to the smaller thickness without sacrificing sensitivity. In a bulk crystal, on the contrary, these two points could never be improved at the same time.

In the scope of this project, a THz near-field detection system is developed which is based on the electro-optic micro-resonator. The micro-resonator is de-

signed as a fibre-coupled device in order to improve the manoeuvrability of the entire probe. The design process of this probe is explained and discussed in detail. Also, the performance of each element in the THz near-field detection system is characterised and evaluated. This leads to a discussion on the performance limitations of the developed THz detection system.

1.4.1 Outline of this Thesis

Chapter 2 demonstrates SPP imaging with the integrated sub-wavelength aperture near-field probe. The imaging capability of the probe is applied to SPP wave imaging on a THz bow-tie antenna in a first example. In a second example, the probe is used to study a SPP wave excited by a strongly focused THz beam directly on the metallic surface of the probe. The obtained image patterns are interpreted based on the presented theory on the SPP coupling mechanism into the PC-antenna. It is shown that the detected E^{SPP} -maps show a spatial derivative of the actual SPP wave patterns and that the original patterns can be reconstructed. Also, the implications of the probe sensitivity to the SPP waves on ordinary near-field microscopy is discussed which is important for any type of microscope employing a similar type of detector.

Chapter 3 introduces the theoretical background of the two most important underlying physical phenomena regarding the electro-optic micro-resonator probe: the electro-optic effect in isotropic crystals and the resonance effect in a Fabry-Pérot cavity. In addition to that, a literature review on electro-optic sampling of electric-fields using comparable probes is presented at the end of this chapter.

Chapter 4 describes the design process of the fibre-coupled electro-optic micro-resonator. The micro-resonator offers many degrees of freedoms in its design, such as the employed material, the geometry, or the resonant wavelength. This chapter discusses the mutual dependence of the design parameters and how each of them influences the optical response of the micro-resonator. An analytical computer program is presented which allows the calculation of the optical response as a function of some selected parameters. Based on the calculations of this computer program, a specific micro-resonator geometry is selected and fabricated. A comparison of the measured sample reflectivity and the simulated results leads to a discussion about fabrication errors and the validity of the analytical model.

Chapter 5 analyses THz pulse transmission through a tapered parallel plate waveguide. This type of waveguide has been chosen for the dispersion-less guidance of THz pulse energy from the THz source to the micro-resonator probe. The spatially confined THz pulse energy at the waveguide output is necessary to provide

a sufficient electric-field strength for the characterisation of the micro-resonator probe. Terahertz transmission through the waveguide is optimised as a function of different geometric parameters in the experimental system. It is shown that especially the gap size between the two waveguide plates dictates the impact of different loss mechanisms. The same parameter also has a crucial impact on the mode composition of the propagating pulse. Numerical simulations prove the appearance of higher-order transverse electric modes and show how these modes can leave their spectroscopic fingerprints on the output waveform. The impact of the higher-order modes can even be present for geometries which allow only single-mode propagation.

Chapter 6 presents the electro-optic detection system. It describes how the introduced electro-optic phase-shift in the probe beam translates into an electrical signal that can be detected and recorded by a measurement unit. It also evaluates the noise floor of the detection system as well as the electric-field strength of the THz pulse. Based on this, the limitations of the employed detection system are shown and discussed.

2 Surface Plasmon Polariton Imaging with an Integrated Aperture Probe

This chapter discusses methods for detection of THz SPP waves using the integrated sub-wavelength aperture near-field probe. The detection element of this probe is a PC-antenna which is integrated in the ultimate proximity of the sub-wavelength aperture. When using probes based on PC-antennas for SPP wave imaging directly on metallic surfaces, one faces a particular problem: surface plasmon polariton waves are closely bound to metallic surfaces and exhibit a polarisation E^{SPP} normal to the respective surfaces. As a consequence, the insertion of a PC-antenna right above the metallic surface of the sample is experimentally difficult to realise. A PC-antenna requires a specific holder as well as metallic contacts to connect it to the detection unit. Also, the gating beam needs to be guided parallel to the sample surface and focusing elements have to be introduced to focus the beam on the PC-antenna. Such elements are highly invasive and, from a practical point of view, they require space. The situation becomes even more challenging when this near-field probe contains a metallic sheet with a sub-wavelength aperture.

Due to these practical problems, near-field probes based on PC-antennas are only inserted into the system at surface edges. This, for example, can be the end of a wire waveguide [127, 135, 148] or the edge of a metallic sheet [138, 149], as it is shown in Fig. 2.1. In both cases, the PC-antennas are positioned at the waveguide ends and are aligned in the same plane as the polarisation of the propagating E^{SPP} (xy -plane). As a result, E^{SPP} imaging is only possible in this plane at a z -position close to the waveguide end and not directly on the surface of the wire waveguide or the metallic sheet.

In this chapter, it is demonstrated that the integrated sub-wavelength aperture near-field probe is sensitive to an electric-field polarisation which is orthogonal to the PC-antenna orientation. This probe can therefore be used for E^{SPP} mapping. The sensitivity allows positioning the near-field probe parallel to the sample surface and not only at its edges. As a result, imaging of the SPP wave distribution directly above a sample surface is possible using a near-field probe with a PC-antenna. This chapter explains the origins of the unexpected sensitivity and demonstrates two different applications of this specific probe to SPP near-field imaging: in a first example, SPP excitation and propagation is studied on the res-

This figure contains third party material and cannot be published in the freely available online version due to copyright issues.

Fig. 2.1: (a) The detection of a THz SPP wave at the tip of a metallic wire waveguide with a PC-antenna in a fibre-coupled THz receiver (from Ref. [135]); (b) Detection of a THz wave at the edge of a metallic sheet with a PC-antenna; the SPP wave is launched in a parallel plate waveguide and a blocking plate is introduced to avoid the detection of energy which is not confined to the metallic sheet (from Ref. [138]).

onant metallic structure of a bow-tie antenna. The second example demonstrates imaging of a SPP wave that is excited by a strongly focused THz beam directly on the metallic surface of the probe itself. These results have been published in Ref. [114, 150].

2.1 The Coupling Mechanism

The integrated sub-wavelength aperture probe was introduced as a probe for ordinary high-resolution THz near-field imaging by Oleg Mitrofanov *et al* [78]. The most important functional components of this probe are the gold screen (600-*nm* thick) with a square-shaped sub-wavelength aperture and the PC-antenna which is integrated at a distance of 5 μm behind the aperture (Fig. 2.2 (a)). The entire structure is integrated on a sapphire substrate for mechanical stability. This type of probe was initially used for imaging the THz electric-field distributions on planar antenna structures [78]. Later, it was applied for the mode characterisation in dielectric-lined hollow metallic THz waveguides [151, 152] and for the investigation of THz pulse transmission in parallel plate waveguides (see Chapter 5). In all these cases, the incident E^{THz} was polarised in the aperture plane and could be detected by the integrated antenna. The application of this probe to SPP detection on metallic surfaces, however, requires this probe to be sensitive to an electric-field which is orthogonal to the orientation of the PC-antenna. Hence, it is essential to understand the underlying coupling mechanism between the integrated probe and the SPP electric-field and the resulting relationship between the detected signal and the electric field causing it.

A propagating SPP wave on a metallic surface exhibits an electric-field normal to the respective surface, which is the z -direction in Fig. 2.2 (c) and (d). The

insertion of the gold surface of the integrated probe into the near-field of the sample causes the electric-field lines to end on the probe surface. This induces charge carriers on the gold surface in order to comply with the boundary conditions at metallic surfaces. The charge distribution on the probe surface corresponds to a mirror image of the original one on the sample, as it is shown in Fig. 2.2(d). In this configuration, the propagation of the electro-magnetic energy of the SPP wave between the two metallic surfaces is similar to the *TEM*-mode propagation in parallel plate waveguides.

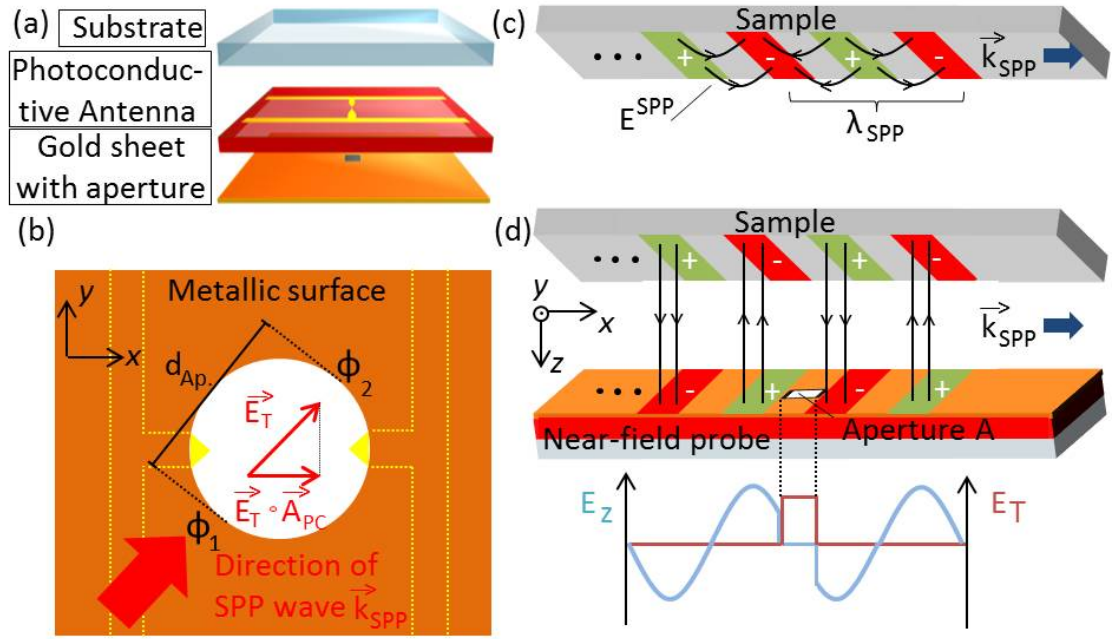


Fig. 2.2: (a) Different components of the integrated near-field probe shown separately; (b) Top view of the probe, showing how E_T couples into the PC-antenna; (c) Schematic image of a SPP propagating along the metallic surface of a sample; the green and the red areas correspond to positive and negative charges, respectively, and the black lines represent the electric-field E^{SPP} ; (d) The same situation as in (c), but with the metallic surface of the integrated near-field probe positioned parallel to the sample; the bottom diagram shows the electric-field component normal to the probe surface E_z (blue line) and the resulting tangential field component across the aperture E_T (brown line); Figures (a), (b) are published in Ref. [114].

When reaching the sub-wavelength aperture, the propagating SPP wave experiences a local disruption: the aperture causes a discontinuity in the surface charge distribution $\Delta\sigma$ and, hence, a potential difference $\Delta\phi = \phi_1 - \phi_2$ at its opposite edges (Fig. 2.2 (b) and (d)). The potential difference results in a tangential electric-field component E_T across the aperture. Since the propagating charge distribution directly follows the SPP electric-field ($\nabla E^{SPP} = \sigma/\epsilon_0$), the tangential electric-field component E_T directly relates to the difference in E^{SPP} at the opposite edges of the aperture. In case of an aperture with a deep sub-wavelength diameter d_{Ap} .

($d_{Ap.} \ll \lambda_{SPP}$), the tangential electric-field E_T can be regarded as the spatial derivative of the E^{SPP} at the location of the aperture. For a SPP wave propagating in the x -direction, for example, this relationship can be written as follows [150]:

$$E_T \propto E^{SPP}(x, y) \Big|_{x+\frac{d_{Ap.}}{2}} - E^{SPP}(x, y) \Big|_{x-\frac{d_{Ap.}}{2}} \propto \frac{d}{dx} E^{SPP}(x, y) \cdot d_{Ap.} \quad (2.1)$$

This equation holds true for a circular aperture with a diameter $d_{Ap.}$ as it is depicted in Fig. 2.2 (b) or for a square-shaped aperture with an edge length $d_{Ap.}$ as shown in Fig. 2.2 (d). In the later experiments, a near-field probe with a square-shaped aperture is used. It has to be emphasised at this point, that the integrated aperture probe is sensitive to the derivative of the SPP electric field E^{SPP} and not to the actual field E^{SPP} itself.

The tangential electric-field component caused by the E^{SPP} couples into the near-field probe and generates a current in the PC-antenna i_{SPP} . Since the PC-antenna has a fixed alignment during the experiments, it can only detect the components of the tangential electric-field which are parallel to the PC-antenna vector \vec{A}_{PC} . Hereby, the vector \vec{A}_{PC} represents the antenna sensitivity A_{PC} with a unit vector \vec{u}_{PC} pointing in the same direction as the antenna orientation. As it is indicated in Fig. 2.2 (b), the sensitivity of the PC-antenna \vec{A}_{PC} to the tangential electric-field \vec{E}_T can be mathematically described as the scalar product between these two vectors. The vector \vec{E}_T is determined by the propagation direction of the SPP wave vector \vec{k}_{SPP} . Taking into account the geometric dependence between \vec{E}_T and the antenna \vec{A}_{PC} and the fact that E_T is the spatial derivative of E^{SPP} (Eq. (2.1)), the induced photocurrent in the probe i_{SPP} due to the SPP electric-field can be written as [114]:

$$i_{SPP}(x, y) = g_1 \nabla E_T \circ \vec{A}_{PC} = g_1 \left(\vec{x} \frac{d}{dx} E^{SPP}(x, y) + \vec{y} \frac{d}{dy} E^{SPP}(x, y) \right) \circ \vec{A}_{PC}. \quad (2.2)$$

The two terms on the right hand side decompose the tangential electric-field E_T in its x - and y -components, respectively. This is the more general case of the PC-antenna introduced in Fig. 2.2, which is only sensitive in the x -direction (Eq. 2.1). The constant g_1 represents all the involved geometric and experimental properties that have an impact on the detection. This includes the aperture size $d_{Ap.}$ and its geometry, the distance between the aperture and the PC-antenna, and the gap between the metallic sheet of the probe and the sample.

As stated earlier, the integrated aperture probe was fabricated as a tool for ordinary near-field microscopy and, hence, it was initially fabricated to be sensitive to an incident transverse THz electric-field E^{THz} . It will be shown in the following

sections that the exclusive detection of the E^{SPP} is experimentally hard to realise and that the incident E^{THz} also has to be taken into account. Consequently, the current detected by the PC-antenna i_{PC-A} is a superposition of the current generated by the SPP wave i_{SPP} and the incident THz electric-field i_{THz} . Therefore, Eq. (2.3) has to be modified by adding i_{THz} . The constant g_2 , similar to g_1 , represents the respective coupling coefficient for the incident transverse THz electric-field to the PC-antenna:

$$i_{PC-A}(x, y) = i_{SPP}(x, y) + i_{THz}(x, y) = g_1 \left(\vec{x} \frac{d}{dx} E^{SPP}(x, y) + \vec{y} \frac{d}{dy} E^{SPP}(x, y) \right) \circ \vec{A}_{PC} + g_2 \frac{d}{dt} \vec{E}^{THz}(x, y) \circ \vec{A}_{PC}. \quad (2.3)$$

2.2 Surface Plasmon Polariton Imaging on a Bow-Tie Antenna

In this section, the integrated sub-wavelength aperture near-field probe is applied to SPP imaging on a bow-tie antenna. Apart from the experimental demonstration of the SPP imaging capability of the probe, this section discusses several interesting SPP-related phenomena: the geometry of the antenna allows the investigation of SPP excitation on the antenna edges, its propagation on the metallic surface, and the generation of SPP interference patterns. This knowledge can be directly applied to the engineering process of novel antenna designs: plasmon resonances on specific THz bow-tie antennas with engineered surfaces ("Sierpinski emitters"), for example, have already been studied numerically and it has been found that the antenna power emission can be increased by 80% compared to normal bow-tie antennas [116].

2.2.1 The Experimental System

The employed experimental system is shown in Fig. 2.3: a Ti:Sapphire laser (Coherent Mira 900) generates 100 fs optical pulses at 820 nm which are split in a pump and probe beam by a polarising beam splitter (PBS). The pump beam is directed through an optical chopper and a mechanical translation stage. It is then focussed on a ZnTe crystal to generate THz pulses with a centre frequency of 2 THz. The non-linear crystal is mounted on a piece of GaAs wafer to block the pump beam and to allow only the THz pulse to propagate further into the waveguide. The waveguide is a hollow dielectric-lined cylindrical metallic waveguide through which the THz pulse propagates as the linearly polarised HE_{11} -mode. Information about the waveguide fabrication process and the propagating mode structure can be found

in Ref. [153] and Ref. [151, 152, 154], respectively. The HE_{11} -mode profile has also been measured experimentally and is graphically inserted in Fig. 2.3 (b). The waveguide used in these experiments has a length of 14.9 cm and an inner diameter of 1.7 mm.

A sample holder (GaAs) is placed at the output of the waveguide with the bow-tie antenna positioned on top of it. The bow-tie antenna is made of gold and has a radius (from its central point to the edge) of $300 \mu\text{m}$ with an opening angle of 90° . The metallic structure has a thickness of 300 nm and the two antenna wings are separated by a $10 \mu\text{m}$ -gap in the antenna centre. This antenna geometry is designed to be resonant at frequencies of a couple of hundreds GHz and, hence, sufficiently far away from THz frequencies.

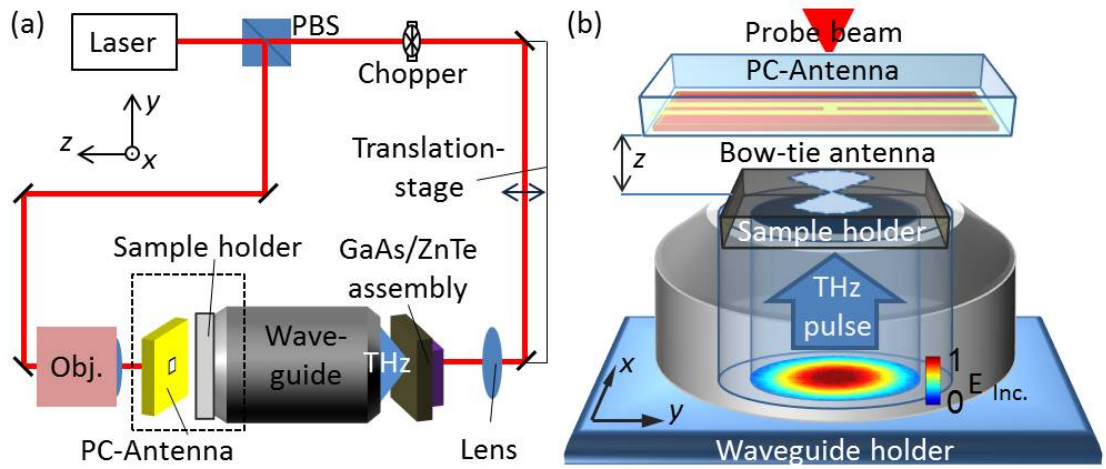


Fig. 2.3: (a) Schematic diagram of the employed experimental system; (b) Detailed image of the dashed box area in (a); Figure (b) is published in Ref. [114].

The probe beam is directed through an objective which focusses the beam on the PC-antenna inside the integrated near-field probe. In the following experiments, a probe with a square sub-wavelength aperture ($d_{Ap.} = 20 \mu\text{m}$) has been chosen to enable high-resolution imaging. The antenna is connected to a current-voltage converter with an amplification of $10 \frac{\text{V}}{\text{nA}}$ and the signal is recorded by a lock-in amplifier with an integration time of 300ms .

The waveguide is mounted on two holders close to its input and output aperture. While the input side is mounted on a fixed stage, the waveguide holder close to the output is attached to a mechanical translation stage. This allows moving the waveguide output in the x - and y -directions (Fig. 2.3 (b)). Consequently, it is the bow-tie structure which is moved with respect to the near-field probe in the later experiments. The probe itself remains in the same position and samples the "shadow region" of the bow-tie antenna which is illuminated from the back side.

Moving the sample, in this case, can be realised more easily in the experimental system than moving the near-field probe. Moving the detector would require the objective and the probe beam path to be spatially translated along with the probe. The bow-tie antenna is rigidly attached to the waveguide output and a uniform illumination of the sample can be considered at any time. Due to the length of the waveguide and a maximum spatial displacement of its output of $\pm 500 \mu\text{m}$ in the xy -plane, the waveguide axis does not deviate more than 0.2° from the z -axis. Input coupling, therefore, can be assumed to be not affected by this translation. The gap between near-field probe and the bow-tie antenna was $15 \mu\text{m}$ in the experiments. The movement of the translation stages and data recording with the lock-in amplifier are controlled by a Labview program during the experiments.

2.2.2 Development of Surface Plasmon Polariton Patterns on a Bow-Tie Antenna

The excitation of SPP waves and the development of electric-field patterns on the bow-tie antenna can be observed in the detected electric-field maps of Fig. 2.4. In this set of experiments, the orientation of the PC-antenna \vec{u}_{PC} and the polarisation of the incident THz pulse \vec{E}^{THz} are both in the x -direction.

The excitation of the SPP waves can be investigated in a space-time map, as it is shown in Fig. 2.4 (a). This figure shows scans along the x -axis through the antenna centre ($y = 0 \mu\text{m}$) for a temporal range of more than 5 ps. While the incident THz wave can be identified as the horizontal lines at the edge of the image ($x > \approx 300 \mu\text{m}$ and $x < \approx -300 \mu\text{m}$), the SPP waves have their distinct signature: they appear as tilted lines in the area of the bow-tie antenna ($\approx -300 \mu\text{m} < x < \approx 300 \mu\text{m}$) and their propagation velocities can be calculated to be the speed of light ($k_{SPP} \approx k_0$ at THz frequencies). Since the spatial scan covers a line at $y = 0 \mu\text{m}$, the tilted lines first appear at the very edge of the antenna ($x = \pm 300 \mu\text{m}$) and its centre ($x = 0 \mu\text{m}$) for a time close to 0.25 ps. At the same time, SPPs are excited at any point along the bow-tie edges. These waves propagate on the bow-tie surface from their specific excitation points in a direction orthogonal to the edge. They are then detected by the probe as soon as they reach the line at $y = 0 \mu\text{m}$. This explains why the electric-field in the centre of a bow-tie wing ($x \approx \pm 150 \mu\text{m}$) can only be detected after a temporal delay. Since the SPP waves are excited at all edges and then superimpose on the antenna surface during their propagation, the space-time map shows a typical interference pattern: the tilted black and white lines are continuously interrupted by spots with zero electric-field strength at positions where the interfering electric-fields are out of phase.

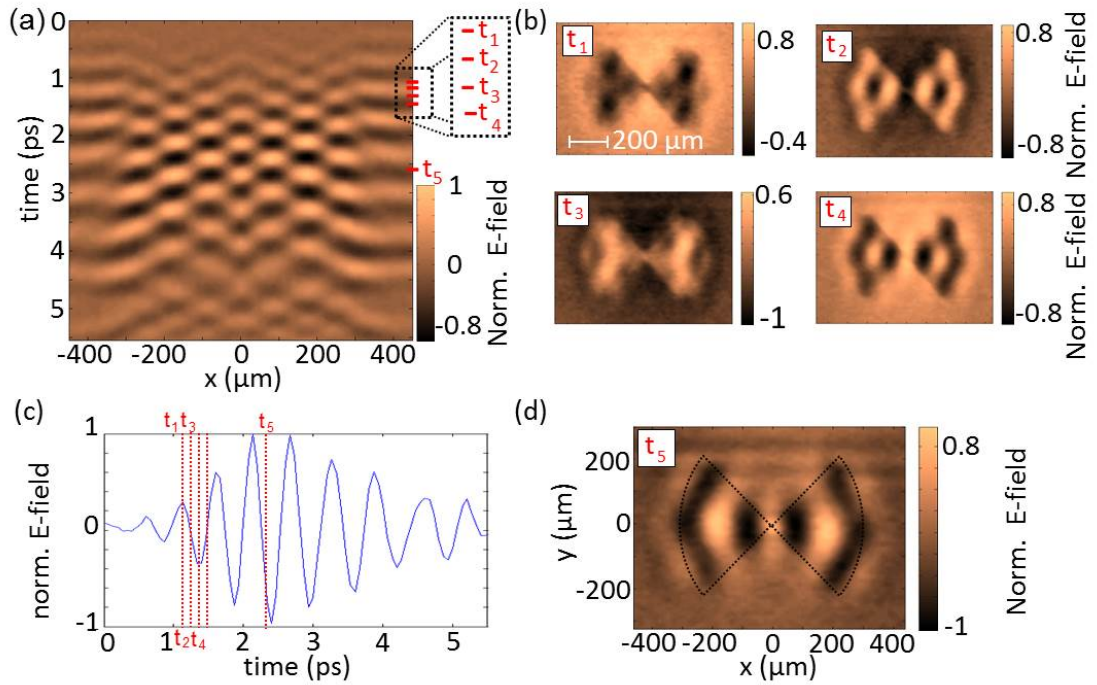


Fig. 2.4: (a) Detected space-time map (xt -map) of the electric-field in the near-field of the bow-tie antenna along a line $y = 0 \mu\text{m}$; (b) Measured near-field images of the bow-tie antenna in the xy -plane for four moments in time as they were indicated in (a); The four maps are normalised to the overall maximum at t_3 ; (c) Detected THz waveform at the centre of the circular waveguide output; (d) Measured near-field image of the antenna for the moment t_5 , the shape of the bow-tie antenna is shown by the dashed line; Figures (a, b, d) are published in Ref. [114].

The SPP wave pattern on the entire bow-tie antenna geometry is measured for four moments in time t_1 to t_4 and can be seen in Fig. 2.4(b). These four moments are indicated in the space-time map in (a) and correspond to a full wave cycle of the incident THz wave. To show the temporal evolution of the incoming THz wave more clearly, the detected THz waveform in the waveguide centre at $x = y = 0 \mu\text{m}$ is shown in Fig. 2.4(c). The temporal moments of interest t_1 to t_4 can also be identified in this plot. These moments were chosen because the standing wave pattern has not been built up fully yet at these early moments in time and, hence, individual waves originating from different antenna edges can be resolved. This makes it easier to investigate the development of the SPP wave pattern on the antenna and to evaluate the coupling mechanism of the near-field probe as it was explained in the previous section.

2.2.2.1 Image Formation on the Bow-Tie Antenna

The detected current by the PC-antenna is caused by a superposition of the incident THz electric-field E^{THz} and the SPP electric-field E^{SPP} , as described in Eq. (2.3). The incident THz field correspond to the horizontal lines at the edges of Fig. 2.4 (a) and the "background colour" in the four images of Fig. 2.4 (b). The electric-field in the shadow-region of the antenna, on the contrary, is the SPP wave. The mapped electric-field distribution, however, only shows the spatial derivative of the actual E^{SPP} . In addition to that, the polarity of the imaged wave also depends on the spatial orientation between the SPP propagation direction \vec{u}_{SPP} and the antenna orientation \vec{u}_{PC-A} . This relationship has a crucial impact on the image formation, as demonstrated in Fig. 2.5.

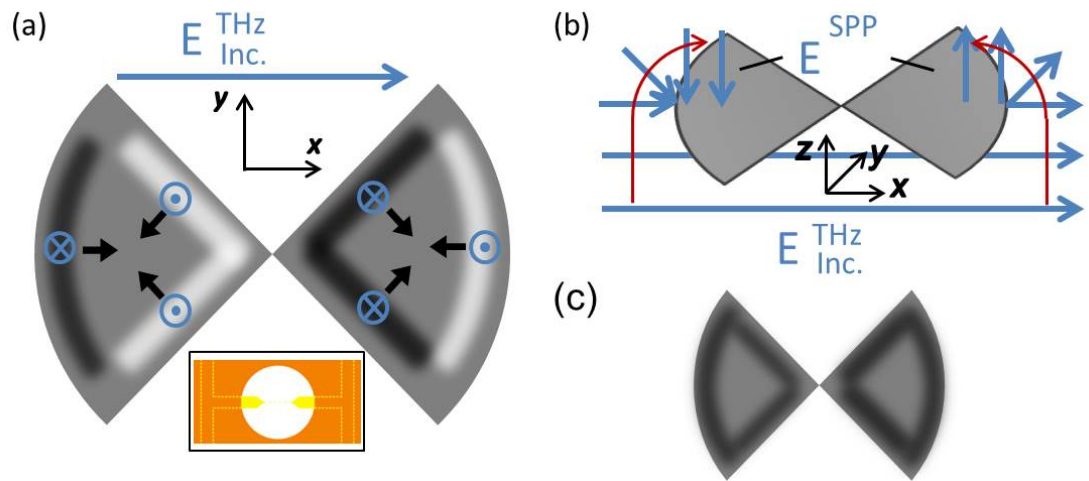


Fig. 2.5: (a) Surface plasmon polariton excitation at the edges of the bow-tie structure; The inset shows the orientation of the near-field probe; (b) The excitation of SPP waves with different polarity at opposite edges of the antenna; (c) Detected image by the near-field probe; Figures (a, c) are published in Ref. [114].

In figure (a), one can see the bow-tie antenna in the xy -plane. The THz electric-field is incident from the back (propagating in positive z -direction) and polarised in the x -direction. This is identical to the experimental circumstances. When the THz pulse hits the sharp edges of the bow-tie antenna, it can either excite an SPP wave with an electric-field component oriented in positive or in negative z -direction. This depends on the spatial orientation of the incoming electric-field with respect to the edge. This is demonstrated in Fig. 2.5 (b), where the THz field "bends around the edge" clockwise on the left side of the antenna and anti-clockwise on the opposite side. As a consequence, the resulting electric-field components "drag" charge carriers along the surface which have different polarity

in order to fulfill the surface boundary condition. This corresponds to SPP waves which are 180° out-of-phase on the two opposite wings of the antenna.

This knowledge can now be applied to Fig. 2.5 (a): at specific edges of the antenna, SPP waves are excited with an electric-field component pointing into the xy -plane (black colour-code), whereas other edges excite SPP waves with the opposite polarisation (white colour-code). After their excitation, the SPP waves propagate in a direction away from the edge towards the centre of an antenna wing. Assuming that the scalar product is positive for a SPP movement in the positive x -direction ($\vec{k}_{SPP} \circ \vec{u}_{PC-A} = 1$), the E^{SPP} in the areas with the black colour-code keep their polarisation. The white areas, on the contrary, are imaged with a 180° phase-shift. Consequently, all the waves are imaged during propagation with a black colour-code as indicated by the black arrows. The resulting image of the E^{SPP} -pattern on the bow-tie antenna detected by the near-field probe is depicted in Fig. 2.5 (c). The electric-field pattern in this case is identical to the one in Fig. 2.4 (b) for the moment t_4 . This confirms the theory of the coupling mechanism and also explains why the measured electric-field patterns are symmetric with respect to the $(x = 0 \mu m, y)$ -plane.

The electric-field pattern on the bow-tie antenna is also imaged for a later moment in time t_5 (Fig. 2.4 (d)). In this case, the SPP waves have been propagating for long enough on the bow-tie antenna to cause a standing wave pattern. This resonant behaviour is strongly supported by the bow-tie geometry. Its round edges can be compared to a lens which forces the SPP waves to propagate between the outer edges and the centre of the antenna. Consequently, for this moment in time, the appearing E^{SPP} field pattern is a superposition of several backward and forward propagating waves.

2.2.2.2 Image Reconstruction of the Original E^{SPP} Pattern

The previous experiments have shown that the knowledge of the coupling mechanism is essential for the correct image interpretation. In addition to that, it also provides a way to reconstruct the original electric-field map: the original E^{SPP} pattern can be obtained by simply inverting the spatial derivation and applying an integration to the measured images. Since the PC-antenna is aligned in the x -direction throughout the experiments, a numerical integration along dx is sufficient for obtaining a correct reconstructed image. Due to the bow-tie geometry and the sensitivity of the probe to the incident THz wave, the reconstructed image would show large distortions especially close to the image centre. These distortions would be caused by an accumulated offset outside the "shadow region" of the bow-tie an-

tenna. In order to mitigate this problem, the electric-field map for the moment t_5 was selected for the reconstruction process. In this case, the "background" caused by the incident THz wave was the lowest for all five electric-field maps. In addition to that, only the part of the map was considered where the sample is present, as indicated by the red dashed lines in Fig. 2.4. Since these measures were still not enough to reduce the offset of the THz electric-field in the image centre, two integrations from the right edge to the centre and from the left edge to the centre were carried out separately. After these operations, both images were merged and the outcome of the reconstruction process can be seen in Fig. 2.6 (b). This image shows the expected anti-symmetric electric-field distribution with opposite polarisations at the round outer edges and the centres of the antenna wings.

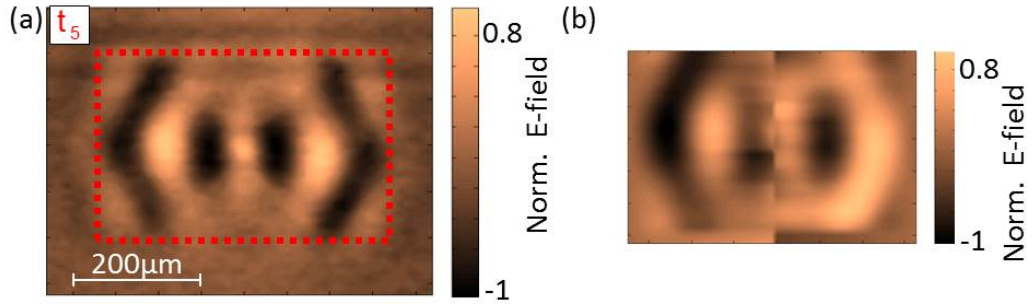


Fig. 2.6: (a) The red dashed box surrounds the area of the electric-field map (Fig. 2.4(d)) used for image reconstruction; (b) Reconstructed E^{SPP} image; Both figures are normalised to their individual maxima; The figures are published in Ref. [114].

2.2.2.3 Exclusive Detection of the Surface Plasmon Waves

The understanding of the different coupling mechanisms for the E^{SPP} and the E^{THz} can also be exploited to discriminate against the incident THz field and to exclusively detect the SPP wave. This is realised in the experiments by rotating the near-field probe by 90° in the xy -plane. Under these circumstances, the PC-antenna should only be sensitive to radiation polarised in the y -direction. Incident THz radiation polarised in the x -direction should therefore not be detected ($\vec{E}^{THz} \circ \vec{u}_{PC-A} = 0$). All other experimental parameters were kept similar to the ones described in Fig. 2.3. The measured electric-field map for this configuration can be seen in Fig. 2.7 (a).

It is obvious that for this configuration the electric-field pattern looks distinctively different from the ones in Fig. 2.4 (b). The moment in time corresponds roughly to the one at t_4 in the respective figure. The E^{SPP} image formation is explained in Fig. 2.7 (b). Since the orientation of the incident THz pulse with re-

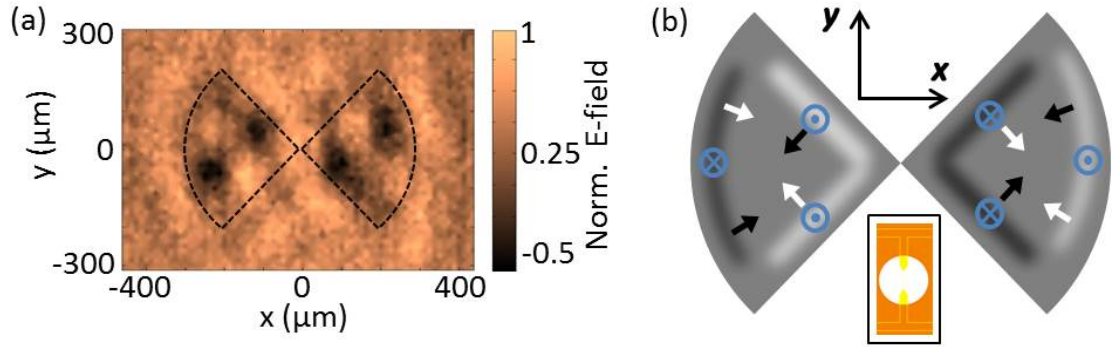


Fig. 2.7: (a) Measured electric-field map with the detector PC-antenna oriented in the y -direction; (b) E^{SPP} image formation on the bow-tie antenna; The inset shows the orientation of the PC-antenna in the near-field probe; Figure (a) is published in Ref. [114].

spect to the bow-tie antenna has not changed in this experiment, the excited SPP pattern on the metallic structure is identical to the one discussed in Fig. 2.5 (a). The PC-antenna, in this case, is sensitive to the tangential electric-field component E_T in the y -direction. As explained earlier, the detected phase of the SPP wave also depends on the direction of its propagation: assuming that SPP waves propagating in the positive y -direction maintain their phases ($\vec{k}_{SPP} \circ \vec{u}_{PC} = 1$) and SPP waves propagating the opposite direction experience a 180° -phase shift ($\vec{k}_{SPP} \circ \vec{u}_{PC-A} = -1$), the SPP waves are imaged with a phase as indicated by the black and white arrows in figure (b). This results in an electric-field pattern as it is visible in the measured electric-field map in Fig. 2.7 (a), confirming the theory of the coupling mechanism.

2.3 Surface Plasmon Waves Excited by a Focused Terahertz Beam

The capability of the integrated near-field probe to image SPPs on the metallic surface of THz devices has been demonstrated in the previous section. Apart from this application, the probe design also allows the investigation of SPP phenomena which take place on the gold surface of the probe itself. In this case, the probe adopts the role of the sample and the detector at the same time. The coupling mechanism, thereby, is almost identical to the one described previously: the propagating SPP wave on the probe surface causes a tangential electric-field component E_T across the aperture and couples into the PC-antenna. The SPP supporting character of the probe is exploited in the following experiments to image SPP waves which are excited by a strongly focused THz beam directly on the probe surface.

The experimental system used for this set of experiments is similar to the one described in Fig. 2.3 (a). Only the bow-tie antenna and the sample holder are replaced by a high-NA silicon lens (radius 1 mm) which is attached directly to the output of the circular waveguide (Fig. 2.8 (a)). This lens is used to strongly focus the propagating linearly polarised HE_{11} -mode on the gold surface of the probe. The focal distance of the Si lens is approximately $40\ \mu\text{m}$ and the minimum THz beam diameter in the focal plane is about $60\ \mu\text{m}$. Throughout all the following experiments, the PC-antenna inside the near-field probe is oriented in the x -direction. The polarisation of the propagating THz pulse inside the waveguide can be rotated arbitrarily in the xy -plane by rotating the pump beam polarisation with a $\lambda/2$ -plate and adjusting the ZnTe crystal orientation accordingly. The probe beam had an optical power of 5 mW and the average power of the chopped pump beam was 200 mW throughout the experiments. The sampling interval for the time-domain waveforms was 67 fs . Similar to the experiments in the previous section, the output of the circular waveguide was scanned with respect to the stationary near-field probe to obtain two-dimensional electric-field maps. The measured electric-field values were recorded by a lock-in amplifier with an integration time of 300 ms . The entire detection system was automated using LabView.

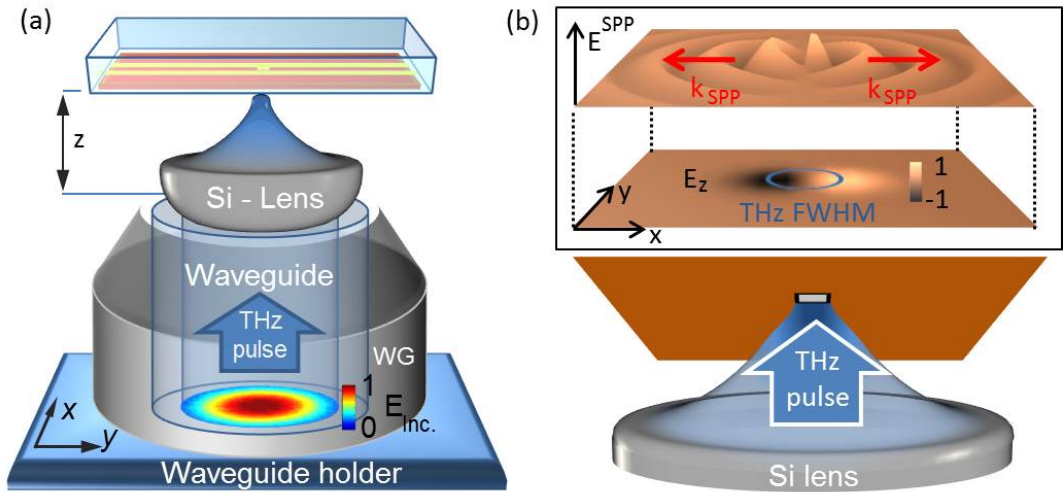


Fig. 2.8: (a) The experimental system for SPP imaging excited by a focused THz beam. This is a detailed view of the dashed box in Fig. 2.3 (a); (b) The simulated E_z -field of a focused THz beam on the surface of the integrated probe and the excited E^{SPP} . Both figures are published in Ref. [114].

The SPP wave was excited directly on the gold surface of the near-field probe by strongly focusing the THz pulse on it. The linearly polarised THz beam exhibits a maximum and a minimum of the longitudinal electric-field component E_z close to the opposite edges of the focused beam spot along an axis parallel to the incident polarisation (bottom image of the inset in Fig. 2.8 (b)). Due to the very small

mismatch between the SPP wavevector k_{SPP} and the free-space wavevector k_0 in the THz range, the induced localised surface charges due to the longitudinal field components can excite a SPP directly on the metal/air interface of the probe. In this case, there is no dielectric needed between the metal and the light source to match the wavevectors k_{SPP} and k_0 , as it is necessary in the optical domain for focused excitation beams [155–157]. The positive and the negative E_z maxima can thereby be considered as two individual "SPP-sources". Each of them causes a separate SPP wave which is inherently 180° out of phase with respect to the other one. The overall SPP wave excited by the focused beam is a superposition of these two waves (top image of the inset in Fig. 2.8 (b)).

The SPP excitation takes place most efficiently in the beam focus. In this spot, the maximum and the minimum of the longitudinal E_z -components are spatially confined to the smallest area. This creates a higher charge density than in any other spot. In addition to that, both "SPP-sources" are spatially separated by about half a wavelength from each other. Therefore, the excited SPP waves overlap in phase along an axis parallel to the incident polarisation, causing a stronger E^{SPP} due to constructive interference .

2.3.1 Imaging of Surface Waves Near a Focused Terahertz Beam

The detected electric-field map for a focused THz beam polarised in the x -direction can be seen in Fig. 2.9 (a). In the experiment, the probe was positioned in the focal spot of the Si lens ($\Delta z = 40 \mu m$). The bright spot in the centre of the field map corresponds to the focused THz beam which the near-field probe is sensitive to in this configuration. In addition to this spot, SPP waves can be observed along the x -direction which appear to move away from the centre as concentric fringes.

A very different pattern can be seen in Fig. 2.9 (b). In this case, the focused THz beam was polarised in the y -direction. Hence, it is not detected by the PC-antenna and the observed pattern is only caused by the SPP wave. In this configuration, the SPP waves are imaged as a spiral-shaped pattern. It also has to be highlighted that this configuration excludes the possibility of measuring an electric-field pattern caused by the diffracted incident THz beam. It is only a negligible portion of the incident THz beam which couples through the sub-wavelength aperture. The major part of the electric-field energy either reflects back into the Si lens or propagates away from the focal beam spot in a radial manner confined in the small air gap between the metallic probe surface and the Si-lens. This light maintains its initial polarisation and should not be detected by the near-field probe.

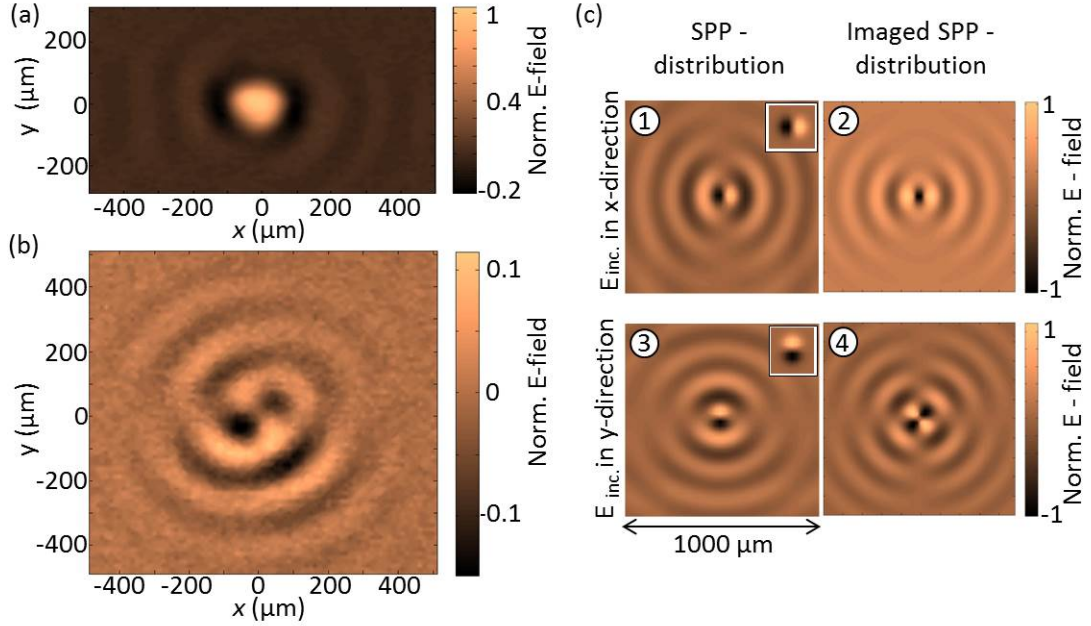


Fig. 2.9: Detected electric-field patterns near a strongly focused incident THz beam polarised in the x -direction (a) and the y -direction (b). In both cases, the PC-antenna is aligned in the x -direction and the field maps are normalised to the maximum in (a); (c) The two electric-field maps in the top row show the simulated SPP-distribution (1) and the imaged SPP-distribution (2) for the incident THz beam polarised in the x -direction. The bottom row shows the simulated SPP-distribution (3) and the imaged SPP-distribution (4) for the THz beam polarised in the y -direction. The insets indicate the simulated E_z -distribution for each row. Images (a, b) and the field maps (2, 4) in (c) are published in Ref. [114, 150].

The detected E^{SPP} patterns are simulated in Fig. 2.9(c), both for an incident THz beam polarised in the x -direction (top row) and in the y -direction (bottom row). To simulate these SPP waves, the E_z -distribution in the focal plane ($z = 0 \mu m$) of a Gaussian beam was calculated according to [15]:

$$E_z(x, y, z = 0, t) = -i 2 \frac{u_{inc}}{kw_0^2} \cdot E_{Gaussian}(t) e^{-\frac{x^2+y^2}{w^2}} \quad (2.4)$$

The variable u_{inc} is the direction of the incident polarisation and represents either x or y . The input Gaussian beam is defined by its maximum electric-field strength $E_{Gaussian}$ and its beam waist w_0 . The calculated E_z -distributions for the two different input polarisations can be seen in the insets of maps 1 and 3 in Fig. 2.9(c). The FWHM of the electric-field in the focal spot is $60 \mu m$ in accordance with the experiments. Each individual point in the simulated $E_z(x, y)$ -map is considered as a SPP source which emits a surface wave in radial direction according to its calculated amplitude. The superposition of all these waves leads

to the electric-field patterns in the maps 1 and 3. These two maps show the original E^{SPP} - distributions on the metal surface of the near-field probe excited by a strongly focused THz beam for two different polarisations.

The imaged E^{SPP} - distributions are obtained by applying a spatial derivative to both electric-field maps 1 and 3 (Eq. (2.1)). Due to the alignment of the PC-antenna in the experiments, a derivation along x has to be applied. The outcome is shown in the maps 2 and 4. One can see that both simulated electric-field maps resemble the measured ones well: for the incident THz beam polarised in the x - direction, the concentric waves propagating in the x - direction are present in the simulated and the measured maps. Only the bright THz spot in the centre is missing in map 2, since it was not considered in the simulations. The spiral-type electric-field pattern is also clearly observable in the simulations for an incident beam polarised in the y - direction. Due to the absence of the incident THz beam, the simulated and the measured electric-field maps show an even better match for this THz polarisation. However, one feature can attract the attention of the reader: an electric-field is present along the line $(x = 0, y)$ in Fig. 2.9 (b), although it should not exist. This can be explained by the offset structure of the employed PC-antenna, which exposes a very small sensitivity to the y - component of the incident field [158]. In addition to that, there is always the possibility of a small misalignment in the detection system which causes a deviation from the intended orthogonal alignment between the excited THz polarisation and the PC-antenna.

In addition to these experimental problems, imaging the SPP-distribution using the near-field probe also changes the symmetry of the original SPP-patterns. A similar phenomenon was discussed in the previous section on the bow-tie antenna and was attributed to the coupling mechanism: since the phase of the measured electric-field also depends on the direction of movement \vec{k}_{SPP} with respect to the antenna orientation \vec{A}_{PC} , both detected electric-field maps in Fig. 2.9 (a, b) exhibit a change in symmetry along a line $(x = 0, y)$

2.3.1.1 Reconstruction of the original pattern

For image reconstruction of the original E^{SPP} - patterns, the same analytical approach was applied to both images that was introduced in the previous section. One can see that both reconstructed images resemble the simulated E^{SPP} - patterns (Maps 1 and 3 in Fig. 2.9 (c)) well, although the merging lines between the left and right integral regions are clearly visible. Also, the central spot in Fig. 2.10 (a) is clearly distorted due to the contributions of the incident transversal THz beam. However, the SPP waves spreading out in the x - direction can clearly be identified.

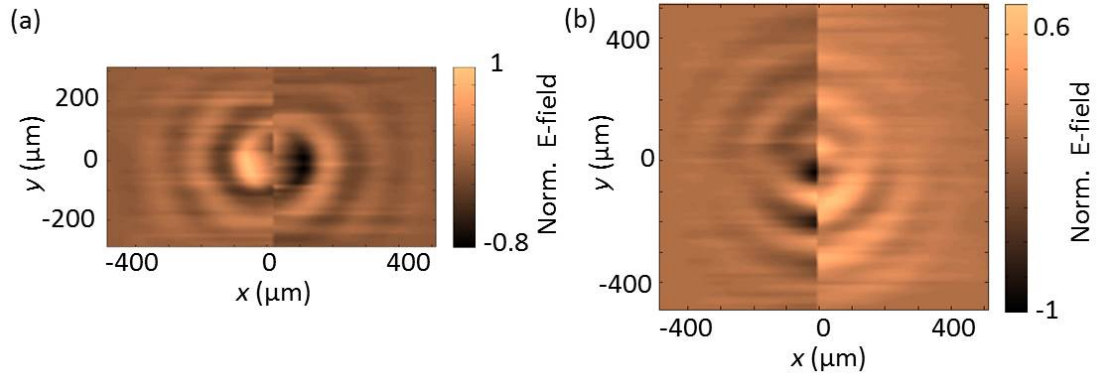


Fig. 2.10: Reconstructed SPP patterns for an incident beam polarised in the x - (a) and the y - (b) direction; Figure (b) is published in Ref. [114].

2.3.2 Surface Plasmon Character of the Detected Field Patterns

The measured electric-field maps in Fig. 2.9 (a, b) agree very well with the E^{SPP} -coupling theory. Also, the incident transversal THz pulse could be excluded from causing the respective patterns in Fig. 2.9 (b). These two points seem to confirm the SPP character of these waves. This subsection now puts its focus on the investigation of SPP wave excitation in the THz focal spot. Similar to the section on the bow-tie antenna, a look at the space-time maps is of revealing nature for this purpose.

Space-time maps were recorded along the x -axis at $y = 0 \mu\text{m}$ (xt -maps in the top row of Fig. 2.11) and along the y -axis at $x = 0 \mu\text{m}$ (yt -maps in the bottom row). This was done for different distances Δz between the surface of the near-field probe and the Si lens, beginning from the focal distance ($\Delta z = 40 \mu\text{m}$) up to $\Delta z = 200 \mu\text{m}$ (Fig. 2.11 (b)). The scans along the respective spatial axes were carried out along a distance of $500 \mu\text{m}$ with an incident THz beam polarised in the x -direction. A time-resolved image was obtained in a temporal range of 4 ps with a step size of 67 fs . The electric-field maps are recorded for different distances z between the Si lens and the near-field probe (Fig. 2.11 (a)).

The xt -maps and the yt -maps for the distances $\Delta z = 200 \mu\text{m}$ (maps 1, 2) and $\Delta z = 100 \mu\text{m}$ (maps 3, 4) are almost identical. Spherical wavefronts are present in all four cases, which corresponds to the wavefronts of the expanding Gaussian-shaped THz pulse. The electric-field maps at $\Delta z = 200 \mu\text{m}$ exhibit a spatially extended wavefront compared to the one at $z = 100 \mu\text{m}$, spanning almost a range of

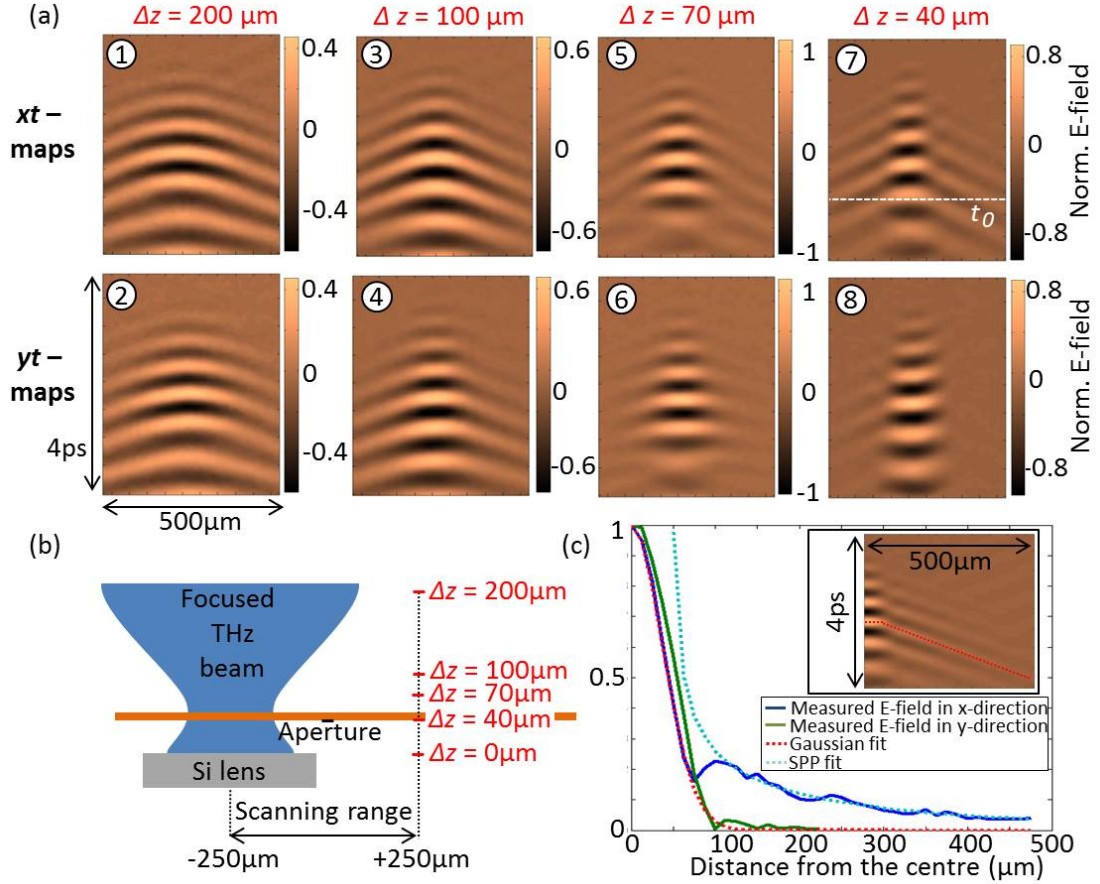


Fig. 2.11: (a) Space-time maps along the x -axis ($y = 0 \mu\text{m}$) (top row) and the y -axis ($x = 0 \mu\text{m}$) (bottom row) for different distances z between the Si lens and the near-field probe; All field maps are normalised to the maximum value at $z = 70 \mu\text{m}$; (b) Schematic diagram of the experimental system; (c) Normalised detected electric-field amplitude along the x - and y -axis as a function of the distance from the centre at $(x = 0 \mu\text{m}, y = 0 \mu\text{m})$; the plotted values are taken along a line as it is shown by the dashed line in the inset; a Gaussian fit and a SPP fit according to Eq. (2.5) are added for comparison; Figures (a, c) are published in Ref. [150].

$400 \mu\text{m}$ along both axes. This is clearly due to the spatial extension of the diverging beam. In addition to that, oscillations appear to last longer at later times of the pulse in all field maps. This can be observed by the thicker horizontal lines at the bottom of each field map compared to the ones at the top. This behaviour is explained by dispersive pulse propagation through the cylindrical waveguide, causing modes with higher frequency components to arrive earlier than the ones with lower frequency components [151].

One can see distinctly different electric-field patterns in the focal plane of the THz beam at $\Delta z = 40 \mu\text{m}$ (maps 7, 8). The temporal evolution of the incident THz beam can be allocated to the series of black and white horizontal crests in the centre of the map. These crests are spatially less extended compared to the other

field maps due to the smallest beam waist in the focal spot. In addition to that, these lines appear to be perfectly horizontal, which resembles the plane wavefront in the beam focus. Apart from the difference in the imaged incident THz beam, one can observe straight lines moving away from the centre. These lines seem to be replacing the spherically diverging waves. It is important to note that these lines are only present in the xt -map and do not appear in the yt -map. These straight lines can be allocated to the same SPP wave which has already been observed in the xy -map in Fig. 2.9(a). The corresponding moment in time t_0 , when Fig. 2.9(a) was recorded, is also indicated by the dashed white line in map 7. Using the space-time maps, one can now explain the origin of the SPP waves in the xy -map: they are excited in the THz beam focus and propagate preferably in a direction determined by the polarisation of the incident beam. This propagation takes place at the speed of light, which can be calculated from the slope of these lines. In the y -direction, on the contrary, the SPP waves cancel each other due to their opposite phases. In these series of experiments, it is also experimentally proved that the SPP excitation is most efficient in the focal spot of the THz beam. For $\Delta z = 70 \mu m$ in field map 5, for example, the straight lines are clearly less pronounced than they are at the focal distance $z = 40 \mu m$.

The space-time maps also allow the estimation of the SPP decay length δ_x for its propagation along the x -axis. Therefore, the electric-field amplitudes were recorded along one of the straight SPP lines that propagate away from the image centre. The electric-field maps 7 and 8 in Fig. 2.11(a) were re-scanned from the centre to $500 \mu m$ to obtain a wider spatial range. The respective xt -map is shown in the inset of Fig. 2.11(c). Also drawn in the figure is a red dashed line showing the SPP wave where the amplitude was recorded from. The amplitude values along a similar trace were also taken in the extended yt -map for comparison, although no SPP wave is present in this case. The evolution of the recorded amplitudes can be seen in Fig. 2.11(c) as the blue and green lines. For distances from the centre smaller than $80 \mu m$, both the amplitudes in the x - and y -directions follow a typical Gaussian-like decay. This can be attributed to the focused incident THz pulse. A Gaussian fit is added to the plot as a red dashed line to emphasise the similarity. However, beginning from a distance of about $\approx 100 \mu m$, an additional electric-field component is present for the scan along the x -axis. According to Ref. [77, 86], this component can be described by a cylindrically diverging SPP wave:

$$E^{SPP}(x, y = 0) = \frac{1}{\sqrt{|x - x_0|}} \cdot e^{-\frac{|x - x_0|}{2 \cdot \delta_{SPP}}} \quad (2.5)$$

The variable δ_{SPP} represents the SPP decay length and x_0 corresponds to the position of the centre of the SPP wave along the x -axis. This point is determined by the maximum value of the E_z -component within the focused THz spot and is at $x_0 = 45 \mu m$ in the experiments. Equation (2.5) has been fitted to the measured value and an E^{SPP} decay length of $\delta_{SPP} = 200 \pm 100 \mu m$ could be estimated. The determined SPP decay length in this experiment is much smaller than the theoretically determined values reaching up to several millimeters [14, 15, 138]. A reason for the reduced decay length could be the presence of the Si lens in the proximity of the probe surface ($\Delta z = 40 \mu m$). The introduction of a dielectric into the E^{SPP} field converts the evanescent wave into a propagating one inside the lens, similarly to frustrated total internal reflection. As the dielectric covers the entire area of where the SPP wave is present, a large portion of the SPP wave is expected to be converted into a propagating wave.

2.4 Suitability of the Integrated Near-Field Probe for Surface Plasmon Imaging

Surface wave imaging with the integrated near-field probe was successfully demonstrated in the previous sections using two different examples: the investigation of SPPs on a bow-tie antenna and in a strongly focused THz beam. In these cases, the SPP imaging capability of this probe seemed to be suitable for the respective applications. The general suitability of this probe for THz SPP imaging, however, needs to be discussed more thoroughly. Also, there are some unique peculiarities of this probe which were not highlighted sufficiently in the previous sections and require further discussion. Therefore, this section emphasises specific probe peculiarities and discusses limitations to its applicability in order to conclude this chapter.

Invasiveness of the Probe

When using this probe for SPP imaging, the comparably large metallic probe surface needs to be introduced parallel to the sample. Metallic elements, however, are expected to be highly invasive in electric-field measurements and cause undesired distortions in the detected electric-field maps. This question was addressed by my colleague Michele Natrella who published his results on this topic in Ref. [159]. He simulated the electric-field patterns in CST Microwave Studio using exactly the same configuration as in the experiments. Also, by using the data of the measured incident THz pulse waveform, he was able to simulate the electric-field distribu-

tions on the bow-tie antenna for the same moments in time t_1 to t_4 as shown in Fig. 2.4 (b). He then compared the excited SPP wave patterns on the bow-tie antenna with and without the presence of the near-field probe (Fig. 2.12). The probe itself was simulated as a gold sheet parallel to the bow-tie antenna.

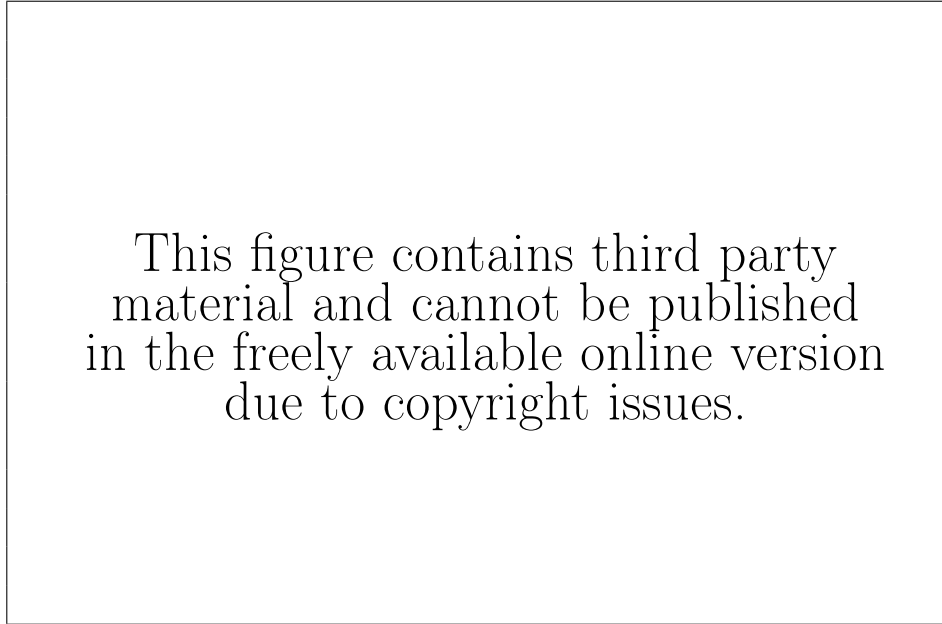


Fig. 2.12: The simulated electric-field patterns on the bow-tie antenna with and without the metallic sheet of the near-field probe being present. The four moments in time correspond to the same moments as in Fig. 2.4 (b). The image was taken from Ref. [159].

The electric-field patterns in both cases appear to be almost identical, suggesting an unexpectedly low level of invasiveness of the probe. This can be explained by the fact that the introduction of the probe does not impose any crucial changes to the E^{SPP} distribution: the E^{SPP} is perfectly orthogonal to the metallic probe surface and, therefore, experiences basically no distortions. Field distortions take only place at the edges of the bow-tie antenna, where the E^{SPP} is not perfectly normal to the probe surface. The measured electric-field maps at the edges of the bow-tie antenna, however, have to be analysed with particular care anyway: in the experiments, both the E^{SPP} and the E^{THz} couple into the probe simultaneously and the electric-field maps at the edges can be considered to be ambiguous.

Imaging Artefacts in Near-Field Microscopy

Sub-wavelength apertures for high-resolution spatial imaging are commonly used, and, therefore, a thorough understanding of the physical processes in the proximity of the aperture is essential. The possible generation of a tangential electric-field component due to propagating surface waves, for example, is essential due to two

reasons: first, this sensitivity can be exploited for SPP wave imaging, as demonstrated previously. Second, this sensitivity can also cause imaging artefacts when using a sub-wavelength aperture in any ordinary near-field microscopy system. The presence of sharp metallic features, as they exist in antenna patches or transmission lines for example, can excite SPPs. The excited SPP wave can couple to the metallic probe surface and propagate along it. It can then cause a tangential electric-field component across the aperture and couple into any detector positioned behind the aperture. Being aware of the possibility of such an imaging artefact is important for the correct interpretation of near-field images. An example can be found in Ref. [78], where the integrated near-field probe was used to image a planar antenna structure. The presence of white and black shadows in the near-field image could not be interpreted without the knowledge presented in this chapter.

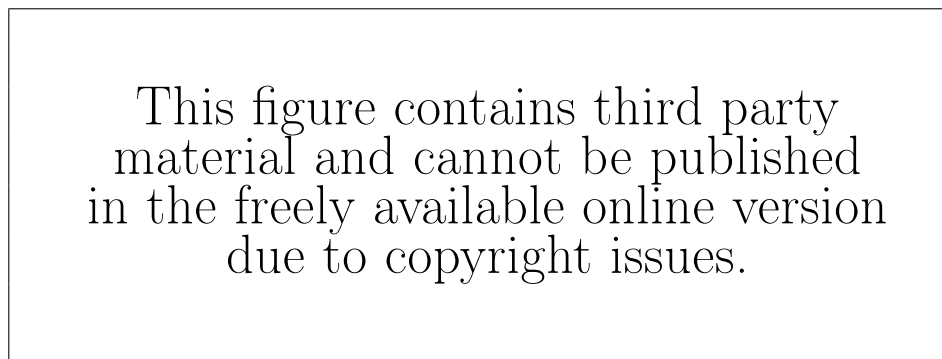


Fig. 2.13: (a) The geometry of a planar antenna which is imaged by the integrated near-field probe; (b) Near-field image of the same antenna exhibiting unexpected white and black shadows (from Ref. [78]).

Surface Plasmon Excitation on the Probe Surface

As demonstrated in the experiments about the SPP wave excitation in the focus of the THz beam, surface waves can be excited on the gold surface of the probe itself. This was an essential feature of the probe when doing this specific type of experiment. Most of the common near-field probes need to be inserted into the E^{SPP} as close to the sample surface as possible to probe the field strength. As soon as such a probe is inserted into the focal spot of the THz beam, it would inherently block a part of the beam from reaching the sample surface and prevent the SPP wave from being excited. Such a configuration, therefore, would not be suitable for performing this type of measurement. In case of the focused THz beam experiments, it was the sensitivity of the employed probe to the electric-field component orthogonal to its own surface which allowed the successful detection of a SPP wave.

Applications and Limitations of the Near-field Probe for SPP Imaging

This type of probe seems to be especially suitable for SPP imaging applications on relatively large metallic surfaces which can block the incident E^{THz} . Similar to the experiments with the bow-tie antenna, this probe scans the E^{SPP} in the "shadow region" of the incident THz excitation beam. In this case, the incident THz beam is blocked by the sample surface itself and the mapped electric-field is only caused by the surface wave. This holds true for all the regions sufficiently away from edges. As a second application, this probe can be used when the insertion of an additional probe into the near-field of the sample would prohibit the conduction of a successful experiment. In this case, one can excite surface plasmons directly on the probe as it was done in the experiment with the focused THz beam.

This type of probe, however, also exhibits specific disadvantages. When using this probe, it is certainly a drawback that only a spatial derivative of the E^{SPP} is detected. Although it is possible to reconstruct the original patterns, there is still some room for improvements. In the experiments, it is especially important to prevent the detection of the incident THz beam to successfully reconstruct the original field map. This, however, can be experimentally difficult to realise as it was shown in the previous examples.

As a further point, this type of probe seems to be not suitable for small metallic samples or for samples with advanced geometries including numerous edges. This, for example, can be a fractal antenna as it is presented in Ref. [115]. This is mainly due to two reasons: first, the mapped electric-field in the proximities of the edges is ambiguous, as explained earlier. Second, the presence of many sub-wavelength features and edges can excite numerous SPP waves which can all propagate along the probe surface and couple into the aperture. This can cause the generation of puzzling electric-field patterns. Both reasons make the correct interpretation and reconstruction of the detected electric-field maps a complex endeavour for samples with advanced geometries.

For these specific applications, the presented near-field probe might not be the most advantageous detector option and different detector types should be considered. Electro-optic crystals, for example, are a potential alternative for SPP detectors and can offer valid solutions to the problems stated above. A THz SPP near-field detection system based on an electro-optic crystal, therefore, was also developed in the scope of this project. It is presented in more detailed throughout the following chapters of this thesis.

2.5 Conclusions

The experiments carried out throughout this chapter have shown that the integrated sub-wavelength aperture near-field probe, as it is normally used for ordinary THz near-field imaging, is sensitive to an electric-field component normal to its metallic surface. The knowledge of this sensitivity is important due to two reasons: first, it allows the explanation of imaging artefacts in near-field microscopy when similar detector types are used. Second, this feature can be exploited for SPP wave imaging. This has been done in the scope of this project and the integrated near-field probe has been successfully applied to two SPP imaging examples.

First, the SPP wave excitation and propagation on the resonant structure of a bow-tie antenna has been investigated. It has been shown that several SPP waves are excited at the sharp edges of the structure. These waves superimpose during propagation, causing a standing wave pattern on the metallic surface. The understanding of the electric-field distribution in the near-field of the antenna is essential for the evaluation of the antenna performance and, hence, for finding the optimum antenna geometry.

Second, the SPP excitation by a focused THz beam directly on the metallic probe surface was investigated. It has been found out that the SPP excitation takes place most efficiently in the THz beam focus. The excited SPP waves propagate along a direction which is determined by the polarisation of the incident THz field. The SPP excitation by an incident free-space beam directly on a metallic surface was reported for the first time in the literature [150].

These examples have demonstrated that the integrated sub-wavelength aperture near-field probe can be used as an efficient SPP imaging tool and help to investigate and understand the physical phenomena of an electro-magnetic surface wave. It has been shown that this probe can provide a vital insight into the role of SPPs in THz devices and that it has the potential for supporting the development of novel THz device concepts.

3 A Micro-Resonator for Electro-Optic Imaging

Electro-optic sampling is a popular phase-sensitive electric-field detection method in microwave [160, 161] and THz [99] technology. In this project, a THz near-field detection system is developed which uses a very particular type of electro-optic probe: an electro-optic micro-resonator.

This chapter is therefore devoted to addressing the topic of electric-field sampling using electro-optic detection crystals. In a first step, the physical phenomenon is explained which this type of detectors depends on: the electro-optic effect in non-linear media. A literature review is then presented to show how this effect is exploited for electric-field detection and mapping. Also, the suitability of electro-optic crystals for SPP imaging is discussed. This finally leads to the introduction of a specific near-field detector geometry which employs a resonant Fabry-Pérot cavity for sensitivity enhancement.

3.1 Optical Properties of Crystals

Crystals are composed of periodic arrays of atoms or molecules with a particular symmetry. The atomic structure of the material governs the response of the crystal to an electro-magnetic excitation. Throughout this project, the alloy $Al_{1-x}Ga_xAs$ is exclusively used as electro-optic material. Therefore, only the atomic structure of this alloy is considered in the following paragraphs and the explanation of the electro-optic effect is limited to this material.

The alloy $Al_{1-x}Ga_xAs$ belongs to the Zinc-Blende group, together with other composites such as InAs, CuCl, and CdTe [162]. Atoms in these crystals form a cubic lattice. The unit cell combines two face-centred cubic lattices, one of which is shifted with respect to the other one by one quarter of the unit cell along the diagonal. In a Zinc-Blende III-V alloy, the lattice is composed of an atom from the III-group and an atom from the V-group. The valence electrons form slightly ionic bonds with their neighbouring atoms due to their different electronegativity. The spatial atom distribution in a GaAs cubic cell is shown in Fig. 3.1.

The symmetry properties of a crystal structure play a decisive role in its optical response and give rise to phenomena such as birefringence, optical rotation, and electro-optical or acousto-optical effects [162]. As it is the case for any medium, the interaction of an electro-magnetic wave with a crystal has to comply with the

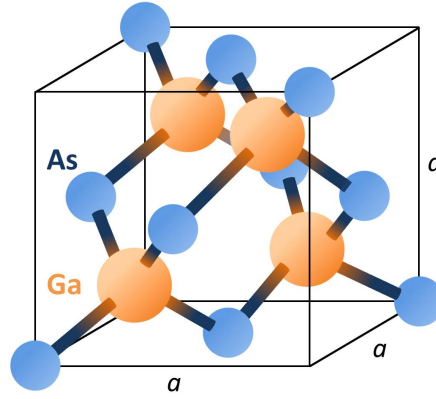


Fig. 3.1: The cubic structure of a GaAs crystal.

Maxwell equations. In a homogeneous and lossless medium, the following space- and time-dependent electric-field vector $E_x(\vec{r}, t)$ propagating in the z -direction can be derived from these equations (a derivation can be found in Appendix C):

$$E_x(\vec{r}, t) = \hat{E}_x \cdot e^{i(\omega \cdot t - \beta_z \cdot z)}. \quad (3.1)$$

The subscript x describes the polarisation direction of the electric-field and the ϵ_x symbolises the permittivity experienced by this polarisation. The value μ_0 is the direction independent permeability of the non-magnetic crystal. The propagation of the electric-field vector in Eq. (3.1) is described by the propagation constant β_z , which depends on the material parameters μ and ϵ as follows:

$$\beta_z^2 = \omega^2 \cdot \mu_0 \cdot \epsilon_x \Rightarrow \beta_z = \omega \cdot \sqrt{\mu_0 \cdot \epsilon_x} \quad (3.2)$$

As a consequence, the propagation of an electric-field with a specific polarisation (along x in Eq. (3.2)) depends on the material permittivity ϵ for this polarisation. Hence, the electric-field propagation inside a material can differ between the orthogonal polarisations, depending on the respective permittivity.

3.1.1 Isotropy and Anisotropy in Crystals

A material possessing a spatially dependent permittivity ϵ is called "optically anisotropic". In this case, the electric-displacement vector \vec{D} and the electric-field vector \vec{E} cannot be simply related by a scalar factor ϵ [163]. For anisotropic materials in a three-dimensional space, a directionally dependent tensor ϵ_{ij} ($i, j = x, y, z$) has to be introduced. Reference [164] has derived the symmetry $\epsilon_{ij} = \epsilon_{ji}$,

which allows rewriting this tensor using only six different elements according to

$$\epsilon_{ij} = \begin{pmatrix} \epsilon_{xx} & \epsilon_{xy} & \epsilon_{xz} \\ \epsilon_{xy} & \epsilon_{yy} & \epsilon_{yz} \\ \epsilon_{xz} & \epsilon_{yz} & \epsilon_{zz} \end{pmatrix} \quad (3.3)$$

Due to its symmetry, this 3x3 matrix can be transformed into a diagonal matrix and can be rewritten as follows:

$$\begin{pmatrix} D_x \\ D_y \\ D_z \end{pmatrix} = \begin{pmatrix} \epsilon_x & 0 & 0 \\ 0 & \epsilon_y & 0 \\ 0 & 0 & \epsilon_z \end{pmatrix} \cdot \begin{pmatrix} E_x \\ E_y \\ E_z \end{pmatrix} . \quad (3.4)$$

The diagonal elements ϵ_x , ϵ_y , and ϵ_z are the Eigenvalues of the permittivity tensor and determine the permittivity ϵ along the respective coordinate axis. Such an axis is also called "principle axis" [165] and determines a "plane" along which a linearly polarised electric-field experiences only one specific permittivity ϵ_i .

In general, "isotropy" is defined as the case for which all three Eigenvalues have the same permittivity ($\epsilon_x = \epsilon_y = \epsilon_z$). In isotropic crystals, the direction of propagation and polarisation of the electromagnetic wave is independent of the spatial alignment of the crystal axis. In the case of an anisotropic crystal, the permittivities ($\epsilon_x, \epsilon_y, \epsilon_z$) are not equal. This optical attribute refers to the term "birefringent". If only one of the permittivities differs from the remaining two, the crystal is called "optically uniaxial". If all three elements are different, the crystal is called "optically biaxial".

A visual interpretation of the geometric properties of a crystal is the so-called "index ellipsoid". It directly connects the principle axes of a material (x, y, z) with their respective refractive indices n_x, n_y, n_z using the ellipsoid equation [162, 166]:

$$\frac{x^2}{n_x^2} + \frac{y^2}{n_y^2} + \frac{z^2}{n_z^2} = 1 . \quad (3.5)$$

In case of an isotropic material, all axes have the same length and the ellipsoid is a sphere. For a birefringent material, the sphere changes into an ellipsoid. Examples of the geometric interpretations are given in Fig. 3.2.

The index ellipsoid provides a very descriptive way of representing the electric-field propagation through the crystal. As it is shown in Fig. 3.3 for a linear polarised electric-field propagating in the z -direction, an intersection plane perpendicular to the propagation direction can be cut through the centre point of the ellipsoid. The electric-field vector of the incident beam can be projected on the respective

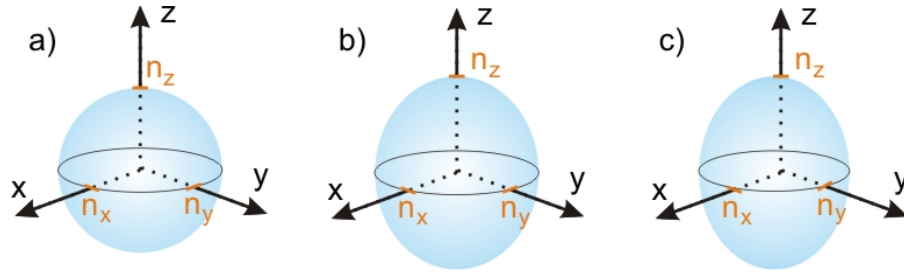


Fig. 3.2: Index ellipsoids for (a) an isotropic material ($n_x = n_y = n_z$), (b) an optically uniaxial material ($n_x = n_y < n_z$), and (c) an optically biaxial material ($n_y < n_x < n_z$).

principle axes n_x and n_y . The electric-field component polarised in the x -direction thereby experiences the refractive index n_x , whereas the y -component experiences the index n_y . In general, maximum two modes of propagation exist through the crystal for any given direction of the incident beam [165].

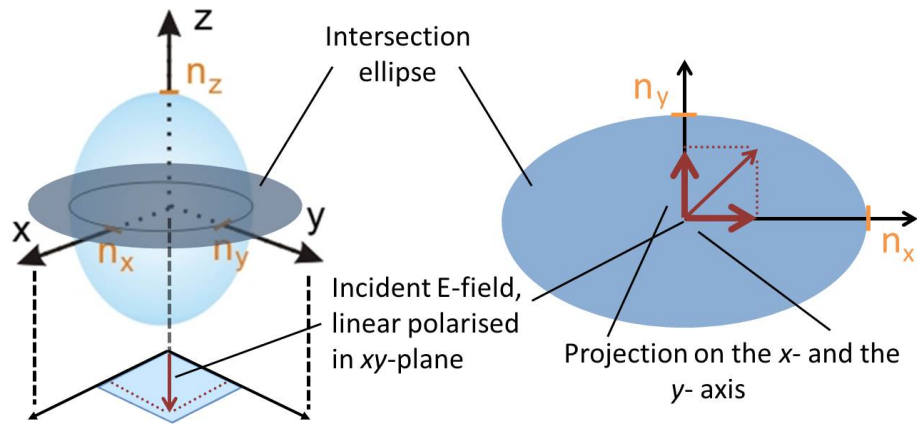


Fig. 3.3: Propagation of a linear polarised electric-field in the "ellipse index plane" and its projection on the principle axis of the ellipsoid.

3.2 The Electro-Optic Effect

Anisotropy is exhibited by some materials as a natural optical property. In addition to that, anisotropy can be caused by the application of an external electric-field: this can either cause birefringence in an initially isotropic media or it can change the optical properties of an anisotropic material. The physical phenomenon is called "electro-optic effect". In initially isotropic materials, the reason for its sudden anisotropy is the deviation of the permittivity ϵ ($\epsilon = \frac{\delta D}{\delta E}$) from a straight line when applying an external electric-field. In this case, ϵ can be expressed as a function of the susceptibility χ and the applied electric-field E as follows [167]:

$$\epsilon(\epsilon_0, \chi, E) = \epsilon_0(1 + \chi^{(1)} + \chi^{(2)} \cdot E + \chi^{(3)} \cdot E^2 + \dots) \quad (3.6)$$

In Eq. (3.6), $\chi^{(1)}$ is the parameter which determines the ϵ_r of the material. The second order term $\chi^{(2)}$ is linearly proportional to the applied electric-field E . It causes the "second-order" electro-optic effect, which is also known as "Pockels Effect". The third order term $\chi^{(3)}$ is proportional to the square of the electric-field and is known as the non-linear "Kerr Effect". It is very small and will be neglected in this thesis.

3.2.1 Mathematical Treatment of the Electro-Optic Effect

Numerous approaches of calculating the change in the refractive indices for any type of crystal group with respect to any direction of incident polarisations can be found in the literature. The most common way to mathematically describe the electro-optic effect is the introduction of the linear electro-optic tensor $\vec{\mathbf{r}}_{i,j}$ ($i = 1-3$ and $j = 1-6$) [167–169]. It gives a direct connection between an applied electric-field $\vec{E} = E_x \cdot \vec{u}_x + E_y \cdot \vec{u}_y + E_z \cdot \vec{u}_z$ and the change in the refractive index Δn :

$$\begin{pmatrix} \Delta \left(\frac{1}{n^2}\right)_1 \\ \Delta \left(\frac{1}{n^2}\right)_2 \\ \Delta \left(\frac{1}{n^2}\right)_3 \\ \Delta \left(\frac{1}{n^2}\right)_4 \\ \Delta \left(\frac{1}{n^2}\right)_5 \\ \Delta \left(\frac{1}{n^2}\right)_6 \end{pmatrix} = \begin{pmatrix} r_{11} & r_{12} & r_{13} \\ r_{21} & r_{22} & r_{23} \\ r_{31} & r_{32} & r_{33} \\ r_{41} & r_{42} & r_{43} \\ r_{51} & r_{52} & r_{53} \\ r_{61} & r_{62} & r_{63} \end{pmatrix} \cdot \begin{pmatrix} E_x \\ E_y \\ E_z \end{pmatrix} . \quad (3.7)$$

The changes in the refractive indices according to the elements on the left side of Eq. (3.7) can be directly applied to permittivity tensor in Eq. (3.4). This gives a new refractive index tensor $\left(\frac{1}{n^2}\right)'$ for the material in case of an applied external electric-field:

$$\left(\frac{1}{n^2}\right)' = \begin{pmatrix} \frac{1}{n_x^2} + \Delta \left(\frac{1}{n^2}\right)_1 & \Delta \left(\frac{1}{n^2}\right)_6 & \Delta \left(\frac{1}{n^2}\right)_5 \\ \Delta \left(\frac{1}{n^2}\right)_6 & \frac{1}{n_y^2} + \Delta \left(\frac{1}{n^2}\right)_2 & \Delta \left(\frac{1}{n^2}\right)_4 \\ \Delta \left(\frac{1}{n^2}\right)_5 & \Delta \left(\frac{1}{n^2}\right)_4 & \frac{1}{n_z^2} + \Delta \left(\frac{1}{n^2}\right)_3 \end{pmatrix} . \quad (3.8)$$

In case of crystals from the Zinc-Blende group, the only non-zero elements in the electro-optic tensor $\vec{\mathbf{r}}_{i,j}$ are $r_{41} = r_{52} = r_{63}$ [162, 165, 170]. Hence, the index ellipsoid equation (Eq. (3.5)) can be rewritten as

$$\frac{x^2}{n_x^2} + \frac{y^2}{n_y^2} + \frac{z^2}{n_z^2} + 2 \cdot r_{41} \cdot (E_x \cdot y \cdot z + E_y \cdot x \cdot z + E_z \cdot x \cdot y) = 1 \quad . \quad (3.9)$$

An externally applied electric-field causes the existence of mixed terms in Eq.

(3.9). These mixed terms cause a rotation of the principal axes additional to the change in the refractive indices Δn . A summary of the changes in the refractive indices for an electric-field incident to different crystal planes of a Zinc-Blende crystal can be seen in Table 3.1.

	E \perp (001)-plane $E_x = E_y = 0, E_z = E$	E \perp (110)-plane $E_x = E_y = \frac{E}{\sqrt{2}}, E_z = 0$	E \perp (111)-plane $E_x = E_y = E_z = \frac{E}{\sqrt{3}}$
n'_x	$n_0 + \frac{1}{2} \cdot n_0^3 \cdot r_{41} \cdot E$	$n_0 + \frac{1}{2} \cdot n_0^3 \cdot r_{41} \cdot E$	$n_0 + \frac{1}{2\sqrt{3}} \cdot n_0^3 \cdot r_{41} \cdot E$
n'_y	$n_0 - \frac{1}{2} \cdot n_0^3 \cdot r_{41} \cdot E$	$n_0 - \frac{1}{2} \cdot n_0^3 \cdot r_{41} \cdot E$	$n_0 + \frac{1}{2\sqrt{3}} \cdot n_0^3 \cdot r_{41} \cdot E$
n'_z	n_0	n_0	$n_0 - \frac{1}{\sqrt{3}} \cdot n_0^3 \cdot r_{41} \cdot E$

Tab. 3.1: Change in the refractive index of all three optical axes for three different cases of incident polarisation [171]; n_0 is the refractive index for $E = 0$.

3.2.2 Physical Explanation of Electro-Optic Effect

The physical origin of the electro-optic effect can be explained by two different reasons: first, a redistribution of bond charges and second, a slight deformation of the crystal lattice caused by spatial displacements of the involved atoms [172, 173]. Both physical processes are caused by the the externally applied electric-field. While the readjustment of the electrons in the bonds due to an applied field can be understood intuitively, the crystal lattice deformation is less simple and needs further explanation. Figure 3.4 (a) shows the spatial distribution of the Ga- and As- atoms in the crystal. The four Ga- atoms and the single As- atom are basically distributed among three different spatial layers with equal distances between them. The four electron bonds between the Ga- atoms and the As- atom are allocated along the two diagonals 1 and 2 and are identical in strength due to the symmetry. This explains the isotropic behaviour of the crystal from a physical point of view.

In addition to the spatial atom distribution, one also has to consider the charge distribution inside the crystal. Each atom forms electronic bonds to four neighbouring atoms, as it can be seen in Fig. 3.1. Since Gallium is a group III element, it can only contribute three valence electrons to these bonds. Therefore, it uses one of the five electrons from the group V element Arsenic. As a result, the Ga- atom has a slightly negative charge, while the As- atom is carrying a slightly positive charge. This is also depicted in Fig. 3.4, where the charge distribution inside the structure is highlighted by a green (positive) and red (negative) colour-code.

The interaction of this crystal with an externally applied electric-field E is

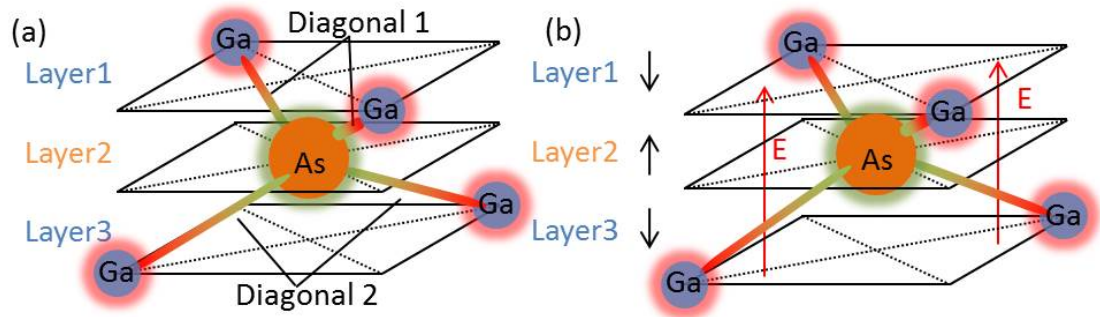


Fig. 3.4: Atomic structure and charge distribution of GaAs before (a) and after (b) the application of an external electric-field.

explained in Fig. 3.4(b). The electric-field applies a force to the charged atoms and induces a movement along the same direction as the applied electric-field. The extent of this movement was measured by X-Ray diffraction in Ref. [174] to be less than 0.01 % of an Angstrom for an applied electric-field of 5.1 MV/m. Due to the charge distribution inside the crystal, layers 2 and 3 move away from each other while the distance between layers 1 and 2 becomes smaller. For this situation, it is clear that the bond electrons in diagonal 1 are "more squeezed" than the ones in diagonal 2. As a consequence of this movement, an incident electric-field with a polarisation along Diagonal 1 feels a different refractive index than along Diagonal 2. The 45° spatial shift of the new principle axes is also clearly visible confirming the predictions of the mathematical model.

3.2.3 The Electro-Optic Effect for Electric-Field Detection

The electro-optic effect can be technologically exploited for a direct measurement of the present electric-field strength. In electro-optic detection systems, an optical beam is used to probe the change in the optical properties of an electro-optic material caused by the external electric-field. In the literature, this is most commonly done employing two different approaches: first, it is possible to determine the change in reflectivity/transmittivity of an electro-optic crystal by measuring the change in intensity of the reflected/transmitted probe beam [175]. Second, one can measure the change in the polarisation state of the optical probe beam after its propagation through the electro-optic crystal. A change in the polarisation state corresponds to a change in the phase relation between the two electric-field components polarised along the principle axes of the crystal (see Fig. 3.3). The accumulated phase-difference due to the electro-optic effect $\Delta\phi_{EO}$ for a probe beam

with an angular frequency ω along the principle axes x' and y' is:

$$\Delta\phi_{EO} = \phi_{x'} - \phi_{y'} = \pi \cdot n_0^3 \cdot r_{eo} \cdot E \cdot \frac{l_{crystal}}{\lambda} = \frac{1}{2} \cdot \pi \cdot n_0^3 \cdot r_{eo} \cdot E \cdot \tau_{prop} \cdot \omega. \quad (3.10)$$

A derivation of this formula can be found in Appendix D. The induced phase-shift is directly proportional to the applied electric-field E . Also, it depends on two parameters of the electro-optic material, the refractive index n_0 and the electro-optic coefficient r_{eo} . The electro-optic phase-shift is also a function of crystal thickness. It can therefore be varied by changing the effective pathlength of the probe beam through the crystal $l_{crystal}$ or, which is equivalent, the propagation time of the probe beam through the crystal τ_{prop} . The experimental realisation of electro-optic measurements in the literature is now presented and discussed in the following section.

3.3 Electric-Field Detection in the Literature

The principle of electro-optic detection for electric-field sampling was introduced in the early 1980's [176]. It established itself as a common method for high-frequency electric-field sampling of integrated electric circuits and antennas [177, 178]. A recent review on the topic electro-optic sensors for microwave field probing can be found in Ref. [179]. One of the major reasons for its use is the high spatial resolution. It is determined by the focal spot size of the probe beam (e.g., 600 nm in Ref. [180]) and, hence, can reach deep sub-wavelength dimensions considering microwave or THz wavelengths. Electro-optic crystals are also commonly used in pump-probe systems leading to sampling intervals in the sub-picosecond range [181, 182]. Electro-optic sampling was also one of the driving forces behind the technological progress in the THz range beginning from the 1990's providing a relatively simple method for coherent THz electric-field detection and imaging [183–185].

Electro-optic detection can be divided in two different approaches: The first one is called "internal sampling". Hereby, the DUT itself is made of an electro-optic material and, hence, has the ability to modulate the probe beam [186, 187]. Although Ref. [188] indicates that internal electro-optic probing is superior in terms of spatial resolution, this method is not considered in this work. Internal sampling can only be realised when an electro-optic material is present as a part of the sample. This limits the applicability of this detection method. Imaging the SPP wave on a bow-tie antenna, as it was demonstrated in the previous chapter for example, would not have been possible with this method. Therefore, the second

approach is applied throughout this project, which is called "external" sampling. In this case, a near-field detector is placed into the electric-field under investigation.

Three typical examples of external electro-optic sampling are shown in Fig. 3.5. In example (a), THz wave detection with a ZnTe crystal is demonstrated. In this case, the E^{THz} and the optical probe beam co-propagate through the detection crystal. During the simultaneous propagation, the THz pulse changes the optical properties of the crystal and modulates the probe beam according to the E^{THz} strength. Since the probe beam penetrates through the detection crystal, this configuration is called probe beam in "transmission mode". The subsequent detection mechanism in the balanced detector is not a matter of interest for now and will be explained in Chapter 6 in more detail. A different configuration is shown in Fig. 3.5 (b). In this case, the THz electric-field bound to a Cu wire is measured with a ZnTe crystal and a probe beam in "reflection mode". In this configuration, the probe beam propagates through the crystal and is reflected at its back facade. From there, it propagates through the crystal for a second time, exits it, and is then detected by the detection system.

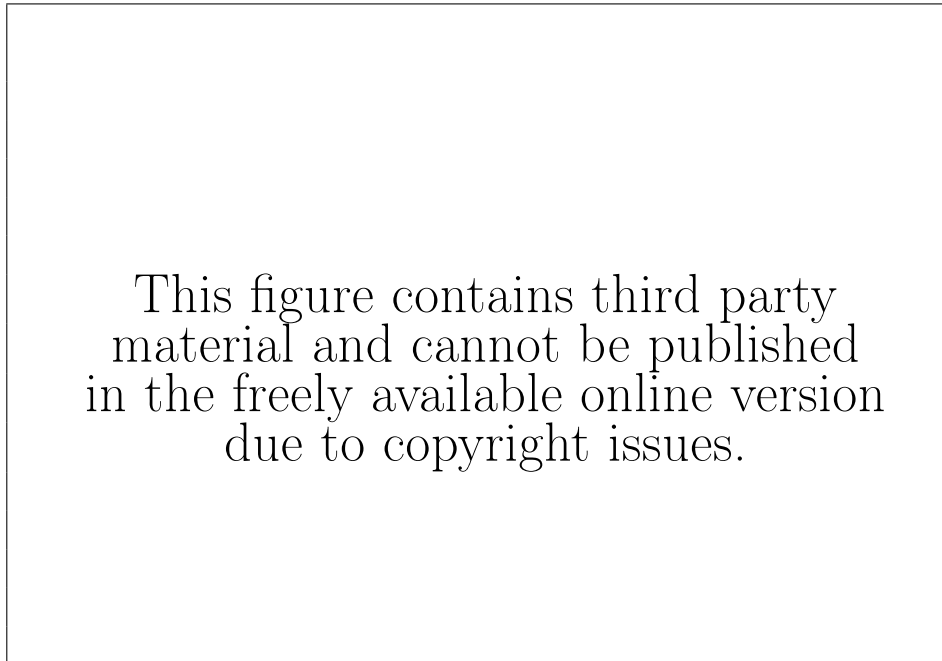


Fig. 3.5: (a) THz electric-field detection with a $150\ \mu\text{m}$ thick ZnTe crystal with a co-propagating probe beam (from [189]); (b) The detection of a THz SPP at the end of a wire with a $1\ \text{mm}$ thick ZnTe crystal in reflection mode (from [136]); (c) Sampling a coplanar waveguide structure with a $1.6\ \mu\text{m}$ thick fibre-coupled $\text{Al}_{0.3}\text{Ga}_{0.7}\text{As}$ probe (from [190]).

In some electro-optic detection systems, the detection crystal is mounted on the tip of an optical fibre to improve the manoeuvrability of the probe. One example is shown in Fig. 3.5 (c). Here, an $\text{Al}_{0.3}\text{Ga}_{0.7}\text{As}$ crystal is mounted to the tip of an

optical fibre and inserted into the electric-field of a coplanar waveguide. The applied signal to the waveguide was a 20 kHz sinusoidal voltage. Due to this low-frequency signal, the electric-field can be considered to be constant for the comparably short propagation time of the optical probe pulse through the detection crystal. In this case, the probe beam experiences a modulation during the whole time being in the crystal. In Ref. [191], for example, a core extended fibre is used to couple more light through the top-surface of the electro-optic crystal. The same crystal has also a high-reflective coating at its bottom surface to ensure that most light is coupled back into the fibre. Also, fibre-coupled detectors provide a possibility of electric-field sampling inside of devices where the insertion of a probe is experimentally very difficult. This is demonstrated in Ref. [160, 192]. In these works, fibre-coupled probes were inserted into a rectangular waveguide and a microwave cavity, respectively, through small holes in the metallic walls.

It has to be highlighted at this point, that the probe presented in Fig. 3.5 (c) is very similar to the electro-optic probe that will be designed throughout this project. But instead of a bulk crystal, an electro-optic micro-resonator will be attached to a fibre-tip. The reasons for replacing a bulk crystal by a resonant structure will be explained in the following sections. This probe will then be applied to E^{SPP} imaging similar to how it is demonstrated in the respective figure for electric-field imaging of a coplanar waveguide.

3.3.1 Electro-optic Detectors for Terahertz Surface Plasmon Imaging

For the detection of surface plasmons, near-field imaging methods are necessary and the electro-optic crystals have to be placed into the proximity of the metallic sample. Electro-optic sampling of the E^{SPP} was successfully demonstrated in the THz range. Two approaches from the literature were exemplarily presented in this thesis in Fig. 1.4 (e) and Fig. 3.5 (b).

In general, electro-optic methods have particular advantages over alternative THz near-field imaging approaches: contrary to methods using metallic needles or sub-wavelength apertures, electro-optic sampling does not require metallic elements which can cause severe electric-field distortions. Due to the absence of a conductor, electro-optic detectors do not support the propagation of SPP waves and, therefore, related imaging artefacts do not have to be taken into account. Also, an aperture and a tip show a particular frequency response, whereas the response of an electro-optic crystal can be considered to be relatively flat over a range of several THz. As a further point, electro-optic crystals are sensitive to only one electric-field

direction. This allows to measure exclusively the E^{SPP} without considering the incident transverse THz excitation beam. In addition to that, the detected signal is directly proportional to the present E^{SPP} and, therefore, represents the actual surface plasmon electric-field pattern.

This list of advantages gives evidence that electro-optic detection is indeed a very promising SPP imaging method. The major practical problem of electro-optic sampling, however, is the small sensitivity of this detection method. The reason for this is the usually small value of the electro-optic parameter r_{eo} (e.g., $r_{eo,GaAs} = 1.42 \text{ pm/V}$). In order to overcome this problem, relatively thick electro-optic crystals are employed to extend the propagation time $\tau_{prop.}$ of the probe beam inside the crystal. Experimental detection systems presented in the literature commonly use crystals with a thickness of hundreds of micrometers [64, 136, 143, 144, 193]. This enhances the induced phase-shift according to Eq. (3.10) and, hence, increases the sensitivity of the probe and improves the spatial resolution. But at the same time, thicker crystals have the disadvantage of increasing the degree of invasiveness. A possibility of extending the optical path length inside the crystal without increasing its thickness is the use of a Fabry-Pérot cavity. The working principle and the advantages of such a cavity are explained in the following section.

3.4 The Fabry-Pérot Etalon

The principle of a Fabry-Pérot interferometer is based on multiple beam interference in an optical cavity. The principle was first developed by Charles Fabry in 1890 and he incorporated this idea into a design together with his colleague Alfred Pérot in 1897 [194]. Two mirrors, separated by a length L , can act as an optical cavity for light incident normal to one of the mirror facades. For particular wavelengths $\lambda = \frac{2L}{n_{FP}}$, a n_{FP} -th order resonance builds up between these two mirrors (see Fig. 3.6 (a)). As a consequence, the sequence of mirrors becomes transparent for the resonant frequency f_{res} . This results in a comb-like transmission spectrum as it can be seen in Fig. 3.6 (b).

The optical properties of the Fabry-Pérot cavity can be described by the Free Spectral Range (FSR) and the Finesse F . The FSR is defined as the separation of two adjacent transmission peaks and is determined by the length of the cavity L :

$$FSR = f_{res,n_{FP}+1} - f_{res,n_{FP}} = \frac{c}{2L} \quad (3.11)$$

The Finesse F of the cavity is the ratio of the FSR to the FWHM of a

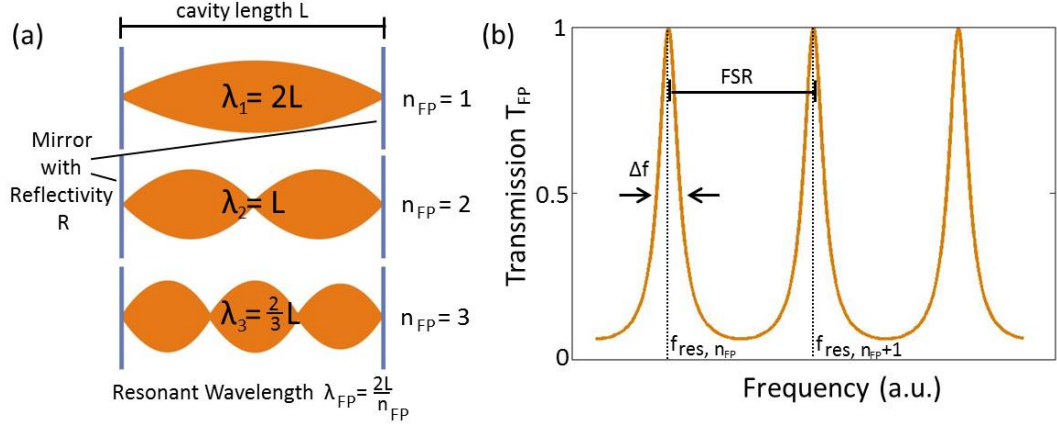


Fig. 3.6: (a) Resonant wavelengths in a cavity with length L ; (b) Transmission spectrum of a Fabry-Pérot Cavity.

transmission peak Δf and depends on the mirror reflectivity R .

$$Finesse F = \frac{\pi\sqrt{R}}{1-R} \quad (3.12)$$

The power transmission spectrum T_{FP} of a Fabry-Pérot cavity is a function of the reflectivity R and the phase retardation $\phi_0 = (2\pi L)/\lambda$ of the incident electric-field:

$$T_{FP} = \left(\frac{(1-R)F}{\pi\sqrt{R}} \right)^2 \cdot \frac{1}{1 + \left(\frac{2F}{\pi} \right)^2 \cdot \sin(\phi_0)^2} \quad (3.13)$$

Fabry-Pérot resonators can be used as optical bandpass filters with very high quality factors (Q -factors). When referring this optical cavity to a bandpass filter, the value Δf in Fig. 3.6 (a) is considered as the bandwidth of the Fabry-Pérot resonator B_{FP} . The Fabry-Pérot Q -factor at a specific resonance frequency $f_{res, n_{FP}}$ is then defined as

$$Q_{FP, n_{FP}} = \frac{f_{res, n_{FP}}}{B_{FP}} \quad (3.14)$$

3.4.1 Fabry-Pérot Resonators in Electro-Optic Sampling

The principle of increasing the sensitivity in electro-optic detection systems using the Fabry-Pérot effect has already been demonstrated in several examples in the literature. In Ref. [193], for example, two high reflective coatings ($R > 0.997$) are employed to enhance the electro-optic effect in a $LiTaO_3$ crystal. Also, asymmetric resonators are presented using high-reflective coatings to enhance the sensitivity in a bulk $LiNbO_3$ -crystal [195]. In an asymmetric resonator, the reflectivities of the two employed mirrors are different from each other. The particular advantage of this configuration will be explained in more detail in the next chapter. The

use of organic polymers in Fabry-Pérot cavities is also widely discussed in the literature [196–199]. Also, the use of distributed Bragg reflectors (DBRs) as high-reflective mirrors in Fabry-Pérot cavities is presented in Ref. [146, 161]. Hereby, $ZnSe$ and MgF_2 layers are used to build a balanced Fabry-Pérot structure to enhance the signal in a $LiTaO_3$ crystal, which serves as the spacer layer. This configuration shows a ten times enhancement compared to the plain $LiTaO_3$ crystal and is successfully applied to electric-field mapping on RF patch-antennas up to 12 GHz.

This selection of examples shows that the idea of electric-field enhancement by employing resonant cavities is not new to the literature. Also, as discussed earlier, the use of fibre-coupled electro-optic probes has already been demonstrated earlier. All these examples, however, only show electric-field sampling up to a frequency of not more than 400 GHz. Examples of SPP imaging were never demonstrated in this particular context at all. In the THz regime, the electro-optic field enhancement by the use of a Fabry-Perot cavity has already been explained theoretically [200, 201] and experimentally [202]. The latter example uses a DBR structure with MgO and air layers to enhance the signal in a $400\ \mu m$ thick GaP crystal by a factor of three. This probe mainly served as experimental proof of principle for the THz electric-field enhancement in a Fabry-Perot cavity. But the dimensions of the probe clearly indicate that it was not made for near-field imaging. The electro-optic micro-resonator for THz near-field microscopy, which is introduced in the next section, is therefore a novel approach in THz SPP imaging devices.

3.5 The Structure of the Micro-Resonator

It is one of the major project goals to design an electric-field probe with a particularly low level of invasiveness. It was therefore decided to use dielectric DBR-layers as high-reflective mirrors in the Fabry-Pérot cavity. This type of mirrors are clearly preferably to metallic coatings which can severely distort the electric-field.

A DBR is a stacked sequence of N subsequent layer pairs with different refractive indices n_1 and n_2 (Fig. 3.7 (a)). The thickness of each individual layer is a quarter of the wavelength in the respective material $\lambda/(4n_i)$ with refractive index n_i . Incident light with a wavelength λ is reflected multiple times at any interface inside the structure. Since light experiences a 180° phase-shift when reflected at an interface with a higher refractive index, light constructively interferes in a direction opposite to the incident light and interferes destructively when propagating further into the DBR structure. Light which is reflected at an interface with a lower refrac-

tive index, on the other hand, also interferes constructively in a direction opposite to the incident light. As a result of the multiple reflections inside this structure, the DBR acts as a bandstop filter for a particular wavelength λ (Fig. 3.7 (b)). The width of the stopband is determined by the difference in the refractive indices n_1 and n_2 and it is wider for a greater mismatch between these indices. The reflectivity of the DBR is determined by the number of multiple reflections within the cavity and, hence, is higher for a greater number N of DBR-layer pairs. For a DBR structure with 15 DBR layer pairs of $GaAs$ and $Al_{0.9}Ga_{0.1}As$, for example, a reflectivity of almost 99% can be achieved at a wavelength of 970 nm. A cavity employing DBR mirrors, therefore, allows adjusting each mirror reflectivity individually simply by varying the number of DBR-layers. Also, this allows the design of asymmetric cavities whose benefits will be discussed later in more detail. As a further advantage of the presented DBR structure, the mirrors themselves are made of electro-optic materials. Hence, they also have a significant contribution to the electro-optic phase-shift, as it will be shown later.

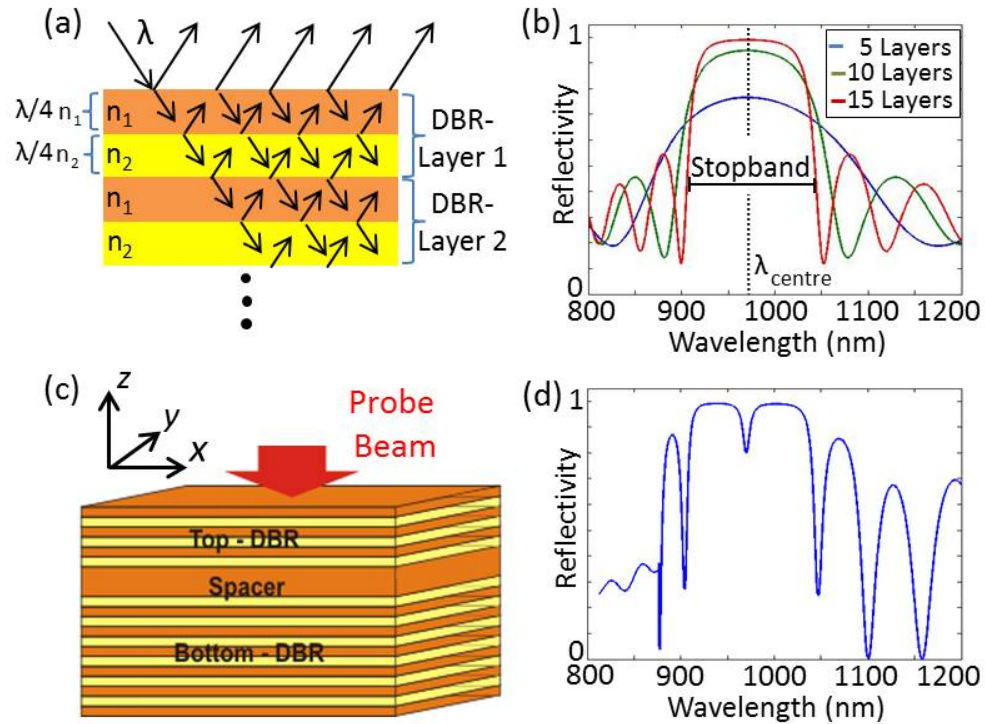


Fig. 3.7: (a) The structure of a DBR and the principle of multiple reflections at any interface; (b) Frequency response of three DBRs with 5, 10, and 15 $GaAs$ and $Al_{0.9}Ga_{0.1}As$ DBR-layers at a central wavelength $\lambda_{centre} = 970\text{ nm}$; (c) A Fabry-Pérot cavity with a Top- and Bottom-DBR and a spacer; (d) The calculated spectral reflectivity of the structure in (c).

The fabrication of DBRs requires the deposition of two different materials sequentially layered upon one another. Since the DBR is made for optical wave-

lengths, this means that these layers are expected to be thinner than 100 nm. Therefore, special fabrication techniques need to be applied. It is very beneficial for this project that University College London facilities provide a possibility of fabricating such a geometry: a molecular beam epitaxy (MBE) machine for growing $Al_xGa_{(1-x)}As$ multi-layer structures.

The Electro-Optic Material $Al_xGa_{(1-x)}As$

The material GaAs is commonly used as an electro-optic detection crystal. It has a relatively low dielectric constant and, hence, a much lower degree of invasiveness compared to other common materials [145] ($\epsilon_{GaAs} \approx 13$ [144], $\epsilon_{LiTaO_3} \approx 43$ [144], $\epsilon_{LiNbO_3} \approx 50$ [203], $\epsilon_{KDP} \approx 50$ [204], $\epsilon_{Bi_{12}SiO_{20}}(\epsilon_{BSO}) \approx 56$ [205]). Since two different materials are necessary for a DBR structure, the compositions $GaAs$ and $Al_{0.9}Ga_{0.1}As$ were selected. The use of $Al_{0.9}Ga_{0.1}As$ was preferred to $AlAs$, because pure $AlAs$ shows a high level of oxidation when exposed to air. This reduces its mechanical stability. The oxidation rate can be reduced dramatically by minimally decreasing the Al content [206]. Therefore, the Al -content was reduced to 90 % in the respective alloy.

The choice of these two compositions has several advantages: despite of the relatively modest electro-optic coefficient of the composition ($r_{eo} = 1.42 \frac{pm}{V}$), the electro-optic effect is nevertheless strong due to their high refractive indices ($n_{GaAs} \approx 3.5$, $n_{Al_{0.9}Ga_{0.1}As} \approx 3$) (Eq. (3.10)). The relatively large difference in the refractive indices additionally guarantees a wide stopband for the DBR mirrors. Moreover, the almost identical lattice constants of both compositions provide a high mechanical stability on a molecular scale: the lattice constant of $GaAs$ is 5.6533 Å and deviates from this value only by 0.1% in case of $Al_{0.9}Ga_{0.1}As$ [207].

In the literature, one can find further electro-optic materials as detector crystals, which are shortly summarised and compared to $GaAs$. The major group is inorganic crystals like Zinc Telluride ($ZnTe$), Gallium Phosphide (GaP), and Gallium Selenide ($GaSe$). Zinc Telluride, for example, has an higher electro-optic coefficient than GaAs ($r_{eo,ZnTe} = 4.04 \frac{pm}{V}$ [208]) but a smaller bandwidth due to its phonon resonance at 5.3 THz [209]. The phonon resonance of $GaAs$ is about 8 THz for comparison [210]. In addition to that, $ZnTe$ needs an mechanically stable counterpart alloy to form a DBR structure, which is difficult to find. In case of the material GaP , both the electro-optic coefficient ($r_{eo,GaP} = 1 \frac{pm}{V}$ [211]) and the bandwidth (7 THz [209]) show an inferior performance to $GaAs$. Another promising material is GaSe with an electro-optic coefficient of $r_{eo,GaSe} = 54.4 \frac{pm}{V}$ [212] and an exceptional bandwidth of 41 THz [107]. This material obviously shows an ad-

vanced performance and should therefore be considered as a promising alternative to GaAs when designing similar micro-resonator structures in the future. Another group of electro-optic materials is organic polymers which show an exceptionally high electro-optic coefficient. The most common examples are 4-dimethylamino-N-methylstilbazolium tosylate ("DAST", with $r_{eo,DAST} = 77 \frac{pm}{V} @ 800 nm$ [213]), N-(4-nitrophenyl)-L-prolinol ("NPP", with $r_{eo,NPP} = 65 \frac{pm}{V} @ 1064 nm$ [214]), and polymethylmethacrylate ("PMC", with $r_{eo,PMC} = 60 \frac{pm}{V} @ 1318 nm$ [215]). DAST, however, has a high absorption coefficient of $300 cm^{-1}$ around 1 THz [216] and the most common polymers currently suffer from a performance decay over time [217]. Also, configurations with polymers and high-reflective coatings are mechanically very fragile and additional layers have to be employed for mechanical stability. Due these reasons, the use of electro-optic polymers is not considered throughout this project.

The Spatial Alignment of the Micro-Resonator in Surface Plasmon Imaging Experiments

The general structure of the micro-resonator and its spatial orientation in the experimental electric-field detection system is determined by the MBE fabrication process: a (100)-oriented *GaAs* wafer is used as the substrate to grow the micro-resonator. The grown structure on this substrate is depicted in Fig. 3.7(c). One can see two DBR structures with layers in the xy -plane and a spacing in between. This spacing introduces the discontinuity in the stopband (Fig. 3.7(d)). It bears the name "spacer" throughout this thesis. The spacer is identical to the resonant cavity in an ordinary Fabry-Pérot structure and its thickness determines the resonant wavelength λ_{res} .

For this spatial DBR-layer orientation, the probe beam has to be incident from the z -direction, as it is shown in Fig. 3.7(c). This gives the opportunity of distinguishing both mirrors: the mirror where the probe beam will be incident to in the later experiments is from now on called "Top-DBR". This means that this mirror will either face free-space in the experiments or, in case of a fibre-coupled probe, that this DBR will be attached to a fibre tip. To be consistent in the nomenclature, the second mirror is called "Bottom-DBR".

In addition to the incident probe beam direction, this spatial configuration also dictates the electric-field orientation this crystal is sensitive to. In order to introduce a phase-shift into the probe beam propagating in the z -direction, the refractive indices along the x - and the y -directions have to change due to the applied electric-field. According to the left row in Tab. 3.1, this is the case for an external

electric-field polarised in the z -direction. This specific spatial sensitivity also determines the experimental configuration for SPP imaging on metallic surfaces: the Bottom-DBR has to be introduced into the near-field of the metallic sample with its DBR layers parallel to the sample surface plane (xy -plane). This is depicted in Fig. 3.8 for a fibre-coupled micro-resonator. Thereby, the E^{SPP} points into the z -direction and induces a phase-shift in a probe beam incident from the negative z -direction.

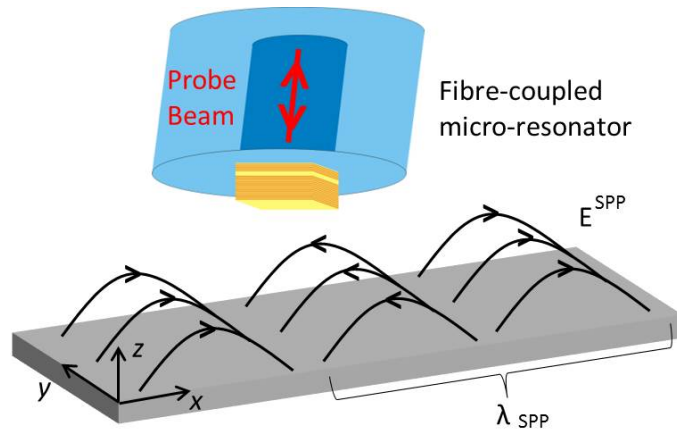


Fig. 3.8: Surface Plasmon detection on a metallic surface with a fibre-coupled micro-resonator.

Although the general structure of the micro-resonator and its spatial alignment for future SPP measurements are now clarified, there are still a lot of open questions which need to be addressed: the micro-resonator design offers many degrees of freedom and an optimal design has to be found. The design process is now presented in the following chapter.

4 Design and Fabrication of the Electro-Optic Micro-Resonator

This chapter describes the design of the micro-resonator probe. It explains the compromises that had to be made to find an optimal design. This chapter also presents the final design of the micro-resonator and justifies this choice.

In the first section, the most important functional parameters of the micro-resonator are discussed. In the next section, a computer program is presented which is capable of calculating the optical response of the micro-resonator. This computer program is then used to evaluate different resonator designs and to find the optimal configuration. In the last section, the measured reflectivity of the fabricated micro-resonator is compared to the simulations and its validity will be discussed.

4.1 Design Considerations

The micro-resonator structure in Fig. 3.7(c) offers numerous degrees of freedom in its design. This section presents the most significant design parameters and discusses their influence on the optical performance. The optimisation of these parameters sometimes sets opposing requirements to the micro-resonator configuration. Therefore, certain compromises have to be made. This will be explained in more detail throughout this section.

The Electro-Optic Enhancement

One of the most important parameters of the micro-resonator is the enhancement of the electro-optic effect in comparison to a bulk crystal. The term "electro-optic enhancement" is from now on defined as the ratio of the electro-optic phase-shift in the micro-resonator $\Delta\phi_{MR}$ to the phase shift in a bulk crystal $\Delta\phi_{Bulk\ Crystal}$ which has the same thickness as the micro-resonator:

$$electro - optic\ enhancement = \frac{\phi_{MR}}{\phi_{Bulk\ Crystal}} \quad (4.1)$$

A large phase-shift ϕ_{MR} requires a long propagation time of the light inside the cavity τ_{prop} . This can either be achieved by a thick spacer or by increasing the mirror reflectivities. These requirements, however, directly increase the thickness of the micro-resonator. This imposes restrictions on its spatial resolution and it

also increases its degree of invasiveness. In addition, a long $\tau_{prop.}$ reduces the THz bandwidth. It will be shown later that the major trade-off in the micro-resonator design has to be made between the electro-optic enhancement on the one side and parameters such as the bandwidth, the spatial resolution, the invasiveness, and the reflectivity on the other side.

The Reflectivity

A high reflectivity of the micro-resonator is essential for two reasons: first, reducing the exposure of the sample to the probe beam can avoid imaging artefacts. Artefacts, for example, can occur when the sample itself contains an electro-optic material. In this case, it is possible that the probe beam penetrates into the sample, experiences an additional phase-shift, and reflects back into the micro-resonator. Also, the optical probe beam can change the carrier density in semiconductors. This can locally disturb the E^{SPP} distribution if the semiconductor is attached directly to the metallic surface under investigation. As a second reason, it is important to reflect as much modulated light as possible back into the detection system. It will be shown later that the detected signal caused by the E^{THz} is directly proportional to the probe beam power incident to the detection unit.

The resonator reflectivity mainly depends on the symmetry of the design and its Q-factor. A cavity with a high Q-factor implies a very narrow Fabry-Pérot bandwidth B_{PF} . As a result, only a small portion of the incident broadband pulse enters the micro-cavity and experiences the electro-optic phase-shift. At the same time, a high Q-factor cavity is almost transparent for the resonance wavelength. This means that the small portion of light inside the cavity does not reflect back into the detection system and the information about the phase-shift gets lost. Also, a transparent cavity contradicts the requirement of a high reflectivity. Consequently, it is important to choose the Fabry-Pérot bandwidth B_{PF} and the resonator reflectivity carefully in order to efficiently detect the electro-optic phase-shift.

In comparison to a bulk *GaAs* crystal, the micro-resonator structure exhibits a superior performance in terms of reflectivity: at a single air/*GaAs*-interface, only $\approx 30\%$ of the intensity is reflected. Using a micro-resonator, this can already be achieved by a small number of DBR-layers.

The Spatial Resolution

The probe beam samples the E^{SPP} in a spatially confined region. This region can be as small as the diffraction-limited spot size of the probe beam, which has a theoretical diameter $\geq 345\text{ nm}$ for $\lambda = 970\text{ nm}$ in GaAs ($\lambda/n_{GaAs} \cdot 1.22$, compare

to Appendix B). It is desired to reach the minimum spot size in the spacer of the micro-resonator. This ensures the smallest spatial resolution because the electro-optic effect mainly takes place in the spacer. To detect high spatial components in the sample proximity, it is necessary to bring the spacer as close as possible to the sample surface. For a high spatial resolution, it is therefore necessary to use only a small number of Bottom-DBR layers and a thin spacer.

The use of DBR-layers limits the spatial resolution when a small probe beam spot is required. A very small beam spot in the spacer requires a strongly focused probe beam. This leads to a wide range of incident angles with respect to the surface normal of the DBR-layers. The DBR design, however, was optimised for light being incident normal to its surface. When light is incident under a tilted angle, the reflectivity band shifts to smaller wavelengths. The same happens to the resonance wavelength of the cavity. As a result, light at $\lambda = 970 \text{ nm}$ incident under a tilted angle does not enter the cavity and is instantly reflected without experiencing the electro-optic phase-shift. In the final version of the near-field detection system, the micro-resonator will be attached to an optical fibre. In this case, there is only a small range of angles under which light can exit the optical fibre and be re-coupled back into it. The spatial resolution of a fibre-coupled probe is determined by the core diameter of the fibre ($\approx 8 \mu\text{m}$ - $10 \mu\text{m}$ for single mode fibre).

Apart from the probe beam spot size in the micro-resonator, the spatial resolution also depends on the capability of the detection system to introduce the probe as close as possible to the sample. The micro-resonator needs to be attached to a holder and the spatial movements of this assembly are determined by the mechanical properties of the translation stage. The micro-resonator, therefore, cannot be considered as a stand-alone unit and the spatial resolution of the entire imaging system needs to be taken into account and evaluated experimentally.

The Level of Invasiveness

The introduction of a dielectric probe into an electric-field has an impact on the measured field distribution. The extent of this impact depends on the geometric dimensions of the probe and on its permittivity [144, 145]. The dielectric properties of the probe are given by the employed alloy $Al_xGa_{(1-x)}As$ and cannot be changed. The resonator thickness, on the other hand, can be changed by varying the number of DBR-layers and the spacer thickness.

In the experimental system, however, the invasiveness of the probe is rather dictated by the properties of the necessary holder than by the transversal dimensions of the probe. In the case of a fibre-coupled probe, the fibre tip can be reduced

to a diameter which is only slightly larger than the core diameter. As a result, the entire probe tip would exhibit only small spatial dimensions and the level of invasiveness can be expected to be small.

The THz Bandwidth

When introducing the micro-resonator into a time-varying electric-field $E^{THz}(t)$, the probe beam experiences a phase-shift from the moment it enters the probe until it exits. Hence, the electro-optic phase-shift $\phi_{EO}(\tau)$ is a convolution of the temporal change in the refractive index $\Delta n(t)$ and the temporal evolution of the probe beam intensity inside the resonator $I^{opt.}(t)$. Due to the almost instant response of the electro-optic effect to the applied electric-field, $\Delta n(t)$ is directly proportional to the present $E^{THz}(t)$ at any time and the convolution can be rewritten as

$$\phi_{EO}(\tau) = const. \cdot \int E^{THz}(t) * I^{opt.}(\tau - t) dt. \quad (4.2)$$

The temporal response of the phase-shift ϕ_{EO} depends on the time of the optical beam being inside the cavity. This time duration is defined as the propagation time $\tau_{prop.}$. It has to be significantly shorter than the THz cycle duration in order to detect the THz pulse. If E^{THz} flips its sign while the probe beam is still in the resonator, the physical mechanism is reversed and the phase-shift decreases. Higher frequency components of E^{THz} flip their sign more quickly than lower ones. Therefore, higher frequency components are affected by the reversed phase-shift at earlier times. This is the reason for the low-pass behaviour of the electro-optic micro-resonator. The THz 3 dB- bandwidth B_{3dB}^{THz} of the resonator is the frequency at which the phase-shift ϕ_{EO} drops to half of its maximum value. In general, a high-Q resonator causes a long propagation time $\tau_{prop.}$ and enhances the phase-shift. But at the same time, it reduces the THz bandwidth. This predicament is one of the major issues when designing this micro-resonator.

The Centre Wavelength λ_{centre} of the Probe Beam Pulse

For an efficient electro-optic probe, the resonant wavelength of the cavity λ_{res} has to be identical to the central wavelength of the probe pulse λ_{centre} . The upper wavelength limit for λ_{centre} in the experimental system is given by the laser source. Preliminary measurements have shown that the laser source is pulsing in a stable state for $\lambda_{centre} < 980 \text{ nm}$. The lower wavelength limit is determined by the *GaAs* absorption edge at 871 nm . Since a broadband probe beam is used, it is important that the entire pulse spectrum is between these two boundaries.

Finding a Compromise

A design has to be found which sufficiently satisfies each of the aforementioned parameters. Some of these parameters, however, impose opposite requirements to the micro-resonator geometry. This is summarised in Tab. 4.1 for a better visual clarity. This table reveals the main predicament of the design process: while certain resonator designs increase the electro-optic enhancement, they have a negative impact on a variety of other parameters. It will be shown in the next section that the trade-off between the electro-optic enhancement and the remaining parameters is the key issue in the design process.

Use of	positive impact on	negative impact on
a thicker spacer	el.-opt. enhancement	spatial resolution, THz bandwidth
more DBR-layers	el.-opt. enhancement, reflectivity	spatial resolution, THz bandwidth
a symmetric design	el.-opt. enhancement	reflectivity, THz bandwidth

Tab. 4.1: Degrees of freedom in the resonator design and their impact on its optical parameters.

The Pulse Width of the Probe Beam τ_{probe}

The use of ultra-short optical sampling pulses was initially intended to ensure an exceptional temporal resolution of the imaging system. Apart from that, a pulsed system provides the advantage of accessing one more degree of freedom: the pulse width of the probe beam τ_{probe} . The pulse width determines the spectral content of the incident probe beam and is crucial for its interaction with the resonant cavity. This parameter is considered separately from the other ones because it allows altering the resonator performance after the fabrication. This can be done, for example, by using optical bandpass filters.

The probe pulse bandwidth is given by the employed laser system. In case of the *Spectra Physics Tsunami*, a Gaussian-shaped pulse with an intensity FWHM of 13 nm is emitted (at $\lambda_{centre} = 970\text{ nm}$). Assuming a transform-limited Gaussian pulse, this bandwidth corresponds to a pulse width of $\approx 98\text{ fs}$. To change the pulse width, a 10 nm band-pass filter can be used in the later experiments. This corresponds to a pulse width of 138 fs . Varying the pulse width can either compensate for fabrication uncertainties or fine-tune the resonator performance. The extent of this tuning capability is discussed later in the chapter.

4.2 Simulation of the Micro-Resonator Response

This section describes the analytical model which is used to calculate the optical response of the electro-optic micro-resonator. This model is the backbone for determining the optimal cavity configuration prior to its fabrication. The simulation, however, is restricted to a subset of the parameters that were introduced in the previous section: these parameters are the 3-dB THz bandwidth, the reflectivity, the resonance wavelength, and the electro-optic enhancement. The selected parameters can be calculated as a function of the probe pulse wavelength, its pulse width, and different micro-resonator configurations. For the selection of these parameters, it was essential that the micro-resonator can be considered as a stand-alone entity. The spatial resolution and the probe invasiveness, on the other hand, depend rather on the properties of the entire imaging system than on the micro-resonator itself. These parameters, therefore, need to be evaluated experimentally.

The simulation consists of two major components: first, the "Optical Admittance Approach". It is used to calculate the optical response of the micro-resonator as a function of the incident optical wavelength. This is essential for the characterisation of the cavity broadband response. Second, the Aframowitz model [218]. This model is used to express the refractive indices $n_{GaAs}(E^{THz}, \lambda)$ and $n_{Al_{0.9}Ga_{0.1}As}(E^{THz}, \lambda)$ as a function of the applied E^{THz} and the optical probe beam wavelength. These two components were incorporated in a simulation to calculate the overall response of the micro-resonator in the time- and frequency-domain.

4.2.1 Optical Admittance Approach

The Optical Admittance Approach is known from the transmission line theory in RF-circuit analysis [219]. A derivation of the involved formula and their application to optical multi-layer stacks can be found in Ref. [220]. In principle, this approach considers the "optical admittance" $y_n = nY$ of a single layer with refractive index n . The value Y is the free-space admittance. Light transmission through an interface between two different layers is calculated by their optical admittance mismatch. In case of a layer with finite thickness d_{Layer} , its optical thickness with respect to the incident wavelength λ is considered by the phase factor δ_{Layer} :

$$\delta_{Layer} = 2\pi n_{Layer} d_{Layer} / \lambda \quad (4.3)$$

Light propagation through a multi-layer stack with q layers (Fig. 4.1), can

be calculated by determining the optical admittance of the entire stack:

$$\begin{pmatrix} E_1/E_{sub} \\ H_1/E_{sub} \end{pmatrix} = \begin{pmatrix} B \\ C \end{pmatrix} = \left(\prod_{r=1}^q \begin{pmatrix} \cos(\delta_{layer r}) & j\sin(\delta_{layer r})/y_r \\ jy_r\sin(\delta_{layer r}) & \cos(\delta_{layer r}) \end{pmatrix} \right) \cdot \begin{pmatrix} 1 \\ y_{sub} \end{pmatrix} \quad (4.4)$$

The last layer, called substrate, is adjacent to the q-th layer of the multi-layer stack. Its thickness is larger than the coherence length of light and is considered as infinitely thick. It serves as the termination of the multi-layer stack in the simulation. The values E_1 and H_1 are the electric- and magnetic- fields at the top interface of layer 1. To keep the right part of the matrix equation more simple, Eq. (4.4) was normalised to the electric field E_{sub} in the substrate. The matrix (B/C), called the "characteristic matrix of the assembly", is the inverse of the optical admittance of the entire multi-layer stack. Using this approach, the reflectivity calculation for a multi-layer stack can be simplified to determining the impedance mismatch at an interface with two different optical admittances: y_0 for the incident medium and $y_{Stack} = (C/B)$ for the multi-layer stack. The complex reflectivity r for an incident electric-field can then be calculated by:

$$r = \frac{y_0 - y_{stack}}{y_0 + y_{stack}} = \frac{y_0 B - C}{y_0 B + C} \quad (4.5)$$

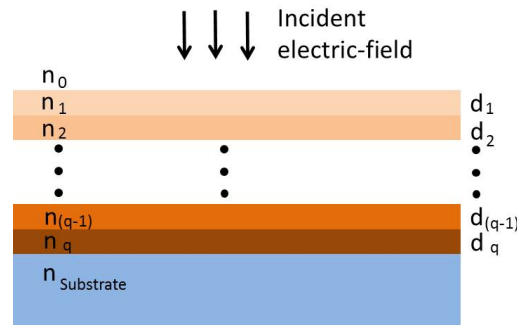


Fig. 4.1: A multi-layer stack for the calculation of the optical response with the Optical Admittance Approach.

4.2.2 Model of the Refractive Index

The Optical Admittance Approach requires an accurate model for the calculation of the refractive index of the material composition $n_{Al_{1-x}Ga_xAs}$. The employed model describes the optical properties of a material by a "single effective oscillator", as it was introduced by Wemple [221, 222]. A molecule is represented by a single

Sellmeier oscillator ($\epsilon_{2,Sellmeier} = 0$) [223] and its permittivity can be calculated by:

$$\epsilon_{real}(\mathcal{E}_{Photon}) - 1 = n^2(\mathcal{E}_{Photon}) - 1 = \frac{\mathcal{E}_d \cdot \mathcal{E}_0}{\mathcal{E}_0^2 - (\mathcal{E}_{Photon})^2}. \quad (4.6)$$

The parameters \mathcal{E}_0 and \mathcal{E}_d represent the average interband transition energy and the oscillator strength of the interband transitions, respectively. Wemple related these parameters to physically sensible material properties such as the anion valency, the coordination number, and the number of valence electrons. In addition, he introduced a correction factor for every material. This model gives a good approximation of the frequency dependent refractive index $n(\mathcal{E}_{Photon})$ for more than 50 ionic and covalent non-metallic materials sufficiently below the bandgap [222]. Equation (4.6) can be rewritten as a power series expansion of \mathcal{E}_{Photon} :

$$\epsilon_{real}(\mathcal{E}_{Photon}) - 1 = M_{-1} + M_{-3}\mathcal{E}_{Photon}^2 + M_{-5}\mathcal{E}_{Photon}^4 + \dots \quad (4.7)$$

The optical moments M_i are related to the single oscillator parameters by $\mathcal{E}_0^2 = \frac{M_{-1}}{M_{-3}}$ and $\mathcal{E}_d^2 = \frac{M_{-1}^3}{M_{-3}}$. One can see that optical moments only up to the third order are used to represent these parameters. This leads to inaccuracies when approaching the band-gap. Therefore, this model is valid only for frequencies sufficiently away from the band-gap. Aframowitz suggested the extension of Wemple's model by an additional term [218]:

$$n^2(\mathcal{E}_{Photon}) - 1 = M_{-1} + M_{-3}\mathcal{E}_{Photon}^2 + \frac{\eta}{\pi}\mathcal{E}_{Photon}^4 \ln \frac{\mathcal{E}_u^2 - \mathcal{E}_{Photon}^2}{\mathcal{E}_l^2 - \mathcal{E}_{Photon}^2} \quad (4.8)$$

The terms \mathcal{E}_u and \mathcal{E}_l are the upper and lower limits of the band-gap, respectively. The variable η can be directly related to \mathcal{E}_0 and \mathcal{E}_d in the Wemple model. A comparison of the refractive indices modelled according to Wemple and Aframowitz can be seen in Fig. 4.2. The GaAs refractive index in the Aframowitz model deviates clearly from the one in Wemple's model close to the band-gap. This deviation is less prominent in the case of AlAs since the wavelengths are still sufficiently far away from the respective bandgap. Experimentally determined values [224–227] clearly match the Aframowitz model better for GaAs. However, the Wemple model seems to be more accurate for AlAs, although the deviation from the Aframowitz model is obviously very small.

Aframowitz also presented a model for the absorption coefficient: he introduced the imaginary part of the permittivity $\epsilon_{2,Afram.}(\mathcal{E}_{Photon}) = \eta \mathcal{E}_{Photon}^4$ for the band-gap region. The GaAs absorption coefficient α_{GaAs} was measured in Ref. [228] and compared to the modelled values in Fig. 4.3(a). The good match of

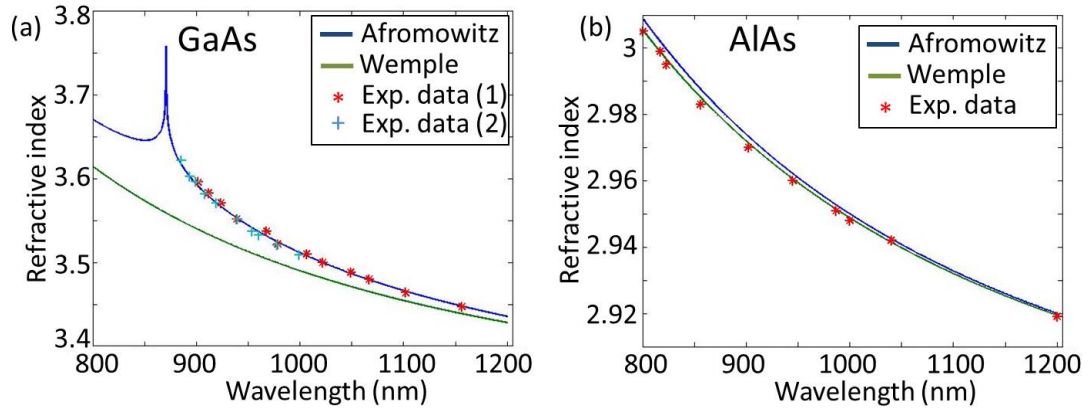


Fig. 4.2: Comparison of the refractive indices modelled by Afromowitz and Wemple for *GaAs* in (a) and *AlAs* in (b). Both models are also compared to experimentally determined values: The values for the red stars in (a) were taken from Ref. [224] and the blue crosses from Ref. [226, 227]. In (b), the experimental data were taken from Ref. [225].

the experimental and the simulated data justifies the use of this refractive index model. As a further benefit, it also allows the calculation of the refractive index of the alloy $Ga_{1-x}Al_xAs$ for any composition x . This is essential for this project since the refractive index of $Al_{0.9}Ga_{0.1}As$ is specifically required.

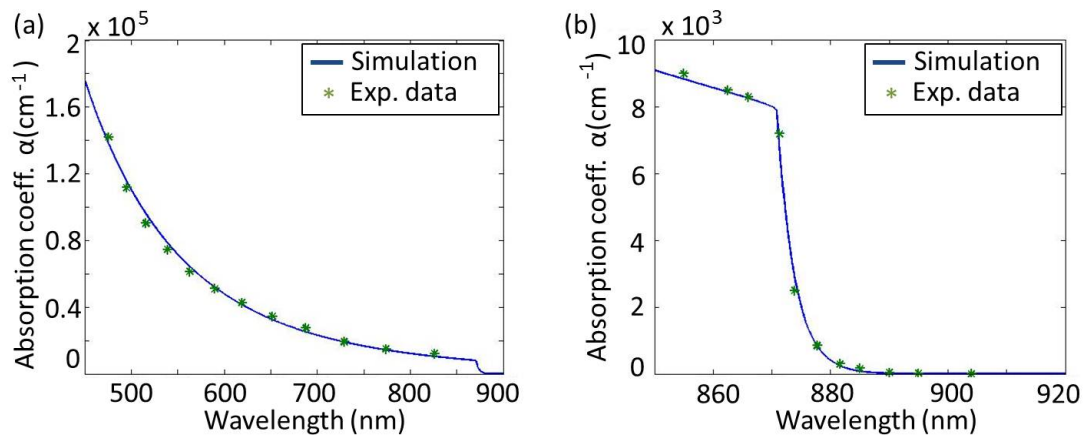


Fig. 4.3: The absorption coefficient α of *GaAs* in the band-gap region (a) and in the proximity of the band-gap edge (b). The experimentally measured values were taken from Ref. [228] in (a) and Ref. [229] in (b).

4.2.2.1 Absorption Characteristics at the Band-Gap Edge

The absorption coefficient α of a semiconductor in the close proximity of the band-gap edge can be described by the so-called "Urbach tail". Urbach discovered that the absorption coefficient decays exponentially in the energy region below the band-

gap ($\mathcal{E}_{Photon} < \mathcal{E}_{Band-gap}$) [230]:

$$\alpha_{Urbach}(\mathcal{E}_{Photon}) = \alpha_0 \cdot e^{\frac{\mathcal{E}_{Photon} - \mathcal{E}_{Band-gap}}{\mathcal{E}_{Urbach}}} \quad (4.9)$$

Hereby, $\mathcal{E}_{Band-gap}$ is the band-gap energy, α_0 is the absorption coefficient directly at the band-gap edge, and \mathcal{E}_{Urbach} is the Urbach fitting parameter. The parameter \mathcal{E}_{Urbach} is in the range between 7.5 meV and 10 meV for GaAs at room temperature [231, 232]. The reasons for the Urbach tail are explained by lattice disorders due to phonons [233–235], thermal fluctuations [231, 232], or mechanical strain caused by impurity states [234, 236].

The exponential decay of the absorption coefficient α_0 is also incorporated into the optical response simulation. In Fig. 4.3(b), the simulated absorption in the proximity of the band-gap for GaAs is compared to experimentally determined values. Both curves matched very well for an Urbach fitting parameter \mathcal{E}_{Urbach} of 5 meV. The use of the Urbach tail in the simulation adds to the accuracy of the refractive index model for wavelengths close to the band-gap.

4.2.3 Calculation of the Optical Response

The Optical Admittance Approach and the Afromowitz model provide an analytic way of calculating the micro-resonator structure and accurately determining the refractive indices. However, a program is still needed that is capable of delivering reliable values in the context of the micro-resonator design process. This program was written in MATLAB and works as follows (A flow diagram can be found in Fig. 4.4):

The user can determine the FWHM of a Gaussian pulse and its central wavelength. This defines the spectral position and the bandwidth of the probe beam. Also, the user can assign values for the number of DBR-layers in the Top- and the Bottom-DBR separately. The thickness of the spacer can be defined by selecting the quantity of $\frac{\lambda}{2n_{GaAs}(\lambda)}$ - GaAs - layers. The respective wavelength λ is defined by the central wavelength of the input Gaussian beam. One can also select the refractive indices of the incident medium n_0 and the substrate $n_{substrate}$ in accordance with the Optical Admittance Approach. This allows accounting for the GaAs substrate wafer and evaluating the impact of an optical glass fibre. The variable parameters in this program are similar to the ones that can be altered during the design process (Number and thickness of DBR- and spacer-layers, incident and substrate medium, resonance wavelength λ_{res}) or in an experiment (probe beam pulse width τ_{probe}). In addition to all these parameters, the user needs to define an electric-field strength

E_{Sim}^{THz} which is necessary for the program to calculate the electro-optic effect.

After defining all these parameters, the program first decomposes the incident Gaussian beam into its Fourier components by applying a FFT. In the next step, it uses the Optical Admittance Approach to calculate the reflection coefficient of the resonator structure. Hereby, the user can choose a wavelength range of interest (normally 800 nm - 1200 nm). Within this range, the program calculates the refractive indices according to the Afromowitz model and the complex reflection coefficient $r_{spectral}^{MR}$ (Eq. (4.5)) for each wavelength, respectively. The spectral intensity reflectivity is calculated by $R_{spectral}^{MR} = (r_{spectral}^{MR} \cdot r_{spectral}^{MR})^*$. The change in the refractive index due to the electro-optic effect is considered by incorporating Eq. (3.10) into the Afromowitz model. The program then multiplies the complex reflection coefficient with the respective complex electric-field components of the incident Gaussian beam. This provides the necessary amplitude and phase information about the reflected pulse. An inverse FFT recovers the temporal pulse shape and allows the examination of the waveform that exits the cavity. In addition to that, a comparison of the waveforms with and without an applied electric-field E_{Sim}^{THz} allows the calculation of the induced phase-shift.

The THz bandwidth of the resonator is calculated by simulating the temporal electric-field evolution in the centre of the spacer. The envelope of this evolution allows an estimation of the propagation time of the probe beam inside the cavity τ_{prop} . The resonator bandwidth is determined by applying a FFT to this envelope.

The overall reflectivity $R_{overall}^{MR}$ is calculated by the ratio of the reflected intensity to the incident one. To do so, all the matrix elements in the two respective MATLAB vectors were added and their ratio determined:

$$R_{overall}^{MR} = \frac{\sum_{n=1}^{n=n_{max.}} I_{reflected}(n)}{\sum_{n=1}^{n=n_{max.}} I_{incident}(n)} \quad (4.10)$$

The electro-optic enhancement is calculated using Eq. (4.1). In a first step, the bulk crystal thickness is matched to the one of the micro-resonator. The phase-shift $\phi_{BulkCrystal}$ is then calculated (Eq. (3.10)) and doubled, since the measurements are done in reflection mode. The phase-shift ϕ_{MR} is calculated in accordance with the experimental detection system: a Wollaston polariser translates the electro-optic phase-shift ϕ_{MR} into an intensity difference which is determined by the ratio $(\frac{I_+ - I_-}{I_+ + I_-})$. The values I_+ and I_- are the intensities of the two beams exiting the Wollaston polariser. As a consequence, the electro-optic phase-shift ϕ_{MR} can be determined by calculating this specific ratio for both orthogonal polarisations in the probe beam path. A more detailed description of this detection mechanism can be found in chapter 6.

A diagram of the computer program is shown in Fig. 4.4. It schematically summarises all the different steps that were explained in this subsection. The program is able to calculate the THz bandwidth, the electro-optic enhancement, and the reflectivity as a function of different micro-resonator configurations, probe beam pulses widths, and central wavelengths. This makes this program a powerful and indispensable tool for the micro-resonator design.

4.3 Determination of the Micro-Resonator Structure

The wide range of parameters that can be varied during the design process was listed in section 4.1. Also, their mutual dependencies were discussed briefly. It is the task of this section to qualitatively evaluate different configurations and to justify the final design of the micro-resonator.

An electro-optic micro-resonator similar to the structure used throughout this project has already been proposed by Oleg Mitrofanov *et al* in Ref. [200, 201]. Both references present asymmetric Fabry-Pérot configurations which are fabricated using the materials $GaAs$ and $Al_{0.9}Ga_{0.1}As$. In Ref. [200], the micro-resonator comprises 6 DBR-layers in the Top-DBR, 1 $\frac{\lambda}{2}$ -layer in the spacer, and 15 DBR-layers in the Bottom-DBR. This configuration was designed for a wavelength of 980 nm. The functionality of this probe was demonstrated by sampling the electric-field of a micro-strip line with a *cw* probe beam. In the publication, the authors do not explain explicitly why this configuration has been chosen. It was only mentioned that a reflectivity of 80% was desired and that the spacer should not be positioned more than $2 \mu m$ away from the sample in a lateral direction.

In Ref. [201], the performance of a micro-resonator consisting of 5 Top-DBR layers and 16 Bottom-DBR layers was theoretically investigated for imaging applications in the pulsed regime. However, no statement about the number of spacer layers was given. The publication mainly focused on the investigation of the THz bandwidth and the electro-optic enhancement as a function of the cavity asymmetry and of the incident pulse width. It was shown that the electro-optic enhancement is stronger for symmetric cavities and for wider pulse widths τ_{pulse} . The THz bandwidth, on the contrary, is reduced in both cases.

Both references presented above give a good insight into the basic working principle of an electro-optic micro-resonator. But they do not describe its design process and do not justify why the selected designs are superior to alternative ones. Also, while Ref. [200] mainly focuses on the reflectivity and the resonator

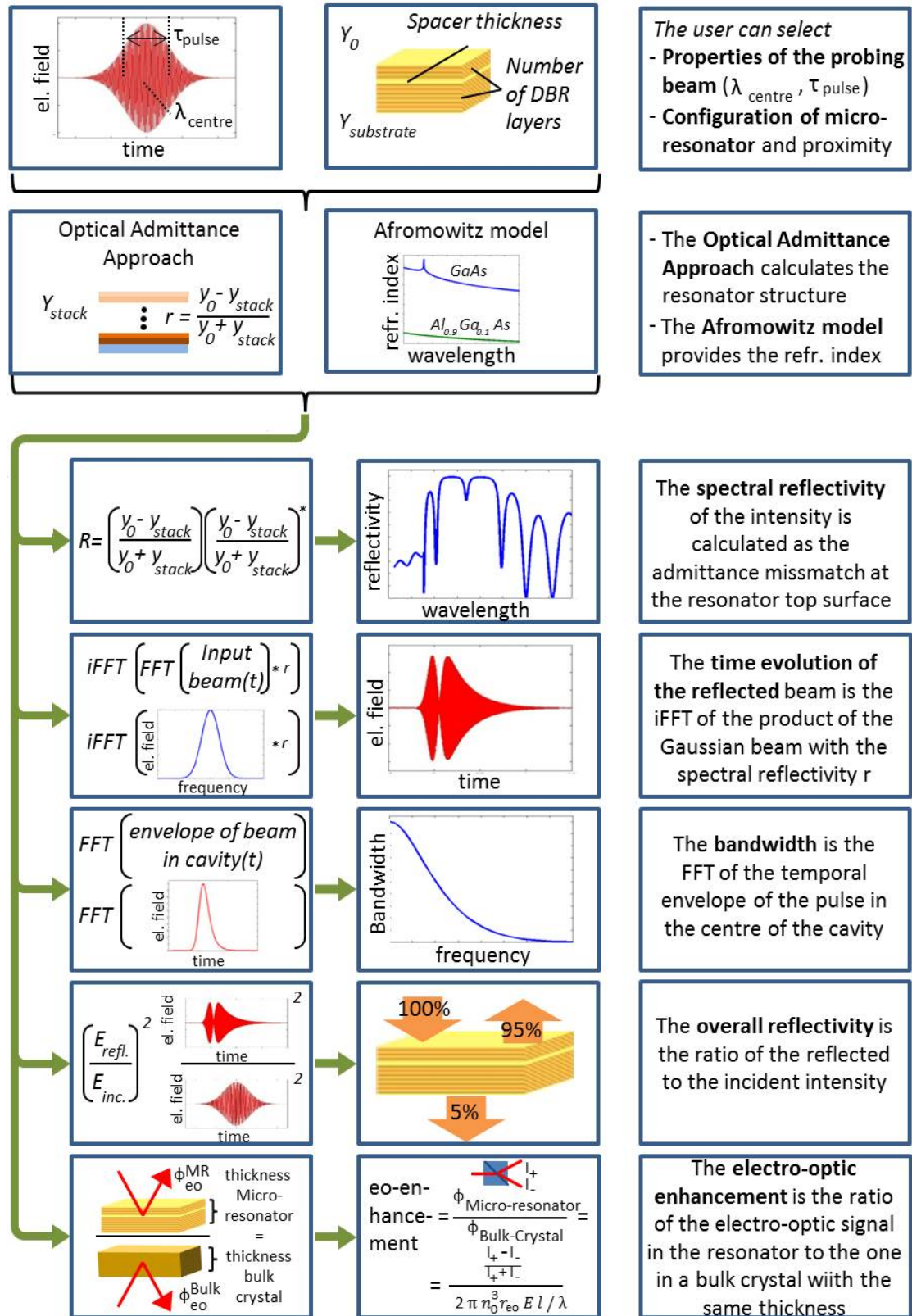


Fig. 4.4: A schematic design of the computer program to simulate the optical response of the micro-resonator.

thickness, Ref. [201] discusses the performance parameter bandwidth and electro-optic enhancement. It is therefore necessary to present a thorough design process and to clearly justify the choice of the selected micro-resonator configuration.

4.3.1 Choice of the Centre Wavelength

Before evaluating different resonator designs, the central wavelength of the probe pulse λ_{centre} is determined in the first instance. The smallest employable wavelength is given by the *GaAs* bandgap edge at 871 nm. Moving the central wavelength closer to this edge should enhance the electro-optic effect due to the increase in the refractive indices of *GaAs* and *Al_{0.9}Ga_{0.1}As*, according to Eq. (3.10). The data given in Fig. 4.5 (a) allow the calculation of the phase-shift enhancement ($\Delta\phi_{eo} / \phi_{eo}$) when moving from 970 nm to 890 nm based on this formula. In the case of *GaAs*, the phase-shift would be enhanced by 6.79% ($(n_0 + \Delta n)^3 / n_0^3$). Applying the same formula to the refractive index of *Al_{0.9}Ga_{0.1}As* leads to an enhancement of 0.73%. Assuming that the phase-shift is experienced equally in both materials, the average phase-shift enhancement would be 3.76%. At the first sight, it seems reasonable to take advantage of this enhancement and to move as close to the bandgap edge as possible.

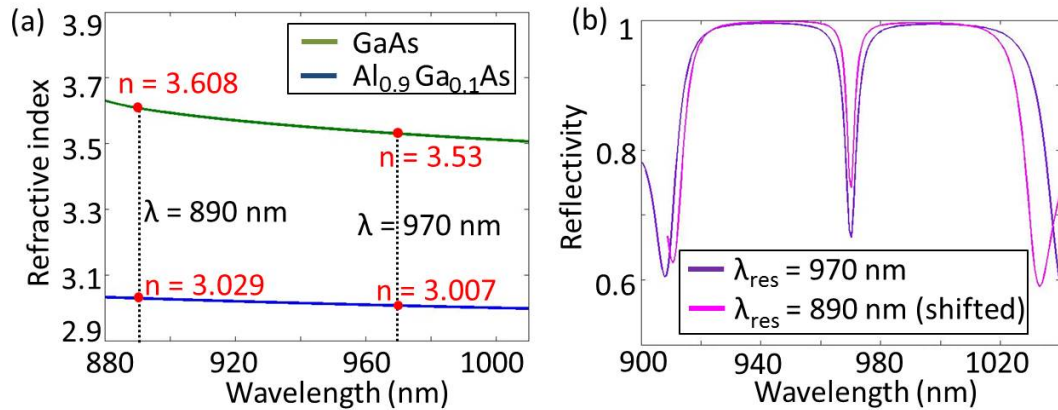


Fig. 4.5: (a) The refractive indices of *GaAs* and *Al_{0.9}Ga_{0.1}As* as a function of the wavelength. The indices at $\lambda = 890 \text{ nm}$ and $\lambda = 970 \text{ nm}$ are highlighted in this plot; (b) The reflectivity curves of two resonators designed for a resonant wavelength at 970 nm and 890 nm. The curve for 890 nm is shifted 80 nm to larger wavelengths for a better comparison.

To evaluate this assumption, the THz 3 dB-bandwidth, the electro-optic enhancement, and the reflectivity are plotted as a function of the central pulse wavelength in Fig. 4.6. For wavelengths larger than 920 nm, all three parameters change only minimally. In the range between 890 nm and 920 nm, on the contrary, the electro-optic enhancement and the THz bandwidth experience a comparably strong

decrease. This range coincides with the wavelengths for which the *GaAs* refractive index deviates from its almost linear behaviour. As a result, the mismatch in the refractive indices between the two compositions increases and changes the response of the cavity. The resonant dip is especially sensitive to changes in the refractive index mismatch, as it can be seen in Fig. 4.5 (b). It shows the reflectivity curves for cavities with a resonant wavelength of 970 nm and 890 nm. For the sake of a better comparison, the spectrum for $\lambda_{res.} = 890 \text{ nm}$ was shifted by 90 nm to overlap with the second curve. It can now be seen that the resonance dip changes its shape when shifting to a different wavelength region.

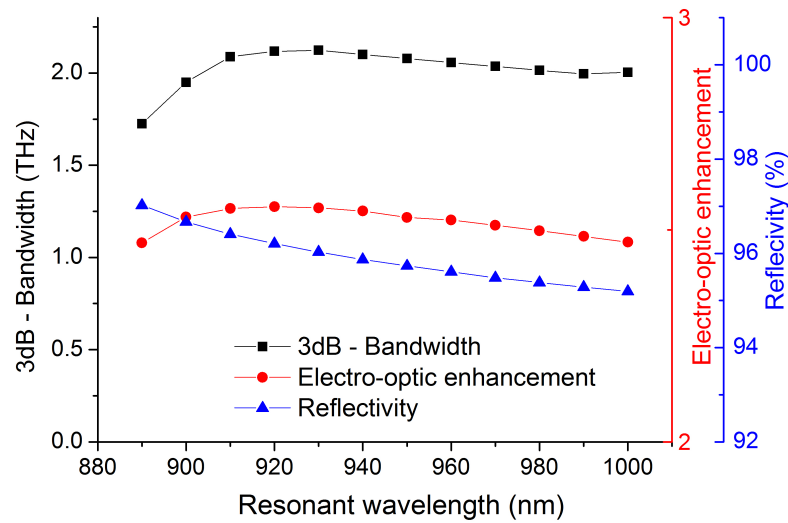


Fig. 4.6: 3dB - bandwidth, electro-optic enhancement, and reflectivity as a function of the resonant wavelength. The simulated design comprised 5 Top-DBR layers, 3 spacer layers, and 15 Bottom-DBR layers. The FWHM of the incident electric-field was 140 fs.

In conclusion, shifting the resonant wavelength closer to the bandgap does not improve the resonator performance noticeably. Indeed, the performance gets even worse for the THz bandwidth and the electro-optic enhancement, especially for wavelengths smaller than 920 nm. Hence, a central pulse wavelength needs to be selected sufficiently away from the wavelength region between the bandgap edge and 920 nm. Preliminary attempts at growing similar micro-resonator structures have shown that the desired resonance wavelength has often been missed by up to 50 nm. In order to ensure to be far enough from 920 nm, a central wavelength of $\lambda_{centre} = 970 \text{ nm}$ was selected and will be used in the following design process.

4.3.2 Minimum Requirements for the Resonator Performance

As a starting point for the design process, it is sensible to define minimum requirements for the functional parameters of the micro-resonator. This sets a limit to the number of eligible configurations. For the overall reflectivity, a minimum value of 90% was chosen. This is in accordance with the high-reflectivity requirement explained previously and the remaining range from 90% to 100% still provides an acceptable tolerance for the design process. For the 3 dB-THz bandwidth a minimum value 1.5 THz was chosen. This seems to be sufficient because preceding experimental trials in the laboratory have shown that the generated THz signal has a smallband character with a peak shortly below 1 THz. The electro-optic enhancement should be significantly higher than 1 in an efficient micro-resonator. Otherwise, the additional design and fabrication effort compared to a bulk crystal is not justified. For the following design process, the electro-optic enhancement was chosen to be ≥ 2 . In comparison to the other two parameters, this value was chosen rather arbitrarily. An additional parameter which should be restrained is the spacer thickness. This thickness can always be extended to achieve a higher sensitivity. As a disadvantage, one would sacrifice the THz bandwidth and the spatial resolution. Therefore, it is the aim of this design process to enhance the electro-optic phase-shift by exploiting the resonance effect in the cavity and not due to the use of an exceptionally thick spacer layer.

In the following simulations, the responses of different micro-resonator configurations were evaluated for a fibre-coupled design. This means that the incident medium was simulated by glass with a refractive index of 1.5. The substrate medium $n_{substrate}$ was air in the simulations. In addition, the incident pulse had an FWHM of 140 fs and a central wavelength of 970 nm. Before starting to simulate the optical response of a potentially infinite number of possible resonator configurations, one should exclude several inappropriate designs.

Restrictions of a Symmetric Resonator

The micro-resonator can be designed as a symmetric or an asymmetric cavity. This subsection investigates which of the two designs is more beneficial. In figure 4.7, the 3dB-bandwidth, the reflectivity, and the electro-optic enhancement are plotted over the number of DBR-layers. Since this was done only for symmetric designs, this number is equal in both mirrors. For each number of DBR-layers N_{DBR} , the number of $\lambda/2$ -spacer layers N_{spacer} is increased from 1 to N_{DBR} . For a specific number N_{DBR} , the maximum values for all three parameters are then plotted in the figure. In case of the reflectivity, the highest value is always achieved

for the maximum spacer thickness ($N_{spacer} = N_{DBR}$). For the 3dB-bandwidth and the electro-optic enhancement, the maximum values were reached for a single spacer layer $N_{spacer} = 1$. It can be seen in this figure that no symmetric configuration fulfills all the minimum requirements at the same time. A number of at least 11 DBR-layers is necessary to obtain an overall reflectivity of at least 90%. However, this number contradicts the bandwidth and electro-optic enhancement requirements. As a result, one has to refrain from using a symmetric design and consider an asymmetric configuration instead.

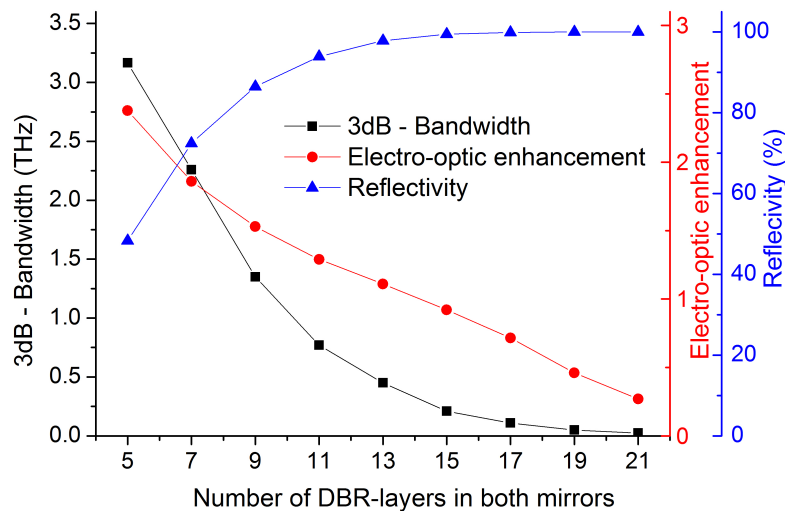


Fig. 4.7: 3dB - bandwidth, electro-optic enhancement, and reflectivity in a symmetric resonator configuration for different numbers of DBR-layers.

The Structure of the Asymmetric Design

The design of an asymmetric cavity offers two fundamentally different configurations with respect to the position of the mirrors: the thicker/thinner mirror can either be used as Top- or Bottom-DBR. Using the thinner DBR as Bottom-DBR brings the spacer closer to the sample and increases the spatial resolution of the probe. It is therefore the preferred option when using this resonator as a near-field detector. However, the simulated time responses in Fig. 4.8 lead to the conclusion that the thicker DBR has to be used as the Bottom-DBR.

The simulation was done using a configuration with 5 and 15 DBR-layers. These mirrors were subsequently used as Top- and Bottom-DBR, respectively. The spacer was kept constant with a thickness of 3 layers ($N_{spacer} = 3$). The blue line in the response curves corresponds to the temporal evolution of the reflected beam

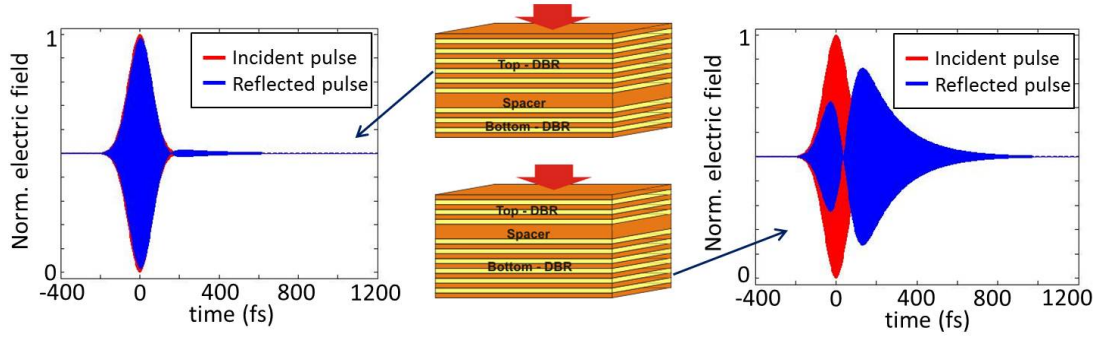


Fig. 4.8: Time evolution of the incident and the reflected beam for two different asymmetric designs.

exactly at the top surface of the Top-DBR. As a reference, the incident beam at the same position is plotted as the red curve. For a configuration with the thicker mirror used as Top-DBR (left hand side), the red line is almost completely covered by the blue one. This means that the incident beam is almost instantly reflected and only a very small portion of the beam enters the resonator. This situation is different on the right hand side for a configuration where the thicker DBR is used as the Bottom-DBR: a considerably larger portion of the incident light enters the resonator and exits it temporally delayed. This temporal response corresponds to the ideal idea of how the resonator should behave for achieving a maximum electro-optic phase-shift. For that reason, only configurations with a higher number of DBR-layers in the Bottom-DBR are considered in the following design process ($N_{Bottom-DBR} > N_{Top-DBR}$).

Limitation in the Resonator Design

In this section, so far, the number of potential resonator configurations was reduced to asymmetric designs with a thicker DBR mirror at the bottom. The remaining configurations are now evaluated with respect to the minimum requirements. The result of this evaluation is summarised in Fig. 4.9. In this schematic plot, the x -axis shows the Q-factor of the resonators according to Eq. (3.14). The y-axis shows the number of DBR-layers in the Bottom-DBR $N_{Bottom-DBR}$. For a horizontal line in the diagram ($N_{Bottom-DBR} = \text{const.}$), all asymmetric designs are included with $N_{Bottom-DBR} > N_{Top-DBR}$. In order to have a manageable amount of data, only odd-multiples of layer numbers were considered ($N_{Bottom-DBR}, N_{Top-DBR}, N_{spacer} = 1, 3, 5, \dots$).

The blue box in the figure covers resonator designs with an overall reflectivity of less than 90%. This means that any configuration with 9 Bottom-DBR layers or less does not fulfill the reflectivity requirement. At the other end of this table

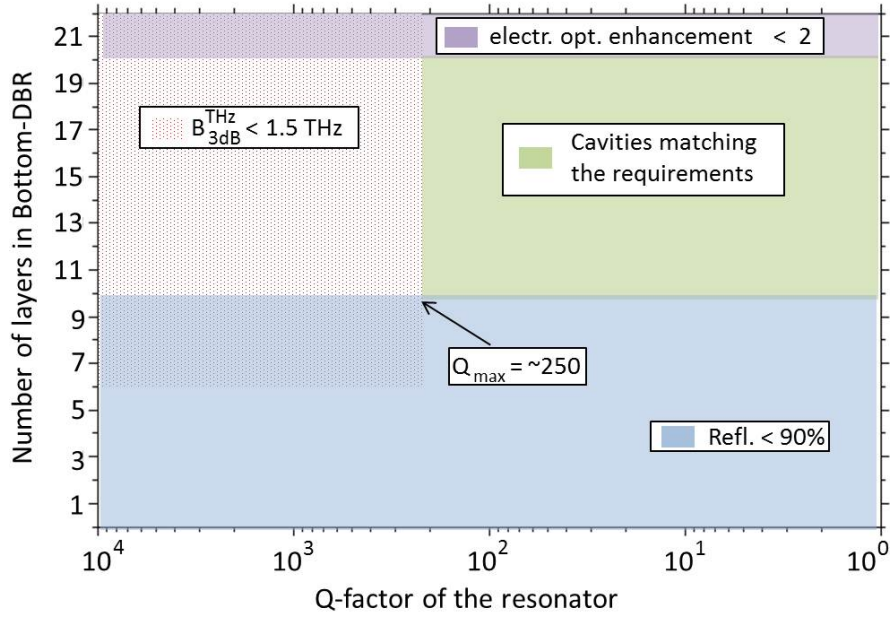


Fig. 4.9: A diagram showing resonator configurations which fulfill the stated requirements as a function of Bottom-DBR layers and Q-factors.

($N_{Bottom-DBR} \geq 21$ DBR-layers), no configuration shows an electro-optic enhancement greater than 2. In a thick micro-resonator with a high number of DBR- and spacer-layers, the absolute value of the phase-shift is certainly higher than in any thin configuration. However, the phase-shift does not increase linearly in this case and the slope ($\frac{d\phi_{eo}}{dN_{layers}}$ becomes smaller for increasing N_{layers}). The phase-shift in a bulk crystal, on the contrary, increases linearly with the thickness according to Eq. (3.10). As a result, the electro-optic enhancement, which is the ratio of these two numbers, decreases for a higher number of cavity layers. Beginning from $N_{Bottom-DBR} = 21$, this value does not exceed the factor 2 anymore.

The last of the three parameters, the bandwidth, can be controlled by the Q-factor of the cavity. To find a relationship between the Q-factor and the required 3 dB-bandwidth ($B_{3dB,min}^{THz} \geq 1.5 THz$), the highest Q-factor Q_{max} for each number of Bottom-DBR layers was recorded that meets this requirement. In all these cases, Q_{max} was in the range between 248 and 277. The majority of Q_{max} values was close to the lower end. Due to this reason, Q_{max} was assigned the value 250. The value Q_{max} means that any resonator with a Q-factor higher than 250 has a 3dB-bandwidth smaller than 1.5 THz. However, it does not mean that every resonator with a Q-factor smaller than 250 has a bandwidth greater than $B_{3dB,min}^{THz}$.

After eliminating these specific areas in Fig. 4.9, only resonators in the green rectangle are left as potential micro-resonator configurations. Since the x -axis is plotted on a logarithmic scale, the number of actually eliminated configurations is

much higher than the visual size of the green area suggests. Indeed, by applying the considerations introduced in this chapter, the number of potential configurations was reduced from a few hundreds to 42.

4.3.3 The Final Design

A table showing the remaining 42 configurations and their most important parameters can be found in Tab. 7.1 in Appendix E. When taking a closer look at this table, one notices that the designs are mostly very similar in their responses and that no configuration stands out due to a distinguished performance. In order to have one more means of evaluation, the electro-optic efficiency was introduced as a new parameter. It is defined as the ratio of the calculated signal strength to the resonator thickness for each individual configuration. Consequently, it provides a value for the signal strength (in ϕ) per length unit (in μm). The configurations in Tab. 7.1 show a variation in this value by more than 30%. In order to select only one of the most efficient resonators, the five designs with the highest efficiencies were selected and summarised in Tab. 4.2.

N_1	N_{Spacer}	N_2	electro-optic enhancement	Reflec-tivity (%)	3dB Band-width (THz)	Efficien-cy ($\phi/\mu m$)
5	3	13	2.6909	91.685	2.0362	1.2163
5	5	13	2.6564	92.917	1.81	1.2004
5	7	13	2.5792	93.8364	1.5837	1.1658
5	3	15	2.511	95.4898	2.0362	1.135
7	1	15	2.6097	93.7811	1.5837	1.1796

Tab. 4.2: The resonator configurations with the top-five values for the electro-optic efficiency listed with their most important parameters. Due to space restrictions, $N_{Top-DBR}$ was replaced by N_1 and $N_{Bottom-DBR}$ by N_2 .

The highlighted configuration with 5 Top-DBR layers, 3 spacer layers, and 15 Bottom-DBR layers has been selected from these five options. Although it exhibits the smallest electro-optic efficiency, it is superior in terms of 3 dB - bandwidth and reflectivity compared to the others. The electro-optic enhancement is almost similar for all 5 configurations.

The spatial dimensions of the selected electro-optic micro-resonator are shown in Fig. 4.10. The overall thickness of the entire structure is about $3.4 \mu m$ and, hence, much smaller than the THz wavelength. The thickness of the spacer comprises only 13.8% of the overall thickness. Since the structure was grown on a

GaAs wafer, an additional $Al_{0.9}Ga_{0.1}As$ layer was introduced as a stop-etch layer. This layer is necessary for the post-fabrication process when the micro-resonator will be removed from wafer by chemical etching.

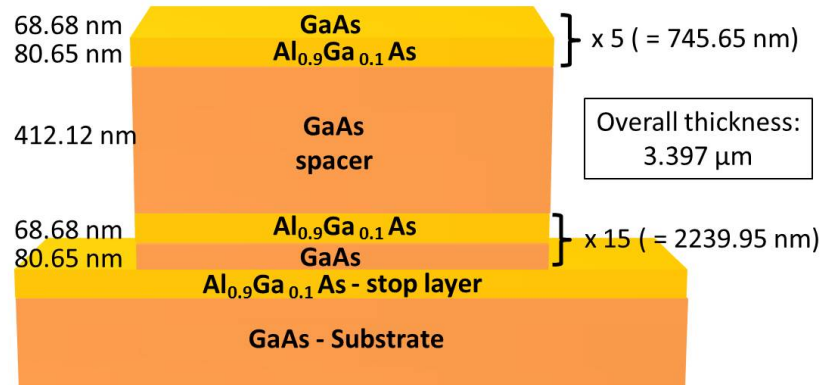


Fig. 4.10: The selected micro-resonator configuration as it is grown on a *GaAs* wafer. The thicknesses of the layers are drawn to scale.

4.3.4 The Influence of the Pulse Width

Since the micro-resonator structure is now fixed, the pulse width provides the only possibility of changing its performance. By making the pulse width smaller or wider, the spectral content of the incident pulse is varied. The 3 dB - bandwidth, the reflectivity, and the electro-optic enhancement were simulated as a function of the pulse width (from 90 fs to 210 fs) in Fig. 4.11 for the selected micro-resonator geometry.

The electro-optic enhancement varies from 1.8 to 3.2 and experiences the largest change among the three parameters. Longer pulses have a smaller spectrum and a larger portion of the beam enters the resonant cavity. As a consequence, the electro-optic phase-shift is enhanced. This, on the other hand, has a negative impact on the 3-dB - bandwidth, which decreases from 2.25 THz to 1.8 THz. However, all these values still fulfill the respective minimum requirement. The reflectivity experiences the smallest change, decreasing from 96.5 % to about 94 %.

As expected, this figure shows that changing the pulse width provides a powerful tool to tune the resonator performance. However, in a real system, the pulse width cannot be tuned arbitrarily: for a specific emission wavelength, the laser only runs in a stable pulsing state for a small range of pulse widths. Therefore, a bandpass filter is used to extend the pulse width without having any impact on the laser emission performance. However, the available bandwidths depend on the optical equipment manufacturers.

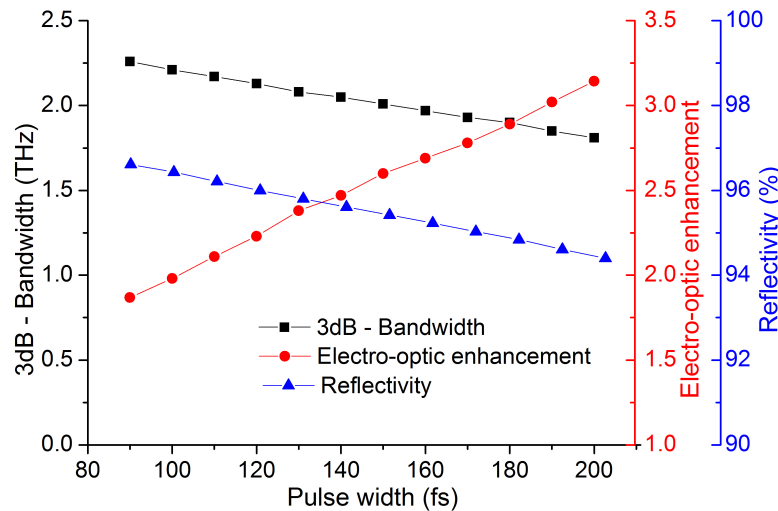


Fig. 4.11: 3db-bandwidth, the electro-optic enhancement, and the reflectivity of the chosen resonator structure as a function of the electric field FWHM of the incident probe beam pulse.

4.3.5 Further Considerations

There are some further interesting points that were investigated during the design process of the micro-resonator. These points do not contribute to the actual design process, however, it is important for the understanding of the micro-resonator. Therefore, the two most important issues are summarised briefly in this section.

The first point is the electro-optic effect in the DBR mirrors. One intuitively assumes that the main contribution of the electro-optic effect takes place in the spacer. However, the simulations show that the phase-shift is 60% smaller when the mirrors experience no electro-optic effect. This simulation was conducted for the final micro-resonator configuration, a pulse width of 140 fs, and DBR mirrors with a "switched off" electro-optic effect. Switching off the electro-optic effect, of course, is possible only in the simulations. However, it gives an interesting insight into how the electro-optic resonator works. The Top-DBR, for example, is thicker than the spacer and light has to pass this mirror twice: on the way to the spacer and back. Light also enters the Bottom-DBR which additionally contributes to the electro-optic phase-shift. As a result, it is important to know that the mirrors have a significant contribution to the probe sensitivity, although it counteracts the intuition. This is very different from most examples in the literature, which employ metallic mirrors. The spacer, however, induces 40% of the overall phase-shift, although its thickness is only about 14% of the micro-resonator thickness.

A further point is the impact of the glass substrate attached to the Top-DBR.

The glass reduces the refractive index contrast at the Top-DBR interface compared to air. As a result, there are more Top-DBR layers necessary to obtain the same reflectivity as it would be the case without the glass substrate. It is therefore recommended to redesign the micro-resonator if fibre coupling is not desired.

4.4 Reflectivity of the Fabricated Micro-Resonator

In the scope of this project, seven micro-resonators samples were fabricated by the UCL MBE facilities. The micro-resonator with the resonance dip closest to the desired wavelength (970 nm) was at $\lambda_{res} = 988\text{ nm}$. In this case, however, the laser source was at the boundary of its operational range. Operating the laser in a continuously pulsing state could not be guaranteed. The second most suitable sample was the micro-resonator with a resonance frequency at 940 nm . Its reflectivity was determined by an optical spectrum analyser within a wavelength range from 800 nm to 1150 nm . The detected intensity was normalised to a gold layer with a reflectivity of 98% . The normalised reflectivity can be seen in Fig. 4.12 (a) and a magnified figure of the resonance dip in (b).

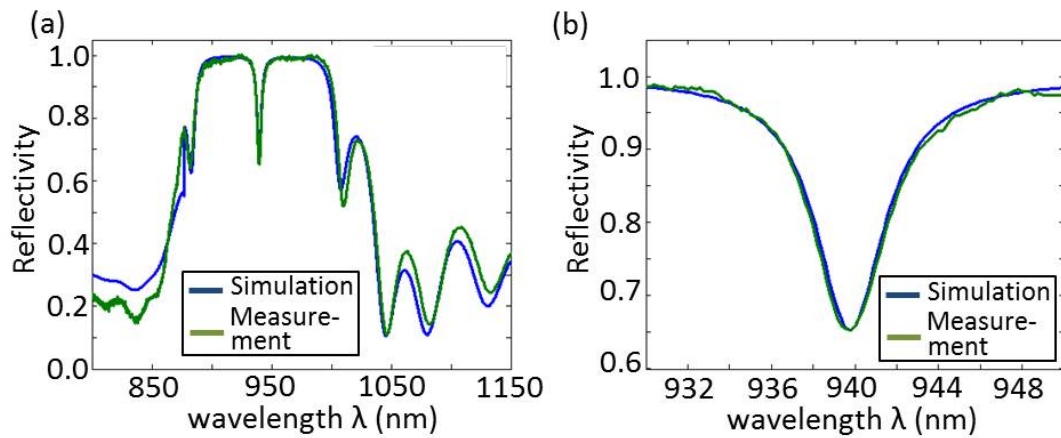


Fig. 4.12: (a) Measured and matched simulated reflectivity of the fabricated micro-resonator; (b) Magnified view of the resonant region in (a).

The fabricated micro-resonator is expected to show an optical response different from Tab. 4.2 due to the shifted resonance wavelength caused by inaccuracies in the fabrication process. Also, one has to consider the configuration shown in Fig. 4.10 in which the micro-resonator is still attached to the wafer. To estimate the optical response of this configuration, the simulated reflectivity curve was matched to the measured one. This provides many potential degrees of freedom: for example, the parameter " x " (Al -content) in the alloy $Al_xGa_{(1-x)}As$ can be varied for both compositions. Also, the thickness of the $GaAs$ - and $Al_{0.9}Ga_{0.1}As$ -layers can be

changed. Thereby, the thickness variations can be different for both compositions and, practically, can also be different for each individual layer. As a consequence, numerous parameters could be incorporated in the simulations and changed until both curves match sufficiently.

In order to limit this number, only two parameters were varied: first, the *Al*-content in both $Al_xGa_{(1-x)}As$ compositions and second, the thickness of the *GaAs*- and $Al_{0.9}Ga_{0.1}As$ -layers. By varying the *Al*-content, one can adjust the width of the stop-band and the depth of the reflectivity dip. Controlling the thickness of the layers allows adjustment of the resonance wavelength and the position of the dip within the stop-band. In the simulations, two separate parameters were introduced for both material compositions. Hence, the thickness of *GaAs*- and $Al_{0.9}Ga_{0.1}As$ -layers could be varied separately. Changing this set of parameters allowed a sufficient match of both curves (Fig. 4.12). Especially the region close to the resonance dip could be matched nicely (Fig. 4.12 (b)). This is important because this region mainly determines the optical response of the resonator.

According to the simulations relying on the matched reflectivity curves, the fabricated resonator has the following values: the *Al*-content in the $Al_{0.9}Ga_{0.1}As$ -composition is 87.1% and the spacer thickness is 395.97 nm. The thickness of a *GaAs* $\lambda/4$ -layer in the DBR is 65.99 nm, whereas the thickness of a $Al_{0.871}Ga_{0.129}As$ -layer is 77.82 nm. The thickness of the entire micro-resonator is 3272.17 nm. When using this configuration in the simulation, one can calculate the 3 dB-bandwidth, the reflectivity, and the electro-optic enhancement for the fabricated micro-resonator (Tab. 4.3). For a better comparison, the values for the ideal configuration at $\lambda_{res} = 970$ nm are added to the table.

	ideal configuration @970 nm	fabricated micro-resonator on wafer	fibre-coupled micro-resonator
$B_{3dB}^{THz}(THz)$	2.0362	1.6364	2.104
Refl. (%)	95.4898	88.1429	95.4534
electro-optic enhancement	2.511	2.3126	2.4235

Tab. 4.3: A comparison of the 3dB-bandwidth, the reflectivity, and the electro-optic enhancement of the ideal electro-optic micro-resonator and the fabricated one (on the wafer and fibre-coupled).

According to this table, the performance of the fabricated fibre-coupled micro-resonator deviates only slightly ($< 4\%$) from the ideal one at $\lambda_{res} = 970$ nm. These deviations should barely be detectable in an experimental system. In case of the

micro-resonator on the wafer, on the other hand, one notes a significant performance drop. The electro-optic enhancement, however, is reduced only by 7.9% and, hence, the E^{THz} should still be detectable with a comparable amplitude.

4.5 Conclusions

This chapter described the design process of the electro-optic micro-resonator that led to the fabrication of a specific resonator configuration. It introduced an analytical computer program for the micro-resonator which is mainly based on two models: first, the Optical Admittance Approach to simulate the response of optical multi-layers and second, the Afromowitz model to accurately calculate the refractive indices of the involved materials. The program considers the micro-resonator as a stand-alone entity and it was therefore limited to calculating three parameters: the reflectivity, the THz 3 dB-bandwidth, and the electro-optic enhancement. These parameters could be calculated as a function of the cavity geometry, the material composition, and the incident wavelength and pulse width.

In a first step, it was evaluated that the resonant wavelength λ_{res} only has a very small impact on the resonator response for wavelengths larger than 920 nm. In order to be sufficiently away from this wavelength, a resonant wavelength of $\lambda_{res} = 970$ nm was selected. In a next step, the number of potential micro-resonator configurations was reduced. Therefore, minimum requirements to the geometry in general were introduced as well as to the three parameters THz 3 dB-bandwidth (> 1.5 THz), electro-optic enhancement (> 2), and reflectivity ($> 90\%$). This limited the number of potential configurations to 42, with all of them showing a very similar optical response. By introducing the electro-optic efficiency, the number of potential configurations was reduced to 5. Among them, a configuration with 5 Top-DBR layers, 3 spacer layers, and 15 Bottom-DBR layers was selected as the most ideal micro-resonator configuration.

This configuration was fabricated by the UCL MBE facilities. Due to fabrication uncertainties, the fabricated micro-resonator structure showed a slightly different performance and the resonance wavelength was shifted to $\lambda_{res} = 940$ nm. By matching the simulated reflectivity curves with the measured ones, the uncertainties of the fabrication process could be determined accurately. Based on these values, the optical response of the fabricated micro-resonator could be calculated. Despite the fabrication uncertainties, the overall performance of the electro-optic micro-resonator did only change negligibly.

5 A Parallel Plate Waveguide for Terahertz Transmission

After the fabrication of the electro-optic micro-resonator, it is the next step of this project to characterise its performance as a probe for THz near-field imaging. The experimental characterisation of the probe requires access to a strong and spatially confined THz electric-field E^{THz} in which the probe can be inserted. In the laboratory, the E^{THz} is generated by optical rectification in a non-linear ZnTe crystal. A THz waveguiding structure is therefore necessary which can guide the emitted THz radiation from the ZnTe crystal to the micro-resonator, similar to how it is depicted in Fig. 5.1.

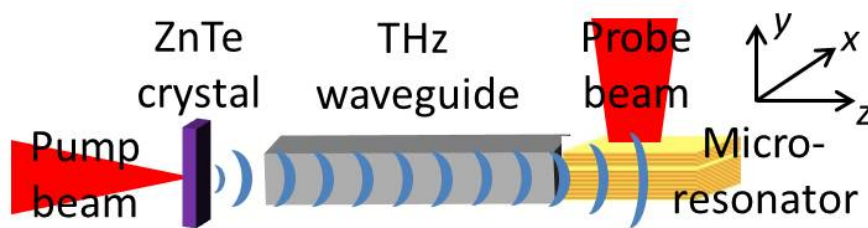


Fig. 5.1: Using a THz waveguiding structure to guide THz radiation from the source to the micro-resonator.

For this specific purpose, an ideal waveguiding structure needs to fulfill certain requirements. First, it should have a broadband frequency response. Preferably, it should have no cut-off frequency so that all the energy generated by the non-linear crystal is delivered to the micro-resonator. Also, it should exhibit small dispersion. Dispersion spreads out the THz pulse and reduces the maximum electric-field strength. Second, the E^{THz} at the waveguide output needs to have a specific polarisation to induce an electro-optic phase-shift in the probe beam. In the configuration shown in Fig. 5.1, for example, the E^{THz} has to be polarised in the y -direction (compare to Fig. 3.8). Thirdly, the waveguide output aperture should have about the same spatial dimensions as the micro-resonator. In this case, all the energy is efficiently delivered to the electro-optic probe. It would be even more beneficial if the waveguide geometry allows one to spatially confine the energy during propagation which causes an electric-field enhancement at its output.

A waveguiding structure which potentially fulfills all these requirements is a parallel plate waveguide (PPWG). Due to this reason, a PPWG is used in the later experiments to guide the E^{THz} from the source to the probe. It is therefore necessary to evaluate the performance of the fabricated PPWG with respect to

its later use in the THz near-field detection system. This is done in this chapter: first, the THz transmission through the PPWG is optimised in order to obtain the the maximum E^{THz} at the PPWG output. Second, the mode structure in the PPWG is investigated and its implications on the transmitted THz waveform are discussed. But before these two questions are addressed, this chapter gives an overview of PPWGs used in the literature. It presents its specific advantages and discusses diverse PPWG applications. A concise summary of the results describing the experimental system, the numerical simulations, the optimum gap size, the leakage radiation, and the mode structure was published in Ref. [237, 238].

5.1 Parallel Plate Waveguides in Terahertz Technology

Parallel plate waveguides consist of two metallic plates with a width w . The plate surfaces are oriented parallel to each other and are separated by the gap size p . An ideal PPWG has an infinite width w and shows perfect conductivity. The boundary conditions imposed by this geometry allow the excitation of the fundamental transverse electro-magnetic (*TEM*) mode. The *TEM*-mode has its electric-field components normal to the metallic plate surfaces. Due to the absence of a cut-off frequency, this electric-field distribution is even valid for a static electric-field ($f = 0$ Hz). The possibility of guiding THz energy in the *TEM*-mode without dispersion and without a frequency cut-off makes the PPWG an interesting tool for many technological applications. This includes signal transmission, near-field imaging, and spectroscopy.

In real-world experiments, however, the assumption of an ideal single-mode *TEM* propagation does not always hold true due to several reasons: first, the plate width often cannot be considered to be infinite. The finite width causes wave reflections at the plate edges. Second, higher-order modes can be excited in the gap and dispersive energy propagation has to be considered. As it will be shown later in this chapter, the presence of multiple modes can even cause the *TEM*-mode to appear dispersive. In summary, even such a relatively simple geometry such as that PPWG requires thorough investigation when it is intended to be used in practical applications. The following section reviews publications on PPWGs particularly in the THz domain and addresses some of practical problems.

5.1.1 Terahertz Parallel Plate Waveguides in Literature

The group of Prof. Daniel Grischkowsky demonstrated sub-ps THz pulse propagation through a copper PPWG in 2001 [239]. They used a sub-wavelength gap size of $108 \mu\text{m}$ and the plate width w was considerably larger than the incident THz beam diameter. Under these circumstances, they realised single-mode *TEM* propagation. The experimentally determined attenuation for this mode was about 0.1 cm^{-1} . The possibility of guiding energy in PPWGs for THz signal transmission was investigated and refined in the following years. This led to waveguides with finite widths [240], to curved waveguides [241], or to approaches using dielectrics instead of metal [242].

Apart from THz signal transmission, PPWGs were also used in THz high-resolution imaging systems taking advantage of the cut-off free *TEM*-mode [127, 243, 244]. The necessarily high spatial energy confinement was achieved by using tapered PPWGs with sub-wavelength output dimensions. The strongest electric-field confinement in a tapered configuration was realised in Ref. [127]. In this work, the E^{THz} is focused to a rectangular area with edge lengths corresponding to $\lambda/260 * \lambda/145$ ($10 \mu\text{m} * 18 \mu\text{m}$). A further application of PPWGs is THz spectroscopy. Small samples of inorganic [245] and organic [246, 247] materials can be placed into the gap between the plates and identified according to their spectroscopic fingerprint using the dispersion-less *TEM*-mode.

The coupling between a guided mode and free-space is also a matter of investigation: an adiabatic compression/extension of the PPWG gap size was suggested to improve the input/output coupling [248]. This idea was refined in Ref. [249] by suggesting an optimised adiabatic compression with almost loss-free input and output coupling. A similar, but significantly simpler structure, was realised using a copper shim as a flare to couple linearly polarised THz radiation into the *TEM*-mode inside a PPWG [246]. This is an intriguing alternative to ordinary PPWGs where the plates begin and end with an abrupt edge. This type of waveguide, however, is optimised for coupling of a THz electric-field with a plane wavefront.

The impedance mismatch at the PPWG output was investigated in Ref. [250]. In this publication, a higher reflectivity of the *TEM*-mode at the PPWG output was measured for a smaller gap size. This indicates a larger impedance mismatch to free-space for a smaller gap size. This result is of particular relevance for the interpretation of experimental results presented later in this thesis.

The electric-field distribution inside the gap has also been investigated. It was, for example, measured and simulated for a doubled-taper geometry in Ref. [251]. In a double-taper configuration, the width w and the gap size p become

adiabatically smaller along the length of the waveguide towards the output. It was found that the electric-field is spatially more confined between the plates for smaller gap sizes. This was also reported for a single taper configuration in Ref. [127]. When using a tapered configuration, very high electric-field strengths can be achieved at the waveguide output. In Ref. [251], for example, an electric-field strength of 140 MV/m was measured with an input THz pulse energy of $0.5 \mu\text{J}$.

The lowest-order transverse-electric (TE_1) mode was investigated as an alternative to the fundamental TEM -mode in Ref. [252–254]: the electric-field components of this mode are parallel to the metallic plates and vanish at the metallic interface. The electric-field maximum is in the centre of the gap. According to these references, there are two distinct advantages of this mode over the TEM -mode: first, the coupling efficiency from an input Gaussian beam to this mode can theoretically reach 99%. For a TEM -mode, a coupling coefficient of maximal 89% is possible when the input Gaussian beam diameter is similar to the gap width. Second, the Ohmic losses of the TE_1 -mode decrease with frequency, which is opposite to the TEM -mode. This makes the TE_1 -mode interesting for applications employing higher frequencies. However, this mode has a cut-off frequency and a dispersive behaviour especially for lower frequencies. Therefore, it is not considered as an option throughout this thesis. A further investigation into the PPWG mode structure was done in Ref. [131]. In this work, a strong electric-field is observed at the PPWG edges, while the electric-field in the centre seems to vanish. This was explained by the formation of a plasmonic edge mode which replaces the TEM -mode for specific frequencies. An alternative explanation of this phenomena will be discussed later in this chapter which relies rather on the existence of mode-interference in PPWGs than on the formation of plasmonic edge modes [255].

5.2 Design of the Parallel Plate Waveguide

The fabricated PPWG is made of aluminium and has the following geometrical properties [237]: the length is 29.4 mm, the input width is $w_{in} = 4.4 \text{ mm}$, and the output width is $w_{out} = 1 \text{ mm}$ (Fig. 5.2(a) and (b)). The corresponding taper angle θ is 3.3° and was chosen according to recommendations in the literature [256]. The plate width at the PPWG input w_{in} was chosen to be clearly larger than the diameter of the incident THz beam ($\approx 500 \mu\text{m}$). Hence, only the gap size is the crucial parameter which determines the PPWG input aperture ($A_{PPWG} = w_{in} * p$) and, consequently, the input coupling. The output width w_{out} is intentionally larger than the THz wavelength to ensure efficient coupling of the E^{THz} to the electro-

optic sample. In order to sample the E^{THz} right in front of the PPWG output, the probe beam has to reach the micro-resonator without being blocked by one of the waveguide plates. This is the reason why the waveguide plates deviate from a rectangular shape in the xy -plane and look similar to a sharp tip when approaching the PPWG output (see Fig. 5.2 (a)).

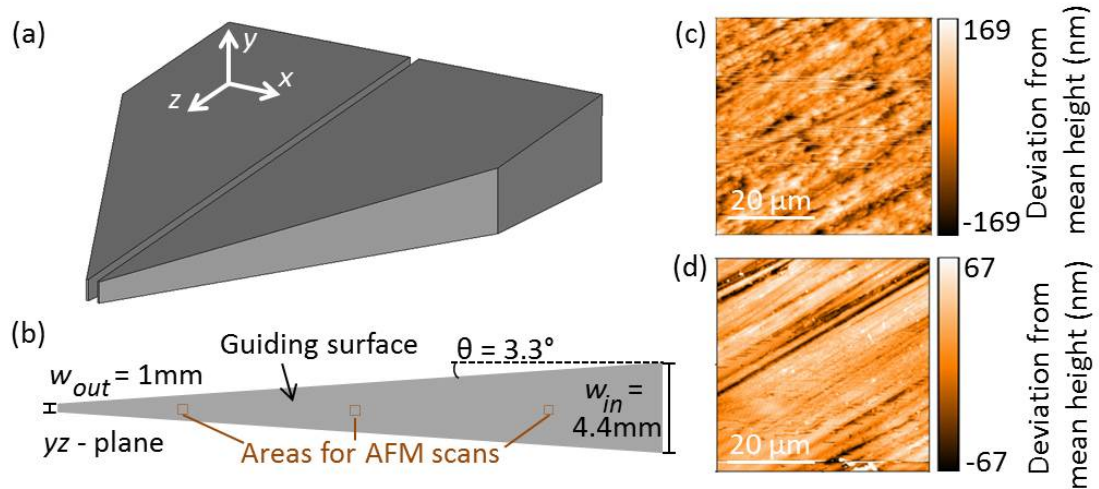


Fig. 5.2: (a) Three-dimensional view of the PPWG; (b) The guiding surface and the most important parameters of the waveguide plate; (c) Image of the AFM scan before polishing; (d) Image of the AFM scan after polishing.

The guiding surfaces were polished with sub-micrometer grit lapping paper to reduce the surface roughness and to remove defects caused in the fabrication process. The surface roughness was measured with an atomic force microscope (AFM) at three different areas along the waveguide, as it is indicated in Fig. 5.2 (b). The areas were squares with $50 \mu m$ edge length and exemplary AFM images before and after the polishing process are shown in Fig. 5.2 (c) and (d). As expected, one can see a much smoother surface in (d) and the average deviation from the mean height decreased from 125 nm to 30 nm. Although a lot of effort was put into the polishing process and different techniques were applied (regarding the applied pressure, direction of movement, and duration of polishing), it was not possible to remove the scratches which can be seen as black lines in image (d). They probably occurred due to the formation of tiny grains while the lapping paper was moved over the surface. The width of these grains is in the order of $1 \mu m$ and, therefore, much smaller than the THz wavelength. Hence, the impact of these scratches on the transmission properties should be minimal and the smoother surface should reduce the transmission losses. This is confirmed by a direct comparison of the THz waveforms in later experiments, in which the transmitted peak-to-peak amplitude is about 16% higher for the waveguide after polishing.

5.2.1 Experimental System

A schematic diagram of the experimental system can be seen in Fig. 5.3 (a) and a photograph of the PPWG in the apparatus is shown in (b). The Coherent Mira 900 is used as a laser source which emits 100 fs pulses at 800 nm with a repetition rate of 76 MHz. The emitted laser beam is split into a pump and a probe beam by a polarising beam splitter (PBS). The probe beam is directed to a high-NA objective (Mitutoyo, M Plan Apo 10x) which focuses the probe beam on the PC-antenna of the integrated sub-wavelength aperture probe. The antenna was oriented to detect the x -component of the incident E^{THz} . The power of the probe beam was $P_{Probe} = 7.3$ mW throughout the experiments. For the fabricated antenna, a minimum probe power of at least 5 mW is recommended to detect an appropriate signal. To avoid thermal damage to the antenna, 10 mW should not be exceeded. Hence, the selected value seems to be a reasonable trade-off. The objective has a focal length of 2 cm and this distance was kept constant in the experiments.

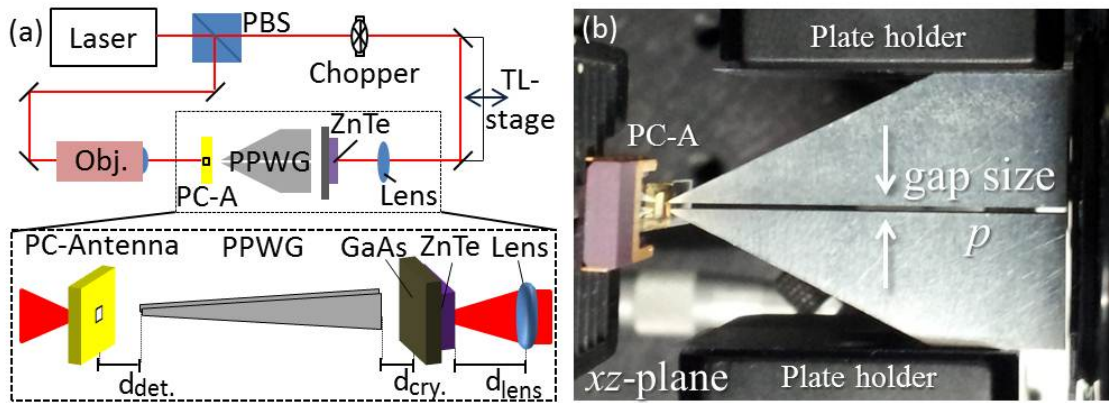


Fig. 5.3: (a) Schematic diagram of the experimental system (xz -plane). A detailed image of the elements inside the dashed box is shown at the bottom from a yz -perspective; (b) Photograph of the PPWG and the integrated near-field probe (xz -plane); Figure (b) is published in Ref. [237].

The pump beam was directed through a chopper wheel to a mechanical translation stage (TL-stage). The use of a chopper wheel ($f_{chopper} \approx 1.3$ kHz) enables small-band low-noise signal detection using lock-in measurement techniques. The translation stage shifts the arrival time of the THz electric-field with respect to the probe beam in steps of either 33 fs or 66 fs. This enables time-resolved detection of the THz pulse with the respective sampling intervals. The pump beam was then directed to a lens which focuses the pump beam into the 1 mm-thick non-linear ZnTe crystal. After exiting the lens, the average pump power was $P_{Pump} = 200$ mW. The ZnTe crystal was mounted on a $500 \mu\text{m}$ -thick GaAs holder to block the optical beam from entering the waveguide and generating current in the PC-antenna. The

GaAs/ZnTe assembly had to be tilted by about 3° to prevent the pump beam from being reflected back into the laser causing an unstable operation state.

The PC-antenna was connected to a current-voltage converter with an amplification of $10 \frac{V}{nA}$ within a bandwidth from 300 Hz to 3 kHz. The voltage was then displayed by a lock-in amplifier with an integration time of 300 ms. The mechanical translation stage and the lock-in amplifier were controlled by a purpose-built LabView program which allowed automated recording of the THz waveforms.

Simulation of the Experimental System

The experimental system is modelled numerically by the commercial software CST Microwave Studio, which uses the finite integration time domain formulation. This simulation gives a direct feedback on the experimentally determined results and, what is more important, it provides an insight into the processes happening inside the PPWG. The additional knowledge of the electric-field distribution is essential for the correct interpretation of the measured results since the experimental detection system alone is only capable of measuring the transmitted THz waveform.

The details of the simulations are described in Ref. [237]. Specifically, the simulated Gaussian beam source was positioned $500 \mu m$ away from the PPWG input with a central frequency of 0.69 THz. The minimum beam waist was $\omega_0 = 280 \mu m$ and the Rayleigh length was $566 \mu m$. The FWHM of the temporal waveform (Gaussian envelope) was ≈ 2 ps (The spectrum and the waveform are shown in Fig. 5.8 (d) on page 110 in the context of the later analysis). The material aluminium was modelled with the bulk conductivity of $\sigma_{Al} = 3.56 \times 10^7 \frac{S}{m}$.

5.3 Characterisation of the Parallel Plate Waveguide

In order to find the best configuration for maximal THz energy transmission from the non-linear crystal to the PPWG output, different parameters were varied in the experimental system. These parameters can be seen in the dashed box of Fig. 5.3 (a): the distance between the gold sheet of the sub-wavelength aperture probe and the output of the PPWG ($d_{det.}$); the distance between the PPWG input and the GaAs surface facing the PPWG ($d_{det.}$); and the distance between the lens and the input surface of the ZnTe crystal (d_{lens}).

A fourth crucial parameter is the gap size p between the plates. Each plate was mounted on a holder that was attached to a separate translation stage. The

holders can be identified as the black rectangles in the photograph in Fig. 5.3 (b). The possibility of changing the gap size allows actively controlling the Ohmic losses, the radiation leakage, the coupling coefficients, and the mode composition inside the waveguide.

5.3.1 Evaluation of the Invasiveness of the Near-Field Probe

Using a near-field probe for sampling the E^{THz} directly at the PPWG output avoids potential pulse distortion caused by far-field focusing elements such as lenses. A reduction of the number of dispersive elements is especially beneficial for the investigation of the mode structure that will be presented later in this section. The introduction of a near-field detector into the proximity of the PPWG output, however, can cause distortions of the propagating THz pulse. This is particularly true for near-field probes including metallic features, such as the integrated sub-wavelength aperture probe. It is therefore necessary to evaluate the invasiveness of this probe before carrying out further experiments.

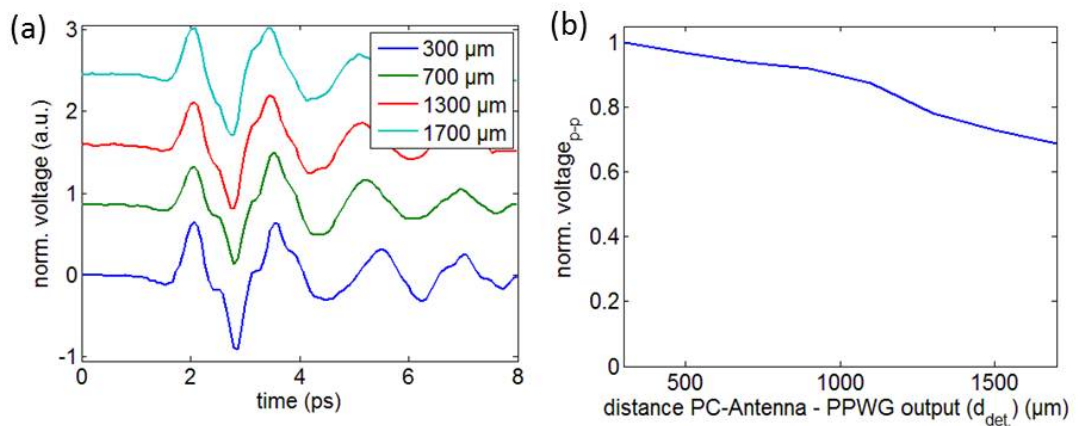


Fig. 5.4: (a) The measured waveforms for four different distances between the PC-antenna and the PPWG output (d_{det}). Each waveform is normalised to its respective maximum and an arbitrary offset is added to distinguish the curves; (b) Normalised peak-to-peak amplitudes of the detected waveforms as a function of d_{det} . The values are normalised to the maximum amplitude at $d_{det} = 300 \mu m$.

The integrated sub-wavelength aperture probe employed in these experiments was similar to the one presented in Chapter 2. But in these experiments, a square-shape aperture with an edge length of $50 \mu m$ was used. In order to evaluate the effect of the near-field probe on the detected THz waveforms, the distance d_{det} between the probe and the PPWG output was varied from $300 \mu m$ to $1700 \mu m$. All the other distances ($d_{cry.}$, d_{lens}) were kept constant and the gap size was $p = 500 \mu m$. The normalised waveforms for four different distances d_{det} are shown

in Fig. 5.4(a). The four waveforms look very similar which indicates that the presence of the near-field probe only has a negligible impact on the measured results. The 30% decay in the peak-to-peak amplitude of the waveforms over the recorded distance $d_{Det.}$ (Fig. 5.4(b)) can be explained by energy divergence outside the waveguide. All four waveforms also exhibit a kink-feature at 2.5 ps and 3.2 ps which seems to change for different gap sizes. This feature is likely to be caused by higher-order modes which will be discussed later in this section.

Another critical point in this configuration is reflection between the metallic probe surface and the PPWG tip. A round-trip would take several ps (2 ps for $d_{det.} = 300 \mu m$, 4.66 ps for $d_{det.} = 700 \mu m$, ...) and a THz reflection should be visible in the waveform for the respective round-trip time. The absence of these features in the waveforms in Fig. 5.4(a) suggests that this type of reflections can be neglected. This can be explained by the spatial dimensions of the PPWG output (Fig. 5.2): the tapered PPWG output provides only a negligible surface that can cause back-reflections into the PC-antenna.

In the following experiments, the detector is kept at a distance of $d_{det.} = 500 \mu m$ away from the PPWG output. This ensures that small experimental errors in the relative position between the detector and the waveguide output only cause a negligible variation of the measured signal amplitude and that the detector always stays in the range in which its low level of invasiveness was verified. This allows a comparative study of THz transmission properties for further waveguide configurations that are presented in the next sections.

5.3.2 Alignment of the Pump Beam

In a first step, the THz generation side of the experimental system is investigated. This involves the optimisation of the THz generation and the coupling of the THz energy into the waveguide. Therefore, the distance between the ZnTe crystal and the lens d_{lens} was varied over several millimetres. The recorded peak-to-peak amplitudes of the THz waveforms are plotted in Fig. 5.5(a). During this set of measurements, the GaAs holder was practically touching the PPWG input ($d_{cry.} = 0 mm$) and the gap size p was $500 \mu m$. Beginning from smaller distances d_{lens} , the amplitude continuously increases until d_{lens} reaches $100 mm$ and decreases again for distances greater than $100 mm$. The general tendency in this plot is expected: the highest amplitude coincides with the focal length of the lens ($100 mm$) and the most efficient THz generation in the non-linear crystal takes place for the highest incident intensity. However, the dip exactly at $100 mm$ is counter-intuitive and needs further explanation. The focal spot is not only the spatial point of highest

optical intensity, but it is also the one with the smallest beam diameter. When the optical beam diameter becomes smaller than the diameter of the excited THz beam, the THz excitation spot behaves similar to a sub-wavelength aperture [257]. As a result, the emission of the THz beam is reduced and second, the emitted beam is very divergent. In order to circumvent this undesired behaviour, a distance between the lens and the ZnTe crystal of $d_{lens} = 97 \text{ mm}$ was chosen. This corresponds to the distance showing the highest THz peak-to-peak amplitude.

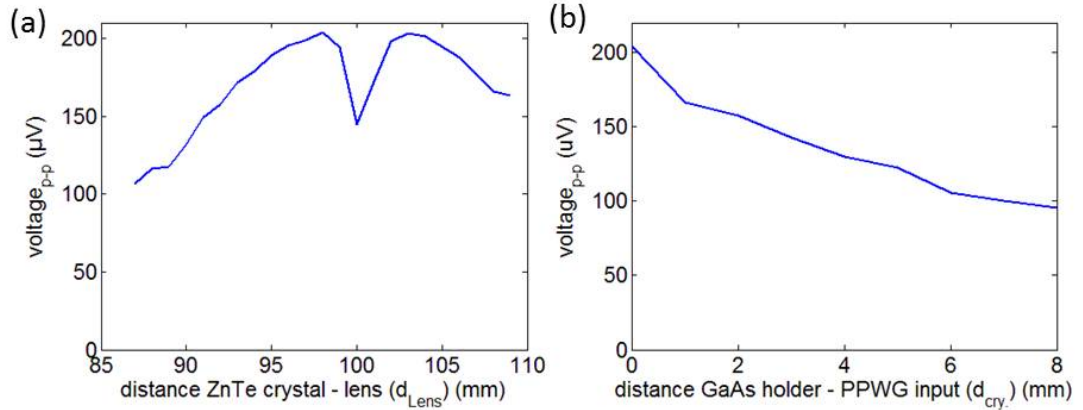


Fig. 5.5: (a) The measured peak-to-peak amplitude of the THz waveforms as a function of the ZnTe crystal - lens distance (d_{lens}); (b) The measured peak-to-peak amplitude of the THz waveforms as a function of the GaAs/ZnTe holder - PPWG input distance ($d_{cry.}$).

In the next step, the distance between the PPWG input and the GaAs/ZnTe assembly $d_{cry.}$ was evaluated. Hereby, this distance was increased from $d_{cry.} = 0 \text{ mm}$ to several millimetres while d_{Lens} was kept constant at 97 mm and the gap size was $p = 500 \mu\text{m}$. For a distance of $d_{cry.} = 0 \text{ mm}$, the GaAs holder basically touches the PPWG input. There was only a small gap which was caused by the 3° -tilt of the GaAs plate as explained earlier. Figure 5.5 (b) shows that the strongest THz signal is transmitted for a configuration where the GaAs/ZnTe assembly is as close to the PPWG input as possible.

As a result of the previous measurements, the optimal values of $d_{cry.}$ and d_{lens} on the THz generation side were found. For the further analysis, it is interesting to know the THz beam diameter at the PPWG input. As stated in Ref. [254], the ratio of the incident beam diameter to the gap size determines the coupling efficiency at the PPWG input. The THz beam diameter was estimated by moving the pump beam focus in the ZnTe crystal along a line in the x -direction ($y = 0 \mu\text{m}$) from one waveguide plate to the other. This procedure shifts the THz excitation point in horizontal direction inside the ZnTe crystal and, hence, the projection of the THz beam onto the PPWG input aperture. This is graphically shown in Fig.

5.6 (a). Every $50 \mu\text{m}$, the peak-to-peak amplitude of the transmitted THz signal was recorded and plotted as the green line in Fig. 5.6 (b). The gap size throughout this scan was kept constant at $500 \mu\text{m}$. Scanning the THz beam along the gap is equivalent to the convolution of the incident beam with the waveguide input aperture. This mathematical operation was computed in Matlab with a gap size $p = 500 \mu\text{m}$ and a Gaussian beam diameter (FWHM) of $500 \mu\text{m}$. The outcome of the convolution is plotted as the blue line in Fig. 5.6 (b), which fits the experimentally measured curve well. When slightly changing the beam diameter ($\pm \approx 20 \mu\text{m}$), however, the two curves still match sufficiently well and this type of measurement gives rather an estimate of the beam diameter than a very accurate value. Hence, the FWHM of the THz beam at the location of the PPWG input was roughly estimated to be around $500 \mu\text{m}$.

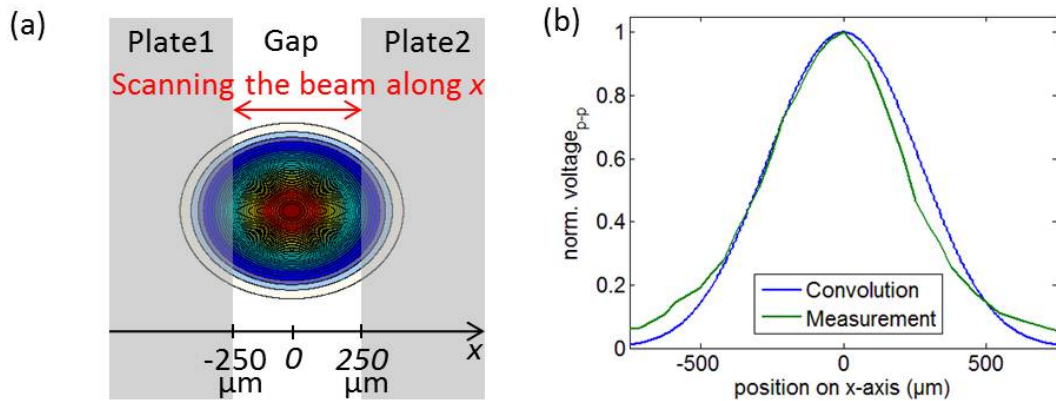


Fig. 5.6: (a) A schematic diagram of how the incident THz Gaussian-type beam is scanned along the input aperture of the PPWG; (b) A comparison of the experimentally determined and the calculated convolution of the input THz beam and the input aperture of the PPWG.

5.3.3 The Optimum Gap Size for Maximum Energy Transmission

The gap size has a significant influence on the transmission properties of the PPWG: it dictates the cut-off frequencies of higher-order modes and the impact of different loss mechanisms. In addition to that, the coupling coefficients between the guided E^{THz} and free-space are directly controlled by the gap size. This includes the input, the output, and the "virtual boundaries" along the plate edges.

The optimal gap size for maximal THz energy transmission is found by opening the gap size from a closed configuration ($p = 0 \mu\text{m}$) up to $p = 3000 \mu\text{m}$ and recording the THz waveforms. The respective peak-to-peak amplitudes are nor-

malised to the overall maximum and plotted in Fig. 5.7 as the red line. The large dots mark the gap sizes for which a value was recorded.

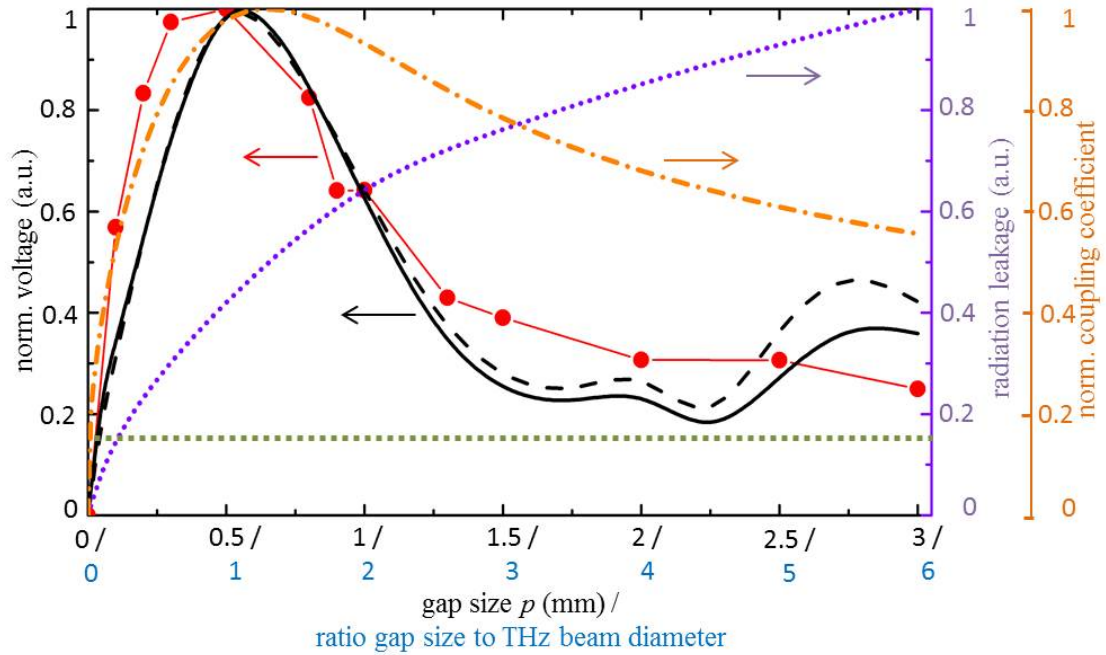


Fig. 5.7: Normalised peak-to-peak amplitudes of the experimental (red line with dots) and simulated (black lines) waveforms as a function of the gap size. The solid and the dashed lines correspond to the simulation with and without the detector present; the calculated coupling coefficient (orange line) and the simulated radiation leakage (violet line) as a function of the gap size. The dashed horizontal line (green) is the detected THz amplitude without the PPWG. A similar plot is published in Ref. [237].

The peak-to-peak amplitude strongly increases up to a gap size of about $500\ \mu\text{m}$. Beginning from that gap size, the amplitude continuously decreases by 75% until the gap size of $3000\ \mu\text{m}$ is reached. The same behaviour of the transmitted THz amplitude as a function of the gap size is confirmed in the simulations, which is shown as the black lines in the figure. In the simulations, the impact of the metallic near-field probe was evaluated once more: the solid black line corresponds to a situation where the PPWG output faces only free-space and the near-field probe is not present. The dashed line, on the contrary, simulates the circumstances that are identical to the experiment and a metallic plate is placed $500\ \mu\text{m}$ away from the output. In the simulations, the values were recorded at a distance of $495\ \mu\text{m}$ away from the PPWG output. The two black lines almost overlap for gap sizes up to $1500\ \mu\text{m}$. This confirms the assumption of the very low invasiveness of the near-field probe in the experiments. Also, the trend of the experimental curve is confirmed in the simulations.

The transmission enhancement of the PPWG in the experimental system can be evaluated by comparing the detected amplitudes with and without the waveguide. This was done by removing the PPWG from the apparatus and detecting the waveform. The peak-to-peak amplitude is 17.5% of the maximum value measured for a gap size of $p = 500 \mu\text{m}$. This amplitude corresponds to the minimum value that justifies the use of the PPWG in the experiments and is plotted as the green dotted line in Fig. 5.7. Apart from very small gap sizes $p \leq 20 \mu\text{m}$, the use of the PPWG obviously enhances the THz transmission from the ZnTe crystal to the spot where the near-field probe is positioned. In case of the optimum gap size of $500 \mu\text{m}$, the signal is enhanced by a factor of 5.7.

The optimum gap size of $500 \mu\text{m}$ is equal to the incident THz diameter. It has already been discussed earlier that the input coupling efficiency from a Gaussian beam to a *TEM*-mode in the PPWG reaches its maximum exactly for this ratio [254]. However, a comprehensive study on the transmission properties of a THz PPWG as a function of its gap size, including coupling and different loss mechanisms, has not been presented in the literature yet. This is done in the remaining part of this section. Thereby, the transmission characteristic in Fig. 5.7 is divided into two regimes, corresponding to a gap size smaller and bigger than the incident THz beam diameter.

Coupling Coefficient

For gap sizes smaller than the incident THz beam diameter, the energy transfer is primarily determined by the coupling coefficient of the waveguide. This coefficient is calculated in Matlab by the overlap integral, which compares the Gaussian beam electric-field profile with the one of the *TEM* mode inside the PPWG [251, 258]:

$$C_{PPWG} = \frac{\left| \int E_{Gaussian}(x, y) \cdot E_{TEM}^*(x, y) dA \right|}{\sqrt{\int |E_{Gaussian}(x, y)|^2 dA} \cdot \sqrt{\int |E_{TEM}(x, y)|^2 dA}} \quad (5.1)$$

The normalised coupling coefficient as a function of the gap size is plotted as the orange line in Fig. 5.7. The steep increase of this value for gap sizes smaller than $500 \mu\text{m}$ is similar to the change in the detected THz amplitude. In the case of these experiments, the spectral Gaussian beam profile has its central frequency at about 0.7 THz. This means that almost all gap sizes below $500 \mu\text{m}$ are sub-wavelength and only single-mode *TEM* propagation can be expected. This justifies the use of Eq. (5.1) and allows us to accurately estimate the electric-field coupled into the PPWG. For gap sizes much greater than the THz beam diameter, one can imagine that the entire electric-field of the Gaussian beam enters the PPWG and excites

different modes. For this regime, the transmission properties are not governed by the input coupling anymore and one has to consider different phenomena.

Ohmic Losses

The Ohmic losses of the *TEM*-mode inside the PPWG are described by [259, 260]:

$$\alpha_{TEM} = \frac{2 n_{gap} R_s}{Z_0 p} \quad (5.2)$$

Here, Z_0 is the free-space impedance, n_{gap} is the refractive index of the material inside the gap, and $R_s = \sqrt{\pi f \mu / \sigma_{DC}}$ is the surface resistance of the PPWG material. The Ohmic losses obviously play a more important role for smaller gap sizes ($\alpha_{TEM} \propto 1/p$). The absorption coefficient was experimentally determined to be $\alpha_{TEM,Co} = 0.1 \text{ cm}^{-1}$ for a copper PPWG with a gap size of $108 \mu\text{m}$ and a spectral pulse peak at 1.1 THz in Ref. [239]. Based on this value and Eq. 5.2, the Ohmic absorption coefficient for the fabricated PPWG ($f = 0.69 \text{ THz}$, $\frac{\sigma_{DC,Al}}{\sigma_{DC,Co}} = 1.65$, $p = 500 \mu\text{m}$) can be estimated to be about $\alpha_{TEM,Al} = 0.013 \text{ cm}^{-1}$. For the waveguide length of 2.94 cm, the Ohmic losses are less than 4% and, hence, very small. This was also evaluated numerically in CST Microwave Studio. The conductivity of aluminium was set to infinity and the transmitted waveforms were compared to the previous ones using the bulk conductivity σ_{Al} . Thereby, no significant change in the amplitude could be noticed. This means conclusively, that Ohmic losses are the most important loss mechanism for small gap sizes, however, they are sufficiently small to be neglected for the waveguide configuration used in these experiments.

Radiation Leakage for Wider Gaps

For gap sizes greater than the incident THz beam diameter, the decrease in the transmitted THz radiation can be mainly contributed to radiation leakage through the "virtual boundaries" along the waveguide edges. The electric-field is spatially less confined in the space between the plates for larger gap sizes and leakage through the open boundaries is more likely to happen.

The stronger leakage for wider gap sizes can also be explained by ordinary transmission line theory [251]: the impedance of a PPWG is $Z_{PPWG} = 120 \cdot \pi \cdot \frac{p}{w}$ [261]. For small gaps ($p \ll w$), the impedance of the PPWG is much smaller than the one of free-space. The large impedance mismatch between the PPWG gap and free-space prevents the energy from leaking through the boundary. When widening the gap size, the PPWG impedance approaches the one of free-space and

decreases the reflection coefficient at the virtual boundary. For a configuration where p is similar to w or even greater ($p \geq w$), the impact of the metallic plates on the propagating THz wave decreases and the waveguide impedance approaches the value of free-space for $p \gg w$ [237].

The radiation leakage $R_{Leak.}$ was estimated in Microwave Studio by the following integral [237]:

$$R_{Leak.} = 2 \cdot \int_{t_{enter}}^{t_{exit}} \int \int_S |E(x, y, z, t)| dsdt \quad (5.3)$$

The variables t_{enter} and t_{exit} correspond to the moments in time when the THz signal enters and exits the PPWG, respectively. The surface S is a plane which is placed in parallel to the waveguide edges in a distance $100 \mu m$ away from them. The width of the surface is $400 \mu m$ wider than the respective gap size and all the electric-field which "leaks" through this surface is considered as radiation leakage in Eq. (5.3). Since radiation obviously leaks out through both sides of the PPWG gap and given the symmetry of the configuration, the integral is multiplied by a factor of two. The integration of the Poynting vector $\vec{P} = \vec{E} \times \vec{H}$ over the surface S would certainly allow a more precise estimation of the energy leakage. However, the employed software was not able to perform this numerical operation due to the high computational effort.

The integral in Eq. (5.3) is plotted for different gap sizes as the violet line in Fig. 5.7. As expected, the radiation leakage increases for bigger gap sizes. This trend can be explained by two reasons: first, the impedance mismatch between the PPWG and free-space becomes smaller for wider gaps and more radiation leaks out. Second, more radiation couples into the waveguide for wider gap sizes and, consequently, the absolute value of the radiation leakage increases.

Since the evaluation of the absolute value of $R_{Leak.}$ followed an expected trend, it can be more insightful to regard the slope of the violet curve in Fig. 5.7: it shows that the increase/decrease in the radiation leakage is more sensitive to gap size changes when the gap size is small. This can be explained by the change in the reflectivity at the virtual PPWG boundary as the function of the gap size: in accordance with ordinary RF circuit theory, the electric-field reflectivity is determined by $r_{PPWG} = \frac{Z_0 - Z_{PPWG}}{Z_0 + Z_{PPWG}}$ and its derivative as a function of p is $\frac{d}{dp} r_{PPWG} = \text{const.} \cdot \frac{1}{p}$. This explains why a small change in the gap size has a large impact on the radiation leakage at gap sizes considerably smaller than the incident THz beam. This knowledge is of high importance when using PPWGs with sub-wavelength gaps for confined energy guidance.

5.4 Mode Structure in a Parallel Plate Waveguide

In this section, the impact of the gap size on the mode structure within the tapered PPWG is investigated. The waveforms as well as the spectra of the transmitted pulses can give a first indication of mode interference within the waveguide. Therefore, the waveforms were analysed for different gap sizes beginning from a closed configuration ($p = 0 \mu m$) up to $p = 3000 \mu m$. The detected waveforms for three gap sizes, covering distinctive regimes, are shown in Fig. 5.8 (a): the temporally shortest pulse is present for the smallest gap ($p = 100 \mu m$). A strong main oscillation is followed by smaller ones which die out at about $t = 10$ ps. For a gap size of $500 \mu m$, the main pulse appears to be extended up to roughly 8 ps. Also, the small oscillations last up to 15 ps. In case of the widest gap size $p = 2000 \mu m$, a distinct pulse is not noticeable anymore and oscillations with a rather uniform amplitude spread out over the whole duration of the scan.

The spectra for the three detected waveforms also show a distinctive behaviour (dotted lines in 5.8 (c)): for gap sizes $p = 100 \mu m$ and $p = 500 \mu m$, minima can be observed at about 0.6 THz and 0.75 THz, respectively. These features should not be present in a pulse with zero dispersion, as it is expected for the *TEM* mode. A more complex spectrum is visible for the largest gap size which indicates the presence of mode beating.

The waveforms for the three cases were also simulated in CST Microwave Studio and can be seen in Fig. 5.8 (b). It is the advantage of the simulation that these waveforms and the spectra can be directly compared to the incident pulse, which is shown in Fig. 5.8 (d). In case of the smallest gap size, the transmitted waveform appears to be a superposition of two consecutive pulses. The delayed arrival time of one pulse with respect to the earlier one suggests the existence of two modes with a different group velocity. The presence of separate modes is also confirmed in the simulated spectrum where the dip at 0.6 THz is visible more clearly than in the experimental one. This is a distinct indication of destructive mode interference between different modes. For a gap size of $p = 500 \mu m$, the simulated pulse is clearly temporally extended with respect to the incident pulse. However, the envelope of the waveform as well as the spectrum appear to have maintained the Gaussian shape of the incident pulse. This can be explained by two modes interfering in phase with each other. Due to the different modal group velocities, the interference pattern changes even for small differences in the propagation distances. This can explain the difference between the simulated and the measured waveforms if the exact length of the PPWG is not perfectly matched in the simulation. Therefore, the two measured modes are not as perfectly in phase as they are in the simula-

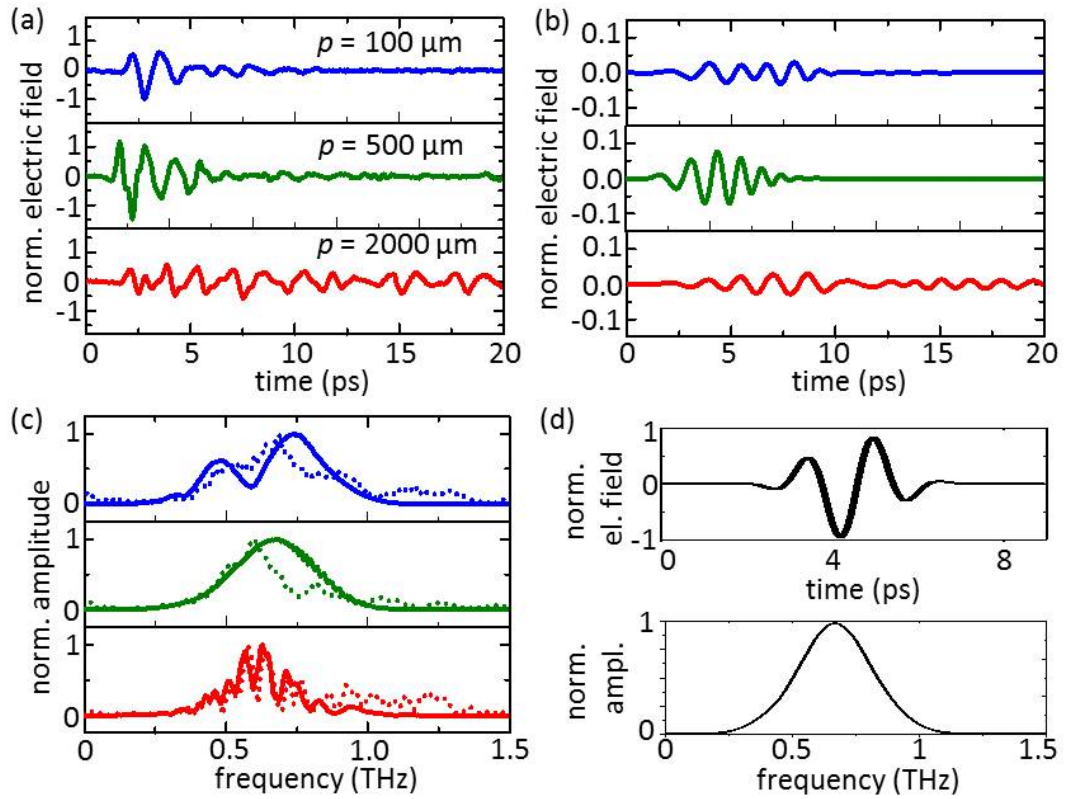


Fig. 5.8: (a) Measured THz pulse waveforms for three different gap sizes p ; the waveforms are normalised to the maximum amplitude at $p = 500 \mu\text{m}$; (b) Simulated waveforms for the same configurations as shown in (a); the waveforms are normalised to the maximum amplitude of the simulated incident THz pulse; (c) Measured (dots) and simulated (lines) spectra of the waveforms in (a, b); the spectra are normalised to their individual maxima; (d) The waveform (top) and the spectrum (bottom) of the simulated incident THz pulse; (Figures (a, b, c) are published in Ref. [237]).

tion. For the widest gap ($p = 2000 \mu\text{m}$), oscillations with a comparable amplitude are present throughout the entire temporal range. This behaviour indicates that the energy is transmitted in several modes. The corresponding spectrum, in this case, is in very good agreement with the experimentally determined one.

The nature of the multi-mode propagation can be examined in more detailed in the numerically computed electric-field distribution inside the PPWG. Figure 5.9 (a) shows the electric-field distribution inside the gap close to the PPWG output in the yz -plane for a gap size of $100 \mu\text{m}$. The straight dark-grey line replicates the plate geometry in the proximity of the PPWG output and the energy propagates in positive z -direction. The existence of two different modes can be clearly seen in this figure. The leading mode, which is framed by a black dashed box, shows a uniform electric-field in the y -direction. This mode can be assigned to the fundamental

TEM -mode because of its electric-field distribution and the highest modal group velocity. The TEM -mode is followed by a different electric-field distribution which is framed by a white dashed box in the figure.

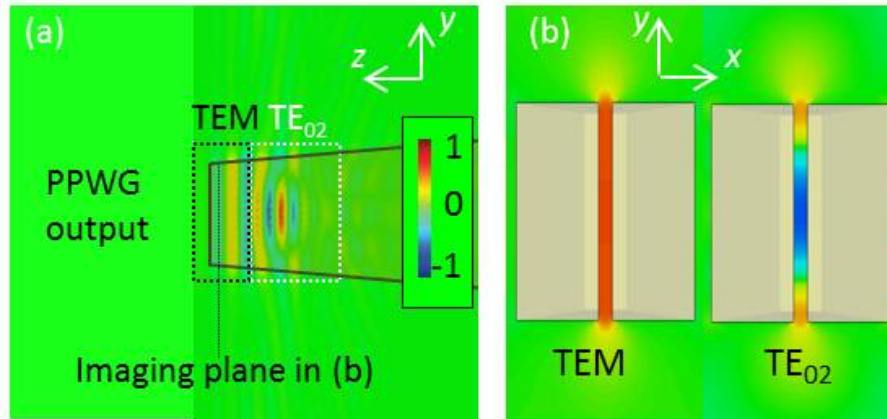


Fig. 5.9: (a) Electric-field distribution inside the PPWG in the yz -plane for a moment in time when the THz pulse is close to the output; (b) Front view of the electric-field distribution in close proximity to the PPWG output; the gap size for (a, b) is $100\ \mu\text{m}$ and all electric-field distributions are normalised to their individual maxima. Both figures are published in Ref. [237].

The two modes can be identified more clearly in Fig. 5.9(b). It shows the electric-field distributions from a front perspective in the xy -plane. The corresponding image plane is $100\ \mu\text{m}$ away from the PPWG output in negative z -direction. The figure on the left side shows the electric-field distribution for the moment in time when the maximum of the leading mode reaches the imaging plane. The uniform electric-field distribution confirms the presence of the TEM -mode. The right hand side of Fig. 5.9(b) shows the electric-field for a later moment in time when the electric-field in the white dashed box reaches the image plane. This distribution has its maximum in the waveguide centre (at $x = 0\ \mu\text{m}$) and exhibits two half-cycles of the electric-field in the y -direction. The electric-field in the x -direction is constant. In accordance with the nomenclature for electric modes in artificial waveguides with artificial boundaries $TE_{m,n}$ [262], this mode is named TE_{02} -mode. In this type of waveguide, the boundary conditions are similar to the one in a PPWG with two metallic and two air boundaries opposite to each other.

5.4.1 The Origin of the Transversal Electric Mode

In PPWGs with sub-wavelength gap sizes, only single-mode TEM propagation is expected. Therefore, it is important to identify the origins of the TE_{02} -mode. A graphical explanation of the excitation of this mode is given in Fig. 5.10. On

the left hand side of this figure, one can see a waveguide with the width w and the electric-field distribution inside the PPWG for two different cases: in the top figure, a tilted TEM -mode propagates inside the waveguide and it is reflected at the top boundary ("diverted TEM -mode"). This boundary corresponds to the "virtual boundary" along the plate edges. In the bottom image, the tilt is rotated in a symmetric manner and the electric-field experiences reflections at the bottom boundary. In both cases, there is also an electric-field which propagates parallel to the boundaries, which is the TEM -mode. Both images describe the electric-field propagation inside the PPWG which exhibits a curved wavefront. While the centre-part of the wavefront can propagate as the TEM -mode, the electric-field closer to the edges has a tilted direction of propagation and, hence, experiences reflections at the PPWG boundaries.

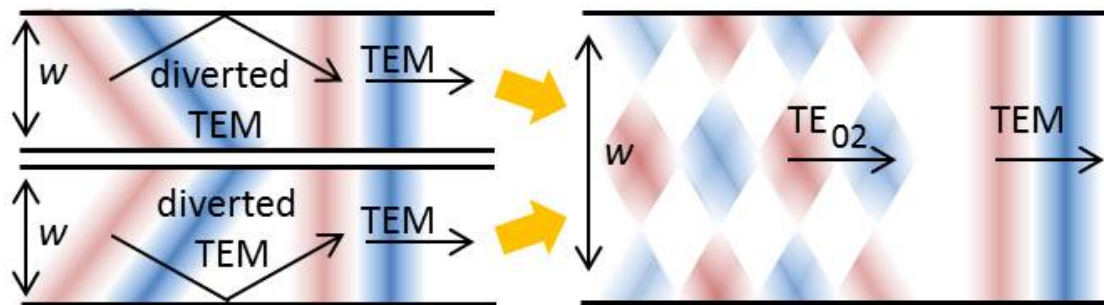


Fig. 5.10: The excitation of the TE_{02} -mode as a result of reflections of the fundamental TEM -mode at the "virtual boundaries" along the waveguide edges.

The resulting mode structure within the PPWG is a superposition of both electric-field distributions depicted on the left hand side. The electric-fields in both figures were overlaid graphically on the right hand side. In this figure, white squares were added whenever a red- and a blue-coded electric-field overlap. This is identical to destructive interference in reality. The resulting electric-field pattern inside the PPWG clearly resembles the one simulated in Fig. 5.9 (a): a part of the energy propagates as the TEM -mode, followed by the TE_{02} -mode.

The excitation of the TE_{02} -mode in Fig. 5.10 was explained on the basis of a THz electric-field with a curved wavefront. In addition to that, a similar situation can occur even for a plane wavefront when the waveguide edges are tilted: in this case, the width w of the PPWG gets adiabatically smaller and the propagating electric-field at the edges is continuously reflected in a direction to the centre of the waveguide. As a result, the excitation of the TE_{02} -mode inside the PPWG can be understood as a process which continuously happens during the time of energy

propagation, rather than a spontaneous mode excitation at the waveguide input.

5.4.2 Practical Implications of Multi-Mode Propagation in Parallel Plate Waveguides

After the existence of different modes is confirmed at this point and their mode structures are identified, it is interesting to discuss the practical implications of this multi-mode behaviour inside the PPWG. The interference of the TEM and the TE_{02} -modes, for example, can lead to unexpected electric-field distributions inside the PPWG. This is shown in Fig. 5.11 for the moment t_1 : the electric-field is partially zero in the waveguide centre and enhanced at its edges. In this case, both modes cancel each other in the centre of the waveguide and interfere constructively at the edges. A similar electric-field distribution was measured in Ref. [131] and explained by the formation of a plasmon-type edge-mode which replaces the TEM -mode at a gap size dependent cut-off frequency. The results in this chapter, however, indicate that the origin of this specific electric-field pattern is attributed to mode interference rather than to the formation of a plasmon edge-mode [237]. For later moments in time, the different modes spatially separate due to their different modal group velocity and the individual modes will be clearly distinguishable, as it is visible in Fig. 5.9 (a).

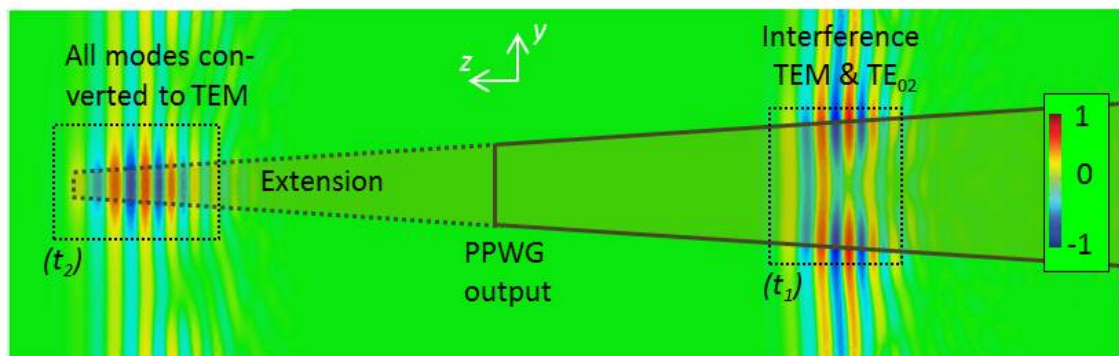


Fig. 5.11: (a) Simulated electric-field distributions for two moments in time t_1 and t_2 inside the waveguide gap ($t_1 < t_2$ and $p = 100 \mu\text{m}$). The straight grey line shows the PPWG geometry covering the final 7 mm of the plate. The dashed grey line shows the extension of the plate to a sub-wavelength width in the simulations. The electric-field distribution for both moments are normalised to their individual maxima.

A further implication of the TE_{02} -mode affects tapered PPWGs with sub-wavelength cross-sectional spatial dimensions. This is unexpected since the TE_{02} -mode runs into cut-off when the plate width reaches a certain threshold. According to rectangular waveguides, the frequency cut-off for this specific mode is given by

$f_{cut-off,TE_{0,n}} = \frac{cn}{2w}$ [261]. In case of the TE_{02} -mode and regarding only the central frequency of the incident pulse at 0.69 THz, the respective mode should run into cut-off for plate widths $w_{cut-off} \leq 400 \mu m$. Since the PPWG was fabricated with an output width larger than $w_{cut-off}$, the electric-field propagation at sub-wavelength sized plate widths could only be investigated numerically. Therefore, the plates lengths were extended in the simulations as it is depicted by the dashed grey line in Fig. 5.11. The plate width at the output was $300 \mu m$ and, hence, smaller than the calculated cut-off width. Although the cut-off frequency is calculated for rectangular waveguides, it could be observed that the TE_{02} mode indeed runs into cut-off at a plate width $w \approx 400 \mu m$.

In the simulations, we note that the side lobes of the TE_{02} -mode leak out through the waveguide edges when approaching the cut-off width. In the centre of the waveguide, the central lobe of the initial TE_{02} -mode propagates further, resulting in an electric-field distribution identical to the TEM -mode. This mode, however, is temporally delayed due to its initially lower group velocity. Therefore, it temporally extends the genuine TEM -mode when arriving at the output. This is the reason for the unexpected dispersive behaviour of the TEM -mode inside the PPWG as it can be observed in Fig. 5.11 for the moment t_2 : although the electric-field distribution in the dashed black box at the very tip of the PPWG appears as a single TEM -mode, it originates from a superposition of two separate modes, the TEM -mode and the TE_{02} -mode.

For the sake of simplicity, effects of mode interference were only explained on the basis of the TEM -mode and the TE_{02} -mode. However, traces of higher-order modes such as the TE_{04} -mode were also found in the simulations which add complexity to the multi-mode interference. But the energy of this mode was sufficiently small to be neglected in the above mentioned considerations.

5.5 Conclusions

In this chapter, the performance of the fabricated tapered PPWG has been evaluated for its later use in the THz near-field detection system. The focus, hereby, has been on the optimisation of the THz energy transfer through the waveguide in order to achieve the strongest THz electric-field strength E^{THz} at the PPWG output. In addition to that, the mode structure within the waveguide has been investigated numerically.

It has been found that the strongest E^{THz} is transmitted when the gap size p between the plates is equal to the incident THz beam diameter. In the case

of these experiments, the respective gap size is $p = 500 \mu\text{m}$. For gap sizes smaller than the incident beam diameter, the THz transmission is limited by the coupling coefficient of the waveguide. The main loss mechanism for gap sizes $p < 500 \mu\text{m}$ is Ohmic loss. In the case of this PPWG, however, the estimated Ohmic losses attenuate the transmitted pulse by less than 4% and, therefore, can be considered to be very small. For gap sizes larger than the incident THz beam diameter, the main loss mechanism is radiation leakage. Radiation leakage occurs due to the smaller impedance mismatch between the PPWG and free-space for wider gap sizes.

Using numerical simulations and analysing the measured transmission spectra through the PPWG, it has been shown that higher-order $TE_{0,n}$ -modes exist within the tapered PPWG. This is essential for the understanding of energy transfer through a PPWG, where single-mode TEM -mode propagation is often assumed. The excitation of the higher-order modes is mainly explained by multiple reflections at the virtual boundaries at the waveguide plate edges. In the presented experiments, this effect has been enhanced due to the curved wavefront of the propagating THz wave and due to the tapered PPWG configuration. In the context of THz near-field detection system using the electro-optic probe, it is essential to know the existence of higher-order modes in the fabricated PPWG. The correct interpretation of the transmitted THz waveforms in the experiments, otherwise, would barely be possible.

6 Electro-optic Detection with a Micro-Resonator

This chapter introduces the experimental system which was developed for the detection of a THz electric-field using the electro-optic micro-resonator. It describes in detail how the detection scheme translates the induced electro-optic phase-shift into a voltage that can be measured by a detection unit. It also presents the home-built balanced detector which is the key element of the detection unit. The measurement of the system noise level gives an estimation of the minimum phase-shift that can be detected. The estimation of the generated E^{THz} in the system leads to a discussion about the limitations of this experimental detection system.

6.1 The Electro-optic Detection System

A schematic diagram of the experimental electro-optic detection system is shown in Fig. 6.1. The electro-optic micro-resonator is positioned directly at the PPWG output. Preliminary simulations in Microwave Studio have shown that this ensures the most efficient coupling of THz energy from the PPWG into the micro-resonator. In this configuration, the E^{THz} experiences only one impedance change from Z_{PPWG} to Z_{MR} . As a result, less energy is reflected back into the waveguide and a stronger E^{THz} is present in the micro-resonator. When inserting the probe into the PPWG gap or when leaving a small air gap between the PPWG output and the probe, the E^{THz} has to pass through two interfaces with an impedance change. As a result, more THz energy gets reflected back into the waveguide and does not contribute to the electro-optic effect.

The E^{THz} transmitted through the waveguide is polarised in the x -direction. Therefore, the DBR-layers are oriented in the yz -plane and the probe beam is propagating in the x -direction, as depicted in Fig. 6.1. The probe beam is focused as close as experimentally possible to the PPWG output since the strongest E^{THz} is expected in the proximity of the output. For points further away from the output, the THz energy diverges and E^{THz} becomes smaller (see Fig. 5.4 (b)).

The employed light source is the Spectra-Physics Tsunami mode-locked Ti:Sapphire laser with a repetition frequency of 80 MHz and an average output power of 500 mW. The laser was tuned to pulse at a central wavelength of $\lambda = 940$ nm. The Gaussian-shaped intensity distribution of the laser pulse was determined by the fibre-coupled laser spectrum analyser from the company IST. The FWHM of the

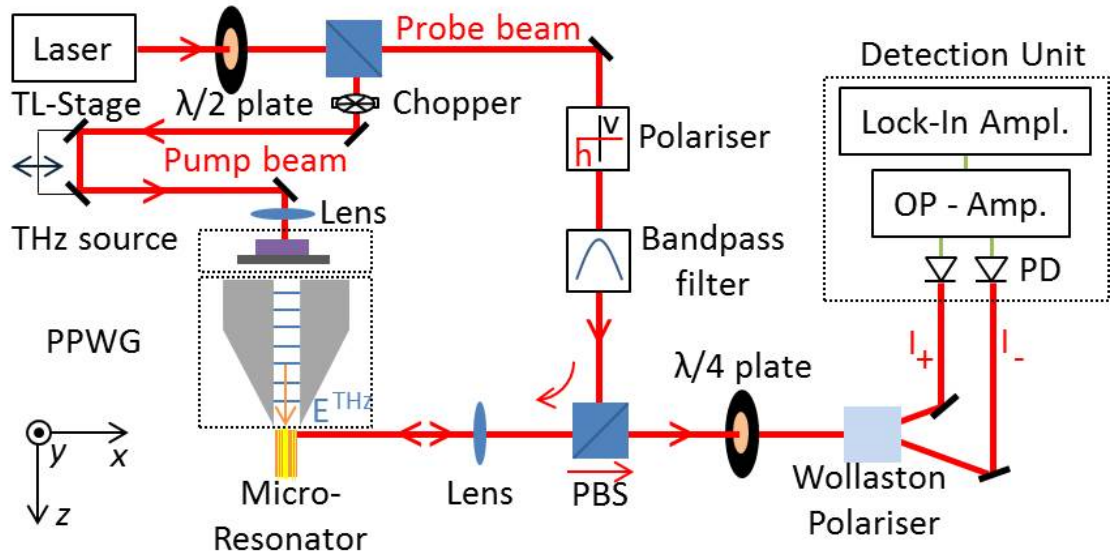


Fig. 6.1: A schematic diagram of the electro-optic detection system used in the experiments (TL-stage stands for translation stage, PBS for polarising beam splitter, PD for photodiode, Op-Amp for operational amplifier, Lock-In Ampl. for Lock-In amplifier).

measured intensity profile is 13 nm. This corresponds to a pulse width of ≈ 100 fs assuming a transform-limited Gaussian pulse. The laser beam is directed to a polarising beam splitter, which separates the beam into a probe and a pump beam. The probe beam is polarised vertically (in the y -direction) with respect to the plane of the optical table. Consequently, the pump beam is polarised in the x -direction in Fig. 6.1. A $\lambda/2$ -waveplate (Thorlabs, WPMH05M-980) in front of the polarising beam splitter allows adjusting the power ratio between the two beam paths.

The pump beam is directed through a mechanical chopper with a chopping frequency of 1.3 kHz and through a mechanical translation stage to allow time-resolved signal detection. The smallest mechanical step size given by the translation stage determines the shortest temporal sampling interval of 6.6 fs. The pump beam is then focused on a 1 mm-thick non-linear ZnTe source to generate THz pulses. This crystal is mounted on a 500 μ m-thick piece of silicon to block the optical beam and to allow only the THz pulse to propagate further.

The probe beam is directed through a Glan-Thompson polariser (New Focus, 5525) with an extinction ratio of $10^5 : 1$ in favour of the vertical polarisation. This defines the reference polarisation for the electro-optic phase-shift measurements in the probe beam path. The beam then passes through a bandpass filter with a central wavelength of 940 nm and a FWHM of 10 nm. This cuts off parts of the frequency components which do not enter the micro-resonator and, hence, are not modulated by the THz field. A polarising beam splitter (Spectra Physics,

10FC16PB.5, $T_p : T_s = 1000 : 1 = \alpha_{PBS}^2$) deflects the incident beam with a vertical polarisation and directs it to a lens (focal length 7.5 cm). The lens focuses the beam onto the front surface of the micro-resonator to a focal spot with a diameter of 30 μm (according to its intensity FWHM). To measure the spot size, the micro-resonator was moved out of the beam focus in the positive z -direction with a micrometer control translation stage. As a result, a portion of the probe beam passes by the micro-resonator without being reflected. The intensity of the beam passing the micro-resonator was measured as a function of the micro-resonator movement. This allows an accurate estimation of the beam spot diameter. Regarding the phase-shift measurements, it is essential that the focal beam spot is significantly smaller than the THz wavelength. Otherwise, the induced phase-shift in the probe beam would be cancelled due to the opposite polarity along a THz wavelength.

The probe beam is partially reflected back into the system after it has experienced the electro-optic phase shift. It passes through the PBS and a zero-order $\lambda/4$ -waveplate (Newport, 10RP44-3) with a very uniform phase-retardance for a range from 715 nm to 1000 nm. Its orthogonal electric-field components are then spatially divided by a Wollaston polariser (CVI Melles Griot, WLST-20.0-CA-670-1064). The electro-optic phase-shift is thereby translated into an intensity difference between the two beams exiting the polariser. The translation of the physical phase-shift into an electrical signal is the key point in this detection system and will be explained in detail in the following subsection. In addition to that, the three most important functional units are discussed in separate sections. These units are highlighted by the dashed black boxes in Fig. 6.1. One of these units is the THz source. It determines the E^{THz} strength in the experimental system and, hence, the expected electro-optic phase-shift. As a second point, the detection unit, determines the noise floor of the system and allows an estimation of the smallest detectable phase-shift. The characterisation of the third functional unit, the PPWG, was performed in such an extent that it was devoted a separate chapter in this thesis (see Chapter 5).

6.1.1 The Detection of the Electro-Optic Phase-Shift

The translation of the electro-optic phase-shift into an intensity difference in the two beam exiting the Wollaston polariser is explained in Fig. 6.2. The four optical elements which change the polarisation state of the probe beam are shown in the top row. The alignment of the optical components is done similar to the electro-optic detection system suggested in Ref. [263]. Initially, the probe beam is linearly polarised in the y -direction before it is incident to the electro-optic micro-resonator.

The linear polarisation is then decomposed into two orthogonal polarisations with equal intensities when entering the electro-optic probe. Due to the electro-optic effect, the two principle axes of the probe are oriented by 45° with respect to the coordinate system. The difference in the refractive indices along the principle axes causes one of the polarisations to exit the resonator temporally delayed with respect to the other polarisation. This temporal delay corresponds to the induced electro-optic phase-shift ϕ_{eo} . The initially linear polarisation thereby changes into a slightly elliptical one.

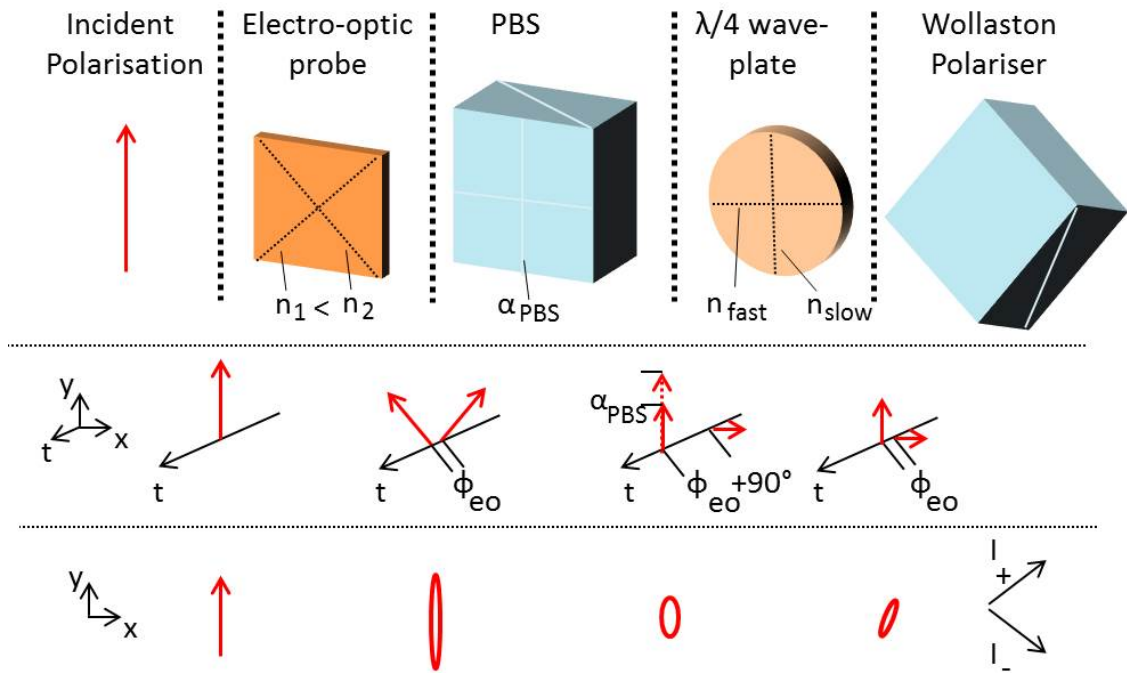


Fig. 6.2: The top row shows the orientation of the incident probe beam polarisation and the optical elements it has to pass sequentially. The middle row decomposes the polarisation of the probe beam along the principle axes and shows the resulting polarisations on a time axes after passing a specific optical element. The bottom row shows the polarisation state of the probe beam after passing a specific optical element.

The principle axes of the PBS are oriented along the x - and the y -directions. As a result, the electric-field components along the two orthogonal polarisations are realigned when entering the PBS. The components in the y -direction, thereby, add constructively. The components in the x -direction, on the contrary, are out-of-phase and add destructively. The subtraction of two electric-field components with a small phase-delay ($\sin(\omega t - \frac{\phi_{eo}}{2}) - \sin(\omega t + \frac{\phi_{eo}}{2}) = \text{const.} \cdot \sin(\omega t + 90^\circ)$) causes an 90° phase-shift with respect to the initial polarisation. When propagating through the PBS, the major part of the vertically polarised light gets reflected and only a small portion passes through this optical element. The splitting ratio of the

reflected to the transmitted vertical electric-field components is determined by the attenuation α_{PBS} . The x -polarised electric-field component, on the other hand, passes through the PBS without being reflected. As a result, the polarisation of the beam exiting the PBS is elliptical as it is depicted in the image. But different from the elliptical polarisation before entering the PBS, this polarisation state is closer to being circular polarised than linear.

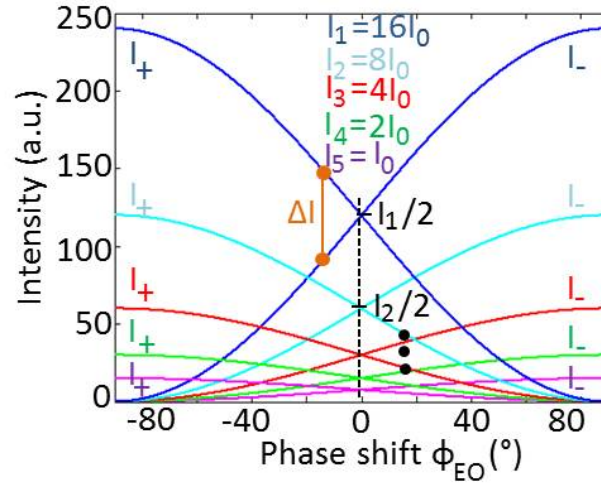


Fig. 6.3: The intensity in both beam paths I_+ and I_- when exiting the Wollaston polariser as a function of the phase-shift ϕ_{EO} for five different input intensities $2^n \cdot I_0$; The difference $\Delta I = I_+ - I_-$ is shown by the orange line.

The $\frac{\lambda}{4}$ -waveplate removes the additional 90° phase-shift which was introduced in the PBS. The Wollaston polariser then splits the incoming beam into two spatially separated beams. A graphical explanation of the intensity distribution in both beam paths I_\pm is given in Fig. 6.3. One can see the light intensities in both beams I_\pm as a function of the electro-optic phase-shift. The change in intensities thereby follows the typical intensity distribution of a Wollaston polariser: while the intensity in the I_+ -beam path follows a $\sin^2(\pi/4 + \phi_{EO})$ -function, the intensity in the I_- -beam path follows a $\cos^2(\pi/4 + \phi_{EO})$ -function. As a consequence, the intensities in both paths are equal for a zero electro-optic phase-shift. As soon as a phase-shift is induced, the intensities in both arms are different by $\Delta I = I_+ - I_-$ (orange line in Fig. 6.3). It has to be noted that the phase-shift ϕ_{EO} is expected to be in the order of 10^{-6} - 10^{-5} and that the induced intensity difference in the figure is highly exaggerated. For the expected order of magnitude, the small-angle approximation is valid and the slope of the I_\pm -curves can be considered to be constant. Consequently, there is a linear relation between the intensity difference and the electro-optic phase-shift ($\Delta I = \text{const.} \cdot \phi_{EO}$). Also, one can see that the intensity difference ΔI is obviously greater for higher input intensities I_0 ($\Delta I \propto I_0$).

The Advantage of this Detection Scheme

The detection scheme shown in Fig. 6.2 linearly translates the electro-optic phase-shift ϕ_{eo} into an intensity difference ΔI . This intensity difference can be detected by two photodiodes. Consequently, this detection scheme allows a straight-forward estimation of the E^{THz} strength measured in the experiments. A beneficial feature of this specific detection system, however, has not been mentioned yet: the use of the PBS in the detection scheme enhances the signal-to-noise ratio (SNR) in the experiments. This can be explained by applying the Jones Matrix formalism [264] to the detection scheme. This formalism allows the calculation of the probe beam polarisation state after passing through each optical component along the beam path. The intensities I_{\pm} can be calculated to [263]:

$$I_{\pm} = \frac{1}{2}\alpha_{PBS}I_0(\alpha_{PBS} \pm \phi_{EO}) = \frac{1}{2}\alpha_{PBS}^2I_0 \pm \frac{1}{2}\alpha_{PBS}I_0\phi_{EO} \quad (6.1)$$

The value I_0 is the probe beam intensity which is incident to the PBS after it is reflected back from the micro-resonator. The detected light in both paths I_{\pm} obviously contains two different parts: first, an intensity carrying no information about the electro-optic phase-shift ($\frac{1}{2}\alpha_{PBS}^2 \cdot I_0$). This part is from now on called "unmodulated light". Second, an intensity which carries information about the electro-optic phase-shift ($\frac{1}{2}\alpha_{PBS}I_0\phi_{EO}$) and which is called "modulated light". The idea of this specific detection system is that unmodulated light is attenuated by a factor of α_{PBS}^2 , while modulated light is attenuated only by α_{PBS} . At this point, it has to be noted that laser intensity fluctuation is a major noise source in the detection system. The induced intensity noise is directly proportional to the incident light intensity. Consequently, the detection noise caused by laser intensity fluctuations is reduced by a factor of α compared to the signal. This corresponds to an increase of the SNR by the same factor α_{PBS} [263]. This holds true for detection systems that are limited by the laser intensity noise.

Figure 6.3 also allows a graphical interpretation of the two terms in Eq. (6.1). For a zero electro-optic phase-shift, the intensities in both beam paths are equal to half of the probe beam intensity ($I_{\pm} = I_1/2, I_2/2, \dots$). This "offset" corresponds to the unmodulated intensity in Eq. (6.1) and it only contributes to the intensity noise in the detection system. As soon as an electro-optic phase-shift is induced, the intensities in both arms change according to the value $\frac{1}{2}\alpha_{PBS}I_0\phi_{EO}$. As already mentioned earlier, the intensity difference due to the electro-optic phase-shift is very small compared to the I_0 ($\Delta I \ll I_0/2$) and, consequently, both beam paths almost exclusively consist of unmodulated light.

Practical Implications of the Experiments

In an ideal case, the PBS attenuates the intensity in the vertical polarisation by a factor α_{PBS} similar to the order of the electro-optic phase-shift ϕ_{EO} . In this case, the electric-field components in the vertical and the horizontal polarisations would have the same amplitude. Hence, the detection system would be perfectly balanced with equal intensities in each beam path I_+ and I_- . In reality, the value α_{PBS} depends on the manufacturer and, what is more important, it can not be varied during the experiment for a fixed probe beam wavelength and alignment of the detection system. For a wavelength of $\lambda = 940 \text{ nm}$, for example, an attenuation factor of $\alpha_{PBS}^2 = 390^{-1}$ was measured.

To compensate for the offset in the value α_{PBS} , the orientation of the $\lambda/4$ -waveplate can be varied during the experiments. This plate is mounted in a rotational stage with micrometer-level rotation control, which allows a very accurate alignment of the principle axes orientation in the yz -plane. Altering the orientation of the waveplate changes the intensities in both optical beam paths I_+ and I_- . As a consequence, the level of balancing can be adjusted manually if necessary. A theoretical proof of this statement can be found in Appendix F. It is, from an experimental aspect, more beneficial to vary only the orientation of the $\lambda/4$ -waveplate and to keep the Wollaston polariser in the same position. The orientation of the Wollaston polariser also determines the angles of refraction for the two optical beams. The orientation of the optical beam paths should not change during the experiments. Therefore, it is experimentally less tedious to change only the orientation of the $\lambda/4$ -waveplate instead of the Wollaston polariser.

6.2 The Balanced Detector

As explained in the previous section, mainly unmodulated light exits the Wollaston polariser and only a very small intensity carries the information about the E^{THz} . It is the task of the detection unit to eliminate the unmodulated light and to enhance the intensity difference induced by the electro-optic phase-shift. This can be realised using a balanced detection scheme. An ideal balanced detector subtracts the equal intensities in both beam paths and only detects the intensity difference ΔI . As a consequence, the unmodulated light in both beam paths is cancelled out and the detected electrical signal is a linear function of ϕ_{EO} (Eq. (6.1)).

The balanced detector in this work is home-built and consists of a detector-stage and a transimpedance-stage (Fig. 6.4 (a)). The Silicon photodiodes NT54-522 from Edmund Optics were chosen due to their long integration time and low noise

response. The anodes and the cathodes of the photodiodes in the detection-stage are mounted in a reversed fashion, which means that the generated photocurrents cancel each other. The response of the photodiodes for a wavelength of 940 nm is $Response_{PD} = 0.65\text{ A/W}$, the junction capacitance $C_{PD} = 87\text{ pF}$, and the shunt resistance $R_{PD} = 600\text{ M}\Omega$. The saturation current is 0.51 mA , which corresponds to a maximum optical input power of $P_{opt} = 0.78\text{ mW}$ at 940 nm . The photodiodes were operated in an unbiased state in order to generate a smaller amount of dark current.

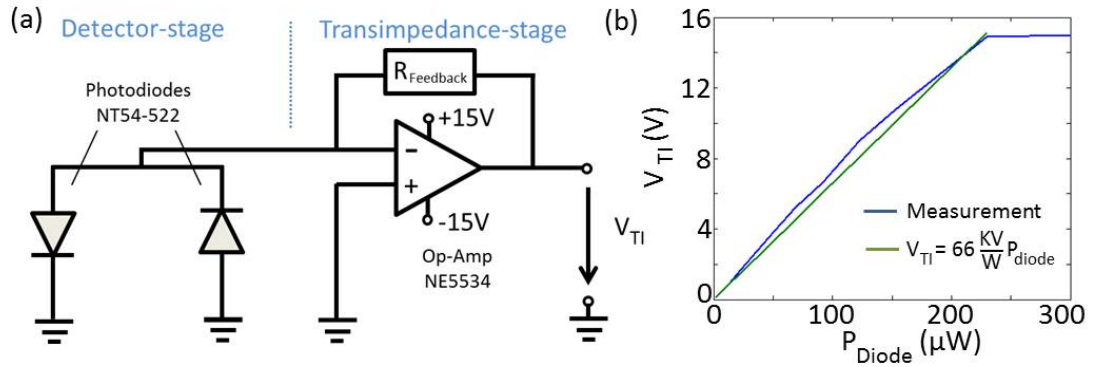


Fig. 6.4: (a) Electric circuit diagram of the balanced detector; (b) Measured and calculated response of the balanced detector.

A current-to-voltage amplifier is required for converting the generated photocurrent into a voltage. Transimpedance amplifiers are commonly used for this purpose. This amplifier is a device with a low-impedance at its input and output. A low-impedance input is necessary to provide a low-ohmic load to the photodiodes. This results in a faster response time and the virtual ground at its input keeps the photodiode voltage close to zero. The two central elements of the transimpedance amplifier are the feedback resistor $R_{Feedback}$ and the operational amplifier (OpAmp). The feedback resistor determines the ratio of the output voltage V_{TI} to the incident current i_{In} ($V_{TI} = -R_{Feedback} \cdot i_{in}$). This allows the calculation of the overall amplification factor of the balanced detector A_{BD} , which is a combination of the photodiodes and the transimpedance stage: $A_{BD} = Response_{PD} \cdot R_{Feedback}$.

Two points have to be taken into account when selecting a suitable resistance for the $R_{Feedback}$: first, it is necessary to consider the voltage output range $V_{TI,min}$ to $V_{TI,max}$ of the OpAmp. This is given by its supply voltage and ranges from -15V to $+15\text{V}$. Second, one has to consider the highest possible input intensities in the beam paths I_+ and I_- for the configuration presented in Fig. 6.1. This was measured to be $P_{PD,max} = 125\text{ }\mu\text{W}$. According to these data, a feedback resistor with $R_{Feedback} = 100\text{ k}\Omega$ was chosen. In this case, the balanced detector amplification

is $A_{BD} = 66 \frac{kV}{W}$ and the highest expectable voltage at the transimpedance amplifier output can be calculated to be $V_{TI} = A_{BD} \cdot P_{PD,max} = 8.25 V$. This guarantees a wide detection range and output voltages sufficiently away from the saturation voltage of the OpAmp. In addition to that, the choice of a very high feedback resistance improves the SNR of the balanced detector. The thermal voltage noise of a resistor is given by $\bar{v}_{RMS} = \sqrt{4kTRB}$, while the voltage output of a transimpedance amplifier V_{TI} is directly proportional to $R_{feedback}$. As a consequence, the SNR increases by a value of $\sqrt{R_{Feedback}}$. The response of the balanced detector was also measured experimentally by detecting the output voltage as a function of P_{PD} . For this measurement, light was incident to only one photodiode and the intensities of both beam paths were combined in this beam path. This was possible by rotating the $\lambda/4$ -waveplate as discussed earlier. The response is a linearly increasing function with a slope corresponding to A_{BD} , as shown in Fig. 6.4 (b).

The low-noise operational amplifier NE5534A from Texas Instruments was selected as OpAmp because of its optimised low-noise performance. This OpAmp has a unity gain bandwidth up to 10 MHz and, therefore, imposes no restrictions on the response time. The voltage V_{TI} is measured by a lock-in amplifier at a chopping frequency of 1.3 kHz and an integration time of 300 ms and recorded by a LabView program.

6.2.1 Level of Balancing

Perfect balancing of the two intensities I_+ and I_- is experimentally hardly feasible. The intensities in both beams can always be slightly different due to, for example, polarisation noise in the laser, dichroism, or statistical processes such as water absorption. As a consequence, the unmodulated intensities in both beam paths are not exactly $\frac{I_0}{2} \alpha_{PBS}^2$ (Eq. 6.1), but rather two different values $I_1 \alpha_{PBS}^2$ and $I_2 \alpha_{PBS}^2$ with I_1 and I_2 slightly deviating from $\frac{I_0}{2}$. Balancing the unmodulated light, therefore, still leads to a residual term $\alpha_{PBS}^2 \cdot (I_1 - I_2)$. The difference in the brackets ($I_1 - I_2$) is from now on called unbalanced intensity $I_{unbal.}$. For a successful detection of the electro-optic phase-shift, the noise due to the unbalanced intensity must be smaller than the modulated intensity ΔI :

$$\begin{aligned} \alpha_{PBS}^2 I_{unbal.} &< \alpha_{PBS} I_0 \phi_{EO} \Leftrightarrow \\ \frac{\alpha_{PBS} I_{unbal.}}{I_0} &< \phi_{EO} \Leftrightarrow \\ \frac{I_{noise}}{I_0} &< \phi_{EO} \end{aligned} \quad (6.2)$$

The intensity I_{noise} in this equation is the unbalanced intensity $I_{unbal.}$ which is attenuated by a factor α_{PBS} . This is due to the specific geometry of the detection system, as describes earlier. The last line of Eq. (6.2) imposes an upper limit on the ratio between the noise level I_{noise} and the input intensity I_0 . This ratio is now defined as the "level of balancing" of the detection system. Since ϕ_{EO} is expected to be very small, the input intensity has to be balanced to a degree of 10^{-5} - 10^{-6} . This sets very high requirements to the detection system. But before presenting the experimentally measured level of balancing and the detection system noise level, it is important to understand the different noise sources of the detection system.

Noise Considerations

There are three major noise sources present in the detection system. The first type of noise is independent of the optical input intensity. It is present in the detection system even for zero input intensity and determines the fundamental noise floor of the detection system. This noise, for example, can occur due to dark noise. It appears in all diodes and can be explained by the random generation of electrons and holes in the depletion region of a semiconductor interface. This type of noise, however, is only important at very low input intensities and, hence, can be neglected throughout the following measurements.

The second type of noise is shot noise. It occurs when charge carriers cross a potential barrier. This process is of statistical nature due to the Boltzman-distributed energy levels of charge carriers. In photodiodes, as they are used in the detection system, this noise occurs at the pn-interface. The mean square shot noise current \bar{i}_{SN}^2 is proportional to the accompanying photocurrent i_{PD} :

$$\bar{i}_{shot\ noise}^2 = \Delta f \cdot q \cdot \bar{i}_{PD} \quad (6.3)$$

The variable Δf represent the detection bandwidth and q is the elementary charge. Due to the linear relationship between the photodiode current and the input intensity, shot noise is proportional to the square-root of I_0 ($\bar{i}_{shot\ noise} \propto I_0$).

The third type of noise is laser noise. It appears due to small intensity variations of the laser and is the only correlated noise source in both beam paths I_{\pm} . In case of an insufficient balancing, these intensity fluctuations translate directly into voltage fluctuations at the transimpedance amplifier output. Due to the linear relationship between the input intensity and the generated photocurrent, the laser noise is directly proportional to the input intensity $\bar{i}_{LN}^2 \propto I_0^2$. If these fluctuations generate a voltage amplitude which is greater than the one caused by the electro-

optic effect, the THz signal is hidden in the noise and can not be detected. This makes intensity noise the major noise source in the employed detection system.

In case of a sufficiently balanced detector, the level of balancing is high enough so that laser noise can be neglected. In this case, the detection system is limited by shot-noise. As described in this section, shot-noise is a statistical process inherent to diodes and, hence, appears uncorrelated in both photodiodes. Therefore, this type of noise cannot be cancelled and defines the noise floor of this experimental detection system. In case of a shot-noise limited system, the SNR of the detection system increases for higher intensity due to the square-root relationship of the shot-noise current to the incident intensity (Eq. (6.3)).

Determination of Noise Floor and Level of Balancing

The noise level of the detection system is measured under exactly the same experimental conditions as they appear in the electro-optic measurements (Fig. 6.1), but without the E^{THz} being present. This can be achieved by running a scan at a moment in time, at which the E^{THz} arrives at the electro-optic micro-resonator after the probing pulse has already exited the probe. For this situation, the electro-optic detection system can be kept in its initial state and only the mechanical translation stage needs to be operated. In a preceding measurement, the exact time delay between the E^{THz} and the probe beam was determined by using the integrated near-field probe instead of the micro-resonator.

In the noise measurements, the intensities in both beam paths I_+ and I_- were increased from $0 \mu W$ (noise of the detector) to the maximum of $P_{PD,max} = 125 \mu W$. For each optical power level, the level of balancing was optimised by realigning the $\lambda/4$ -waveplate. The noise was recorded by the lock-in amplifier over a period of 12 minutes with a sampling interval of 1 s, giving 721 sampling points per scan. The option of a phase-sensitive lock-in measurement was selected (X Measurement) as it will be the case in later experiments. Since noise is distributed equally over all phases, an arbitrary value for the phase could be chosen. The recorded voltage noise values were then processed by removing the offset and calculating the \bar{v}_{RMS} -values for each input power.

Figure 6.5 (a) shows the detected X_{RMS} for different input powers. One can identify the noise floor of the system ($v_{RMS,system}$) when no light is incident. This relates to the signal independent noise as explained earlier. The theoretical shot noise level of the combined photodetectors was also calculated according to Eq. (6.3), assuming a detection bandwidth of the lock-in amplifier of $0.8 Hz$ ($\tau_{LI} = 300 ms$). The shot noise is added to the figure with an offset that corresponds to $v_{RMS,system}$.

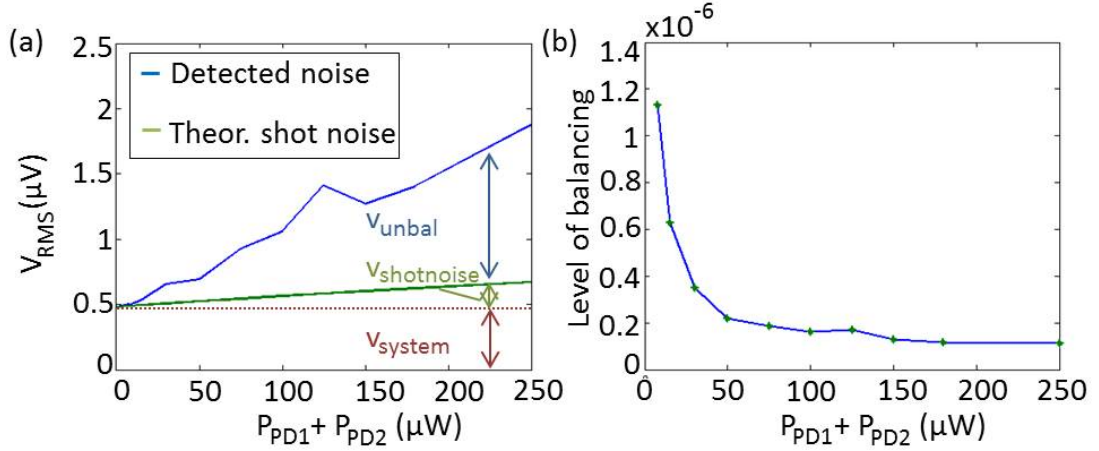


Fig. 6.5: (a) Detected X_{RMS} and calculated shot-noise level as a function of the optical power incident to both photodiodes $P_{PD1} + P_{PD2}$; (b) Calculated level of balancing of the as a function of the incident power. The green stars show the measurement points.

The detected noise level increases as a straight line for higher input powers, except for a small pike at $125 \mu m$. The figure shows that the detection system obviously is not shot noise limited, however, the detected noise floor noise is close to the theoretical shot noise limit of the experimental system.

The calculated level of balancing can be seen in Fig. 6.5 (b). The balanced detector obviously shows a better performance for higher input powers. Beginning from $P_{PD1} + P_{PD2} > 50 \mu W$, the level of balancing reaches a level of about $0.2 \cdot 10^{-6}$ (for a lock-in amplifier integration time of $300 ms$). This value determines the smallest detectable phase-shift $\phi_{eo,min}$. According to Eq. (3.10) and using an effective cavity length of $l_{eff} = 8 \mu m$ (\approx resonator thickness * electro-optic enhancement) and an average refractive index of $n_{av.} = 3.3$, one can calculate the minimum electric-field strength E_{min}^{THz} which is necessary to detect a THz signal:

$$E_{min}^{THz} > \frac{\phi_{eo,min} \cdot \lambda}{\pi \cdot n_{av.}^3 \cdot r_{eo} \cdot l_{eff.}} \approx 150 \frac{V}{m} \quad (6.4)$$

6.3 The Terahertz Source

Since the noise floor of the detection system has been measured, it is now important to know whether or not the generated E^{THz} is strong enough to induce a sufficient electro-optic phase-shift. Therefore, the mechanism of optical rectification is explained in detail and the expected E^{THz} is estimated.

6.3.1 Optical Rectification in the Non-Linear Crystal ZnTe

Optical rectification is a second-order non-linear optical effect and is closely related to the Pockels effect described in Chapter 3. It relies on the interaction of the electric-field of an optical beam $E^{opt.}$ with a non-linear dielectric. A particularly strong electric-field $E^{opt.}(\omega)$ induces large electron displacements in the dielectric. In crystals with an asymmetric charge distribution, the electrons do not follow the oscillation of the external electric-field in a linear manner. As a result, the temporal evolution of the electron motion in the crystal can be decomposed in a linear and a non-linear part. The non-linear part consists of two frequency components: A DC-part $E(\omega = 0)$ ("Rectification") and one with double frequency $E(2\omega)$ ("Second Harmonic Generation").

In case of an incident optical pulse $E^{opt.}(t) = E_0 e^{-(t/\tau_{pulse})^2} \cos(\omega t)$ with a pulse duration τ_{pulse} much longer than the optical frequency ($1/\tau_{pulse} \ll \omega$), the induced rectified non-linear polarisation in the medium replicates the incident pulse envelope (Fig. 6.6 (a)). The time-varying polarisation of the medium acts as a source of electro-magnetic radiation. The generated THz waveform is similar to the second temporal derivative ($\frac{\partial^2}{\partial t^2}$) of the incident pulse envelope (Fig. 6.6 (a)) [99] and its amplitude is directly proportional to the square of the incident electric field ($E^{THz}(t) \propto |E^{opt.}(t)|^2$) [55]. The spectral bandwidth of the generated radiation is roughly the inverse of the optical pulse duration (Fig. 6.6 (b)). Hence, it is possible to generate ultrashort THz pulses using sub-ps optical pulses.

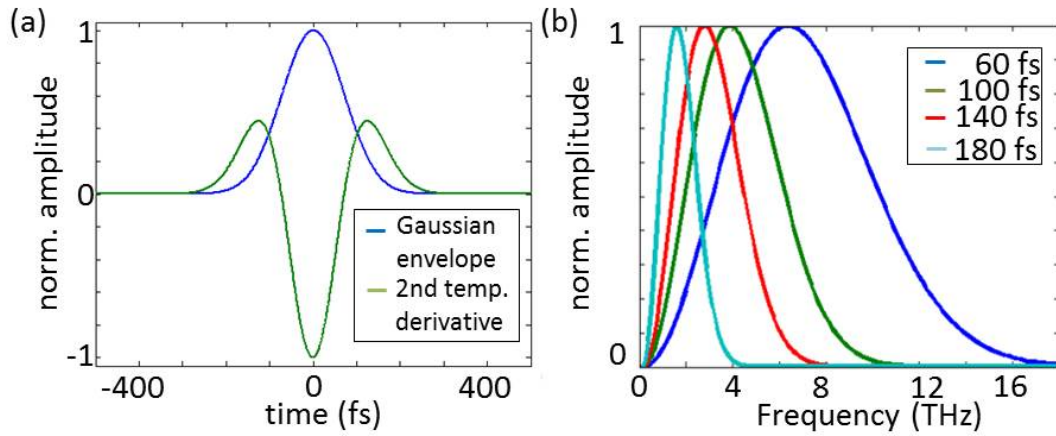


Fig. 6.6: (a) Envelope of an optical pump pulse with a FWHM of 120fs and its second temporal derivative, which corresponds to the generated E^{THz} waveform; (b) Spectra of THz pulses generated by optical pulses with different FWHMs (related to the intensity).

A (110)-cut ZnTe crystal with a thickness of 1 mm is employed as the non-linear material. The process of rectification as it was explained above is only valid

for the ideal case of a dispersion-less material. Without dispersion, the optical and the THz pulse would propagate co-linearly with the same velocity and the THz pulse gets constantly amplified. In reality, dispersion causes two unwanted effects: first, the pulses themselves are dispersed due to their inherent broadband character. In addition to that, the THz and the optical pulses are separated by about 500 THz in the spectrum. For optimal phase matching, the optical pulse envelope needs to travel at the same velocity as the respective THz components. Therefore, the following condition has to be fulfilled:

$$n_{gr.}^{opt.} = n_{THz} \quad (6.5)$$

The variable $n_{gr.}^{opt.}(\lambda) = c/v_{gr.} = n_{opt.}(\lambda) - \lambda \frac{dn_{opt.}}{d\lambda}$ is the group velocity of the optical beam. To visualise the refractive index mismatch, Fig. 6.7 shows the THz refractive index $n(f_{THz})$ and the group refractive index for the optical pump beam $n_{gr.}^{opt.}$. The formula for the refractive indices are taken from Ref. [55]. The semi-transparent yellow rectangle highlights the regions of interest in the THz range (0-1.63 THz for the fabricated resonator) and the red one depicts the range of interest for the optical pump pulse ($\lambda = 940 \text{ nm} \pm 10 \text{ nm}$).

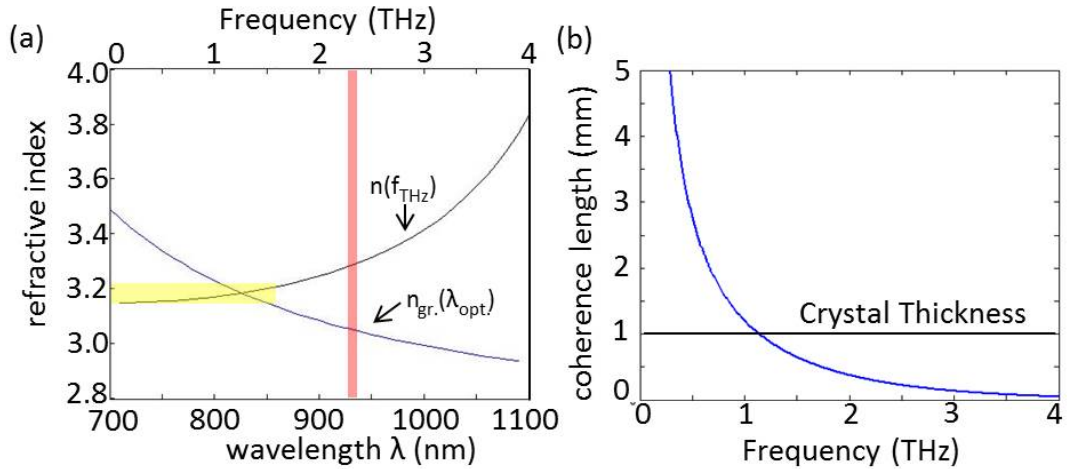


Fig. 6.7: (a) The refractive index $n(f_{THz})$ and the group refractive index $n_{gr.}(\lambda_{opt.})$ as a function of the optical wavelength and THz frequency); (b) The coherence length for ZnTe as a function of the THz frequency.

A physical parameter which quantifies this mismatch is the coherence length l_c . It is the length the optical pulse needs to propagate before it lags or leads the THz wave by a $\pi/2$ phase-shift. Beginning from l_c , the optical beam generates an electric-field which is out-of-phase to the one that is already present. These fields interfere destructively and the E^{THz} is reduced. The coherence length can

be calculated by [265]:

$$l_c = \frac{c}{2 \cdot f_{THz} |n_{gr.}^{opt.} - n^{THz}|} \quad (6.6)$$

The coherence length for an optical beam ($\lambda = 940 \text{ nm}$) in ZnTe is plotted as a function of THz frequency in Fig. 6.7 (b). For the ZnTe crystal thickness of 1 mm only low frequency components smaller or equal 1.14 THz are continuously amplified during the rectification process. Frequency components at 1.73 THz , on the other hand, are expected to vanish. For this frequency, the coherence length is half of the crystal thickness and, therefore, two THz electric-fields are generated with equal amplitudes and a 180° phase-shift. As a consequence, the expected E^{THz} spectrum contains frequencies between 0 THz and 1.73 THz .

6.3.2 Terahertz Electric-Field Estimation

In the non-linear rectification process, the generated E^{THz} is directly proportional to the optical pump beam power P_{Pump} . The measured power P_{Pump} in the experimental system is 400 mW . This corresponds to pulse energy of 5 nJ which is averaged over 12.5 ns (repetition rate of the laser = 80 MHz). Knowing the pulse duration of a single pulse ($\approx 100 \text{ fs}$ FWHM), one can estimate its peak power to be 50 kW ($400 \text{ mW} \cdot 12.5 \text{ ns}/100 \text{ fs}$). An optical beam spot diameter of $50 \mu\text{m}$ was estimated. This value relies on the measurement of the probe beam diameter in a comparable experimental system ($30 \mu\text{m}$, see page 118). Based on this diameter, one can determine an optical intensity of $\approx 25 \frac{\text{MW}}{\text{mm}^2}$ in the focal beam spot. The optical power is assumed to be distributed equally over the beam spot area ($A_{pump} = 2000 \mu\text{m}^2$) for the sake of simplicity.

Data from the literature can now be used to estimate the energy conversion efficiency for optical rectification. According to Ref. [266], this efficiency is a constant value of $1.5 \cdot 10^{-4}$ for optical intensities ranging from $10 \frac{\text{MW}}{\text{mm}^2}$ to $2 \frac{\text{TW}}{\text{mm}^2}$. Consequently, the energy in a THz pulse \mathcal{E}^{THz} is 0.75 pJ . The energy can now be used to determine the electric-field strength at the input aperture of the PPWG using the energy flux density: $\mathcal{E}^{THz}/A_{PPWG} = \frac{1}{2} \int E^{THz}(t)^2/Z_{air} dt$. The value A_{PPWG} is the area of the THz beam which corresponds to the THz beam diameter of $500 \mu\text{m}$ at the PPWG input. The integral on the right side of the equation was calculated in Matlab using the same THz waveform as shown in Fig. 6.6 (a). Matching the integral with the calculated THz energy density allows the calculation of the E^{THz} strength at the PPWG input to be 190 kV/m . The simulations conducted in the previous chapter on the PPWG transmission properties show that the E^{THz} strength is reduced by 91% at the PPWG output. This is mainly due to reflections

at the PPWG input and output caused by the impedance mismatch to free-space and radiation leakage. The Ohmic losses, as discussed in the previous chapter, are negligible. As a result, the E^{THz} strength at the PPWG output is 17.1 kV/m .

This estimation shows that the E^{THz} strength at the PPWG output is expected to be larger than the E_{min}^{THz} by a factor of ≈ 114 . In this estimation, however, reflections at the ZnTe/Si/air interfaces in the crystal holder assembly and experimental misalignments were not taken into account. Also, when using the waveform in Fig. 6.6 (a), it was assumed that all THz frequency components are generated in the rectification process. Due to the coherence length of the ZnTe crystal, however, it is expected that the E^{THz} spectrum contains only frequencies between 0 THz and 1.73 THz . When comparing this with the THz spectrum in Fig. 6.6 (b), one realises that only a small portion of the THz spectrum is generated.

These considerations lead to the conclusion that the E^{THz} at the PPWG output can be expected to be smaller than 17.1 kV/m . This reduction, however, is difficult to estimate in theory and must be evaluated in the experiments. In experimental trials using this configuration, THz pulses were not detected. This leads to the conclusion that the E^{THz} in the experiments is indeed much smaller than theoretically calculated.

6.4 Conclusions

In this chapter, the electro-optic near-field detection system has been introduced. A special focus has been put on the explanation of the detection scheme which converts the electro-optic phase-shift in the probe beam into an intensity difference in the two beams exiting the Wollaston polariser $\Delta I = I_+ - I_-$. This intensity difference is then converted into an electrical signal by the detection unit.

The home-built balanced detector has been presented. A balanced detector is necessary to compensate for laser intensity fluctuations, which are the main noise source in the detection system. An E^{THz} can only be detected when the balancing of the input intensities is done to a level which is smaller than the phase-shift. This level of balancing has been experimentally measured to be of the order of $2 \cdot 10^{-7}$. When using this detection system, electric-fields higher than $150 \frac{\text{V}}{\text{m}}$ can be detected theoretically. A discussion about the generated E^{THz} in the system, however, leads to the conclusion that the E^{THz} in the experiments might not be strong enough to induce a detectable phase-shift. This has also been confirmed in experimental trials, in which no electro-optic phase-shift has been measured.

7 Conclusions and Future Work

The field of Terahertz technology has greatly advanced during the last two decades and THz radiation is now exploited for many applications: terahertz imaging and sensing technology has already shown unique capabilities ranging from scientific and medical research to industrial monitoring and security screening. Future THz communication technology will increase bitrates and offer additional communication channels to fulfill the growing demand for information exchange.

Some of the present-day applications have an increasing need for the characterisation, generation, and manipulation of light in spatial dimensions smaller than the wavelength. For these applications, it is possible to use a particular form of electro-magnetic waves: surface plasmons, which allow the development of highly-integrated "light circuits", high-sensitivity sensors, or single-molecule spectroscopy systems. The thorough investigation of this physical phenomenon is one of the key requirements for its use in later applications. Due to the non-radiative character of this radiation, however, specific near-field probes are necessary for surface plasmon detection and imaging.

It has been the task of this project to develop methods for THz surface plasmon imaging. In this work, two different probes have been introduced. They employ the two most commonly used phase-sensitive THz detectors: a PC-antenna and an electro-optic crystal. Hereby, typical problems of current near-field detection systems relying on these two detection principles have been identified and addressed. As a result, this thesis discusses two types of near-field probes for THz surface plasmon imaging.

Surface Plasmon Imaging with the Integrated Sub-Wavelength Aperture Near-Field Probe

In this work, it has been demonstrated that the combination of a PC-antenna and a sub-wavelength aperture can be used for surface plasmon imaging directly on a metallic sample surface. The coupling mechanism of the E^{SPP} into the antenna has been explained and it has been shown that this probe detects a spatial derivative of the actual E^{SPP} . By applying a simple integration, it has been possible to successfully reconstruct the original SPP pattern.

The sensitivity of this probe to the E^{SPP} has been applied to two different imaging examples. In the first one, the SPP pattern on a bow-tie antenna has been imaged. In this example, it has been demonstrated how the integrated near-field probe can be exploited for the investigation of surface plasmon phenomena on THz

devices. In a second example, a surface plasmon wave has been imaged that has been excited by a strongly focused THz beam directly on the metallic surface of the near-field probe. The SPP excitation by an incident free-space beam is possible due to the very small mismatch between the SPP wavevector and the one of free-space. Also, it is the advantage of the specific probe geometry that no additional near-field probe has to be inserted into the beam focus which potentially prevents the SPP excitation. By using this probe, the SPP excitation by a strongly focused beam directly on a metallic surface has been reported for the first time throughout this project.

For the THz research community, the results of this work are of particular interest because it extends the applicability of PC-antennas to SPP imaging directly on metallic surfaces. The use of PC-antennas for THz surface plasmon imaging, so far, has been restricted to the detection of the surface plasmon waves at metallic edges. The reason is the spatial orientation between the PC-antenna and the E^{SPP} on metallic surfaces, which makes the insertion of the near-field probe an experimentally challenging endeavour. By combining a PC-antenna with a sub-wavelength aperture, one obtains a tool for SPP detection which is suitable for SPP imaging especially on large metallic surfaces. In addition to that, the sensitivity of the probe to the orthogonal E^{THz} component can explain imaging artefacts when using PC-antennas in ordinary near-field microscopy. One has to be aware that a PC-antenna in a near-field imaging system can be sensitive to orthogonal electric-field components which can leave their unexpected footprints in the near-field image.

For future applications, it is interesting to investigate the impact of the aperture size and shape on the response of the antenna to the E^{SPP} . If this response is different from the one to the incident transverse E^{THz} , one can use the aperture geometry to either discriminate against or enhance one of them.

The Terahertz Near-field Detection System Based on an Electro-Optic Micro-Resonator Probe

In the second part of this thesis, the electro-optic detection system for THz SPP imaging has been introduced. The key element of this system is an electro-optic micro-resonator. In standard electro-optic detection systems, relatively thick electro-optic crystals are introduced into the near-field of the sample. Thick crystals are necessary to ensure a sufficient sensitivity. The use of thick crystals as near-field probes, however, increase the level of invasiveness and also reduces the spatial resolution of the imaging system. In order to mitigate these problems, a micro-resonator

probe has been developed. This type of probe is expected to show a lower level of invasiveness and a higher spatial resolution without sacrificing the sensitivity.

The design process of the micro-resonator has been explained in detail. The optimum resonator geometry has been found by using a home-written computer program which allowed the calculation of the micro-resonator optical response. By establishing minimum requirements for the 3dB THz bandwidth ($>1.5 THz$), the electro-optic enhancement (>2), and the reflectivity ($>90\%$), it has been possible to find an optimum micro-resonator geometry. The micro-resonator has then been fabricated by the UCL MBE facilities and its reflectivity has been measured by an optical spectrum analyser. Due to fabrication errors, the resonance wavelength of the fabricated micro-resonator has been shifted from $970 nm$ to $940 nm$. The change in the optical response due to this error, however, has been only very small ($<4\%$ performance decay) according to the simulations.

In a next step, the micro-resonator has been embedded in an electro-optic detection system. To translate the electro-optic phase-shift into an electrical signal, a home-built balanced detection scheme has been used. The balanced detector uses two photodiodes and a transimpedance amplifier as current-to-voltage converter. The level of balancing of this detector has been measured to be about $2 \cdot 10^{-7}$. Hence, this detection system should allow the measurement of an electro-optic phase-shift with a comparable order of magnitude.

The developed electro-optic detection system can now be applied to future SPP imaging applications. In a first step, the micro-resonator probe has to be attached to an optical fibre. The micro-resonator has been optimised for a fibre-coupled probe and, hence, it should show its best performance in this configuration. The fibre-coupled micro-resonator can then be used as a low-invasive probe with a high sensitivity and exceptional spatial resolution for THz SPP imaging. Regarding the context of the project, it would be interesting to measure the SPP distribution on a bow-tie antenna similar to the measurement with the integrated near-field probe. This would provide a direct comparison of these two probes regarding their sensitivities and levels of invasiveness. Also, the coupling theory of the integrated near-field probe could be experimentally evaluated.

A Parallel Plate Waveguide for Terahertz Transmission

A waveguiding structure was necessary in the electro-optic detection system to guide the THz radiation from its source to a spatially confined spot which the micro-resonator can be inserted into. To fulfill this task, a tapered PPWG has been selected because of its cut-off and dispersion-less transmission properties. Also, the

electric-field distribution of the *TEM*-mode inside the waveguide ensures a strong electro-optic effect in the micro-resonator and a relatively simple spatial alignment of the resonator with respect to the waveguide output.

In a first step, the waveguide gap has been optimised for maximum THz signal transmission from the source to the output. It has been found that the strongest E^{THz} is transmitted for a gap size which is similar to THz beam diameter at the PPWG input. In the case of the experiments, this gap size was $500\ \mu m$. For gap sizes smaller than $500\ \mu m$, the THz energy transmission is mainly governed by the input and output coupling of the waveguide. For gap sizes larger than $500\ \mu m$, on the contrary, it is the radiation leakage through the virtual boundaries which causes the decay in the transmitted E^{THz} .

In a second step, the mode structure inside the waveguide has been investigated. By analysing the transmitted THz spectra, typical indications of mode interference have been visible. This has led to the conclusion that the single-mode *TEM*-mode propagation inside this waveguide is often oversimplified. Using numerical simulations in CST Microwave Studio, higher-order $TE_{0,n}$ -modes have been identified which have never been reported in the literature before. The appearance of these modes has been explained by the finite dimensions of the tapered waveguide structure. This geometry causes reflections of the propagating THz energy at the waveguide boundaries and, hence, the excitation of higher-order modes. These modes can be excited for any plate width wider than the THz wavelength and they are independent of the gap size. Especially the latter point has to be highlighted, because related work in the literature mainly focuses on high-order modes which run into cut-off for sub-wavelength gap sizes. This is also the reason why single-mode *TEM*-mode propagation is often assumed inside PPWGs with sub-wavelength gap sizes. Being aware of these higher-order modes, therefore, is essential for the correct interpretation of electric-field patterns inside a tapered PPWG.

Further simulations have shown that the $TE_{0,n}$ -modes can leave their spectroscopic fingerprints on the transmitted THz waveform even after running into cut-off. This is surprising, because only the *TEM*-mode is expected to propagate for sub-wavelength plate widths and gap sizes. The $TE_{0,n}$ -modes, however, can partially convert into the *TEM*-mode before running into cut-off. This causes the genuine *TEM*-mode to appear dispersive because of the initially different group velocities of the $TE_{0,n}$ -modes. This knowledge is essential when using PPWGs with sub-wavelength dimensions for THz spectroscopy.

Future work can concern with the experimental evaluation of the multi-mode structure inside the PPWG. For this purpose, one can use the electro-optic micro-

resonator probe to detect the electric-field patterns in the output plane of the PPWG at different moments in time. Although this is not a SPP measurement, the developed near-field probe would be a suitable detector for this configuration. This type of measurements would give a valuable insight into the mode structure inside the PPWG and it would also underline the wide applicability of the developed THz near-field probe.

This Work in the Context of Terahertz Technology

Despite the tremendous progress in the field of THz technology throughout the last twenty years regarding sources, detectors, and applications, this frequency range still seems to be in its infancy compared to its two neighbours in the electromagnetic spectrum, the RF-range and the optical range. The undiscovered potential of the THz frequency range, therefore, should serve as the motivation for future research and the development of new applications. The investigation and the understanding of these future technologies requires the visualisation of physical processes at THz frequencies. By developing two different THz near-field microscopes for SPP imaging, the results of this project will contribute to the understanding of THz phenomena and can aid in the progress of THz device development.

Bibliography

- [1] J. C. Maxwell. On physical lines of force. *The London, Edinburgh and Dublin Philosophical Magazine and Journal of Science*, 4th Series, Mar. 1861.
- [2] M. Faraday. *On the various forces in nature*. Chatto & Windus, 1873.
- [3] H. C. Oerstedt. *The soul in nature*. Dawsons of Pall Mall, 1852.
- [4] A. -M. Ampère and J. Babinet. *Exposé des nouvelles découvertes sur l'électricité et le magnétisme*. Chez Méquignon-Marvis, 1822.
- [5] C. A. Coulomb. *Premier, second, et troisieme memoire sur l'electricite et le magnetisme*. Histoire de l'Academie royale des sciences, 1778.
- [6] J. Zenneck. Über die Fortpflanzung ebener elektromagnetischer Wellen längs einer ebenen Leiterfläche und ihre Beziehungen zur drahtlosen Telegraphie. *Annalen der Physik*, 23:846–866, Sep. 1907.
- [7] J. R. Wait. The ancient and modern history of EM ground-wave propagation. *IEEE Antennas and Propagation Magazine*, 40(5):7–24, Oct. 1998.
- [8] R. W. Wood. Remarkable spectrum from a diffraction grating. *Philos. Magazine*, 10:396–402, Jun. 1902.
- [9] R. H. Ritchie. Plasma losses by fast electrons in thin films. *Phys. Rev.*, 106(5):874–881, Jun. 1957.
- [10] T. Turbadar. Complete absorption of light by thin metal films. *Proc. Phys. Soc.*, 73:40–44, Sep. 1958.
- [11] H. Raether. *Surface Plasmons on smooth and rough surfaces and on gratings*. Springer Verlag, 1964.
- [12] Kh. V. Nerkararyan. Superfocusing of a surface polariton in a wedge-like structure. *Phys. Lett. A*, 237:103–105, Dec. 1997.
- [13] J. Takahara, S. Yamagishi, H. Taki, A. Morimoto, and T. Kobayashi. Guiding of a one-dimensional optical beam with nanometer diameter. *Opt. Letters*, 22(7):475–477, Apr. 1997.
- [14] S. A. Maier. *Plasmonics: Fundamentals and Applications*. Springer, 2007.

- [15] L. Novotny and B. Hecht. *Principles of Nano-optics*. Cambridge University Press, 2006.
- [16] S. Kawata. *Near-field optics and surface plasmon polaritons*. Springer Verlag, 2001.
- [17] W. L. Barnes, A. Dereux, and T. W. Ebbesen. Surface plasmon subwavelength optics. *Nature*, 424:824–830, Aug. 2003.
- [18] J. Heber. Surfing the wave. *Nature*, 461:720–722, Oct. 2009.
- [19] S. Lal, S. Link, and N. J. Halas. Nano-optics from sensing to waveguiding. *Nature Photonics*, 1:641–648, Nov. 2007.
- [20] K. Tanaka and M. Tanaka. Simulations of nanometric optical circuits based on surface plasmon polariton gap waveguide. *Appl. Phys. Lett.*, 82(8):1158–1160, Feb. 2003.
- [21] T. W. Ebbesen, C. Genet, and S. I. Bozhevolnyi. Surface-plasmon circuitry. *Phys. Today*, pages 44–50, May 2008.
- [22] S. Kawata, Y. Inouye, and P. Verma. Plasmonics for near-field nano-imaging and superlensing. *Nature Photonics*, 3:388–394, Jun. 2009.
- [23] Y. C. Martin, H. F. Hamann, and H. K. Wickramasinghe. Strength of the electric field in apertureless near-field microscopy. *J. Appl. Phys.*, 89(10):5774–5778, May 2001.
- [24] H. Knobloch, G. von Szada-Borrryszkowski, S. Woigk, A. Helms, and L. Brehmer. Dispersive surface plasmon microscopy for the characterization of ultrathin organic films. *Appl. Phys. Lett.*, 69(16):2336–2337, Oct. 1996.
- [25] R. Gordon, D. Sinton, K. L. Kavanah, and A. G. Brolo. A new generation of sensor based on extraordinary optical transmission. *Accounts of Chem. Research*, 41(8):1049–1057, Aug. 2008.
- [26] F. Miyamaru, S. Hayashi, C. Otani, K. Kawase, Y. Ogawa, H. Yoshida, and E. Kato. Terahertz surface-wave resonant sensor with a metal hole array. *Opt. Letters*, 31(8):1118–1120, Apr. 2006.
- [27] Y.-T. Chang, Y.-C. Lai, C.-T. Li, C.-K. Chen, and T.-J. Yen. A multi-functional plasmonic biosensor. *Opt. Express*, 106(9):9561–9569, Apr. 2011.

- [28] S. Nie and S. R. Emroy. Probing single molecules and single nanoparticles by surface-enhanced raman scatterin. *Science*, 275:1102–1106, Feb. 1997.
- [29] J. Homola, S. S. Yee, and G. Gauglitz. Surface plasmon resonance sensors: review. *Sensors and Actuators B*, 54(1):3–15, Jan. 1999.
- [30] H. A. Atwater and A. Polman. Plasmonics for improved photovoltaic devices. *Nature Materials*, 9:205–213, Mar. 2010.
- [31] R. F. Oulton, V. J. Sorger, T. Zentgraf, R. -M. Ma, C. Gladden, L. Dai, G. Bartal, and X. Zhang. Plasmon lasers at deep subwavelength scale. *Nature*, 461:629–632, Oct. 2009.
- [32] L. Novotny and N. van Hulst. Antennas for light. *Nature Photonics*, 5:83–90, Feb. 2011.
- [33] Q. -H. Park. Optical antennas and plasmonics. *Contemp. Physics*, 50(2):407–423, Mar. 2009.
- [34] D. K. Gramotnev and S. I. Bozhevolnyi. Plasmonics beyond the diffraction limit. *Nature Photonics*, 4:83–91, Feb. 2010.
- [35] J. A. Schuller, E. S. Barnard, W. Cai, Y. C. Jun, J. S. White, and M. L. Brongersma. Plasmonics for extreme light concentration and manipulation. *Nature Materials*, 9:193–204, Mar. 2010.
- [36] T. Xu, Y. -K. Wu, X. Luo, and L. J. Guo. Plasmonic nanoresonators for high-resolution colour filtering and spectral imaging. *Nature Comm.*, 59:1–5, Aug. 2010.
- [37] J. -C. Weeber, Y. Lacroute, and A. Dereux. Optical near-field distributions of surface plasmon waveguide modes. *Phys. Rev. B*, 68(11):115401, Sep. 2003.
- [38] G. Veronis and S. Fan. Modes of subwavelength plasmonic slot waveguides. *J. Lightwave Tech.*, 25(9):2511–2521, Sep. 2007.
- [39] M. I. Stockman. Nanofocusing of optical energy in tapered plasmonic waveguides. *Phys. Rev. Lett.*, 93(13):137404, Sep. 2004.
- [40] H. Ditlbacher, J. R. Krenn, G. Schider, A. Leitner, and F. R. Aussenegg. Two-dimensional optics with surface plasmon polaritons. *Appl. Phys. Lett.*, 81(10):1762–1764, Jul. 2002.

- [41] J.-S. Huang, T. Feichtner, P. Biagioni, and P. Hecht. Impedance matching and emission properties of nanoantennas in an optical nanocircuit. *Nano Lett.*, 9(5):1897–1902, Mar. 2009.
- [42] V.R. Almeida, C.A. Barrios, R.R. Panepucci, and M. Lipson. All-optical control of light on a silicon chip. *Nature*, 431:1081–1084, Oct. 2004.
- [43] K.F. MacDonald, M.I. Stockman, and N.I. Zheludev. Ultrafast active plasmonics. *Nature Photon.*, 3:55–58, Jan. 2009.
- [44] W.A. Challener, C. Peng, A.V. Itagi, D. Karns, W. Peng, Y. Peng, X. Yang, X. Zhu, N.J. Gokemeijer, Y.-T. Hsia, G. Ju, R.E. Rottmayer, M.A. Seigler, and E.C. Gage. Heat-assisted magnetic recording by a near-field transducer with efficient optical transfer energy. *Nature Photon.*, 3:220–224, Mar. 2009.
- [45] K.L. Kelly, E. Coronado, L.L. Zhao, and G.C. Schatz. The influence of size, shape, and dielectric environment. *J. Phys. Chem. B*, 107(3):668–677, Jan. 2003.
- [46] J.J. Mock, D.R. Smith, and G.C. Schultz. Local refractive index dependence of plasmon resonance spectra from individual nanoparticles. *Nano Lett.*, 3(4):485–491, Mar. 2003.
- [47] J.A. Matteo, D.P. Fromm, Y. Yuen, P.J. Schuck, W.E. Moerner, and L. Hesselink. Spectral analysis of strongly enhanced visible light transmission through single c-shaped nanoapertures. *Appl. Phys. Lett.*, 85(4):648–650, Jul. 2004.
- [48] C. Genet and T.W. Ebbesen. Light in tiny holes. *Nature*, 445:39–46, Jan. 2007.
- [49] M.A. Seo, H.R. Park, S.M. Koo, D.J. Park, J.H. Kang, O.K. Suwal, S.S. Choi, P.C.M Planken, G.S. Park, N.K. Park, Q.H. Park, and D.S. Kim. Terahertz field enhancement by a metallic nano slit operating beyond the skin-depth limit. *Nature Photonics*, 3:152–156, Mar. 2009.
- [50] X.R. Huang, R.W. Peng, Z. Wang, F. Gao, and S.S. Jiang. Charge-oscillation-induced light transmission through subwavelength slits and holes. *Phys. Rev. A*, 76:035802, Sep. 2007.
- [51] C.G. Biris and N.C. Panoiu. Nonlinear pulsed excitation of high-Q optical modes of plasmonic nanocavities. *Opt. Express*, 18(16):17165–17179, Nov. 2010.

- [52] A. Nahata, R. A. Linke, T. Ishi, and K. Ohashi. Enhanced nonlinear optical conversion from a periodically nanostructured metal film. *Opt. Lett.*, 88(6):423–425, Mar. 2003.
- [53] L. R. Hirsch, R. J. Stafford, J. A. Bankson, S. R. Sershen, B. Rivera, R. E. Price, J. D. Hazle, N. J. Halas, and J. L. West. Nanoshell-mediated near-infrared thermal therapy of tumors under magnetic resonance guidance. *Proc. Nat. Acad. Science*, 100(23):13549–13554, Nov. 2003.
- [54] M. Kaell. Inverse sensitivity. *Nature Materials*, 11:570–571, July 2012.
- [55] Y.-S. Lee. *Principles of Terahertz Science and Technology*. Springer Verlag, 2009.
- [56] A. Otto. Excitation of nonradiative surface plasma waves in silver by the method of frustrated total reflection. *Zeitschrift für Physik*, 216:398–410, Jul. 1968.
- [57] E. Kretschmann. Die Bestimmung der Oberflächenrauigkeit dünner Schichten durch Messung der Winkelabhängigkeit der Streustrahlung von Oberflächenplasmaschwingungen. *Optics Comm.*, 10(4):353–356, Apr. 1974.
- [58] G. Gaborit, D. Armand, J.-L. Coutaz, M. Nazarov, and A. Shkurinov. Excitation and focusing of terahertz surface plasmons using a grating coupler with elliptically curved grooves. *Appl. Phys. Lett.*, 94:231108, Jun. 2009.
- [59] E. Devaux, T. W. Ebbesen, J.-C. Weeber, and A. Dereux. Launching and decoupling surface plasmons via micro-gratings. *Appl. Phys. Lett.*, 83(24):4936–4938, Dec. 2003.
- [60] S. Hayashi, T. Kume, T. Amano, and K. Yamamoto. A new method of surface plasmon excitation mediated by metallic nanoparticles. *Jpn. J. Appl. Phys.*, 35(2):331–334, Mar. 1996.
- [61] M. W. Knight, N. K. Grady, R. Bardhan, F. Hao, P. Nordlander, and N. J. Halas. Nanoparticle-mediated coupling of light into a nanowire. *Nano Lett.*, 7(8):2346–2350, Jul. 2007.
- [62] J. Kim, J. Kim, K. I. B. Song, S. Q. Lee, E. U. N.-K. Kim, S.-E. U. L. Choi, Y. Lee, and K.-H. O. Park. Near-field imaging of surface plasmon on gold nano-dots fabricated by scanning probe lithography. *J. Microscopy*, 209(3):236–240, Mar. 2002.

- [63] T. Kume, S. Hayashi, and K. Yamamoto. Light emission from surface plasmon polariton mediated by metallic fine particles. *Phys. Rev. B*, 55(7):4774–4782, Feb. 1997.
- [64] A. J. L. Adam, J. M. Brok, M. A. Seo, K. J. Ahn, D. S. Kim, J. H. Kang, Q. H. Park, M. Nagel, and P. C. M. Planken. Advanced terahertz electric near-field measurements at sub-wavelength diameter metallic apertures. *Opt. Express*, 16(10):7407–7417, May 2008.
- [65] J. R. Krenn, A. Dereux, J. C. Weeber, E. Bourillot, E. Lacroute, and J. P. Goudonnet. Squeezing the optical near-field zone by plasmon coupling of metallic nanoparticles. *Advances in Optics and Photonics*, 82(12):2590–2593, Mar. 1999.
- [66] J. R. Knab, A. J. L. Adam, M. Nagel, E. Shaner, M. A. Seo, D. S. Kim, and P. C. M. Planken. Terahertz near-field vectorial imaging of subwavelength apertures and aperture arrays. *Opt. Express*, 17(17):15072–15086, Aug. 2009.
- [67] A. V. Zayats and I. I. Smolyaninov. Near-field photonics: surface plasmon polaritons and localized surface plasmons. *J. Opt. A*, 5(5):16–50, Jun. 2006.
- [68] A. Degiron and T. W. Ebbesen. The role of localized surface plasmon modes in the enhanced transmission of periodic subwavelength apertures. *J. Optics A*, 7:90–96, Jan. 2005.
- [69] S. Enoch, E. Popov, M. Neviere, and R. Reinisch. Enhanced light transmission by hole arrays. *J. Opt. A*, 4:83–87, Aug. 2002.
- [70] A. J. Huber, F. Keilmann, J. Wittborn, J. Aizpurua, and R. Hillenbrand. Terahertz near-field nanoscopy of mobile carriers in single semiconductor nanodevices. *Nano Letters*, 8(11):3766–3770, Jul. 2008.
- [71] L. Novotny and S. J. Stranick. Near-field optical microscopy and spectroscopy with pointed probes. *Annu. Rev. Phys. Chem.*, 2:303–331, Dec. 1985.
- [72] E. Abbe. Beiträge zur Theorie des Mikroskops und der mikroskopischen Wahrnehmung. *Archiv für Mikroskopische Anatomie*, 9(1):413–418, 1873.
- [73] E. H. Synge. A suggested method for extending the microscopic resolution into the ultramicroscopic region. *Phil. Mag.*, 6:356–362, 1928.
- [74] E. A. Ash and G. Nichols. Super-resolution aperture scanning microscope. *Phil. Mag.*, 237:510–512, Feb. 1972.

- [75] E. - G. Steward. *FOURIER OPTICS: an introduction*. Ellis Horwood Physics Series, 1983.
- [76] T. Klar, M. Perner, S. Grosse, G. von Plessen, W. Spirkl, and J. Feldmann. Surface-enhanced optical microscopy. *Phys. Rev. Lett.*, 80(19):4249–4252, May 1998.
- [77] B. Hecht, H. Bielefeldt, L. Novotny, Y. Inouye, and D. Pohl. Local Excitation, Scattering, and Interference of Surface Plasmons. *Phys. Rev. Lett.*, 77(9):1889–1892, Aug. 1996.
- [78] O. Mitrofanov, M. Lee, J. W. P. Hsu, I. Brener, R. Harel, J. F. Federici, J. D. Wynn, L. N. Pfeiffer, and K. W. West. Collection-mode near-field imaging with 0.5-THz pulses. *IEEE J. Sel. Top. Quantum Electron.*, 7(4):600–607, Aug. 2001.
- [79] M. I. Stockman. Nanofocusing of optical energy in tapered plasmonic waveguides. *Phys. Rev. Lett.*, 93(13):137404, Sep. 2004.
- [80] N. A. Janunts, K. S. Baghdasaryan, Kh. V. Nerkarayan, and B. Hecht. Excitation and superfocusing of surface plasmon polaritons on a silver-coated optical fibre tip. *Opt. Comm.*, 253:118–124, Apr. 2005.
- [81] A. Polman and H. A. Atwater. Plasmonics: optics at the nanoscale. *Materials Today*, page 56, Jan. 2005.
- [82] B. Hecht, B. Sick, U. P. Wild, O. J. F. Oliver, and D. W. Pohl. Scanning near-field optical microscopy with aperture probes: Fundamentals and applications. *J. Chem. Phys.*, 112(18):7761–7774, May 2000.
- [83] A. Passian, A. Lereu, A. Wig, F. Meriaudeau, T. Thundat, and T. Ferrell. Imaging standing surface plasmons by photon tunneling. *Phys. Rev. B*, 71(16):165418, Apr. 2005.
- [84] J. - C. Weeber, J. Krenn, A. Dereux, B. Lamprecht, Y. Lacroute, and J. Goudonnet. Near-field observation of surface plasmon polariton propagation on thin metal stripes. *Phys. Rev. B*, 64(4):1–9, Jul. 2001.
- [85] R. C. Reddick, R. J. Warmack, and T. L. Ferrell. New form of scanning optical microscopy. *Rapid Comm.*, 39(1):767–772, Jan. 1989.

- [86] A. Bouhelier, F. Ignatovich, A. Bruyant, C. Huang, J. - C. Weeber, A. Dereux, G.P. Wiederrecht, and L. Novotny. Surface plasmon interference excited by tightly focused laser beams. *Opt. Letters*, 32(17):2535–2537, Sep. 2007.
- [87] M. Specht, J.D. Pedarnig, W.M. Heckl, and T.W. Haensch. Scanning Plasmon Near-Field Microscope. *Phys. Rev. Lett.*, 68(4):476–481, Jan. 1992.
- [88] K.G. Lee, H.W. Kihm, J.E. Kihm, W.J. Choi, H. Kim, C. Ropers, D. J. Park, Y.C. Yoon, S.B. Choi, D.H. Woo, J. Kim, B. Lee, Q.H. Park, C. Lienau, and D.S. Kim. Vector field microscopic imaging of light. *Nature Photonics*, 1(1):53–56, Jan. 2007.
- [89] R. D. Grober, R. J. Schoelkopf, and D. E. Prober. Optical antenna towards a unity efficiency near-field optical probe. *Appl. Phys. Lett.*, 70(11):1354–1356, Mar. 1997.
- [90] H. Ditlbacher, J.R. Krenn, N. Felidj, B. Lamprecht, G. Schider, M. Salerno, A. Leitner, and F.R. Aussenegg. Fluorescence imaging of surface plasmon fields. *Appl. Phys. Lett.*, 80(3):404–406, Jan. 2002.
- [91] H. Ditlbacher, J.R. Krenn, A. Hohenau, A. Leitner, and F.R. Aussenegg. Efficiency of local light-plasmon coupling. *Appl Phys. Lett.*, 83(18):3665–3667, Nov. 2003.
- [92] A. Bouhelier and G. P. Wiederrecht. Excitation of broadband surface plasmon polaritons: Plasmonic continuum spectroscopy. *Phys. Rev. B*, 71(19):195406, Dec. 2005.
- [93] B. Hecht, D.W. Pohl, H. Heinzelmann, and L. Novotny. Tunnel near-field optical microscopy: TNOM-2. *Ultramicroscopy*, 61:99–104, May 1995.
- [94] B. Hecht, H. Heinzelmann, and D.W. Pohl. Combined aperture SNOM/PSTM: best of both worlds? *Ultramicroscopy*, 57:228–234, Jan. 1995.
- [95] M. Koch. Terahertz-Technologie: Quo Vadis? *Photonik*, 4:68–71, Apr. 2005.
- [96] X. - C. Zhang. Terahertz wave imaging: horizons and hurdles. *Phys. in Med. and Biol.*, 47:3667–3677, Oct. 2002.
- [97] B. Ferguson and X. - C. Zhang. Materials for terahertz science and technology. *Nature Materials*, 1(1):26–33, Sep. 2002.

- [98] A. G. Davies, E. H. Linfield, and M. B. Johnston. The developments of terahertz sources and their applications. *Phys. in Med. and Biol.*, 47:3679–3689, Oct. 2002.
- [99] P. C. M. Planken, C. E. W. M. van Rijmenam, and R. N. Schouten. Optoelectronic pulsed THz systems. *Semiconductor Science and Technology*, 20:121–127, Jun. 2005.
- [100] A. Nahata, D. H. Auston, and T. F. Heinz. Coherent detection of freely propagating terahertz radiation by electro-optic sampling. *Appl. Phys. Lett.*, 68(2):150–152, Jan. 1996.
- [101] Q. Wu and X. - C. Zhang. Free-space electro-optics sampling of mid-infrared pulses. *Appl. Phys. Lett.*, 71(10):1285–1287, Sep. 1997.
- [102] J. A. Valdmanis and G. Mourou. Subpicosecond electrooptic sampling: principles and applications. *IEEE J. Quantum Electr.*, 22(1):69–78, Jan. 1986.
- [103] P. R. Smith, D. H. Auston, and M. C. Nuss. Subpicosecond photoconductive dipole antennas. *IEEE J. Quantum Electr.*, 24(2):255–260, Feb. 1988.
- [104] M. van Exter and D. Grischkowsky. Characterisation of an Optoelectronic Terahertz beam system. *IEEE Trans. Microw. Theory and Techniques*, 38(11):1684–1690, Nov. 1990.
- [105] D. H. Auston, K. P. Cheung, and P. R. Smith. Picosecond photoconducting Hertzian dipoles. *Appl. Phys. Lett.*, 45(3):284–286, May 1984.
- [106] A. Bitzer, A. Ortner, and M. Walther. Terahertz near-field microscopy with subwavelength spatial resolution based on photoconductive antennas. *Appl. Optics*, 49(19):1–6, Jul. 2010.
- [107] C. Kuebler, R. Huber, S. Tuebel, and A. Leitensdorfer. Ultrabroadband detection of multi-terahertz field transients with GaSe electro-optic sensors: Approaching the near infrared. *Appl. Phys. Lett.*, 85(16):3360–3362, Oct. 2004.
- [108] D. H. Auston and K. P. Cheung. Coherent time-domain far-infrared spectroscopy. *J. Opt. Soc. Am. B*, 2(4):606–612, Apr. 1985.
- [109] B. B. Hu and M. C. Nuss. Imaging with terahertz waves. *Opt. Letters*, 20(16):1716–1719, Aug. 1995.

- [110] M. Tonouchi. Cutting-edge terahertz technology. *Nature Photonics*, 1(2):97–105, Feb. 2007.
- [111] G. Samulat. Vorstoß in die Terahertzlücke. *Spektrum der Wissenschaft*, pages 84–89, Apr. 2008.
- [112] D. M. Mittleman, M. Gupta, R. Neelamani, R. G. Baraniuk, J. V. Rudd, and M. Koch. Recent advances in terahertz imaging. *Appl. Phys. B*, Apr. 1999.
- [113] A. Dobroiu, C. Otani, and K. Kawase. Terahertz-wave sources and imaging applications. *Meas. Sci. Technol.*, 17:161–174, Sep. 2006.
- [114] R. Mueckstein, C. Graham, C. C. Renaud, A. J. Seeds, J. A. Harrington, and O. Mitrofanov. Imaging and analysis of thz surface plasmon polariton waves with the integrated sub-wavelength aperture probe. *J. of Infrared, Millimeter, and Terahertz waves*, 32(8-9):1031–1042, Aug. 2011.
- [115] F. Miyamaru, Y. Saito, M. W. Takeda, L. Liu, B. Hou, W. Wen, and P. Sheng. Emission of terahertz radiations from fractal antennas. *Appl. Phys. Lett.*, 95(22):221111, Dec. 2009.
- [116] P. Maraghechi and A. Y. Elezzabi. Enhanced THz radiation emission from plasmonic complementary Sierpinsky fractal emitters. *Opt. Express*, 18(26):27336–27345, Dec. 2010.
- [117] B. You, J.-Y. Lu, W.-L. Chang, C.-P. Yu, T.-A. Liu, and J.-L. Peng. Subwavelength confined terahertz waves on planar waveguides using metallic gratings. *Opt. Express*, 21(5):6009–6019, Mar. 2013.
- [118] W. Zhu, A. Agrawal, and A. Nahata. Planar plasmonic terahertz guided-wave devices. *Opt. Express*, 16(9):6216–6226, Apr. 2008.
- [119] J. B. Pendry, L. Martin-Moreno, and F. J. Garcia-Vidal. Mimicking surface plasmons with structured surfaces. *Science*, 305:847–848, Aug. 2004.
- [120] D. Marin-Cano, O. Quevedo-Teruel, E. Moreno, L. Marin-Morena, and F. J. Garcia-Vidal. Waveguided spoof surface plasmons with deep-subwavelength lateral confinement. *Opt. Lett.*, 36(23):4635–4637, Dec. 2011.
- [121] K. Kawase, Y. Ogawa, Y. Watanabe, and H. Inoue. Non-destructive terahertz imaging of illicit drugs using spectral fingerprints. *Opt. Express*, 11(20):2549–2554, Sep. 2003.

- [122] M. R. Leahy-Hoppa, M. J. Fitch, X. Zheng, L. M. Hayden, and R. Osiander. Wideband terahertz spectroscopy of explosives. *Chem. Phys. Lett.*, 434:227–230, Dec. 2007.
- [123] J. F. Federici, B. Schulkin, F. Huang, D. Gary, R. Barat, F. Oliveira, and D. Zimdars. THz imaging and sensing for security applications - explosives, weapons, and drugs. *Semicond. Sci. and Technol.*, 20:266–280, Jun. 2005.
- [124] P. H. Siegel. Terahertz technology in biology and medicine. *IEEE Trans. Microw. Theory And Techn.*, 52(10):2438–2447, Oct. 2004.
- [125] O. Mitrofanov, C. C. Renaud, and A. J. Seeds. Terahertz probe for spectroscopy of sub-wavelength objects. *Opt. Express*, 20(6):6197–6202, Mar. 2012.
- [126] Q. Chen, Z. Jiang, G. X. Xu, and X. - C, Zhang. Near-field terahertz imaging with a dynamic aperture. *Opt. Lett.*, 25(15):1122–1124, Dec. 2000.
- [127] H. Zhan, R. Mendis, and D. M. Mittleman. Superfocusing terahertz waves below $\lambda/250$ using plasmonic parallel-plate waveguides. *Opt. Express*, 18(9):9643–9650, Apr. 2010.
- [128] K. Wang, D. M. Mittleman, N. C. J. van der Valk, and P. C. M. Planken. Antenna effects in terahertz apertureless near-field optical microscopy. *Appl. Phys. Lett.*, 85(14):2715–2717, Aug. 2004.
- [129] J. Saxler, J. Gomez Rivas, C. Janke, H. Pellemans, P. Bolivar, and H. Kurz. Time-domain measurements of surface plasmon polaritons in the terahertz frequency range. *Phys. Rev. B*, 69(15):1–4, Apr. 2004.
- [130] T. H. Isaac, W. L. Barnes, and E. Hendy. Determining the terahertz optical properties of subwavelength films using semiconductor surface plasmons. *Appl. Phys. Lett.*, 93(24):241115, Dec. 2008.
- [131] J. Liu, R. Mendis, and D. M. Mittleman. The transition from a TEM-like mode to a plasmonic mode in parallel-plate waveguides. *Appl. Phys. Lett.*, 98(23):2311131, Jun. 2011.
- [132] H. - T. Chen, R. Kersting, and G. C. Cho. Terahertz imaging with nanometer resolution. *Appl. Phys. Lett.*, 83(15):3009–3077, Aug. 2003.

- [133] M. Wächter, M. Nagel, and H. Kurz. Frequency-dependent characterization of THz Sommerfeld wave propagation on single-wires. *Opt. Express*, 13(26):10815–10822, Dec. 2005.
- [134] A. Bitzer and M. Walther. Terahertz near-field imaging of metallic subwavelength holes and hole arrays. *Appl. Phys. Lett.*, 92(23):231101, Jun. 2008.
- [135] K. Wang and D.M. Mittleman. Metal wires for terahertz wave guiding. *Nature*, 432:379–379, Nov. 2004.
- [136] N.C.J. van der Valk and P.C.M. Planken. Effect of a dielectric coating on terahertz surface plasmon polaritons on metal wires. *Appl. Phys. Lett.*, 87(7):071106, Aug. 2005.
- [137] T.-I. Jeon, J. Zhang, and D. Grischkowsky. THz Sommerfeld wave propagation on a single metal wire. *Appl. Phys. Lett.*, 86(16):161904, Apr. 2005.
- [138] M. Gong, T.-I. Jeon, and D. Grischkowsky. THz surface wave collapse on coated metal surfaces. *Opt. Express*, 17(19):17088–17101, Sep. 2009.
- [139] A. Bitzer, H. Merbold, A. Thoman, T. Feurer, H. Helm, and M. Walther. Terahertz near-field imaging of electric and magnetic resonances of a planar metamaterial. *Opt. Express*, 17(5):3826–3834, Mar. 2009.
- [140] A. Bitzer, A. Ortner, and M. Walther. Terahertz near-field microscopy with subwavelength spatial resolution based on photoconductive antennas. *Appl. Optics*, 19(19):E1–E6, Mar. 2010.
- [141] M. A. Seo, A. J. L. Adam, J. H. Kang, J. W. Lee, S. C. Jeoung, Q. H. Park, P. C. M. Planken, and D. S. Kim. Fourier-transform Terahertz near-field imaging of one-dimensional slit arrays: mapping of electric-field-, magnetic-field-, and Poynting vectors. *Opt. Express*, 15(19):11781–11789, Sep. 2007.
- [142] A. J. L. Adam, J. M. Brok, P. C. M. Planken, M. A. Seo, and D. S. Kim. THz near-field measurements of metal structures. *Comptes Rendus Physique*, 9(2):161–168, Mar. 2008.
- [143] L. Guestin, A. J. L. Adam, J. R. Knab, M. Nagel, and P. C. M. Planken. Influence of the dielectric substrate on the Terahertz electric near-field of a hole in a metal. *Opt. Express*, 17(20):17412–17425, Sep. 2009.

- [144] K. Yang, L. P. B. Katehi, and J. F. Whitaker. Electro-optic field mapping system utilizing external gallium arsenide probes. *Appl. Phys. Lett.*, 77(4):486–488, Jul. 2000.
- [145] X. Wu, D. Conn, J. Song, and K. Nickerson. Invasiveness of $LiTaO_3$ and GaAs probes in external electro-optic sampling. *J. of Lightwave Techn.*, 11(3):448–453, Mar. 1993.
- [146] D.-J. Lee and F. Whitaker. An optical-fiber-scale electro-optic probe for minimally invasive high-frequency field sensing. *Opt. Express*, 16(262):21587–21597, Dec. 2008.
- [147] S. Seitz, M. Bieler, G. Hein, K. Pierz, and U. Siegner. Characterization of an external electro-optic sampling probe: Influence of probe height on distortion of measured voltage pulses. *J. Appl. Phys.*, 100(11):113124, Dec. 2006.
- [148] J. A. Deibel, K. Wang, M. D. Escarra, and D. M. Mittleman. Enhanced coupling of terahertz radiation to cylindrical wire waveguides. *Opt. Express*, 14(1):279–290, Jan. 2006.
- [149] T.-I. Jeon and D. Grischkowsky. Thz zenneck surface wave (THz surface plasmon) propagation on a metal sheet. *Appl. Phys. Lett.*, 88(6):061113, Feb. 2006.
- [150] R. Mueckstein and O. Mitrofanov. Imaging of Terahertz surface plasmon waves excited on a gold surface by a focused beam. *Opt. Express*, 8(11):1381–1386, Feb. 2011.
- [151] O. Mitrofanov, T. Tan, P. R. Mark, B. Bowden, and J. A. Harrington. Waveguide mode imaging and dispersion analysis with terahertz near-field microscopy. *Appl. Phys. Lett.*, 94(17):171104, Apr. 2009.
- [152] B. Bowden, J. A. Harrington, and O. Mitrofanov. Low-loss modes in hollow metallic Terahertz waveguides with dielectric coatings. *Appl. Phys. Lett.*, 93(18):181104, Nov. 2008.
- [153] B. Bowden, J. A. Harrington, and O. Mitrofanov. Fabrication of terahertz hollow-glass metallic waveguides with inner dielectric coatings. *J. Appl. Phys.*, 104(9):093110, Nov. 2008.
- [154] O. Mitrofanov and J. A. Harrington. Dielectric-lined cylindrical metallic THz waveguides: mode structure and dispersion. *Opt. Express*, 18(3):1898–1903, Sep. 2010.

- [155] H. Kano, S. Mizuguchi, and S. Kawata. Excitation of surface-plasmon polaritons by a focused laser beam. *Near-field optics and surface plasmon polaritons, Topics Appl. Phys.*, 81(4):189–206, Apr. 2001.
- [156] H. Kano, S. Mizuguchi, and S. Kawata. Excitation of surface-plasmon polaritons by a focused laser beam. *J. Opt. Soc. Am. B*, 15(4):1381–1386, Apr. 1998.
- [157] W. Chen, R.L. Nelson, D.C. Abeysinghe, and Q. Zhan. Optimal plasmon focusing with spatial polarization engineering. *OPN Optics and Photonics News*, pages 36–41, Oct. 2009.
- [158] Y. Cai, I. Brener, J. Lopata, J. Wynn, L. Pfeiffer, and J. Federici. Design and performance of singular electric field terahertz photoconducting antennas. *Appl. Phys. Lett.*, 71(15):2076–2078, Aug. 1997.
- [159] M. Natrella, O. Mitrofanov, R. Mueckstein, C. Graham, C.C. Renaud, and A. J. Seeds. Modelling of surface waves on a thz antenna detected by a near-field probe. *Opt. Express*, 20(14):16023–16032, Jul. 2012.
- [160] K. Yang, P.B. Katehi, and J.F. Whitaker. Electric field mapping system using an optical-fiber-based electrooptic probe. *IEEE Microw. and Wireless Comp. Lett.*, 11(4):164–166, Apr. 2001.
- [161] D.-J. Lee, M.-H. Crites, and J.F. Whitaker. Electro-optic probing of microwave fields using a wavelength-tunable modulation depth. *Meas. Sci. Technol.*, 19:115301, Sep. 2008.
- [162] A. Yariv and P. Yeh. *Optical Waves in Crystals*. John Wiley & Son, 2003.
- [163] A. Yariv. *Introduction to Optical Electronics*. Holt McDougal, 1977.
- [164] M. Born and E. Wolf. *Principles of Optics*. Cambridge University Press, 2003.
- [165] A. Yariv. *Quantum Electronic*. John Wiley & Son, 1989.
- [166] T.A. Maldonado and T.K. Gaylord. Electrooptic effect calculations: simplified procedure for arbitrary cases. *Appl. Opt.*, 27(24):5051–5066, Dec. 1988.
- [167] N.C.J. van der Valk, T. Wenckebach, and P.C.M. Planken. Full mathematical description of electro-optic detection in optically isotropic crystals. *J. Opt. Soc. Am. B*, 21(3):622–631, Mar. 2004.

- [168] L. Duvillaret, S. Rialland, and J. -L. Coutaz. Electro-optic sensors for electric field measurements. II. Choice of the crystals and complete optimization of their orientation. *J. Opt. Soc. Am. B*, 19(11):2704–2715, Nov. 2002.
- [169] M. J. Gunning and R. E. Raab. Algebraic determination of the principle refractive indices and axes in the electro-optic effect. *Appl. Opt.*, 37(36):8438–8447, Dec. 1998.
- [170] J. F. Nye. *Physical properties of crystals*. Oxford University Press, 2002.
- [171] S. Namba. Electro-optical effect of zincblende. *J. Opt. Soc. Am.*, 51(1):76–79, Jan. 1961.
- [172] R. L. Kelly. Pockels Effect in Zinc-Blende-Structure Ionic Crystals. *Phys. Rev.*, 151(2):721–726, Nov. 1966.
- [173] C.-C. Chih and A. Yariv. A theoretical model of the linear electro-optic effect. *J. Phys. C: Solid State Physics*, 15:825–846, May 1982.
- [174] I. Fujimoto. Direct Detection of Electric-Field-Induced Microscopic Structural Changes in $LiNbO_3$ by Modulation X-Ray Diffraction. *Phys. Rev. Lett.*, 40(14):941–944, Apr. 1978.
- [175] L. Duvillaret, S. Rialland, and J. -L. Coutaz. Electro-optic sensors for electric field measurements. I. Theoretical comparison among different modulation techniques. *J. Opt. Soc. Am. B*, 19(11):2692–2703, Nov. 2002.
- [176] R. C. Alferness, N. P. Economou, and L. L. Buhl. Picosecond optical sampling technique for measuring the speed of fast electro-optic switch/modulators. *Appl. Phys. Lett.*, 37(7):597–599, Oct. 1980.
- [177] T. Pfeifer, H. - M. Heiliger, T. Löffler, C. Ohlhoff, C. Meyer, G. Lüpke, H. G. Roskos, and H. Kurz. Optoelectronic on-chip characterization of ultrafast electric devices: Measurement techniques and applications. *IEEE J. Sel. Top. Quantum Electr.*, 2(3):586–604, Sep. 1996.
- [178] K. Yang, G. David, J.-G. Yook, I. Papapolymerou, L.P.B. Katehi, and J.F Whitaker. Electrooptic mapping and finite-element modeling of the near-field pattern of a microstrip patch antenna. *IEEE Trans. Microw. Theory Techn.*, 48(2):288–294, Feb. 2000.

- [179] D.-J. Lee, N.-W. Kang, J.-H. Choi, J. Kim, and J.F. Whitaker. Recent advances in the design of electro-optic sensors for minimally destructive microwave field probing. *Sensors*, 11:806–824, Jan. 2011.
- [180] C. Zhanguo, J. Gang, and Y. Maobin. External electro-optic measuring system with high spatial resolution and high voltage sensitivity by using an electro-optic solid immersion probe. *J. Phys. D: Appl. Phys.*, 34:3078–3082, Oct. 2001.
- [181] J. A. Valdmanis, G. A. Mourou, and C.W. Gabel. Subpicosecond electrical sampling. *IEEE J. Quant. Electr.*, 19(4):644–647, Apr. 1983.
- [182] J. A. Valdmanis. 1 THz-bandwidth prober for high-speed devices and integrated circuits. *Electr. Lett.*, 23(24):1308–1310, Nov. 1987.
- [183] Q. Wu and X.-C. Zhang. Free-space electro-optic sampling of terahertz beams. *Appl. Phys. Lett.*, 67(24):3523–3525, Dec. 1995.
- [184] Z. Jiang and X.-C. Zhang. Terahertz imaging via electrooptic effect. *IEEE Trans. Microw. Theory Techn.*, 47(12):2644–2650, Dec. 1999.
- [185] P. U. Jepsen, C. Winnewisser, M. Schall, V. Schyja, S.R. Keiding, and H. Helm. Detection of thz pulses by phase retardation in lithium tantalate. *Phys. Rev. E*, 53(4):3052, Apr. 1996.
- [186] L. Le Quang, D. Erasme, and B. Huyart. Fabry-Perot enhanced real-time electro-optic probing of MMICs. *Electron. Lett.*, 29(5):498–499, Mar. 1993.
- [187] D. Le Quang, D. Erasme, and B. Huyart. MMIC-calibrated probing by CW electrooptic modulation. *IEEE Trans. on Microwave Theory and Techniques*, 43(5):1031–1036, May 1995.
- [188] H. B. Zhang, R. Wang, H. Yang, D.M. Zhang, M.B. Yi, G.Q. Wang, and Z.C. Ma. Comparison of spatial resolution in internal and external electro-optic. *Opt. and Quant. Electr.*, 34:757–764, Nov. 2001.
- [189] Park. S.-G., M.R. Melloch, and A.M. Weiner. Analysis of Terahertz waveforms measured by photoconductive and electrooptic sampling. *Appl. Phys. Lett.*, 35(5):810–819, May 1999.
- [190] S.M. Chandani. Fiber-based probe for electrooptic sampling. *IEEE Phot. Tech. Lett.*, 18(12):1290–1292, Jun. 2006.

- [191] S. Wakana, T. Ohara, M. Abe, E. Yamazaki, M. Kishi, and M. Tsuchiya. Fiber-edge electrooptic/magneto-optic probe for spectral-domain analysis of electromagnetic field. *IEEE Trans. Microwave Theory and Techniques*, 48(12):2611–2616, Jan. 2000.
- [192] R.M. Reano, L.P.B. Katehi, and J.F. Whitaker. Simultaneous measurements of electric and thermal fields utilizing an electrooptic semiconductor probe. *IEEE Trans. on Microwave Theory and Techniques*, 49(12):2523–2531, Dec. 2001.
- [193] G. Gaborit, M. Guillermo, J.-L. Coutaz, L. Duvillaret, S. Kassi, and D. Romanini. High-finesse Fabry-Perot electro-optic sensors with enhanced sensitivity and high spatial resolution. *Appl. Opt.*, 46(11):2001–2009, Apr. 2007.
- [194] J.F. Mulligan. Who were Fabry and P erot? *Am. J. Phys.*, 66(9):797–802, Sep. 1998.
- [195] W.-K. Kuo, P.-Y. We, and C.-C. Lee. A Fabry-Perot electro-optic sensing system using a drive-current-tuned wavelength laser diode. *Rev. Sci Instr.*, 81:53107, May 2010.
- [196] G. Gaborit, G. Martin, L. Duvillaret, J.-L. Coutaz, C.-T. Nguyen, R. Hierle, and J. Zyss. Electrooptic probe based on an organic microcavity. *IEEE Phot. Techn. Lett.*, 17(10):2140–2142, Jun. 2005.
- [197] J. Xu, L. Zhou, and M. Thakur. Electro-optic modulation using an organic single crystal film in a fabry-perot cavity. *Appl. Phys. Lett.*, 72(2):153–154, Nov. 1998.
- [198] K. Chen, H. Zhang, D. Zhang, H. Yang, and M. Yi. External electro-optic sampling utilizing a poled polymer asymmetric fabry-perot cavity as an electro-optic probe tip. *Opt. and Laser Techn.*, 34:449–452, Apr. 2002.
- [199] D.M. Zhang, M.B. Yi, K.X. Chen, X.J. Tian, W. Sun, and A.L. Hou. Electro-optic measurement of poled polymer-based asymmetric Fabry-Perot cavity. *Opt. and Quantum Electron.*, 35:1183–1190, Sep. 2000.
- [200] O. Mitrofanov, A. Gasparyan, L.N. Pfeiffer, and K.W. West. Electro-optic effect in an unbalanced AlGaAs/GaAs microresonator. *Appl. Phys. Lett.*, 86(20):202103, May 2005.
- [201] O. Mitrofanov. Terahertz near-field electro-optic probe based on a microresonator. *Appl. Phys. Lett.*, 88(9):091118, Mar. 2006.

- [202] H. Shirai, K. Uzumi, S. Koshiba, S. Nakanishi, H. Itoh, and N. Tsurumachi. Enhancement of terahertz detection efficiency in electro-optical sampling using fabry-perot microcavity structure. *Phys. Status Solidi C*, 8(2):356–358, Dec. 2011.
- [203] M. S. Heutmaker, G. T. Harvey, and P. F. Bechtold. Electro-optic sampling of high-speed silicon integrated circuits using a GaAs probe tip. *Appl. Phys. Lett.*, 59(2):146–148, Jul. 1991.
- [204] F. Taenzler. Contactless characterization of microwave integrated circuits by device internal indirect electro-optic probing. *IEEE Eleventh Annual VLSI Test Symposium*, pages 120–122, Apr. 1993.
- [205] R. Hofmann and H. - J. Pfeleiderer. Simulations of the potential distribution and the resulting measurement signal in longitudinal external electro-optic probe tips. *Microelectr. Eng.*, 31:377–384, 1996.
- [206] K. D. Choquette, K. M. Geib, C. I. H. Ashby, R. D. Twesten, O. Blum, H. Q. Hou, D. M. Follstaedt, B. E. Hammons, D. Mathes, and R. Hull. Advances in selective wet oxidation of algaas alloys. *IEEE J. Sel. Top. Quant. Electr.*, 3(3):916–926, Jun. 1997.
- [207] E. D. Palik. *Handbook of Optical Constants of Solids II*. Academic Press, 1998.
- [208] Q. Wu and X. - C. Zhang. Ultrafast electro-optic field sensors. *Appl. Phys. Lett.*, 68(12):1604–1606, Mar. 1996.
- [209] Q. Wu and X. - C. Zhang. 7 terahertz broadband GaP electro-optic sensor. *Appl. Phys. Lett.*, 70(14):1784–1786, May 1997.
- [210] G. C. Cho, P. Y. Han, X. - C. Zhang, and H. J. Bakker. Optical phonon dynamics of GaAs studied with time-resolved terahertz spectroscopy. *Opt. Lett.*, 25(21):1609–1611, Nov. 2000.
- [211] F. - T. Arecchi and E. O. Schulz-Dubois. *Laser Handbook*. Elsevier, New York, 1973.
- [212] K. Liu, J. Xu, and X. - C. Zhang. GaSe crystals for broadband terahertz wave detection. *Appl. Phys. Lett.*, 85(6):863–865, Aug. 2004.

- [213] F. Pan, G. Knöpfle, C. Bosshard, S. Follonier, R. Spreiter, M. S. Wong, and P. Günter. Electro-optic properties of the organic salt 4-N,N-dimethylamino-4-N-methyl-stilbazolium tosylate. *Appl. Phys. Lett.*, 69(1):13–15, Jul. 1996.
- [214] J. Xu, L. Zhou, and M. Thakur. Measurement of electro-optic effects in single crystal films of N-(4-nitrophenyl)-L-prolinol. *Appl. Phys. Lett.*, 69(9):1197–1198, Jun. 1996.
- [215] Y. Shi, C. Zhang, H. Zhang, J. H. Bechtel, L. R. Dalton, B. H. Robinson, and W. H. Steier. Low halfwave voltage polymeric electro-optic modulators achieved by controlling chromophore shape. *Science*, 288:119–122, Apr. 2000.
- [216] M. Walther, K. Jensby, S. R. Keiding, H. Takahashi, and H. Ito. Far-infrared properties of dast. *Opt. Lett.*, 25(12):911–913, Jun. 2000.
- [217] A. M. Sinyukov and L. M. Hayden. Generation and detection of terahertz radiation with multilayered electro-optic polymer films. *Opt. Lett.*, 27(1):55–57, Jan. 2002.
- [218] M. A. Afromowitz. Refractive index of $Ga_{1-x}Al_xAs$. *Solid State Comm.*, 15:59–63, Feb. 1974.
- [219] R. W. P. King. *Transmission Line Theory*. McGraw-Hill, New York, 1955.
- [220] H. A. MacLeod. *Thin-Film optical filters*. Institute of Physics Publishing, 2001.
- [221] S. H. Wemple and M. DiDomenico. Optical dispersion and the structure of solids. *Phys. Rev. Lett.*, 23(20):1156–1160, 1969.
- [222] S. H. Wemple and M. DiDomenico. Behaviour of the electronic constant in covalent and ionic materials. *Phys. Rev. B*, 3(4):1338–1351, Feb. 1971.
- [223] W. Sellmeier. Zur Erklärung der abnormen Farbenfolge im Spektrum einiger Substanzen. *Ann. der Physik und Chemie*, 143:272–281, 1871.
- [224] D. T. F. Marple. Refractive index of GaAs. *J. Appl. Phys.*, 35(4):1241–1242, Apr. 1964.
- [225] R. E. Fern. Refractive Index of AlAs. *J. Appl. Phys.*, 42(9):3499–3500, Aug. 1971.

- [226] D. D. Sell, H. C. Casey, and K. W. Wecht. Concentration dependence of the refractive index for n- and p- type GaAs between 1.2 and 1.8 eV. *J. Appl. Phys.*, 45(6):2650–2657, Feb. 1974.
- [227] H. C. Casey, D. D. Sell, and M. B. Panish. Refractive index of AlGaAs between 1.2 and 1.8 eV. *Appl. Phys. Lett.*, 24(2):63–65, Sep. 1974.
- [228] M. D. Sturge. Optical absorption of Gallium Arsenide between 0.6 and 2.75 eV. *Phys. Rev.*, 127(3):768–773, Aug. 1962.
- [229] D. E. Aspnes and A. A. Studna. Dielectric functions and optical parameters of si, ge, gap, gaas, gasb, inp, inas, and insb from 1.5 to 6.0 ev. *Phys. Rev. B*, 27(2):985–1009, Jan. 1983.
- [230] F. Urbach. The long-wavelength edge of photographic sensitivity and of the electronic absorption of solids. *Phys. Rev.*, 92(5):1324, Oct. 1953.
- [231] S. R. Johnson and T. Tiedje. Temperature dependence of the Urbach edge in GaAs. *J. Appl. Phys.*, 78(1):5809–5811, Nov. 2006.
- [232] C. W. Greeff and H. R. Glyde. Anomalous Urbach tail in GaAs. *Phys. Rev. B*, 51(3):1778–1783, Jan. 1995.
- [233] G. Antonioli, D. Bianchi, and P. Franzosi. Intrinsic Urbach rule and electron-photon interaction in GaAs and related III-V compounds. *Physica Status Solidi B*, 106(1):79–84, Jan. 1981.
- [234] D. Redfield. The direct absorption edge in covalent solids. *Appl. Phys. Lett.*, 11(4):138–140, Aug. 1967.
- [235] J. D. Dow and D. Redfield. Toward a unified theory of Urbach’s rule and exponential absorption edges. *Phys. Rev. B*, 5(2):594–610, Jan. 1972.
- [236] J. I. Pankove. Absorption edge of impure Gallium Arsenide. *Phys. Rev.*, 140(6):2059–2065, Dec. 1965.
- [237] R. Mueckstein, M. Navarra-Cía, and O. Mitrofanov. Mode interference and radiation leakage in a tapered terahertz parallel plate waveguide. *Appl. Phys. Lett.*, 102(14):141103, Apr. 2013.
- [238] R. Mueckstein, M. Navarra-Cía, and O. Mitrofanov. Origins of dispersive terahertz pulse propagation in tapered parallel plate waveguides. *Conference of Lasers and Electro-Optics (CLEO)*, Jun. 2013.

- [239] R. Mendis and D. Grischkowsky. Undistorted guided-wave propagation of subpicosecond terahertz pulses. *Opt. Letters*, 26(11):846–848, Jun. 2001.
- [240] M. Waechter, M. Nagel, and H. Kurz. Metallic slit waveguide for dispersion-free low-loss terahertz signal transmission. *Appl. Phys. Lett.*, 90(6):61111, Feb. 2007.
- [241] M. Waechter, M. Nagel, and H. Kurz. Low-loss terahertz transmission through curved metallic slit waveguides fabricated by spark erosion. *Appl. Phys. Lett.*, 92(16):161102, Apr. 2008.
- [242] M. Nagel, A. Marchewka, and H. Kurz. Low-index discontinuity terahertz waveguides. *Opt. Express*, 14(14):9944–9954, Sep. 2006.
- [243] N. Klein, P. Lahl, U. Poppe, F. Kadlec, and P. Kuzel. A metal-dielectric antenna for terahertz near-field imaging. *J. Appl. Phys.*, 98(1):014910, Jul. 2005.
- [244] J. Liu, R. Mendis, D. M. Mittleman, and N. Sakoda. A tapered parallel-plate-waveguide probe for THz near-field reflection imaging. *Appl. Phys. Lett.*, 100:311011, Jan. 2012.
- [245] D. G. Cooke and P. U. Jepsen. Time-resolved THz spectroscopy in a parallel plate waveguide. *Phys. Status Solidi A*, 206(5):997–1000, Apr. 2009.
- [246] M. Theuer, S. Sree Harsha, and D. Grischkowsky. Flare coupled metal parallel-plate waveguides for high resolution terahertz time-domain spectroscopy. *J. Appl. Phys.*, 108(11):113105, Dec. 2010.
- [247] J. S. Melinger, N. Laman, S. Sree Harsha, and D. Grischkowsky. Line narrowing of terahertz vibrational modes for organic thin polycrystalline films within a parallel plate waveguide. *Appl. Phys. Lett.*, 89(25):251110, Dec. 2006.
- [248] J. Zhang and D. Grischkowsky. Adiabatic compression of parallel-plate metal waveguides for sensitivity enhancement of waveguide thz time-domain spectroscopy. *Appl. Phys. Lett.*, 86(6):061109, Feb. 2005.
- [249] S. - H. Kim, E. S. Lee, Y. B. Ji, and T. - I. Jeon. Improvement of THz coupling using a tapered parallel-plate waveguide. *Opt. Express*, 18(2):1289–1295, Jan. 2010.

- [250] M. Mbonye, R. Mendis, and D.M. Middleman. Study of the impedance mismatch at the output end of a THz parallel-plate waveguide. *Appl. Phys. Lett.*, 100:111120, Mar. 2012.
- [251] K. Iwaszczuk, A. Andryieuski, A. Lavrinenko, Z.-C. Zhang, and P. U. Jepsen. Terahertz field enhancement to the MV/cm regime in a tapered parallel plate waveguide. *Opt. Express*, 20(8):8344–8355, Mar. 2012.
- [252] E.S. Lee, J.S. Jang, S.H. Kim, Y.B. Ji, and T.-I. Jeon. Propagation of single-mode and multi-mode terahertz radiation through a parallel-plate waveguide. *J. Korean Phys. Soc.*, 53(4):1891–1896, Oct. 2008.
- [253] R. Mendis and D.M. Middleman. Comparison of the lowest-order transverse-electric (TE₁) and transverse-magnetic (TEM) modes of the parallel-plate waveguide for terahertz pulse applications. *Opt. Express*, 17(17):14839–14850, Aug. 2009.
- [254] R. Mendis and D.M. Middleman. An investigation of the lowest-order transverse-electric (TE₁) mode of the parallel-plate waveguide for the THz pulse propagation. *J. Opt. Soc. Am. B*, 26(9):6–13, Sep. 2009.
- [255] M. Navarra-Cía, R. Mueckstein, and O. Mitrofanov. Comment on "The transition from a TEM-like mode to a plasmonic mode in parallel plate waveguides". *Appl. Phys. Lett.*, 98(23):231113, Jun. 2013.
- [256] H. Zhan, R. Mendis, and D.M. Middleman. Characterisation of the terahertz near-field output of parallel-plate waveguides. *J. Opt. Soc. Am. B*, 28(3):558–566, Mar. 2011.
- [257] J.Z. Xu and J.Z. Zhang. Optical rectification in an area with a diameter comparable to or smaller than the center wavelength of terahertz radiation. *Opt. Letters*, 27(12):1067–1069, Jun. 2002.
- [258] G. Gallot, S.P. Jamison, R.W. McGowan, and D. Grischkowsky. Terahertz waveguides. *J. Opt. Soc. Am. B*, 17(5):851–863, May 2000.
- [259] C.-A. Balanis. *Advanced Engineering Electromagnetics*. John Wiley & Sons, Inc., 1989.
- [260] N. Marcuvitz. *Waveguide Handbook*. Peregrinus, 1993.
- [261] S. Ramo, J.R. Whinnery, and T. Van Duzer. *Fields and waves in communications electronics*. John Wiley & Sons, Inc., 1994.

- [262] M. Beruete, M. Navarro-Cía, and M. S. Ayza. Understanding anomalous extraordinary transmission from equivalent circuit and grounded slab concepts. *IEEE Trans. Microw. Theorie and Techn.*, 59(9):2180–2188, Sep. 2011.
- [263] O. Mitrofanov. Laser excess noise reduction in optical phase-shift measurements. *Appl. Opt.*, 42(14):2526–2531, May 2003.
- [264] R. C. Jones. A new calculus for the treatment of optical systems. *J. Opt. Soc. Am.*, 31:488–493, Jul. 1941.
- [265] A. Nahata, A. S. Weling, and T. F. Heinz. A wideband coherent terahertz spectroscopy system using optical rectification and electro-optic sampling. *Appl. Phys. Lett.*, 69(16):2321–2323, Oct. 1996.
- [266] S. Vidal, J. Degert, M. Tondusson, J. Oberle, and E. Freysz. Impact of dispersion, free carriers, and two-photon absorption on the generation of intense terahertz pulses in ZnTe crystals. *Appl. Phys. Lett.*, 98:191103, May 2011.
- [267] S. Mair. *Entwicklung eines optischen Nahfeld-Spektrometers im Terahertz-Bereich*. Thesis (PhD), University of Stuttgart, 2003.
- [268] K. Michel. *Die Grundzüge der Theorie des Mikroskops in elementarer Darstellung*. Wissenschaftliche Verlagsgesellschaft m.b.H., Stuttgart, 1964.

Symbols and Abbreviations

Latin Letter	Unit	
A_{BD}	[1]	Amplification of a balanced detector
\vec{A}_{PC}	[1]	Antenna vector
A_{PPWG}	[m^2]	Input aperture of the parallel plate waveguide
B_{3dB}^{THz}	[Hz]	3 db- THz Bandwidth of the micro-resonator
B_{FP}	[Hz]	Bandwidth of a Fabry Perot Cavity
c	[m/s]	Vacuum speed of light
C_{PB}	[F]	Junction Capacitance of a photodiode
C_{PPWG}	[1]	Coupling coefficient of a PPWG
$d_{Ap.}$	[m]	Diameter of a round aperture
$d_{cry.}$	[m]	Distance between the GaAs holder and the parallel plate waveguide input
$d_{det.}$	[m]	Distance between the near-field probe and the parallel plate waveguide output
$d_{far-field}$	[m]	Distance between two points that can be resolved in the far-field
d_{lens}	[m]	Distance between lens and the ZnTe crystal
d_{Layer}	[m]	Thickness of a layer
\vec{D}	[C/m ²]	Electric displacement vector
D_x, D_y, D_z	[C/m]	Electric displacement in the x, y, z -direction
E	[V/m]	Electric field
E_x, E_y, E_z	[V/m]	Electric field polarised in the x, y, z -direction
\vec{E}	[V/m]	Electric field vector
\mathcal{E}_0	[J]	Average transition energy in the Wemple model
$\mathcal{E}_{Band-gap}$	[J]	Band-gap energy
\mathcal{E}_d	[J]	Oscillator strength of the interband transition in the Wemple model
$E_{Gaussian}$	[V/m]	Electric field profile of a Gaussian beam
$\mathcal{E}_l, \mathcal{E}_u$	[J]	Lower and upper limit of the band-gap
$E^{opt.}$	[V/m]	Electric field of an optical beam
\mathcal{E}_{photon}	[J]	Energy of a photon
E_{sub}	[V/m]	Electric field in the wafer substrate
E^{SPP}	[V/m]	SPP electric field
$E^{SPP,x}, E^{SPP,z}$	[V/m]	SPP electric field polarised in the x, z -direction

Latin Letter	Unit	
E_T	$[V/m]$	Tangential electric field component
E_{TEM}	$[V/m]$	Electric field profile of the TEM mode
E^{THz}	$[V/m]$	THz electric field
E_{Urbach}	$[J]$	Urbach fitting parameter
$E(\vec{r}, t)$	$[V/m]$	Time - and space dependent electric-field
$f_{res, n_{FP}}$	$[Hz]$	Resonant frequency of a Fabry Cavity of the n_{FP} -th order
f_{THz}	$[Hz]$	THz frequency
$f_{Chopper}$	$[Hz]$	Chopper frequency
$f_{cut-off}$	$[Hz]$	Cut-off frequency
F	$[1]$	Finesse of a Fabry Perot Cavity
ΔI	$[W/m^2]$	Intensity difference of the beams exiting the Wollaston polariser
i_{in}	$[A]$	Incident current
i_{PC-A}	$[A]$	Current generated in a photoconductive antenna
i_{PD}	$[A]$	Current generated in a photodiode
$i_{Shotnoise}$	$[A]$	Shot noise current
i_{SPP}	$[A]$	Current generated by the SPP wave
i_{THz}	$[A]$	Current generated by the THz wave
I_0	$[W/m^2]$	Optical intensity of the probe beam incident to the Wollaston polariser
I_+, I_-	$[W/m^2]$	Optical intensities in the two beams exiting the Wollaston polariser
I_{noise}	$[W/m^2]$	Intensity of the noise
$I^{opt.}$	$[W/m^2]$	Optical intensity
$I_{reflected}, I_{incident}$	$[W/m^2]$	Optical intensity of the reflected and incident light
$I_{unbal.}$	$[W/m^2]$	Unbalanced intensity
k_0	$[1/s]$	Wavevector of a free propagating wave
l_c	$[m]$	Coherence Length in a crystal
$l_{crystal}$	$[m]$	effective pathlength in a crystal
L	$[m]$	Cavity length of a Fabry Perot Resonator

Latin Letter	Unit	
M_i	[1]	Optical moment i-th order in the Wemple model
n	[1]	Refractive index
n_0	[1]	Refractive index of a material without an electric-field present
$n_{av.}$	[1]	Average refractive index
n_{gap}	[1]	Refractive index of the gap material in a parallel plate waveguide
$n_{gr.}^{opt.}$	[1]	Group refractive index for optical frequencies
n_{FP}	[1]	n_{FP} -th order of a Fabry Perot cavity
$n_{substrate}$	[1]	Refractive index of the wafer substrate
n_{THz}	[1]	Refractive index in the THz range
n_x, n_y, n_z	[1]	refractive indices along the principle axes x, y, z
$N_{Bottom-DBR}$	[1]	Number of layers in the bottom - DBR
N_{DBR}	[1]	Number of layers in the DBR
N_{Spacer}	[1]	Number of layers in the spacer
$N_{Top-DBR}$	[1]	Number of layers in the top - DBR
p	[m]	Gap size in a parallel plate waveguide
P_{PD}	[W]	Optical power incident to a photodiode
P_{Probe}, P_{Pump}	[W]	Optical power of the probe and pump beam
q	[C]	Elementary charge
$Q_{FP, n_{FP}}$	[1]	Q-Factor of a Fabry Perot cavity of the n_{FP} -th order
Q_{max}	[1]	Maximum Q-Factor to fulfill the micro-resonator requirements
r	[m/V]	Electro-optic coefficient
\vec{r}_{ij}	[m/V]	Linear electro-optic tensor
$r_{spectral}^{MR}$	[$\%$]	Spectral reflection coefficient of the micro-resonator
r_{PPWG}	[$\%$]	Electric-field reflectivity for a PPWG

Latin Letter	Unit	
R	[%]	Reflectivity
$R_{Feedback}$	[Ω]	Feedback resistance
$R_{Leak.}$	[W]	Leakage radiation power
R_{PD}	[Ω]	Shut resistance of a photodiode
R_S	[Ω/m^2]	Surface resistance
\bar{v}_{RMS}	[V]	Root mean square of the voltage
V_{TI}	[V]	Output voltage of a transimpedance amplifier
$\vec{u}_x, \vec{u}_y, \vec{u}_z$	[1]	Unity vectors in the x, y, z -directions
\vec{u}_{PC-A}	[1]	Unity vector of the photoconductive antenna
t	[s]	Time
T_{FP}	[%]	Transmission of a Fabry-Perot cavity
w	[m]	Width of the parallel plate waveguide plate
w_{in}, w_{out}	[m]	Width of the parallel plate waveguide plate at the input and output
y_0	[S]	Optical Admittance of the incident medium
y_n	[S]	Optical Admittance of a layer with refractive index n
y_{stack}	[S]	Optical Admittance of a layer stack
Y	[S]	Optical Admittance of free-space
x, y, z	[1]	Cartesian coordinate axes
Z_0	[S]	Optical Impedance of free-space
Z_{MR}	[S]	Optical Impedance of the micro-resonator
Z_{PPWG}	[S]	Optical Impedance of a PPWG

Greek Letter	Unit	
α	$[cm^{-1}]$	Absorption coefficient
α_0	$[cm^{-1}]$	Absorption coefficient directly at the bandgap edge
α_{PBS}	[1]	Attenuation of the PBS
α_{TEM}	$[cm^{-1}]$	Absorption coefficient of the TEM mode
β	$[1/s]$	Propagation constant of an electric field
β_{zx}	$[1/s]$	Propagation constant of an electric field with a propagation in z - and polarisation in x -direction
$\chi^{(n)}$	$[F/m]$	Susceptibility of the n - (th) order
δ_d	$[m]$	Electric-field $\frac{1}{e}$ -decay length of the surface plasmon polariton into a dielectric
δ_{Layer}	$[m]$	Optical thickness of a layer
δ_m	$[m]$	Electric-field $\frac{1}{e}$ -decay length of the surface plasmon polariton into a metal
δ_{SPP}	$[m]$	Electric-field $\frac{1}{e}$ -decay length of the surface plasmon polariton along its propagation direction
ϵ_0	$[F/m]$	Vacuum permittivity
ϵ_d	$[F/m]$	Permittivity of a dielectric
ϵ_{ij}	$[F/m]$	Tensor element of the permittivity tensor with $i, j = x, y, z$
ϵ_m	$[F/m]$	Permittivity of a metal
ϵ_{needle}	$[F/m]$	Permittivity of a dielectric needle
$\epsilon_x, \epsilon_y, \epsilon_z$	$[F/m]$	Permittivity along a principle axis x, y, z
ϕ_0	$[\circ]$	Phase retardation in a Fabry Perot cavity
$\phi_{BulkCrystal}$	$[\circ]$	Induced electro-optic phase-shift in a bulk crystal
ϕ_{EO}	$[\circ]$	Phase shift induced due to the electro-optic effect
$\phi_{EO,x} \phi_{EO,y}$	$[\circ]$	Phase shift induced due to the electro-optic effect along the principle axes x, y
ϕ_{MR}	$[\circ]$	Induced electro-optic phase-shift
	$[\circ]$	in the micro-resonator

Greek Letter	Unit	
λ	[nm]	Wavelength
λ_0	[nm]	Wavelength of an optical imaging system
λ_{centre}	[nm]	Centre wavelength of an optical pulse
λ_{res}	[nm]	Resonant wavelength in the micro-resonator cavity
λ_{SPP}	[nm]	Wavelength of the SPP wave
μ_0	[H/m]	Permeability in vacuum
ω	[1/s]	Angular frequency
ω_0	[m]	Beam waist of a Gaussian beam
σ	[C/m ²]	Surface charge distribution
σ_{Al}	[S/m]	Conductivity per length unit for aluminium
σ_{DC}	[S/m]	DC Conductivity per length unit
τ_{BD}	[s]	Time response of the balanced detector
τ_{LI}	[s]	Integration time of the Lock-in amplifier
$\tau_{prop.}$	[s]	Propagation time of the probe beam through the crystal
τ_{probe}	[s]	Pulse width of the probing beam

Abbreviation

AFM	Atomic Force Microscope
<i>cw</i>	Continuous Wave
DBR	Distributed Bragg Reflector
DUT	Device Under Test
FFT	Fast Fourier Transform
FSR	Free Spectral Range
FWHM	Full Width Half Maxima
LSP	Localised Surface Plasmon
MBE	Molecular Beam Epitaxy
NA	Numerical Aperture
OpAmp	Operational Amplifier
PBS	Polarising Beam Splitter
PC-Antenna	Photoconductive Antenna
PPWG	Parallel Plate Waveguide
PSTM	Photon Scanning Tunneling Microscope
Q-Factor	Quality Factor
RMS	Root Mean Square
SNOM	Scanning Near-Field Optical Microscope
SPP	Surface Plasmon Polariton
TEM	Transverse Electro-Magnetic
TE	Transverse Electric
TL-Stage	Translation Stage
THz	Terahertz
THz TDS	Terahertz Time Domain Spectroscopy

List of Figures

- 1.1 (a) Propagation of a surface plasmon polariton on a metallic surface; (b) Surface plasmon dispersion relation; Electric-field E_z into the dielectric and the metal at THz frequencies (c) and at optical frequencies (d). 12
- 1.2 (a) Far-field detection of light reflected by protrusions with spatial dimensions bigger (left) and smaller (right) than the employed wavelength λ_0 ; (b) A step function and its low-pass response for three cut-off frequencies; (c) Evanescent electric field decay for k-vectors bigger than k_0 16
- 1.3 (a) Electro-optic sampling with a $30 \mu m$ -thick ZnTe crystal (from Ref. [101]); (b) Near-field microscopy with a integrated near-field probe (from Ref. [78]); (c) Dynamic aperture approach (from Ref. [126]); (d) A metallic tip acting as a scattering probe; the far-field THz detector includes a PC-antenna (from Ref. [127]); (e) A metallic tip scans a sample; the far-field THz detector also includes a PC-antenna (from Ref. [128]). 21
- 1.4 (a) Converting the E^{SPP} into a free-space beam (from Ref. [129]); (b) Detection of the E^{SPP} along a metallic wire with a photoconductive-type probe (from Ref. [133]); (c) Probing the "edge plasmons" inside a parallel plate waveguide with a needle-probe (from Ref. [131]); (d) SPP detection with a Silicon on Sapphire chip in the shading region of sub-wavelength holes; The SPP wave is shown in the bottom image for a specific moment in time (from Ref. [134]); (e) SPP detection with an electro-optic crystal in the shadow region of a sub-wavelength aperture (from Ref. [64]); the inset shows the measured E^{SPP} -distribution in the proximity of the aperture. 23
- 2.1 (a) The detection of a THz SPP wave at the tip of a metallic wire waveguide with a PC-antenna in a fibre-coupled THz receiver (from Ref. [135]); (b) Detection of a THz wave at the edge of a metallic sheet with a PC-antenna; the SPP wave is launched in a parallel plate waveguide and a blocking plate is introduced to avoid the detection of energy which is not confined to the metallic sheet (from Ref. [138]). 29

2.2	(a) Different components of the integrated near-field probe shown separately; (b) Top view of the probe, showing how E_T couples into the PC-antenna; (c) Schematic image of a SPP propagating along the metallic surface of a sample; the green and the red areas correspond to positive and negative charges, respectively, and the black lines represent the electric-field E^{SPP} ; (d) The same situation as in (c), but with the metallic surface of the integrated near-field probe positioned parallel to the sample; the bottom diagram shows the electric-field component normal to the probe surface E_z (blue line) and the resulting tangential field component across the aperture E_T (brown line); Figures (a, b) are published in Ref. [114].	30
2.3	(a) Schematic diagram of the employed experimental system; (b) Detailed image of the dashed box area in (a); Figure (b) is published in Ref. [114].	33
2.4	(a) Detected space-time map (xt -map) of the electric-field in the near-field of the bow-tie antenna along a line $y = 0 \mu m$; (b) Measured near-field images of the bow-tie antenna in the xy -plane for four moments in time as they were indicated in (a); The four maps are normalised to the overall maximum at t_3 ; (c) Detected THz waveform at the centre of the circular waveguide output; (d) Measured near-field image of the antenna for the moment t_5 , the shape of the bow-tie antenna is shown by the dashed line; Figures (a, b, d) are published in Ref. [114].	35
2.5	(a) Surface plasmon polariton excitation at the edges of the bow-tie structure; The inset shows the orientation of the near-field probe; (b) The excitation of SPP waves with different polarity at opposite edges of the antenna; (c) Detected image by the near-field probe; Figures (a, c) are published in Ref. [114].	36
2.6	(a) The red dashed box surrounds the area of the electric-field map (Fig. 2.4 (d)) used for image reconstruction; (b) Reconstructed E^{SPP} image; Both figures are normalised to their individual maxima; The figures are published in Ref. [114].	38
2.7	(a) Measured electric-field map with the detector PC-antenna oriented in the y -direction; (b) E^{SPP} image formation on the bow-tie antenna; The inset shows the orientation of the PC-antenna in the near-field probe; Figure (a) is published in Ref. [114].	39

2.8	(a) The experimental system for SPP imaging excited by a focused THz beam. This is a detailed view of the dashed box in Fig. 2.3 (a); (b) The simulated E_z -field of a focused THz beam on the surface of the integrated probe and the excited E^{SPP} . Both figures are published in Ref. [114].	40
2.9	Detected electric-field patterns near a strongly focused incident THz beam polarised in the x -direction (a) and the y -direction (b). In both cases, the PC-antenna is aligned in the x -direction and the field maps are normalised to the maximum in (a); (c) The two electric-field maps in the top row show the simulated SPP-distribution (1) and the imaged SPP-distribution (2) for the incident THz beam polarised in the x -direction. The bottom row shows the simulated SPP-distribution (3) and the imaged SPP-distribution (4) for the THz beam polarised in the y -direction. The insets indicate the simulated E_z -distribution for each row. Images (a, b) and the field maps (2, 4) in (c) are published in Ref. [114, 150].	42
2.10	Reconstructed SPP patterns for an incident beam polarised in the x - (a) and the y - (b) direction; Figure (b) is published in Ref. [114].	44
2.11	(a) Space-time maps along the x -axis ($y = 0 \mu m$) (top row) and the y -axis ($x = 0 \mu m$) (bottom row) for different distances z between the Si lens and the near-field probe; All field maps are normalised to the maximum value at $z = 70 \mu m$; (b) Schematic diagram of the experimental system; (c) Normalised detected electric-field amplitude along the x - and y -axis as a function of the distance from the centre at ($x = 0 \mu m$, $y = 0 \mu m$); the plotted values are taken along a line as it is shown by the dashed line in the inset; a Gaussian fit and a SPP fit according to Eq. (2.5) are added for comparison; Figures (a, c) are published in Ref. [150].	45
2.12	The simulated electric-field patterns on the bow-tie antenna with and without the metallic sheet of the near-field probe being present. The four moments in time correspond to the same moments as in Fig. 2.4 (b). The image was taken from Ref. [159].	48
2.13	(a) The geometry of a planar antenna which is imaged by the integrated near-field probe; (b) Near-field image of the same antenna exhibiting unexpected white and black shadows (from Ref. [78]). . .	49
3.1	The cubic structure of a GaAs crystal.	53

3.2	Index ellipsoids for (a) an isotropic material ($n_x = n_y = n_z$), (b) an optically uniaxial material ($n_x = n_y < n_z$), and (c) an optically biaxial material ($n_y < n_x < n_z$).	55
3.3	Propagation of a linear polarised electric-field in the "ellipse index plane" and its projection on the principle axis of the ellipsoid.	55
3.4	Atomic structure and charge distribution of GaAs before (a) and after (b) the application of an external electric-field.	58
3.5	(a) THz electric-field detection with a $150 \mu m$ thick ZnTe crystal with a co-propagating probe beam (from [189]); (b) The detection of a THz SPP at the end of a wire with a $1 mm$ thick ZnTe crystal in reflection mode (from [136]); (c) Sampling a coplanar waveguide structure with a $1.6 \mu m$ thick fibre-coupled $Al_{0.3}Ga_{0.7}As$ probe (from [190]).	60
3.6	(a) Resonant wavelengths in a cavity with length L ; (b) Transmission spectrum of a Fabry-Pérot Cavity.	63
3.7	(a) The structure of a DBR and the principle of multiple reflections at any interface; (b) Frequency response of three DBRs with 5, 10, and 15 GaAs and $Al_{0.9}Ga_{0.1}As$ DBR-layers at a central wavelength $\lambda_{centre} = 970 nm$; (c) A Fabry-Pérot cavity with a Top- and Bottom-DBR and a spacer; (d) The calculated spectral reflectivity of the structure in (c).	65
3.8	Surface Plasmon detection on a metallic surface with a fibre-coupled micro-resonator.	68
4.1	A multi-layer stack for the calculation of the optical response with the Optical Admittance Approach.	75
4.2	Comparison of the refractive indices modelled by Afromowitz and Wemple for GaAs in (a) and AlAs in (b). Both models are also compared to experimentally determined values: The values for the red stars in (a) were taken from Ref. [224] and the blue crosses from Ref. [226, 227]. In (b), the experimental data were taken from Ref. [225].	77
4.3	The absorption coefficient α of GaAs in the band-gap region (a) and in the proximity of the band-gap edge (b). The experimentally measured values were taken from Ref. [228] in (a) and Ref. [229] in (b).	77
4.4	A schematic design of the computer program to simulate the optical response of the micro-resonator.	81

4.5	(a) The refractive indices of $GaAs$ and $Al_{0.9}Ga_{0.1}As$ as a function of the wavelength. The indices at $\lambda = 890\text{ nm}$ and $\lambda = 970\text{ nm}$ are highlighted in this plot; (b) The reflectivity curves of two resonators designed for a resonant wavelength at 970 nm and 890 nm. The curve for 890 nm is shifted 80 nm to larger wavelengths for a better comparison.	82
4.6	3dB-bandwidth, electro-optic enhancement, and reflectivity as a function of the resonant wavelength. The simulated design comprised 5 Top-DBR layers, 3 spacer layers, and 15 Bottom-DBR layers. The FWHM of the incident electric-field was 140 fs.	83
4.7	3dB-bandwidth, electro-optic enhancement, and reflectivity in a symmetric resonator configuration for different numbers of DBR-layers.	85
4.8	Time evolution of the incident and the reflected beam for two different asymmetric designs.	86
4.9	A diagram showing resonator configurations which fulfill the stated requirements as a function of Bottom-DBR layers and Q-factors. . .	87
4.10	The selected micro-resonator configuration as it is grown on a $GaAs$ wafer. The thicknesses of the layers are drawn to scale.	89
4.11	3db-bandwidth, the electro-optic enhancement, and the reflectivity of the chosen resonator structure as a function of the electric field FWHM of the incident probe beam pulse.	90
4.12	(a) Measured and matched simulated reflectivity of the fabricated micro-resonator; (b) Magnified view of the resonant region in (a). .	91
5.1	Using a THz waveguiding structure to guide THz radiation from the source to the micro-resonator.	94
5.2	(a) Three-dimensional view of the PPWG; (b) The guiding surface and the most important parameters of the waveguide plate; (c) Image of the AFM scan before polishing; (d) Image of the AFM scan after polishing.	98
5.3	(a) Schematic diagram of the experimental system (xz -plane). A detailed image of the elements inside the dashed box is shown at the bottom from a yz -perspective; (b) Photograph of the PPWG and the integrated near-field probe (xz -plane); Figure (b) is published in Ref. [237].	99

5.4	(a) The measured waveforms for four different distances between the PC-antenna and the PPWG output ($d_{det.}$). Each waveform is normalised to its respective maximum and an arbitrary offset is added to distinguish the curves; (b) Normalised peak-to-peak amplitudes of the detected waveforms as a function of $d_{det.}$. The values are normalised to the maximum amplitude at $d_{det.} = 300 \mu m$	101
5.5	(a) The measured peak-to-peak amplitude of the THz waveforms as a function of the ZnTe crystal - lens distance (d_{lens}); (b) The measured peak-to-peak amplitude of the THz waveforms as a function of the GaAs/ZnTe holder - PPWG input distance ($d_{cry.}$).	103
5.6	(a) A schematic diagram of how the incident THz Gaussian-type beam is scanned along the input aperture of the PPWG; (b) A comparison of the experimentally determined and the calculated convolution of the input THz beam and the input aperture of the PPWG.	104
5.7	Normalised peak-to-peak amplitudes of the experimental (red line with dots) and simulated (black lines) waveforms as a function of the gap size. The solid and the dashed lines correspond to the simulation with and without the detector present; the calculated coupling coefficient (orange line) and the simulated radiation leakage (violet line) as a function of the gap size. The dashed horizontal line (green) is the detected THz amplitude without the PPWG. A similar plot is published in Ref. [237].	105
5.8	(a) Measured THz pulse waveforms for three different gap sizes p ; the waveforms are normalised to the maximum amplitude at $p = 500 \mu m$; (b) Simulated waveforms for the same configurations as shown in (a); the waveforms are normalised to the maximum amplitude of the simulated incident THz pulse; (c) Measured (dots) and simulated (lines) spectra of the waveforms in (a, b); the spectra are normalised to their individual maxima; (d) The waveform (top) and the spectrum (bottom) of the simulated incident THz pulse; (Figures (a, b, c) are published in Ref. [237]).	110
5.9	(a) Electric-field distribution inside the PPWG in the yz -plane for a moment in time when the THz pulse is close to the output; (b) Front view of the electric-field distribution in close proximity to the PPWG output; the gap size for (a, b) is $100 \mu m$ and all electric-field distributions are normalised to their individual maxima. Both figures are published in Ref. [237].	111

5.10	The excitation of the TE_{02} -mode as a result of reflections of the fundamental TEM -mode at the "virtual boundaries" along the waveguide edges.	112
5.11	(a) Simulated electric-field distributions for two moments in time t_1 and t_2 inside the waveguide gap ($t_1 < t_2$ and $p = 100 \mu m$). The straight grey line shows the PPWG geometry covering the final 7 mm of the plate. The dashed grey line shows the extension of the plate to a sub-wavelength width in the simulations. The electric-field distribution for both moments are normalised to their individual maxima.	113
6.1	A schematic diagram of the electro-optic detection system used in the experiments (TL-stage stands for translation stage, PBS for polarising beam splitter, PD for photodiode, Op-Amp for operational amplifier, Lock-In Ampl. for Lock-In amplifier).	117
6.2	The top row shows the orientation of the incident probe beam polarisation and the optical elements it has to pass sequentially. The middle row decomposes the polarisation of the probe beam along the principle axes and shows the resulting polarisations on a time axes after passing a specific optical element. The bottom row shows the polarisation state of the probe beam after passing a specific optical element.	119
6.3	The intensity in both beam paths I_+ and I_- when exiting the Wollaston polariser as a function of the phase-shift ϕ_{EO} for five different input intensities $2^n \cdot I_0$; The difference $\Delta I = I_+ - I_-$ is shown by the orange line.	120
6.4	(a) Electric circuit diagram of the balanced detector; (b) Measured and calculated response of the balanced detector.	123
6.5	(a) Detected X_{RMS} and calculated shot-noise level as a function of the optical power incident to both photodiodes $P_{PD1} + P_{PD2}$; (b) Calculated level of balancing of the as a function of the incident power. The green stars show the measurement points.	127
6.6	(a) Envelope of an optical pump pulse with a FWHM of 120fs and its second temporal derivative, which corresponds to the generated E^{THz} waveform; (b) Spectra of THz pulses generated by optical pulses with different FWHMs (related to the intensity).	128
6.7	(a) The refractive index $n(f_{THz})$ and the group refractive index $n_{gr.}(\lambda_{opt.})$ as a function of the optical wavelength and THz frequency); (b) The coherence length for ZnTe as a function of the THz frequency.	129

7.1	Diffraction limit of a focused beam.	179
7.2	The orientation of the angles α and β with respect to the coordinate system and the principle axes of the waveplate and the polariser. . .	187

List of Tables

3.1	Change in the refractive index of all three optical axes for three different cases of incident polarisation [171]; n_0 is the refractive index for $E = 0$	57
4.1	Degrees of freedom in the resonator design and their impact on its optical parameters.	73
4.2	The resonator configurations with the top-five values for the electro-optic efficiency listed with their most important parameters. Due to space restrictions, $N_{Top-DBR}$ was replaced by N_1 and $N_{Bottom-DBR}$ by N_2	88
4.3	A comparison of the 3dB - bandwidth, the reflectivity, and the electro-optic enhancement of the ideal electro-optic micro-resonator and the fabricated one (on the wafer and fibre-coupled).	92
7.1	Resonator configurations that fulfill the minimum requirements listed with their respective electro-optic enhancement, reflectivity, 3 dB - bandwidth, phase shift, and efficiency; Due to space restrictions, $N_{Top-DBR}$ was replaced by N_1 , N_{spacer} by N_2 , and $N_{Bottom-DBR}$ by N_3 . The maximum value for each column is highlighted with a blue background and the five configurations with the maximum electro-optic efficiency are highlighted in bold. The line with the final design is highlighted with a red background.	185

Appendix

Appendix A

Derivation of the Surface Plasmon Polariton Dispersion Relation

The time- and space-dependent electric-field $\vec{E}(\vec{r}, t)$ and magnetic-field $\vec{B}(\vec{r}, t)$ vectors are solutions to the wave equation:

$$\nabla^2 \vec{E}(\vec{r}, t) - \frac{1}{c^2} \frac{\partial^2}{\partial t^2} \vec{E}(\vec{r}, t) = 0, \quad (7.1)$$

$$\nabla^2 \vec{B}(\vec{r}, t) - \frac{1}{c^2} \frac{\partial^2}{\partial t^2} \vec{B}(\vec{r}, t) = 0. \quad (7.2)$$

The surface plasmon polariton can be described as an electro-magnetic wave which propagates in a direction parallel to the metal surface, which will be the x -direction in the following. The metal-dielectric interface is set at $z=0$ (metal part is $z < 0$) and the propagating electric-field has components in the x - and z -direction $\vec{E}(\vec{r}, t) = (E_x(\vec{r}, t), 0, E_z(\vec{r}, t))$ and the magnetic-field only a component in the y -direction $\vec{H}(\vec{r}, t) = (0, H_y(\vec{r}, t), 0)$. The subscripts "d" and "m" in the following stand for the electro-magnetic field propagating either in the dielectric or the metal. Taking into account these definitions, the solutions to the wave equations in the dielectric ($z > 0$) are

$$\vec{H}_d(\vec{r}, t) = (0, H_{d,y}, 0) e^{i(k_{d,x}x + k_{d,z}z - \omega t)}, \quad (7.3)$$

$$\vec{E}_d(\vec{r}, t) = (E_{d,x}, 0, E_{d,z}) e^{i(k_{d,x}x + k_{d,z}z - \omega t)}. \quad (7.4)$$

For the metal $z < 0$, the solutions are:

$$\vec{B}_m(\vec{r}, t) = (0, B_{m,y}, 0) e^{i(k_{m,x}x - k_{m,z}z - \omega t)}, \quad (7.5)$$

$$\vec{E}_m(\vec{r}, t) = (E_{m,x}, 0, E_{m,z}) e^{i(k_{m,x}x - k_{m,z}z - \omega t)}. \quad (7.6)$$

The wavevectors components in both the dielectric and the metal satisfy:

$$k_{d,x}^2 + k_{d,z}^2 = \epsilon_d k_0^2, \quad (7.7)$$

$$k_{m,x}^2 + k_{m,z}^2 = \epsilon_m k_0^2. \quad (7.8)$$

The boundary conditions along a dielectric/metal interface force the tangen-

tial electric- and magnetic- field components to be continuous:

$$k_{d,x} = k_{m,x} (= k_x), \quad (7.9)$$

$$E_{d,x} = E_{m,x}, \quad (7.10)$$

$$H_{d,y} = H_{m,y}. \quad (7.11)$$

Taking into account one of the Maxwell equations ($\nabla \times \vec{H}(\vec{r}, t) = \epsilon \frac{\partial \vec{E}(\vec{r}, t)}{\partial t}$) with $H_x, H_z = 0$, one can find the relations:

$$k_{d,z} H_{d,y} = -\omega \epsilon_d E_{d,x}, \quad (7.12)$$

$$-k_{m,z} H_{m,y} = -\omega \epsilon_m E_{m,x}. \quad (7.13)$$

Using these equations together with Eq. (7.9) - (7.11) leads to

$$\frac{k_{d,z}}{\epsilon_d} = -\frac{k_{m,z}}{\epsilon_m}. \quad (7.14)$$

Combing this equation with Eq. (7.7) and (7.8) leads to similar dispersion relations as they are presented in Eq. 1.1 to 1.3 in Chapter 1:

$$k_{d,z}^2 = \frac{\epsilon_d^2}{\epsilon_d + \epsilon_m} k_0^2, \quad (7.15)$$

$$k_{m,z}^2 = \frac{\epsilon_m^2}{\epsilon_d + \epsilon_m} k_0^2, \quad (7.16)$$

$$k_x^2 = \pm \frac{\epsilon_d \epsilon_m}{\epsilon_d + \epsilon_m} k_0^2. \quad (7.17)$$

Appendix B

Diffraction Limit in Optical Imaging Systems

In his publication (Ref. [72]), Ernst Abbe investigates the focusing capabilities of an optical microscope. He thereby uses Huygens principles, which states that the wavefront of a propagating wave can be considered as infinite waveflats emanating from every point of the original wavefront. One can apply this principle to a point source which is focused by a lens, as shown in Fig. 7.1. (A similar derivation of the beam spot diameter in the beam focus is done in Ref. [267]).

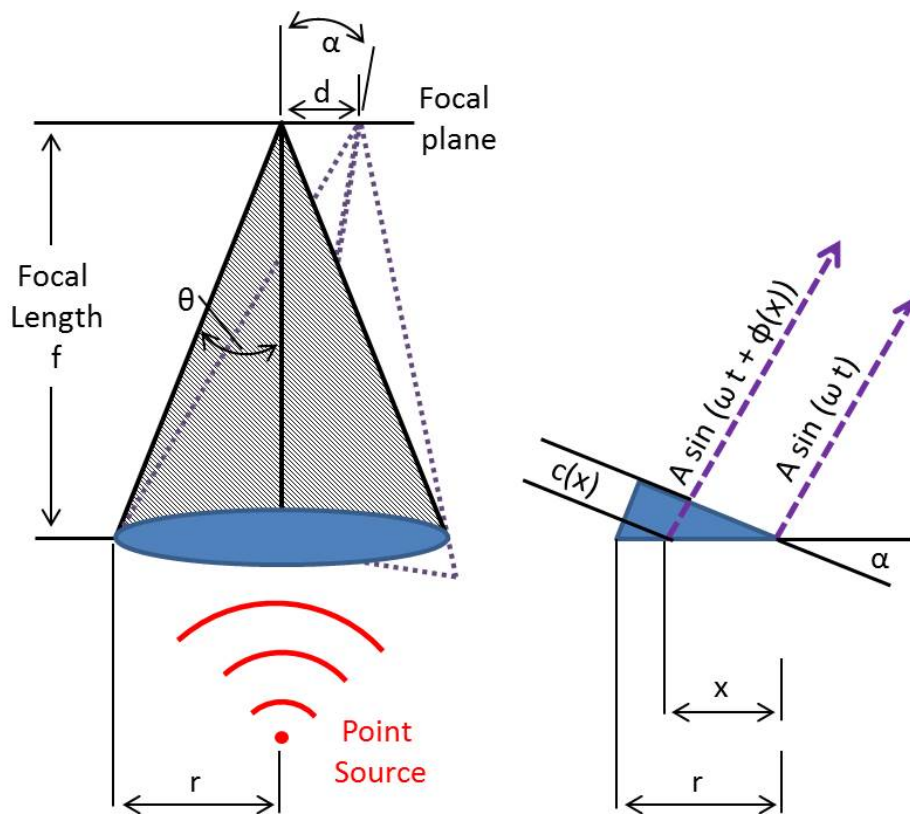


Fig. 7.1: Diffraction limit of a focused beam.

This figure shows a point source which illuminates a lens with a finite width r . In this example, the shape of the lens does not play a role and the lens is considered as a line with an infinite number of point sources distributed along a distance $2r$ which focuses the incident light on a screen in the focal plane. The distance in the propagation length between a wave emitted at the centre of the length and at a distance x away from the centre is

$$c(x, \alpha) = x \cdot \sin(\alpha). \quad (7.18)$$

This leads to a phase-difference

$$\phi(x, \alpha) = 2\pi \frac{c(x, \alpha)}{\lambda_0}, \quad (7.19)$$

where λ_0 is the wavelength of the optical imaging system. Considering an amplitude A and an angular frequency ω , this propagating wave can be described by:

$$A \sin(\omega t + \phi(x, \alpha)). \quad (7.20)$$

An integration of all point sources along x leads to the overall electric-field as a function of α :

$$\begin{aligned} E(\alpha) &= \int_{-r}^r A \sin(\omega t + \phi(x, \alpha)) dx = \\ &= \int_{-r}^r A \sin(\omega t + 2\pi \frac{x \sin(\alpha)}{\lambda_0}) dx = \\ &= 2 \cdot A \cdot r \frac{\sin(2\pi \frac{r \sin(\alpha)}{\lambda_0})}{2\pi \frac{r \sin(\alpha)}{\lambda_0}} \cdot \sin(\omega t). \end{aligned} \quad (7.21)$$

In the geometrical configuration above, the ratios $\frac{r}{\sin\theta}$ and $\frac{d}{\sin\alpha}$ are identical, which allows rewriting Eq. (7.22) as a function of d and θ . This shows the electric-field distribution in the focal plane:

$$E(d, \theta) = 2 \cdot A \cdot r \frac{\sin(2\pi \frac{d \sin(\theta)}{\lambda_0})}{2\pi \frac{d \sin(\theta)}{\lambda_0}} \cdot \sin(\omega t). \quad (7.22)$$

As a result, the electric-field distribution in the focal plane is described by a sinc-function. For the respective intensity distribution $I(d, \theta) = (E(d, \theta))^2$, the focal spot has a radius (from the centre to its first Intensity minimum) of d_0

$$d_0 = \frac{\lambda_0}{2 \sin(\theta)}. \quad (7.23)$$

The same derivation has been done for the three-dimensional case [268], which gave the results

$$d_0 = 1.22 \frac{\lambda_0}{2 \sin(\theta)}. \quad (7.24)$$

Assuming a theoretical numerical aperture of $2 \cdot \theta = 180^\circ$ in Eq. (7.24), the spatially smallest focal spot of an optical beam is $1.22\lambda_0$. An optical imaging system can only resolve two different focal spots when the maximum of the one spot spatially overlaps with the minimum of the second spot. Therefore, the resolving capability is limited to half of the beam diameter in the focal spot, which is $0.61\lambda_0$

Appendix C

Propagation of Electro-Magnetic Waves in Crystals

Propagation of electromagnetic waves through a medium has to comply with the Maxwell equations. In a homogeneous and lossless medium, the mutual relation of both space- and time-dependent electric- and magnetic-field vectors $\vec{\mathbf{E}}(\vec{\mathbf{r}}, t)$ and $\vec{\mathbf{H}}(\vec{\mathbf{r}}, t)$ is given by [165]:

$$\nabla \times \vec{\mathbf{E}}(\vec{\mathbf{r}}, t) = -\mu \cdot \frac{\delta}{\delta t} \vec{\mathbf{H}}(\vec{\mathbf{r}}, t) \quad (7.25)$$

and

$$\nabla \times \vec{\mathbf{H}}(\vec{\mathbf{r}}, t) = \epsilon \cdot \frac{\delta}{\delta t} \vec{\mathbf{E}}(\vec{\mathbf{r}}, t). \quad (7.26)$$

Assuming a plane waveform in a Cartesian coordinate system which is uniform in the x - y -plane ($\frac{\delta}{\delta x} = \frac{\delta}{\delta y} = 0$) and propagating along the z -axis, Eq. (7.25) and (7.26) can be rewritten as the following six relations:

$$\frac{\delta}{\delta z} E_y(\vec{\mathbf{r}}, t) = \mu \cdot \frac{\delta}{\delta t} H_x(\vec{\mathbf{r}}, t) \quad (7.27)$$

$$\frac{\delta}{\delta z} E_x(\vec{\mathbf{r}}, t) = -\mu \cdot \frac{\delta}{\delta t} H_y(\vec{\mathbf{r}}, t) \quad (7.28)$$

$$\frac{\delta}{\delta z} H_y(\vec{\mathbf{r}}, t) = -\epsilon \cdot \frac{\delta}{\delta t} E_x(\vec{\mathbf{r}}, t) \quad (7.29)$$

$$\frac{\delta}{\delta z} H_x(\vec{\mathbf{r}}, t) = \epsilon \cdot \frac{\delta}{\delta t} E_y(\vec{\mathbf{r}}, t) \quad (7.30)$$

$$0 = \mu \cdot \frac{\delta}{\delta t} H_z(\vec{\mathbf{r}}, t) \quad (7.31)$$

$$0 = \epsilon \cdot \frac{\delta}{\delta t} E_z(\vec{\mathbf{r}}, t) \quad (7.32)$$

Hereby, the subscript indicates the direction of polarisation of the respective field. The last two equations (7.31) and (7.32) show that no longitudinal field component of the electric nor magnetic wave exists. This means, that both field components of the plane wavefront only oscillate in the x - y -plane.

The polarisations of both the electric and magnetic field components are now chosen to be parallel to the coordinate axes x and y . This means for an arbitrary beam, that either the pair of field elements $E_x(\vec{\mathbf{r}}, t)$ and $H_y(\vec{\mathbf{r}}, t)$ or $E_y(\vec{\mathbf{r}}, t)$ and

$H_x(\vec{\mathbf{r}}, t)$ exist. Here, the first pair is randomly selected and the second one is set to 0. As a consequence, Eq. (7.28) and (7.29) are the only none-vanishing equations. Using both remaining equations and eliminating $H_y(\vec{\mathbf{r}}, t)$, one obtains the following equation:

$$\frac{\delta^2}{\delta z^2} E_x(\vec{\mathbf{r}}, t) = \epsilon_x \cdot \mu \cdot \frac{\delta^2}{\delta t^2} E_x(\vec{\mathbf{r}}, t) \quad (7.33)$$

In this case, the value ϵ_x describes the specific permittivity which the electric-field vector experiences while propagating along the z -axis and oscillating along the x -axis and μ represents the respective permeability. Since only non-magnetic materials are considered in the scope of this work, the permeability μ is always set to μ_0 for all kind of polarisations and propagation directions. One solution to the differential equation (7.33) is

$$E_x(\vec{\mathbf{r}}, t) = \hat{E}_x \cdot e^{i(\omega t - k_z z)}. \quad (7.34)$$

Using Eq. (7.33) and (7.34), the dependence of the propagation constant k on the material parameters μ and ϵ in this case is as follows:

$$k_z^2 = \omega^2 \cdot \mu_0 \cdot \epsilon_x \Rightarrow k_z = \omega \cdot \sqrt{\mu_0 \cdot \epsilon_x} \quad (7.35)$$

Hereby, the wave vector k_z represents a wave that propagates in the z -direction and is polarised in x -direction. Consequently, as it can be seen in Eq. (7.35), the propagation constant k of the electric-field component of an electromagnetic wave with a specific polarisation depends on the value of the respective permittivity ϵ of the material.

Although this example only shows the electric-field propagating along the z axis and polarised in the x -direction, spatial alignments along different coordinate axes also give valid solutions to the Maxwell's equations. As a consequence, wave propagation through a crystal depends on the spatial alignment of the crystal with respect to the incident beam when the crystal has different material parameters for different coordinate axes.

Appendix D

Derivation of the Electro-Optic Phase-Shift ϕ

A birefringent material can have different refractive indices along its optical axes, dependent on the polarisation of the incident electric-field. When an optical beam passes through this material, the polarisation of the beam splits up with respect to the principle axes of the material. Due to that, the electro-magnetic energy distributed among the two orthogonal polarisations propagates with different velocities and a phase shift $\Delta\phi$ is introduced.

In this example, the principle crystal axes are chosen to be in the xy - plane and the propagation takes place along the z - axis. The electric-field with a polarisation along the electro-optically induced x' - axis of the crystal can be described by

$$E_{x'}(t, z) = \hat{E}_{x'} \cdot e^{j(\omega t - k'_{x'} \cdot z)} = \hat{E}_{x'} \cdot e^{j(\omega t - \frac{2 \cdot \pi \cdot n_{x'}}{\lambda} \cdot z)}. \quad (7.36)$$

According to Tab. 3.1, one can rewrite this equation as

$$E_{x'}(t, z) = \hat{E}_{x'} \cdot e^{j(\omega t - \frac{2\pi z}{\lambda} \cdot (n_0 - \frac{1}{2} \cdot n_0^3 \cdot r_{41} \cdot E_z))}. \quad (7.37)$$

The electric-field component along the y' - axis can be written in the same manner:

$$E_{y'}(t, z) = \hat{E}_{y'} \cdot e^{j(\omega t - \frac{2\pi z}{\lambda} \cdot (n_0 + \frac{1}{2} \cdot n_0^3 \cdot r_{41} \cdot E_z))}. \quad (7.38)$$

For a propagation distance $z = l$, the phase difference $\Delta\phi$ is equal to

$$\Delta\phi = \phi_{x'} - \phi_{y'} = \pi \cdot n_0^3 \cdot r_{41} \cdot E \cdot \frac{l}{\lambda} = \frac{1}{2} \cdot \pi \cdot n_0^3 \cdot r_{41} \cdot E \cdot \tau_{prop.} \cdot \omega \quad (7.39)$$

with $\tau_{prop.}$ being the propagation time of the probing beam through the crystal. Taking a look at Eq. 7.39, it is obvious that the phase difference directly depends on the length of the crystal l , its propagation time through it $\tau_{prop.}$, and on the frequency of the probing beam.

Appendix E

Micro-Resonator Configurations Fulfilling the Minimum Performance Requirements

N_1	N_2	N_3	electro-optic enhancement	Reflec-tivity (%)	3dB Band-width (THz)	Phase shift ($^\circ$)	Efficien-cy ($\phi/\mu m$)
1	7	11	2.0628	92.1267	3.3925	2.5675	0.9324
1	9	11	2.099	92.6366	3.1674	2.8731	0.9471
1	11	11	2.0997	93.0949	2.9412	3.1349	0.9491
3	7	11	2.5799	90.0032	2.4887	3.5594	1.1661
3	9	11	2.5189	90.9558	2.2625	3.7879	1.1385
3	11	11	2.4399	91.7466	2.0362	3.9722	1.1028
3	11	11	2.4399	91.7466	2.0362	3.9722	1.1028
3	1	13	2.0869	92.1518	3.3923	2.3834	0.9432
3	3	13	2.3084	93.133	2.9412	2.923	1.0434
3	5	13	2.3889	93.9261	2.7149	3.3216	1.0798
3	7	13	2.3944	94.5669	2.4887	3.6267	1.0823
3	9	13	2.36	95.0903	2.2625	3.8676	1.0667
3	11	13	2.3046	95.5237	2.0362	4.0631	1.0417
3	13	13	2.239	95.887	1.81	4.2254	1.012
5	3	13	2.6909	91.685	2.0362	3.7706	1.2163
5	5	13	2.6564	92.917	1.81	4.0522	1.2004
5	7	13	2.5792	93.8364	1.5837	4.2547	1.1658
3	3	15	2.1019	96.3117	2.9412	2.9453	0.95
3	5	15	2.1965	96.742	2.7149	3.3507	0.9928
3	7	15	2.2203	97.0885	2.4887	3.6627	1.0036
3	9	15	2.2044	97.371	2.2625	3.9102	0.9963
3	11	15	2.1664	97.6044	2.0362	4.1118	0.9791
3	13	15	2.1163	97.8	1.81	4.2796	0.9565
3	15	15	2.0602	97.966	1.81	4.422	0.9312
5	1	15	2.4192	94.5428	2.4887	3.4161	1.0935
5	3	15	2.511	95.4898	2.0362	3.8576	1.135
5	5	15	2.5042	96.1635	1.81	4.1582	1.1319
5	7	15	2.4521	96.6643	1.5837	4.3761	1.1083
7	1	15	2.6097	93.7811	1.5837	4.0374	1.1796

N_1	N_2	N_3	electro-optic enhancement	Reflectivity (%)	3dB Bandwidth (THz)	Phase shift ($^\circ$)	Efficiency ($\phi/\mu m$)
3	5	17	2.0273	98.2661	2.7149	3.3662	0.9163
3	7	17	2.0631	98.4516	2.4887	3.6819	0.9325
3	9	17	2.0604	98.6025	2.2625	3.9329	0.9312
3	11	17	2.0353	98.7271	2.0362	4.1377	0.9199
5	1	17	2.2303	97.0755	2.4887	3.4504	1.0081
5	3	17	2.336	97.5861	2.0362	3.9041	1.0559
5	5	17	2.3476	97.9478	1.81	4.2151	1.0611
5	7	17	2.3138	98.2173	1.5837	4.4416	1.0458
7	1	17	2.4687	96.6341	1.5837	4.1526	1.1158
5	1	19	2.0622	98.4446	2.4887	3.4687	0.9320
5	3	19	2.1751	98.7174	2.0362	3.9289	0.9831
5	5	19	2.1992	98.9106	1.81	4.2454	0.994
5	7	19	2.1787	99.0537	1.5837	4.4765	0.9847
7	1	19	2.3195	98.2011	1.5837	4.2146	1.0484

Tab. 7.1: Resonator configurations that fulfill the minimum requirements listed with their respective electro-optic enhancement, reflectivity, 3 dB - bandwidth, phase shift, and efficiency; Due to space restrictions, $N_{Top-DBR}$ was replaced by N_1 , N_{spacer} by N_2 , and $N_{Bottom-DBR}$ by N_3 . The maximum value for each column is highlighted with a blue background and the five configurations with the maximum electro-optic efficiency are highlighted in bold. The line with the final design is highlighted with a red background.

Appendix F

Jones Matrix Formalism for the Detection System

The Jones formalism is used to calculate the change in the polarisation state for the probe beam when it propagates through the different components of the detection system. The beam is vertically polarised when hitting the sample and its further propagation through the PBS, the $\lambda/4$ -waveplate, and the Wollaston Polariser (compare to Fig. 6.1) can be described by [263]:

$$\epsilon_1 = R\left(\frac{\pi}{4} + \beta\right) N_{wp} R(\alpha) N_{PBS} R\left(-\frac{\pi}{4}\right) N_S R\left(\frac{\pi}{4}\right) \epsilon_0. \quad (7.40)$$

The matrix N_{wp} represents the $\lambda/4$ -waveplate, N_S the sample, and N_{PBS} the polarising beam splitter with the values:

$$N_{wp} = \begin{pmatrix} e^{j\pi/4} & 0 \\ 0 & e^{-j\pi/4} \end{pmatrix}, \quad (7.41)$$

$$N_{PBS} = \begin{pmatrix} \alpha_{PBS} & 0 \\ 0 & 1 \end{pmatrix}, \quad (7.42)$$

$$N_S = \begin{pmatrix} e^{j\phi_{EO}/2} & 0 \\ 0 & e^{-j\phi_{EO}/2} \end{pmatrix}. \quad (7.43)$$

The incident linear polarised beam is represented by a one-column vector with the electric-field strength E_0 ($\epsilon_0 = \begin{pmatrix} E_0 \\ 0 \end{pmatrix}$) and the output beam is $\epsilon_1 = \begin{pmatrix} E_+ \\ E_- \end{pmatrix}$ with two electric-field strengths in the spatially separated beam paths. The matrix $R(\theta)$ is the rotation matrix, which aligns the polarisations of the beam with respect to the principle axes of the optical components in the beam path:

$$R(\theta) = \begin{pmatrix} \cos(\theta) & -\sin(\theta) \\ \sin(\theta) & \cos(\theta) \end{pmatrix}. \quad (7.44)$$

The formula in Ref. [263] was slightly altered compared to the one presented in the respective publication: an additional matrix $R(\alpha)$ is added which accounts for a small misalignment angle α between the principle axes of the $\lambda/4$ -waveplate and the coordinate system (Fig. 7.2). Also, the angle β is added to take into account small misalignments of the Wollaston Polariser. The angle β is thereby the angle between the principle axes of the rotated $\lambda/4$ -waveplate (with respect

to the introduced angle α) and the principle axes of the Wollaston polariser.

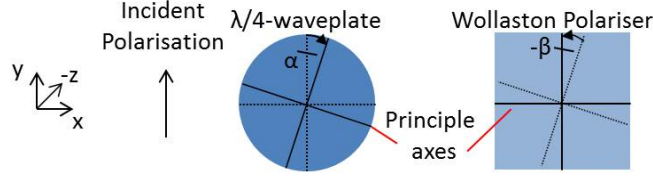


Fig. 7.2: The orientation of the angles α and β with respect to the coordinate system and the principle axes of the waveplate and the polariser.

For a zero THz field ($\phi_{EO} = 0$), the first three elements in Eq. (7.40) can be neglected and the electric-field components E_+ and E_- can be calculated to:

$$E_+ = \alpha_{PBS} E_0 (\cos(\alpha) \cdot \cos(\frac{\pi}{4} + \beta) \cdot e^{j\frac{\pi}{4}} - \sin(\alpha) \cdot \sin(\frac{\pi}{4} + \beta) \cdot e^{-j\frac{\pi}{4}}) = \frac{\alpha_{PBS} E_0}{\sqrt{2}} (\cos(\frac{\pi}{4} + \beta + \alpha) + j \cos(\frac{\pi}{4} + \beta - \alpha)). \quad (7.45)$$

$$E_- = \alpha_{PBS} E_0 (\sin(\frac{\pi}{4} + \beta) \cdot \cos(\alpha) \cdot e^{j\frac{\pi}{4}} + \cos(\frac{\pi}{4} + \beta) \cdot \sin(\alpha) \cdot e^{-j\frac{\pi}{4}}) = \frac{\alpha_{PBS} E_0}{\sqrt{2}} (\sin(\frac{\pi}{4} + \beta + \alpha) + j \sin(\frac{\pi}{4} + \beta - \alpha)). \quad (7.46)$$

In a next step, one can calculate the intensities in each beam ($E = E \cdot E^*$):

$$I_+ = \frac{\alpha_{PBS}^2 I_0}{2} (\cos^2(\frac{\pi}{4} + \beta + \alpha) + \cos^2(\frac{\pi}{4} + \beta - \alpha)), \quad (7.47)$$

$$I_- = \frac{\alpha_{PBS}^2 I_0}{2} (\sin^2(\frac{\pi}{4} + \beta + \alpha) + \sin^2(\frac{\pi}{4} + \beta - \alpha)) \quad (7.48)$$

One can now see that the intensities in both beam paths can be changed by altering the angles α and β . For a perfectly aligned detection system, both angles are zero and the intensities in both paths are $\frac{1}{2} \alpha_{PBS}^2 I_0$, which complies with Eq. (6.1) for $E^{THz} = 0$.

In the measurements throughout this work, only the $\lambda/4$ -waveplate was moved. The Wollaston polariser was kept steady, perfectly aligned to the coordinate system. According to the definition of the angles in Fig. 7.2, this means that $\beta = -\alpha$ for all times. Hence, Eq. (7.47) and (7.48) can be simplified to:

$$I_+ = \frac{\alpha_{PBS}^2 I_0}{2} (0.5 + \cos^2(\frac{\pi}{4} - 2\alpha)), \quad (7.49)$$

$$I_- = \frac{\alpha_{PBS}^2 I_0}{2} (0.5 + \sin^2(\frac{\pi}{4} - 2\alpha)). \quad (7.50)$$